STRUCTURAL, MAGNETIC, THERMAL, MESOMORPHIC AND DENSITY FUNCTIONAL THEORETICAL STUDIES OF COMPLEXES OF COPPER(II) AND IRON(II) WITH CARBOXYLATE IONS AND 2,2'-BIPYRIDINE LIGANDS

LAILATUN NAZIRAH OZAIR

FACULTY OF SCIENCE

UNIVERSITY OF MALAYA

KUALA LUMPUR

2016

UNIVERSITI MALAYA

ORIGINAL LITERARY WORK DECLARATION

Name of Candidate: LAILATUN NAZIRAH OZAIR

Registration/Matric No: SHC120096

Name of Degree: DOCTOR OF PHILOSOPHY

Title of Project Paper/Research Report/Dissertation/Thesis ("this Work"):

STRUCTURAL, MAGNETIC, THERMAL, MESOMORPHIC AND DENSITY FUNCTIONAL THEORETICAL STUDIES OF COMPLEXES OF COPPER(II) AND IRON(II) WITH CARBOXYLATE IONS AND 2,2'-BIPYRIDINE LIGANDS

Field of Study: Material Chemistry

I do solemnly and sincerely declare that:

(1) I am the sole author/writer of this Work;
(2) This Work is original;
(3) Any use of any work in which copyright exists was done by way of fair dealing and for permitted purposes and any excerpt or extract from, or reference to or reproduction of any copyright work has been disclosed expressly and sufficiently and the title of the Work and its authorship have been acknowledged in this Work;
(4) I do not have any actual knowledge nor do I ought reasonably to know that the making of this work constitutes an infringement of any copyright work;
(5) I hereby assign all and every rights in the copyright to this Work to the University of Malaya ("UM"), who henceforth shall be owner of the copyright in this Work and that any reproduction or use in any form or by any means whatsoever is prohibited without the written consent of UM having been first had and obtained;
(6) I am fully aware that if in the course of making this Work I have infringed any copyright whether intentionally or otherwise, I may be subject to legal action or any other action as may be determined by UM.

Candidate's Signature Date: 08 September 2016

Subscribed and solemnly declared before,

Witness's Signature Date: 08 September 2016

Name: ASSOC. PROF. DR. NORBANI ABDULLAH

Designation:

ABSTRACT

This research is focused on the syntheses and characterization of magnetic, thermally stable and mesomorphic complexes of copper(II) and iron(II) of general formula $[Cu_2(RCOO)_4(bpy)_2]$ and $[Fe(RCOO)_2(bpy)]$ (R = $CH_3(CH_2)_{6-14}$, *p*-$CH_3(CH_2)_{9-15}C_6H_4$; bpy = 2,2'-bipyridine), respectively, and study their magnetic properties (for the copper(II) complexes) and structures (for the iron(II) complexes) by density functional theories (DFT). The structures of ligands and complexes were deduced by CHN elemental analyses, ^{1}H-NMR spectroscopy (for ligands), FTIR spectroscopy, UV-vis spectroscopy, and X-ray crystallography (for single crystals). The magnetic susceptibilities of complexes were determined at room temperature by the Gouy method, their thermal stabilities by thermogravimetry (TG), and their mesomorphic properties by differential scanning calorimetry (DSC) and polarizing optical microscopy (POM). The geometry optimization and frequencies calculations were done using Gaussian09W package with DFT B3LYP method and 6-31G basis set. A total of nine copper(II) complexes and eight iron(II) complexes were successfully synthesised and characterised. All copper(II) complexes have square pyramidal Cu(II) centres with monodentate and *syn-anti* bridging carboxylato ligands, were magnetic, thermally stable (T_{dec} ranged from 173 ^oC to 272 ^oC), and mesomorphic. All iron(II) complexes were octahedral with a mixture of high spin (HS) and low spin (LS) iron(II) atoms at room temperature, and thermally stable (T_{dec} ranged from 152 ^oC to 160 ^oC). The alkylcarboxylate complexes, except for $[Fe_2(CH_3(CH_2)_{10}COO)_4(bpy)]$, were not mesomorphic,. The arylcarboxylate complexes were mesomorphic. The molecular modelling for copper(II) complex (**1**) and iron(II) complexes (**6** and **16**) showed good agreement between the experimental and theoretical data.

ABSTRAK

Penyelidikan ini berfokuskan sintesis dan pencirian kompleks magnetik, stabil terma dan mesomorfik kuprum(II) dan ferum(II), masing-masing dengan formula umum $[Cu_2(RCOO)_4(bpy)_2]$ dan $[Fe(RCOO)_2(bpy)]$ (R = $CH_3(CH_2)_{6-14}$, *p*-$CH_3(CH_2)_{9-15}C_6H_4$; bpy = 2,2'-bipyridine), dan mengkaji sifat magnet (bagi kompleks kuprum(II)) dan struktur (bagi kompleks ferum(II)) melalui teori ketumpatan fungsian (DFT). Struktur ligan dan kompleks dideduksikan secara analisis unsur CHN, spektroskopi ^{1}H-NMR (untuk ligan), spektroskopi FTIR, spektroskopi UV-nampak, dan kristolagrafi sinar X (untuk hablur tunggal). Kerentanan magnet kompleks ditentukan pada suhu bilik melalui kaedah Gouy, kestabilan terma melalui termogravimetri (TG), dan sifat mesomorfik melalui kalorimetri imbasan perbezaan (DSC) dan mikroskopi pengutuban optik (POM). Pengoptimum geometri dan pengiraan frekuensi dilakukan dengan menggunakan pakej Gaussian09W dengan kaedah DFT B3LYP dan set asas 6-31G. Sejumlah sembilan kompleks kuprum(II) dan lapan kompleks ferum(II) berjaya disintesis dan dicirikan. Semua kompleks kuprum(II) mempunyai pusat Cu(II) piramid sisi empat sama dengan ligan karboksilat monodentat dan titian *syn-anti*, magnetik, stabil terma (T_{urai} dalam julat 173 ^oC hingga 272 ^oC), dan mesomorfik. Semua kompleks ferum(II) adalah oktahedral dengan campuran atom ferum(II) spin tinggi (HS) dan spin rendah (LS) pada suhu bilik, dan stabil terma (T_{urai} dalam julat 152 ^oC hingga 160 ^oC). Kompleks alkilkarboksilat, kecuali $[Fe_2(CH_3(CH_2)_{10}COO)_4(bpy)]$, adalah tidak mesomorfik. Kompleks arilkarboksilat adalah mesomorfik. Pemodelan molekul bagi kompleks kuprum(II) (**1**) dan kompleks ferum(II) (**6** dan **16**) menunjukkan persamaan yang baik antara data eksperimen dengan data teori.

ACKNOWLEDGEMENTS

The process of earning a doctorate and writing a dissertation would not possible without the help and support of kind people around me. Above all, thanks to ALLAH for bestowing his great mercy to me.

I would like to express my deepest appreciation to my supervisor, Assoc. Prof. Dr. Norbani Abdullah, who was helpful and offered such invaluable assistance, support and guidance. Without her guidance and persistent help, this research would not have been possible.

Particularly, I would like to thank my husband, Mohd Firdaus Mohd Iskandar, for his consistent love, support and sacrifices through this journey.

I owe my deepest gratitude to my beloved daughter, Adeleia Sophia for her understanding and endless love, and my parents Ozair Saidin and Dr. Zamrudah Zainuddin, for their support in every aspect of this research.

I am indebted to my colleagues from the inorganic chemistry research laboratory, my friends and all staff in the Chemistry Department, University of Malaya, for the invaluable assistance.

Last but not least, I would like to acknowledge the scholarship from Ministry of Higher Education Malaysia (MyPhD) and the following grants for this research: Fundamental Sciences of Self Assembly High Impact Research Grant (UM.C/625/1/HIR/MOHE/05) and University of Malaya Postgraduate Research Grant (PG023-2013A).

TABLE OF CONTENTS

LIST OF FIGURES

LIST OF TABLES

LIST OF SCHEMES

CHAPTER 1: INTRODUCTION

Metallomesogen is a metal-containing liquid crystal. The main interest in this research area is to study the possibility of combining the properties of liquid crystals, such as fluidity, ordered molecular arrangement in one or two dimension and self-healing, with the properties associated with metal(II) ions, especially those of the transition metals (colour, magnetism, high electron density, redox ability).

Combining the characteristics between metallomesogen and magnetism showed a few interesting properties such as paramagnetic liquid crystal and the molecular orientation in the magnetic field can be controlled [1,2].

The main objectives of this research were to (a) synthesize and characterize thermally stable, magnetic and mesomorphic complexes of general formulae $[Cu_2(RCOO)_4(bpy)_2]$ and $[Fe_2(RCOO)_4(bpy)]$, where R = $CH_3(CH_2)_{6-14}$ and $CH_3(CH_2)_{9-15}C_6H_4$, and bpy = 2,2'-bipyridine (**Scheme 1.1**), (b) study the magneto-structural correlation for selected copper(II) complexes and structural confirmation for selected iron(II) complexes by comparing the theoretical and experimental FTIR data using density functional theories (DFT), and (c) ascertain if magnetism and mesomorphism may be tuned by changing the chain length of the alkylcarboxylate and as well as the effect of inserting an aromatic ring in the carboxylate ligands.

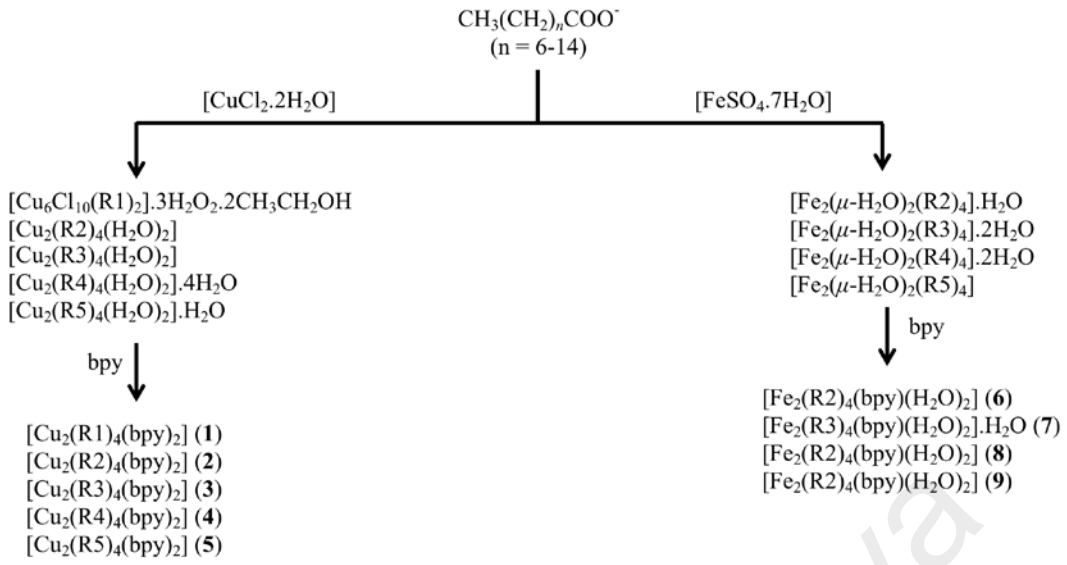

(a)

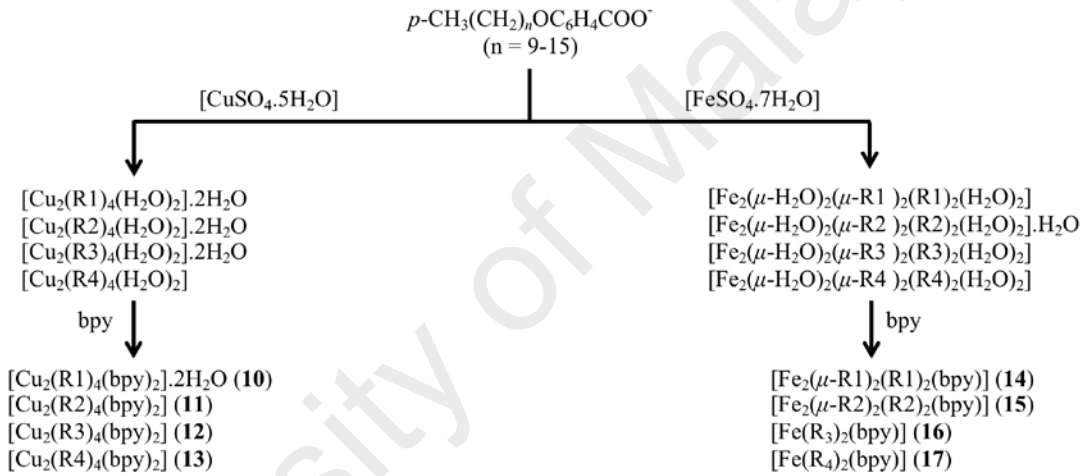

(b)

Scheme 1.1 Synthetic steps for; (a) Complexes **1-9.** R1 = $CH_3(CH_2)_6COO$; R2 = $CH_3(CH_2)_8COO$, R3 = $CH_3(CH_2)_{10}COO$, R4 = $CH_3(CH_2)_{12}COO$ and R5 = $CH_3(CH_2)_{14}COO$; (b) Complexes **10-18**, R1 = *p*-$CH_3(CH_2)_9OC_6H_4COO$, R2 = *p*-$CH_3(CH_2)_{11}OC_6H_4COO$, R3 = *p*-$CH_3(CH_2)_{13}OC_6H_4COO$ and R4 = *p*-$CH_3(CH_2)_{15}OC_6H_4COO$

A total of 17 complexes were obtained with four of them single crystals. The structures of the crystals were determined by X-ray crystallography, while the structures for non-crystalline complexes were deduced by combining the data from elemental analyses and spectroscopies (^{1}H-nuclear magnetic resonance for organic ligands, FTIR and UV-vis). The magnetic susceptibility of the complexes was studied using the Gouy

method. The thermal properties were studied using the thermogravimetry (TG), and mesomorphic properties by differential scanning calorimetry (DSC) and polarizing optical microscopy (POM).

The findings from this research were published in two ISI journals, and presented at three conferences, as listed below and shown in **Appendix 1**.

1. Abdullah, N.; Sharmin, N.; **Ozair, L.N**.; Nordin, A. R.; Mohd. Nasir, W. S. N.; Mohamadin, M. I., *Structures and mesomorphism of complexes of tetrakis(4-chlorobenzoate-μ-O, O')bis(ethanol)dicopper(II) with different N-donor ligands*. Journal of Coordination Chemistry, 2015, 68(8), 1347-1360.
2. Abdullah, N.; Hashim, R.; Ozair, L. N.; Al-Hakeem, Y.; Samsudin, H.; Anita Marlina, Salim, M.; Mohd. Said, S.; Subramanian, B.; Nordin, A. R., *Structural, mesomorphic, photoluminescence and thermoelectric studies of mononuclear and polymeric complexes of copper(II) with 2-hexyldecanoato and 4,4'-bipyridine ligands*. Journal of Material Chemistry C, 2015, 3, 11036-11045.
3. Lailatun Nazirah Ozair, Naima Sharmin, Nur Syamimi Ahmad Tajidi, Norbani Abdullah, Zainudin Arifin, *Structural and mesogenic properties of copper(II) carboxylates with different N-donor ligands*, Joint Malaysia-UK Symposium on Inorganic Chemistry, 5 December, 2013, Deparment of Chemistry, Faculty of Science, University of Malaya (Poster).
4. Lailatun Nazirah Ozair, Norbani Abdullah, *Synthesis, thermal studies and optical textures of* $[Cu_2(C_nH_{2n+1}COO)_4(2,2'\text{-bipyridine})_2(H_2O)_2]$, The International Conference on Ionic Liquid, 11-13 December, 2013, Langkawi Island, Kedah, Malaysia (Oral).
5. Lailatun Nazirah Ozair, Norbani Abdullah, *Synthesis, structural, optical properties and magnetism of* $[Cu_2(C_nH_{2n+1}COO)_4(2,2'\text{-bipyridine})_2]$ *and* $[Cu_2(C_nH_{2n+1}OC_6H_4COO)_4(2,2'\text{-bipyridine})_2]$, 2015 International Conference on

Engineering, Technology and Applied Science – Fall Session, 10-12 November, 2015, Nagoya, Japan (Oral).

This thesis is divided into five chapters. **Chapter 1** briefly introduces the objectives of the research and list the papers published and presented at conferences. **Chapter 2** covers the theory and literature reviews on copper(II) and iron(II) carboxylates, focussomg on the structural elucidation followed by magnetic, thermal and mesomorphic properties. Relevant theoretical concepts are also presented in this chapter. **Chapter 3** presents the experimental part of the research, covering the materials used in the research, the syntheses of the ligands and complexes, and instrumental techniques for their characterization. **Chapter 4** contains the results and discussion, and finally **Chapter 5** presents the conclusions and suggestions for future works. A list of references and appendixes are included at the end the thesis.

CHAPTER 2: THEORY AND LITERATURE RIVIEW

2.1 Introduction

This chapter covers the chemistry of copper(II) carboxylates and iron(II) carboxylates, and their complexes with N-donor ligands. It includes the basic concepts used for the elucidation of their structures, namely single crystal X-ray crystallography, elemental analyses, FTIR spectroscopy, UV-vis spectroscopy, ^{1}H-NMR spectroscopy, and magnetism. These are followed by studies on their thermal stability by thermogravimetry (TG), mesomorphisms by polarizable optical microscopy (POM) and differential scanning calorimetry (DSC), and finally, the correlation between structure and the concept of molecular modeling.

2.2 Copper(II) carboxylates

2.2.1 Syntheses and structures

Copper(II) carboxylates are usually dimeric complexes with the general formula, $[Cu_2(RCOO)_4]$. They are easily prepared from cheap non-poisonous starting materials, usually by reacting a copper(II) salt with a carboxylate ion [3] or from the reaction of the corresponding carboxylic acids with copper(II) carbonate or copper(II) acetate [4-6] (**Scheme 2.1**).

$$Cu^{2+} + 2\ RCOO^{-} \rightarrow [Cu(RCOO)_2]$$

$$CuCO_3(OH)_2 + 2RCOOH \rightarrow [Cu(RCOO)_2] + 2H_2O + CO_2$$

$$Cu(CH_3COO)_2 + 2RCOOH \rightarrow [Cu(RCOO)_2] + 2CH_3COOH$$

Scheme 2.1 Reaction equations for the formation of $[Cu_2(RCOO)_4]$

Most copper(II) carboxylates were reported to adopt the paddle-wheel structure [7,8]. In this structure, four bidentate carboxylates ligands were bridged to each copper(II) and forming a basal plane (**Figure 2.1(a)**). The free axial position of the

copper(II) may be occupied with an oxygen or a nitrogen donor atom from the solvent molecules such as methanol [4], acetonitrile [9], pyridine [10] (**Figure 2.1(b)**) or by an oxygen atom of another dimer forming an oligomeric chain [11] (**Figure 2.1(c)**).

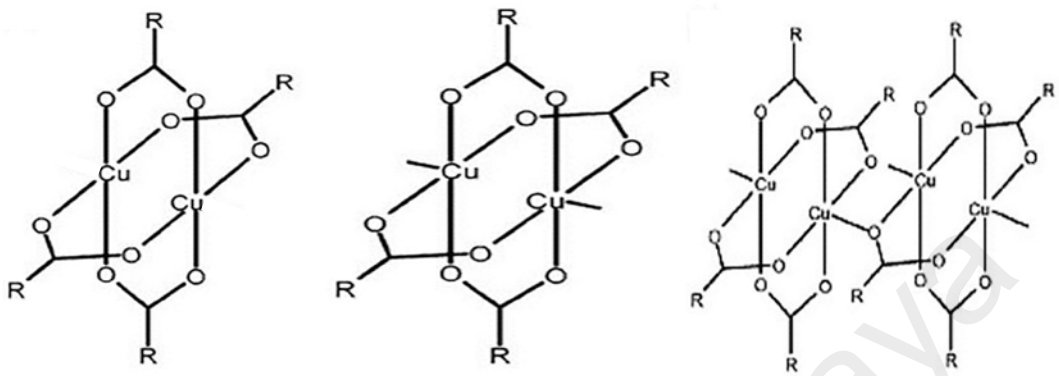

(a) (b) (c)

Figure 2.1 Paddle-wheel structure of: (a) $[Cu_2(RCOO)_4]$; (b) $[Cu_2(RCOO)_4(L)_2]$ and (c) polymeric $[Cu_2(RCOO)_4]$

Carboxylate ions ($RCOO^-$) have varieties of binding modes (Scheme 2.2). However, the ions mostly show three main bridging coordination modes in copper(II) complexes, such as syn-syn, syn-anti and anti-anti (Figure 2.2).

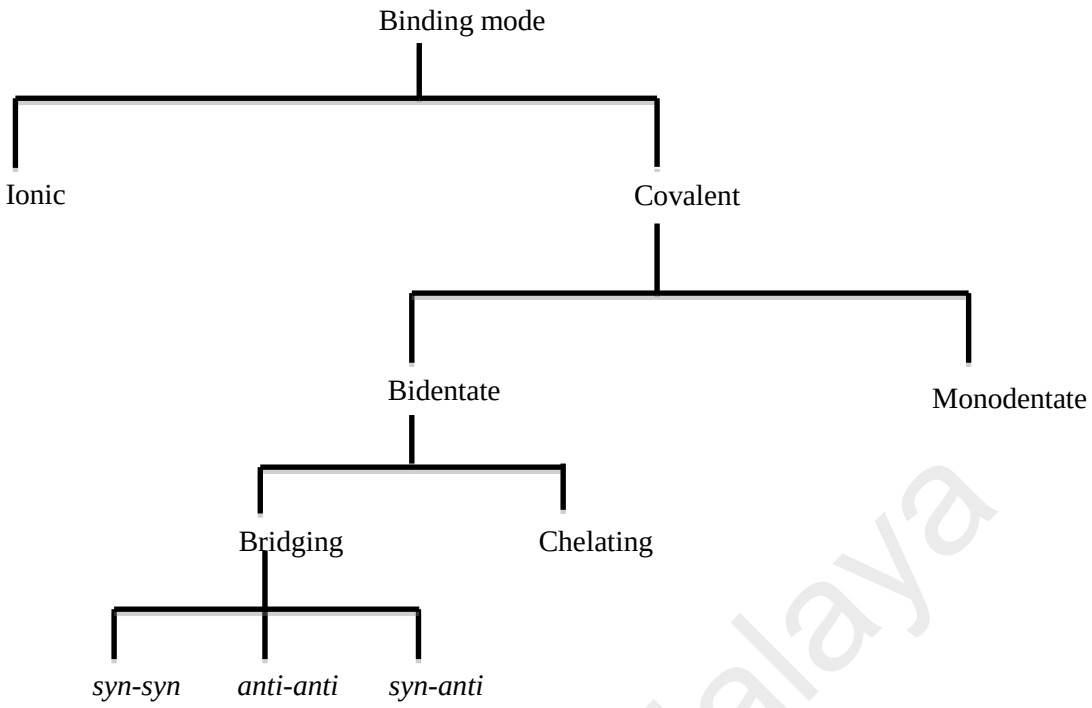

Scheme 2.2 Binding modes of carboxylate ions

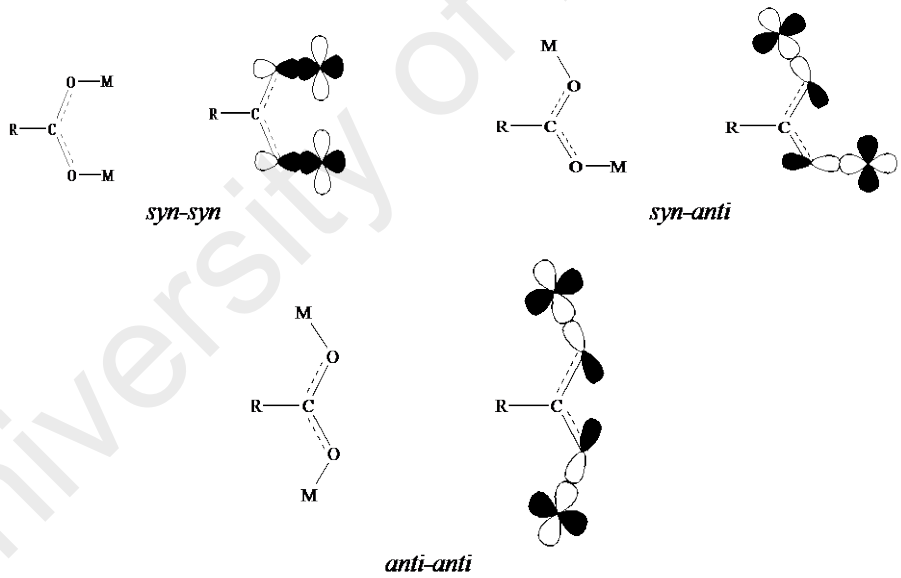

Figure 2.2 Bridging coordination modes of $RCOO^-$ ligand

FTIR spectroscopy may be used to deduce the binding mode of $RCOO^-$ ion to the metal centre, based on the difference (Δ) between the values for $\upsilon_{asymCOO}$ and υ_{symCOO}. The value of $\upsilon_{asymCOO}$ is normally found in the range of 1678-1541 cm^{-1}, while that for the υ_{symCOO} is normally found in the range of 1417-1202 cm^{-1} [12]. The Δ value of less than 120 cm^{-1} usually indicates chelating carboxylate group, while value in the

range of 130-180 cm^{-1} indicates bridging coordination mode. A complex with a monodentate carboxylate group has a larger Δ_{COO} value (>200 cm^{-1}). The general trend is shown below:

$$\Delta(\text{chelating}) < \Delta(\text{ionic}) < \Delta(\text{bridging}) < \Delta(\text{monodentate})$$

FTIR spectrum also shows the presence of other functional groups. As examples, the aliphatic groups (CH_2 asymmetric and symmetric) peaks are found in the range of 2960-2850 cm^{-1}, C=C aromatic peak is found in the range of 1600-1500 cm^{-1}, and a peak for the C-N bond stretch is found in the range of 1300-1100 cm^{-1} [13-16].

The geometry of both copper(II) atoms in copper(II) carboxylates with the paddle-wheel structure is square pyramidal. However, copper(II) is geometrically plastic, and may show other geometries, such as octahedral (distorted due to Jahn-Teller effect), square planar and tetrahedral. These geometries may be inferred from the wavelength of its d-d band in the UV-vis spectrum [17,18].

UV-visible spectroscopy (UV-vis) covers the electromagnetic region from ultraviolet to near infrared regions (200-1000 nm). An important equation from UV-vis is known as Beer-Lambert's law: $A = \varepsilon cl$, where A is the absorbance (no unit), ε is the molar absorptivity ($dm^3\ mol^{-1}\ cm^{-1}$), c is the molarity of the solution (mol dm^{-3}) and l is the path length of the light (dimension of a cell or cuvette in cm). The molar absorptivity is to measure of how strongly a chemical species absorbs light at a given wavelength.

The d-d transitions refer in the visible region (lower energy) and the intensity is much lower than the charge transfer (CT) bands. From the crystal-field theory, the five degenerate d orbitals from the metal ion split in the presence of ligands. The splitting depends on the metal ion, ligands and geometry of the complex (**Figure 2.3**).

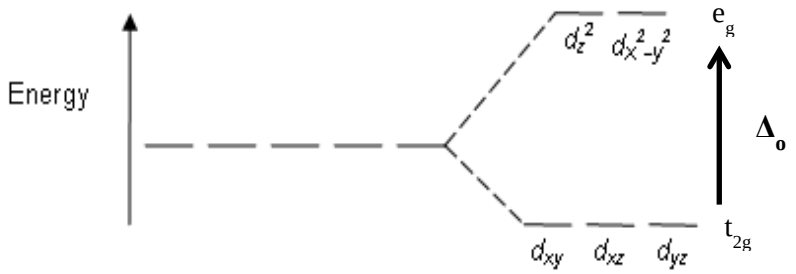

(a)

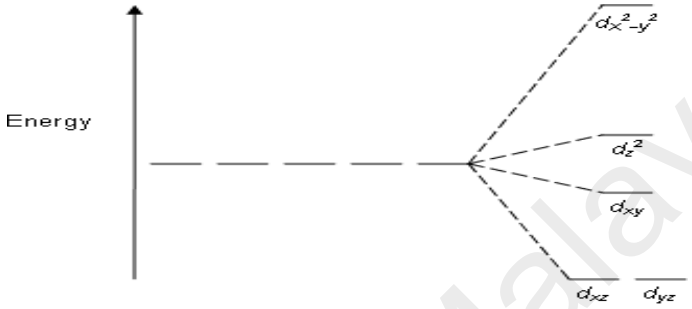

(b)

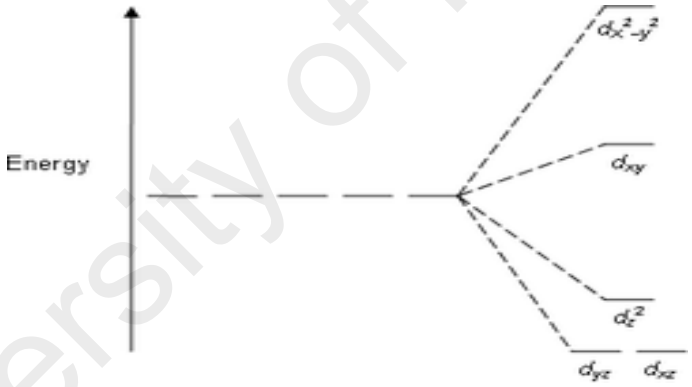

(c)

Figure 2.3 The energy of the d-orbitals in an (a) octahedral, (b) square pyramidal, and (c) square planar geometry

In an octahedral complex, 3d orbitals split into three lower energy t_{2g} orbitals (*xy*, *xz*, *yz*) and two higher energy e_g orbitals (z^2, x^2-y^2). In a square pyramidal complex, the 3d orbitals split into two lower energy (*xz*, *yx*) followed by *xy* and z^2. The highest energy level was x^2-y^2, while in a square planar complex, z^2 orbital is lower than xy orbital.

According to the Laporte rule, the d-d transition is forbidden but multiplicity allowed for the octahedral and square planar complexes (complexes with centre of

inversion). Thus, these complexes usually show a weak band ($\varepsilon \sim 1\text{-}10\ dm^3\ mol^{-1}\ cm^{-1}$) with pale colour. On the other hand, complexes with no centre of inversion such as tetrahedral and square pyramidal, are not governed by this rule. Therefore they have stronger band(s) ($\varepsilon \sim 100\ dm^3\ mol^{-1}\ cm^{-1}$) and are more intense in colour.

For first-row transition metal complexes, the electronic transitions are d-d and charge transfer (CT), which may either be ligand-to-metal charge transfer (LMCT) or metal-to-ligand charge transfer (MLCT). LMCT refers to an electronic excitation from the ligand orbital ("oxidation") to the metal orbital ("reduction"), and opposite applies to the MLCT. The CT bands reside in the high energy region and were highly intense ($\varepsilon > 10^3\ dm^3\ mol^{-1}\ cm^{-1}$).

For copper(II) carboxylates, the favourable coordination environment at the metal(II) centre is square pyramidal and the d-d band is expected at about 700 nm [19]. The band for a tetrahedral complex is normally at about 800 nm, and a square planar complex at about 600 nm [20]. Another characteristic for dinuclear copper(II) carboxylates is a shoulder band at about 300 nm [21].

Copper(II) ion has one unpaired electron as its valence electronic configuration is $3d^9$. Hence, it forms paramagnetic complexes. A paramagnetic material has one or more unpaired electrons (the overall spin quantum number is be greater than zero).

Magnetic properties of a material can be deduced from the value of its effective magnetic moment (μ_{eff}). This can be calculated from the following equations:

$$\chi_M = \chi_g \times M_r$$

$$\chi_M^{corr} = \chi_M - \chi_D$$

$$\mu_{eff} = 2.828(\chi_m^{corr}\, T)^{1/2}$$

where χ_M is molar magnetic susceptibility, χ_g is gram magnetic susceptibility (reading from the instrument), M_r is the molar mass, χ_D is the magnetic susceptibility corrected

from half value of M_r x 10^{-6} [22], χ_M^{corr} is the corrected molar magnetic susceptibility, and T is the absolute temperature.

For dinuclear copper(II) complexes, there are magnetic interactions between the unpaired electron on each copper(II) centre. These interactions may either be antiferromagnetic, ferromagnetic and ferrimagnetic. The unpaired electrons in an antiferromagnetic material align with the directions of the neighbouring spins anti-parallel to each other (**Figure 2.4(a)**). In contrast, the unpaired electrons in a ferromagnetic material are aligned in the same direction in the absence of an external magnetic field (**Figure 2.4(b)**), resulting in a strong and permanent magnet. In a ferrimagnetic material, some of the electronic spins are arranged in a parallel pattern but with different strength of the magnetic spin (**Figure 2.4(c)**) [23-24].

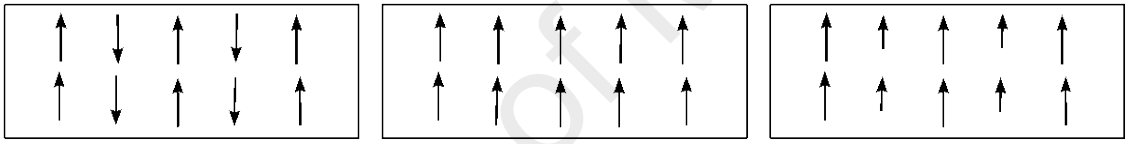

(a) (b) (c)

Figure 2.4 Electron spin alignment (a) antiferromagnetism; (b) ferromagnetism; and (c) ferrimagnetism

The difference in the energy of the singlet ground state and triplet excited state dependes on the magnitude of the magnetic interaction (2J). The value can be calculated using the Bleaney-Bowers equation, shown below for a dimeric copper(II) complex:

$$\chi_M = 2Ng^2\beta^2/(3kT)*\{1+1/3\exp(-2J/kT)\}^{-1} + 0.12 \times 10^{-3}$$

The 2J value is negative if the interaction is antiferromagnetic, and positive if the interaction is ferromagnetic. For dinuclear copper(II) carboxylates, there are several factors affecting the 2J values. Firstly, the value is dependent on the Cu---Cu distance. A larger Cu---Cu distance leads to a smaller overlapping of the δ-bonding between the two copper(II) atoms, resulting in a lower coupling constant [25].

The 2J values also depend on the basicity of the ligand attached at the axial position of the copper(II) centres. Stronger antiferromagnetic interactions are found for

complexes with weaker axial ligands (weaker σ donation) [26]. For example, the 2J value for $[Cu_2(O_2CCH_3)_4(H_2O)_2]$ with H_2O ligands coordinated at both axial positions, was -299 cm^{-1}, but the value was lower (2J = -284 cm^{-1}) when H_2O was replaced with NH_3, indicating weaker antiferromagnetic interaction [27].

The 2J values also depend on the substituents at the aromatic ring of arylcarboxylato ligands. For example, Rodríguez-Fortea *et al.*, showed that electron-withdrawing groups reduced the strength of the exchange coupling [27].

Another factor affecting the 2J values is the Cu-O bridging bonds. Basically, the super-exchange pathway mechanism was through the Cu-O-C(R)-O-Cu bridges [28]. A strongly bonded R to COO results in a stronger Cu-O bond in the CuO_4 basal plane. Thus, when the Cu-O bond decreased, the coupling constant value increased. An antiferromagnetic interaction is found in a complex with Cu-O-Cu angle (θ), $95.34^o < \theta < 101.9^o$, and ferromagnetic interaction when the angle is larger than 101.9^o [29].

Copper(II) arylcarboxylates were found to have the paddle-wheel structure. An example is $[Cu_2(OOCC_6H_5)_4(CH_3CH_2OH)_2]$ (Figure 2.5), reported by Hamza and Kickelbick [4]. It was the unreacted starting material from the reaction of $[Cu_2(OOCC_6H_5)_4(CH_3CH_2OH)_2]$ and benzyol peroxide. The complex was blue crystals obtained after a few days. It crystallised in the monoclinic C_2/c group.

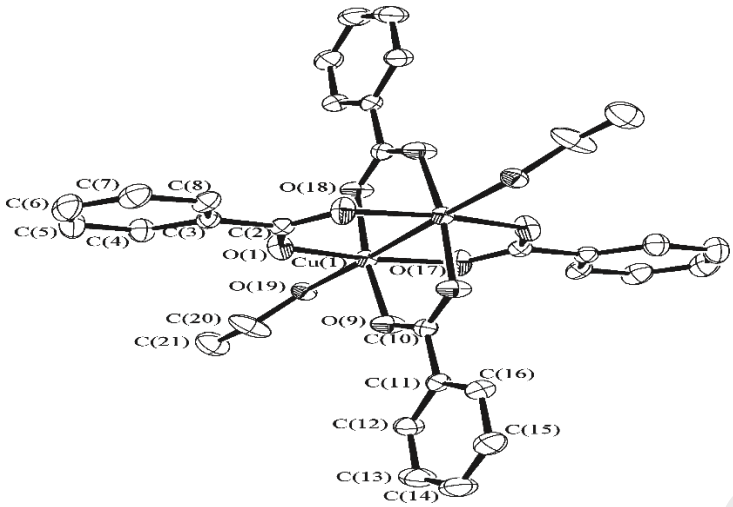

Figure 2.5 ORTEP view of the molecular structure of $[Cu_2(OOCC_6H_5)_4(CH_3CH_2OH)_2]$ displaying the thermal ellipsoids at 30% probability. H atoms are omitted for clarity [4]

Copper(II) alkylcarboxylates were also found to adopt the paddle-wheel structure. For example, Abdullah *et al*. reported bluish-green crystals of $[Cu_2(CH_3(CH_2)_5COO)_4]$ (**Figure 2.6**) [30], formed when the blue powder formed in the reaction of $CH_3(CH_2)_5COONa$ with $CuCl_2.2H_2O$ was recrystallized from THF-MeOH. Its molecular structure showed a triclinic polymorph with $P\bar{1}$ space group. As expected for a dinuclear paddle-wheel structure, its FTIR spectrum gave the Δ_{COO} value of 173 cm^{-1}, while its UV-vis spectrum showed a band at 671 nm (ε_{max} = 375 M^{-1} cm^{-1}). Its μ_{eff} value was 1.6 BM, while the theoretical value for a dinuclear copper(II) (S = ½, g = 2) is 2.43 BM ($\chi_m T$ = 0.375 cm^3 K mol^{-1} per copper(II) [22]. Hence, this complex exhibited a strong antiferromagnetic interaction between the unpaired electron of each copper(II) centre.

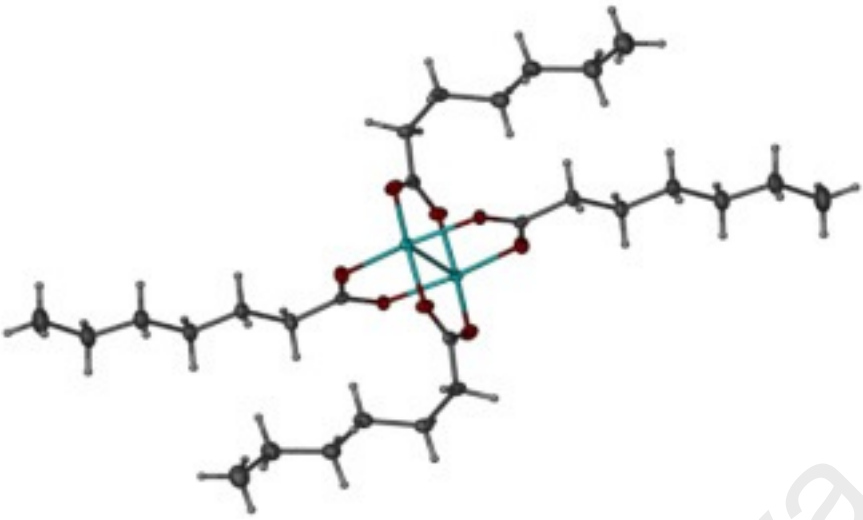

Figure 2.6 Crystal structure of $[Cu_2(CH_3(CH_2)_5COO)_4]$ [30]

However in 2011, Castro *et al*. reported an unexpected hexanuclear copper(II) carboxylate, $[Cu_6(O_2CC_6H_2(OCH_2CH_3)_3)_{12}]$ (**Figure 2.7**) [31]. The complex was obtained as green crystals from the reaction of $[Cu_2(O_2CCH_3)_4].2H_2O$ with 3,4,5-tri(ethoxy)benzoic acid in methanol:ethanol (85:15 v/v). Its molecular structure showed syn-syn bridges, syn-anti bridges and an oxygen atom bridging in either syn or anti conformations to the copper(II) centres. Each copper(II) atom was pentacoordinated to five carboxylate ligands in pseudo square pyramidal geometry (ΔCOO value was 162 cm^{-1}, and λ_{max} was 685 nm (ε_{max} = 505 M^{-1} cm^{-1}). Its μ_{eff} value was 5.44 BM (g_{iso} = 2.28).

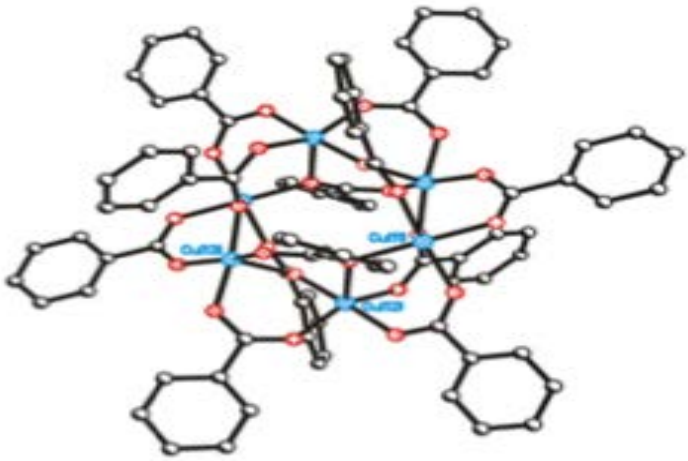

Figure 2.7 Crystal structure of $[Cu_6(O_2CC_6H_2(OCH_2CH_3)_3)_{12}]$ [31]

2.2.2 Thermal and mesomorphic properties

Copper(II) carboxylates were reported to be thermally stable, and when the ligands are alkylcarboxylate ions or have alkyl(oxy) chains, to exhibit liquid crystal properties. The thermal stability of a complex may be determined by thermogravimetry (TG). In this technique, the percentage weight loss of a sample is measured as it is heated (usually up to 1000 ^{o}C) in a controlled N_2 atmosphere. Most copper(II) carboxylates decomposed at about 200 ^{o}C due to the decarboxylation of the ligand and loss of CO_2 [32]. For example, $[Cu_2(CH_3(CH_2)_5COO)_4]$ was stable up to 280 ^{o}C [30].

Liquid crystal (LC) is a state of matter between the solid and liquid states. Hence, LC materials are fluidic but their molecules arranged in an orderly manner as in solids (**Figure 2.8**).

Solid Liquid crystal Liquid

Figure 2.8 Molecular arrangement in a solid, a liquid crystal and a liquid

Friedrich Reinitzer discovered LC in 1888 when he claimed that cholesteryl benzoate has two distinct melting points. During his experiment he observed that the compound did not melt directly on heating, but instead changed into a hazy liquid (mesophase), and only became a clear transparent liquid (isotropic) on further heating. This behavior is characteristic of a LC. The temperature at which a material changes to a mesophase (M) is known as its melting temperature, and the temperature when a mesophase changes to an isotropic liquid (I) is known as its clearing temperature.

There are two general types of liquid crystals: lyotropic LC and thermotropic, LC (**Scheme 2.3**). For lyotropic LC, the mesomorphic properties were observed in solutions and controlled by concentrations, while for thermotropic LC, the

mesomorphic properties were induced by heat. Thermotropic LC can be further divided into several types, depending on the shapes of the molecules, specifically rod-like for calamitic LC and disc-like for discotic LC.

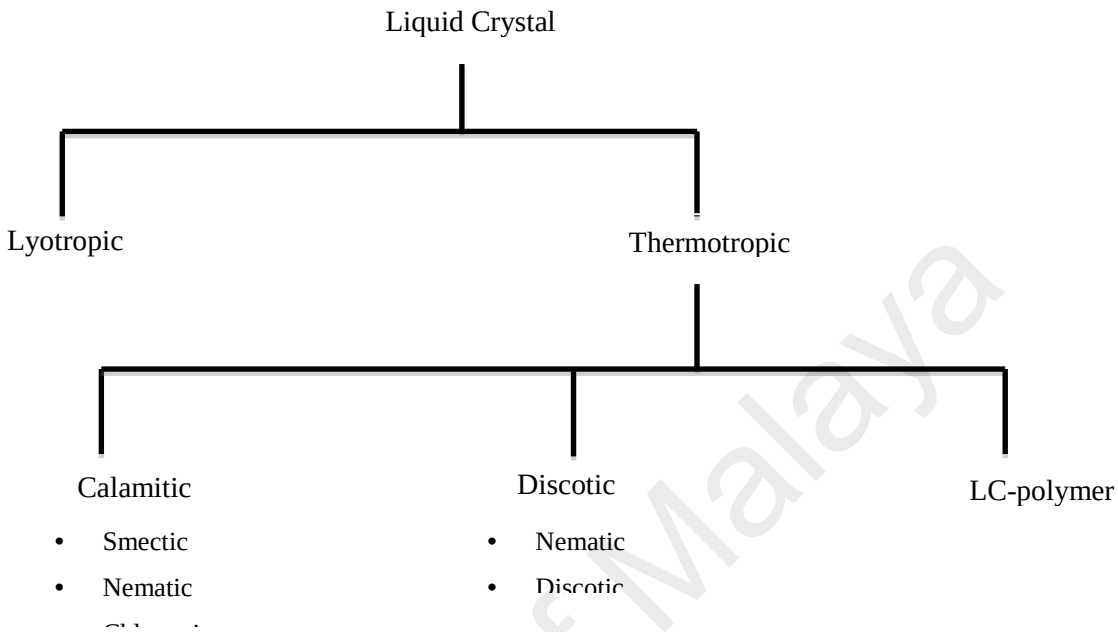

Scheme 2.3 Classification of liquid crystals

In designing liquid crystals, the mesogens require long alkyl(oxy) chain (C_nH_{2n+1}(O); n > 8). Calamitic LC are compounds with rod-like structures, and exhibited nematic and smectic mesophases (**Figure 2.9**). The nematic mesophase (N) is the least ordered and very fluid, and usually displayed a schlieren texture when viewed under a polarizing optical microscope (**Figure 2.10(a)**) [33]. On the other hand, the smectic mesophase is more positionally oriented and ordered. Two most commonly found smectic mesophases are smectic A (SmA) (**Figure 2.10(b)**) and smectic C (SmC) (**Figure 2.10(c)**).

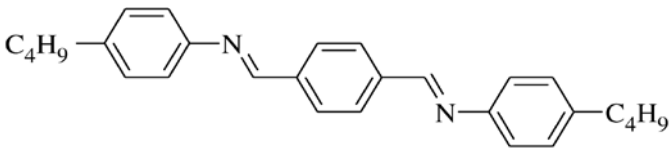

Figure 2.9 An example of a molecular structure for calamitic LC

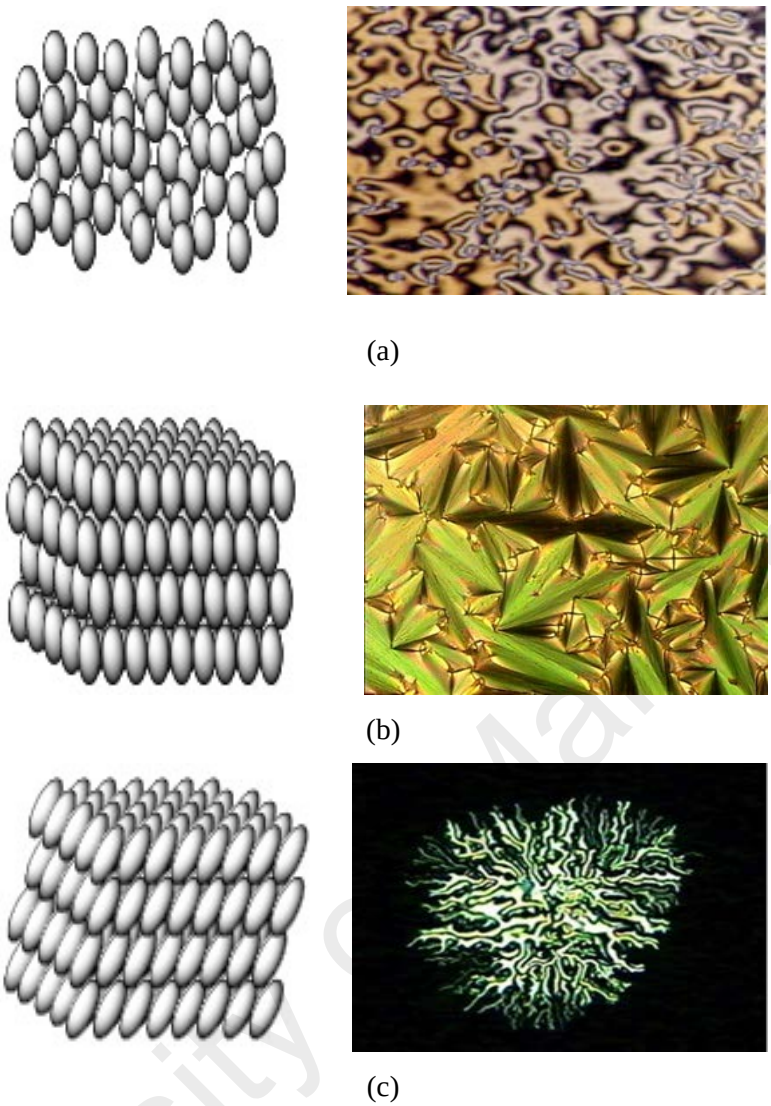

Figure 2.10 Examples of calamitic LC textures (a) nematic; (b) smectic A; and (c) smectic C

Discotic mesogens have disc-like structures, and exhibited discotic nematic (N_D) and columnar (Col) mesophases (**Figure 2.11**).

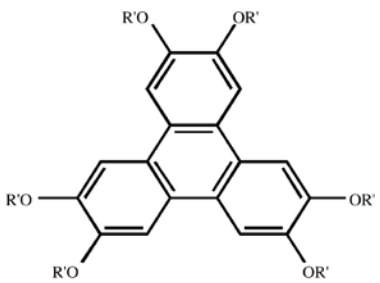

Figure 2.11 An example of molecular structure for discotic LC (R = *p*-$C_nH_{2n}C_6H_4CO$-)

In the N_D mesophase, which is not commonly observed, the molecules were aligned in a parallel direction and can rotate around the molecular long axis (hence, there is orientational but with no positional order). In the columnar mesophase, the molecules stack in a column and give rise to different arrangements, such as hexagonal columnar (Col_h), rectangular columnar (Col_r) and tetragonal columnar (Col_{tet}). The columns formed are parallel to one another and periodic in two-dimensional array (**Figure 2.12**) [34].

Figure 2.12 An example of *Col_h* mesophase

The mesogenic properties of a material are normally studied by differential scanning calorimetry (DSC) and polarizing optical microscopy (POM).

DSC is used to study the thermal transition, and give informations such as glass transition temperature, melting temperature and clearing temperature [35]. A DSC scan provides an accurate method of measuring the heat capacities and enthalpy changes (ΔH). The enthalpy of transition (area under a curve) can be expressed using the formula below:

$$\Delta H = \int_{T_1}^{T_2} \left(\frac{\partial H}{\partial T}\right)_P dT = \int_{T_1}^{T_2} C_P \, dT$$

An endothermic process (absorption of the heat) may be due to melting, clearing, and chemical reaction, while an exothermic process may be due to crystallization and bond formation [36-38] (**Figure 2.13**).

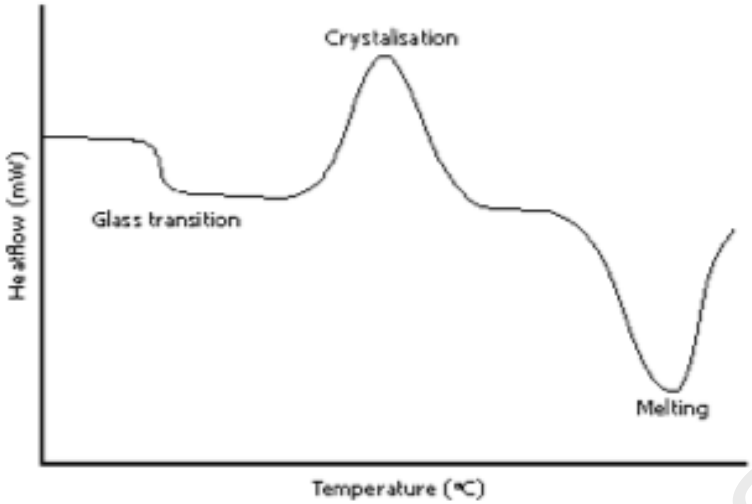

Figure 2.13 An example of a DSC scan

LC made up of compounds containing metal ions are known as metallomesogens. Copper(II)-containg metallomesogens, one of a large group of materials exhibiting liquid crystalline properties, are usually square planar complexes and exhibit either calamitic or discotic mesophases. These metallomesogens are of interest as they were magnetic and hence may be aligned using weak magnetic fields as well as function as low-dimensional materials.

For example, in 1990 Attard *et al*. reported that copper(II) alkylcarboxylates promoted discotic mesophase (**Figure 2.14**). This arises from the disc-like shape of the two copper(II) polar cores coordinated with four carboxylate ligands in the paddle-wheel structure. The symmetry of this complex is generally hexagonal [39].

Figure 2.14 Discotic mesophase exhibited by copper(II) alkylcarboxylates [39]

Ramos *et al.* reported green-blue crystals of tetrakis(μ-o-$CH_3(CH_2)_8COO)_4$dicopper(II) (**Figure 2.15**), prepared from the reaction of decanoic acid with copper(II) carbonate [40]. The complex crystallised in the triclinic $P\bar{1}$ space group. Its structure was paddle wheel (CuO_4O chromophore) [41]. The dimers were linked into an oligomeric chain by Cu-O bonds (axial ligation). The Δ_{COO} value from its FTIR spectrum was 173 cm^{-1}, in agreement with the bridging bidentate carboxylato ligand as revealed by its crystal structure. The complex melted at room temperature and decomposed at 260 ^oC (below its clearing temperature). The DSC showed an exotherms at 80 ^oC with ΔH value of 27.4 kJ mol^{-1} Hence, POM observation failed to capture any liquid crystal images. However by adopting the technique by Demus et al. [42], which is evaporating solvent at the liquid crystal phase temperature, a visual observation of mesophase was carried out with the microscope. This method showed a birefringent fluid phase without any texture as a proof of crystal phase. A typical hexagonal columnar discotic liquid crystal was observed (**Figure 2.16**).

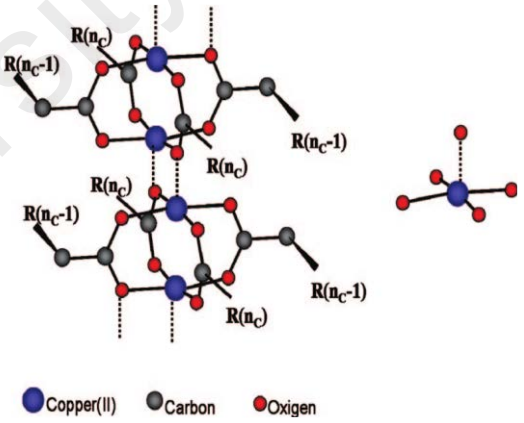

Figure 2.15 Molecular structure of tetrakis(*μ*-o-decanoato)dicopper(II), showing two paddle-wheel units linked through Cu-O(axial) bonds [40]

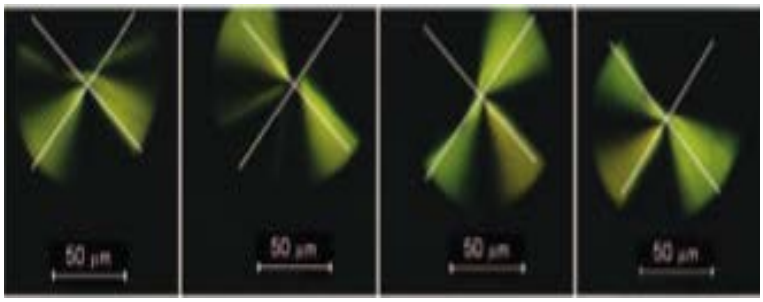

Figure 2.16 Hexagonal columnar discotic phase [40]

2.2.3. Complexes of copper(II) carboxylates with N-donor ligands

Copper(II) ion has a higher preference for N-donor ligands than O-donor ligands. Accordingly, copper(II) carboxylates were found to react with N-donor ligands, such as pyridine and 2,2'-bipyridine. The main objectives of such reactions were to obtain crystalline products and to study the correlation between structure and magnetism.

An example is $[Cu_2(L)_4(py)_4].2CH_2Cl_2$ where L = (1,8-naphthalimido)ethanoate and py = pyridine (**Figure 2.17**), reported by Reger *et al.* [43]. The complex was obtained as dark blue crystals from the reaction 1,8-naphthalimido)ethanoate with copper(II) acetate and tweleve drops of pyridine. It crystallised in a triclinic ($P\bar{1}$) system. The molecule was dinuclear with square pyramidal geometry at both copper(II) centres. The two copper(II) centres were bridged by two oxygen atoms from two monodentate carboxylato ligand. The equatorial position of each copper(II) centre was coordinated by two nitrogen atoms of pyridine ligands. The Cu-O axial length (2.381(2) Å) and the Cu---Cu distance (3.38 Å) were longer than normally found in a paddle-wheel dimeric copper(II) carboxylate (Cu-O = 1.9 Å, Cu---Cu = 2.6 Å).

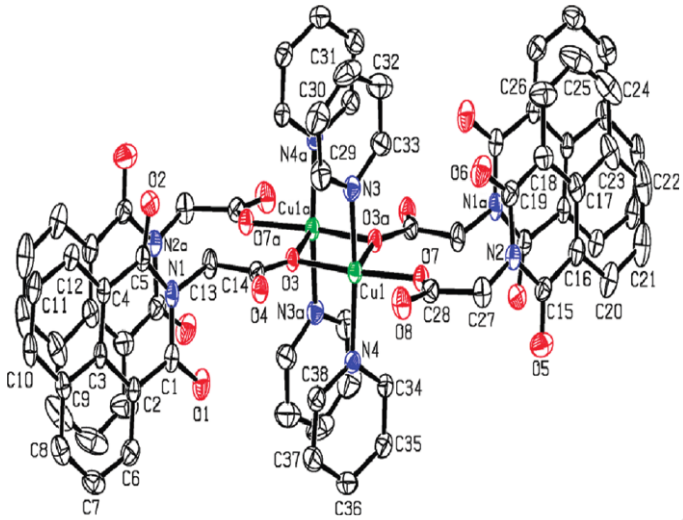

Figure 2.17 Molecular structure of $[Cu_2(L)_4(py)_4].2CH_2Cl_2$ [43]

The binding mode of the carboxylato ligand in $[Cu_2(L)_4(py)_4].2CH_2Cl_2$ was syn-anti. Its magnetic data suggested a weak antiferromagnetic interaction (J = -1.7 cm^{-1}). Its TGA data showed that it was thermally stable up to 120 ^oC with a total weight loss of 84.5% due to loss of two pyridine molecules and four carboxylato ligands (calcd: 84.1%). The final residual weight of CuO at temperatures above 551 ^oC was 10.0% (calcd: 10.2%).

Another example is $[Cu_2(CH_3(CH_2)_{14}COO)_4(2,2'\text{-bipyridine})_2].2CH_3OH$ (**Figure 2.18**), reported by Nazeer *et al.* [44]. It was obtained as dark blue crystals from the reaction of $[Cu_2(p\text{-}H_2NC_6H_4COO)_2(CH_3(CH_2)_{14}COO)_2]$ with 2,2'-bipyridine. Its molecules crystallised in a triclinic $P\bar{1}$ crystal system, and showed syn-anti coordination mode of the carboxylato ligand.

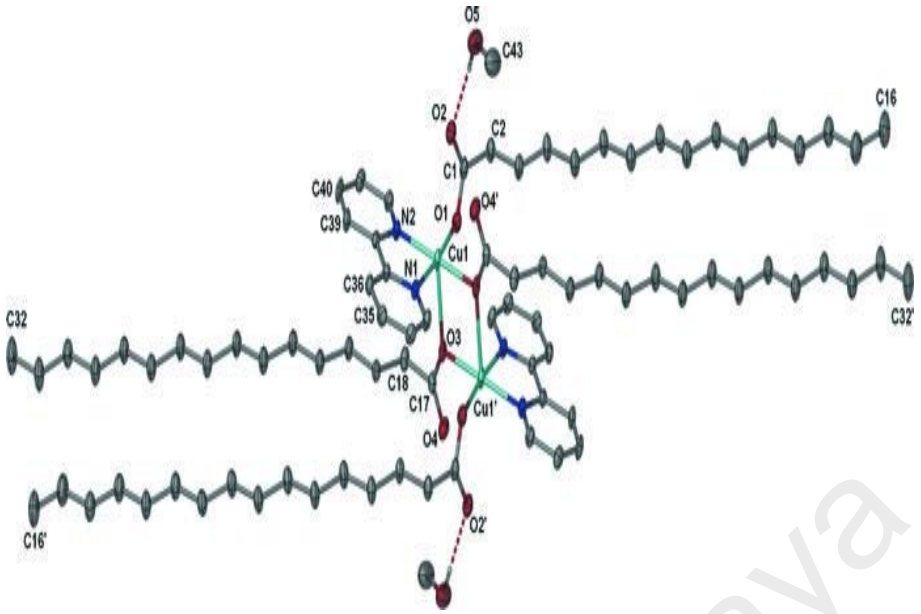

Figure 2.18 Crystal structure of $[Cu_2(CH_3(CH_2)_{14}COO)_4(2,2'\text{-bipyridine})_2].2CH_3OH$ [44]

In 2007, Baggio *et al*. reported a dinuclear copper(II) complex, $[Cu(oda)(phen)]_2.6H_2O$, where oda = oxydiacetate and phen = 1,10-phenantroline (**Figure 2.19**) [45]. The dimer was built up with each copper(II) atom residing in a CuN_2O_4 octahedral geometry. The equatorial positions were occupied with two nitrogen atoms form phen (Cu1-N1 = 2.005(4) and Cu1-N2 = 2.024(4) Å) and two oxygen atoms from oda ligand (Cu1-O1A = 1.937(4) and Cu1-O5A = 1.977(3) Å). The axial position was occupied by the oxygen atom of oda (Cu1-O3A = 2.488(3) Å) and a bridging oxygen from oda (Cu1-O5A = 2.330(3) Å). This resulted in a distorted octahedral geometry at the copper(II) centre. The Cu1 atom was coplanar with N1, N2, O1A and O5A atoms, with the maximum deviation of 0.03 Å at N2. The bridging Cu-O at each copper(II) centre consists of one normal and a longer Cu-O distance; 1.977(3) Å and 2.330(3) Å, respectively. The bridging Cu-O-Cu angles was 104.72(14)^o, leading to a large Cu—Cu separation of 3.417(2) Å due to the syn-anti coordination modes of the carboxylate ligands. In comparison, the normal Cu—Cu distance of syn-syn bridged dimers was in the range of 2.6-2.7 Å [46,47]. The $\chi_m T$ value was 0.84 cm^{-1} K mol^{-1} at

50K (μ_{eff} = 2.6 BM). This indicates a ferromagnetic coupling between two copper(II) centres.

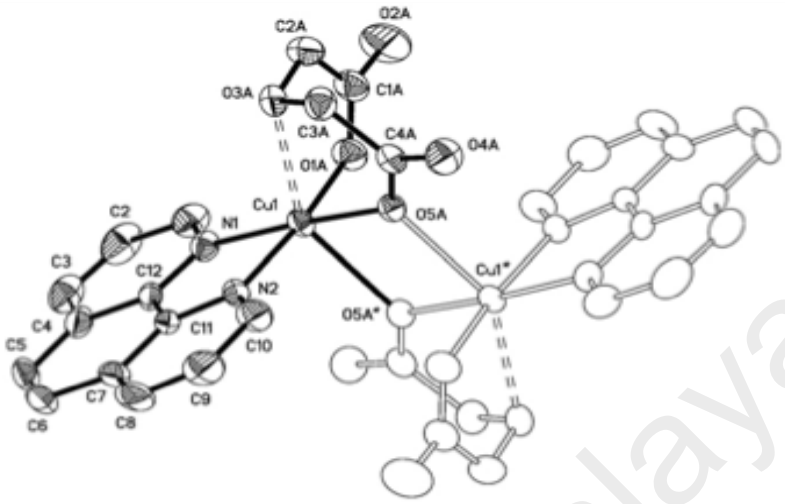

Figure 2.19 Crystal structure of $[Cu(oda)(phen)]_2.6H_2O$ [45]

Another crystal was $[Cu_2(3\text{-}HOC_6H_4COO)_4(4\text{-acetylpyridine})_2].6H_2O$ (**Figure 2.20**), reported by Youngme *et al.* [25]. In this complex, both copper(II) atoms were linked by four carboxylato ligands in the syn-syn configuration (Δ_{COO} = 173 cm^{-1}). The pyridyl nitrogen atom was axially coordinated completing the square pyramidal coordination geometry (λ_{max} = 743 nm). The important bond distances were Cu–O = 1.958 to 1.970 Å, Cu–N = 2.181(2) Å, and Cu...Cu = 2.654(1) Å. These were in the ranges for typical dinuclear paddle-wheel units in Cu(II) carboxylates. At 350 K, the $\chi_m T$ value was 0.575 cm^3 K mol^{-1}, which was lower than the spin-only value for two non-interacting Cu(II) ion (0.75 cm^3 K mol^{-1}). The $\chi_m T$ value decreased to 0.014 cm^3 K mol^{-1} at 50 K, and the J value was -278.5 cm^{-1}, indicating a strong antiferromagnetic interaction.

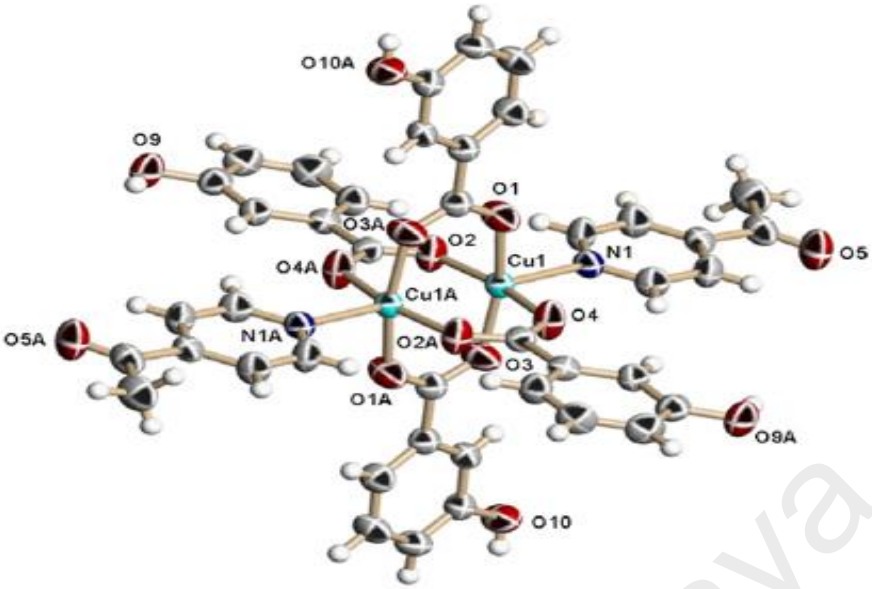

Figure 2.20 Crystal structures of $[Cu_2(3\text{-}HOC_6H_4COO)_4(4\text{-acetylpyridine})_2].6H_2O$ [25]

Konar *et al*. reported the crystal structure and magnetic properties of $[Cu(pyrazine\text{-}2,3\text{-}dicarboxylate)(H_2O)_2]$. (**Figure 2.21**) [48]. It was obtained as blue needle-like crystals from the reaction of disodium salt of pyrazine 2,3-dicarboxylate with $Cu(ClO)_4.6H_2O$. The molecules crystallised in the orthorhombic P*bca* system. The binding mode of the bridging carboxylato ligand was syn-anti. This complex showed a weak antiferromagnetic interaction ($J = -0.5\ cm^{-1}$)

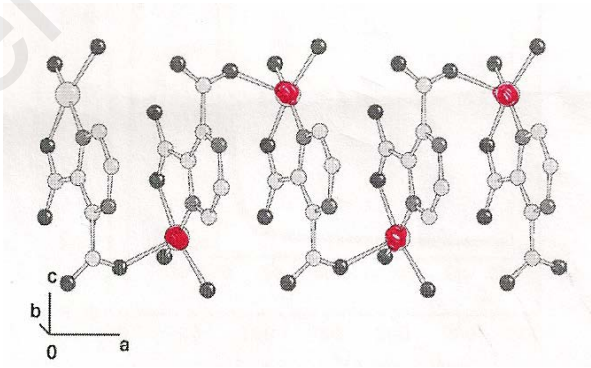

Figure 2.21 Molecular structure of $[Cu(pyrazine\text{-}2,3\text{-}dicarboxylate)(H_2O)_2].H_2O$ [48]

In 2012, Abdullah *et al*. reported the violet crystals of $[Cu(R)_2(bpy)_2].RH$ where R = 2-hexyldecanoate ion and bpy = 4,4'-bipyridine (**Figure 2.22(a)**) obtained from the reaction of $[Cu(R)_4(RH)_2]$ with 4,4'-bipyridine. Its molecules crystallised in a monoclinic P_{21}/n space group system. Its molecular structure showed that its behaved as

an elongated octahedral copper(II) atom in the CuO_4N_2 chromophore. The copper(II) centre was hexacoordinated with two chelating bidentate carboxylate ligand at the basal position and two bpy molecules at both axial positions. The Δ_{COO} value of 149 cm^{-1} was in a good agreement with the chelating bidentate carboxylate ligand. Its electronic spectrum showed two d-d bands at 700 nm (ε_{max} = 218 M^{-1} cm^{-1}) and 383 nm (ε_{max} = 127 M^{-1} cm^{-1}). Its μ_{eff} value was 1.85 BM at 298 K, indicating antiferromagnetic interactions. This molecule was thermally stable up to 240 ^{o}C. Based on combined DSC and POM data, the complex behaved as a thermotropic LC. By POM, the molecule was observed to clear to the isotropic liquid at 81 ^{o}C on heating, and on cooling, an optical texture was observed 71.9 ^{o}C (an exotherm at 66.3 ^{o}C, ΔH = 29.7 kJ mol^{-1}) (Figure 2.22(b)) [49].

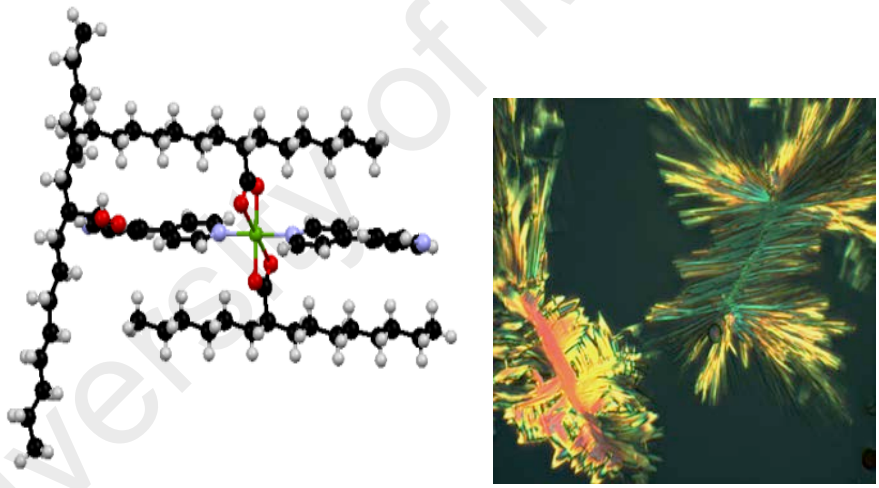

(a) (b)

Figure 2.22 (a) Molecular structure of $[Cu(R)_2(bpy)_2]$.RH; (b) optical textures of $[Cu(R)_2(bpy)_2]$.RH at 71.9 ^{o}C on cooling from 81.0 ^{o}C [49]

In the same paper, Abdullah *et al.* reported a polymeric $[Cu_2(R)_4(bpy)]_n$ (R = 2-hexyldecanoate ion, bpy = 4,4'-bipyridine), and its structure (**Figure 2.23**) was proposed based on combined analytical data. The Δ_{COO} value was 186 cm^{-1}, and the *d-d* bands were 700 nm (ε_{max} = 387 M^{-1} cm^{-1}) and 400 nm (ε_{max} = 209 M^{-1} cm^{-1}). The μ_{eff} value, calculated for the dimeric repeating unit, was 1.59 BM at 298 K, indicating a strong antiferromagnetic interaction between the copper(II) centres. The polymer

suffered a major weight loss of 90.7% at 220 ^{o}C indicating the decomposition of all carboxylate and bpy ligands (calcd; 90.3%). Its DSC showed a strong endothermic peak at 48.3 ^{o}C (ΔH = 35.7 kJ mol^{-1}) and two weak exothermic peaks at 131.7 ^{o}C and 151.7 ^{o}C on heating, and three corresponding exothermic peaks with similar enthalpies on cooling. Its POM photomicrographs showed that the molecule started to clear to an isotropic liquid at 184 ^{o}C, and dendritic optical textures of Col_H mesophase was observed on cooling at 180.6 ^{o}C (**Figure 2.24(a)**). This mesophase then coalesced to a mosaic texture with homeotropic region on cooling at 133 ^{o}C (**Figure 2.24(b)**). However when a new sample was heated to 190 ^{o}C (above its isotropization temperature), dendritic textures reappeared at almost the same temperature as before on cooling, followed by nematic globules (Col_N) at 160 ^{o}C (**Figure 2.24(c)**).

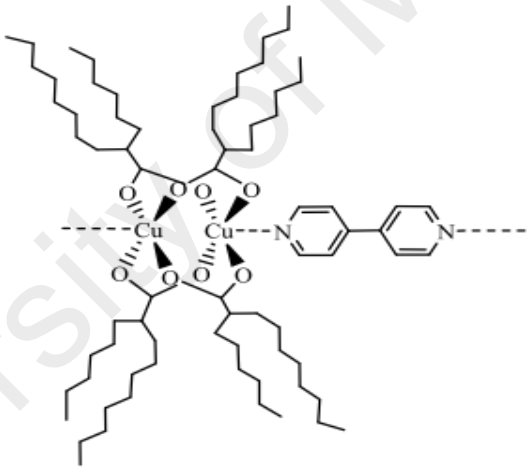

Figure 2.23 Proposed structure of $[Cu_2(R)_4(bpy)]_n$ [49]

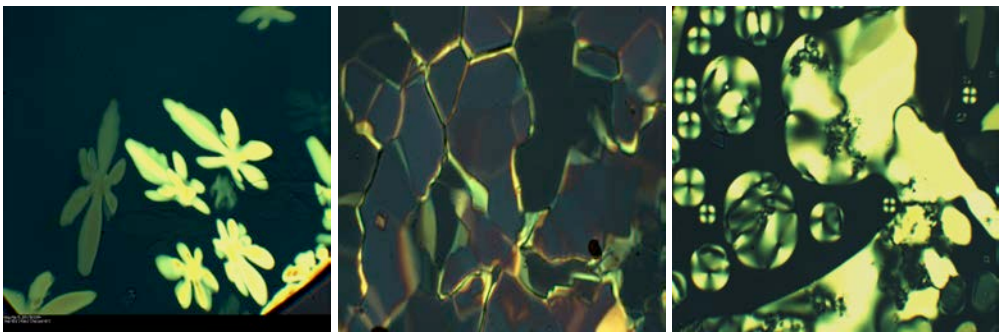

(a) (b) (c)

Figure 2.24 Photomicrographs of $[Cu_2(R)_4(bpy)]_n$ at: (a) 180.6 ^oC on cooling from 185 ^oC, (b) 133 ^oC on cooling from 185 ^oC, and (c) 160 ^oC on cooling from 190 ^oC [49]

2.3 Iron(II) carboxylates

2.3.1 Syntheses and structures

There are only a few reports on the syntheses and structures of iron(II) carboxylates in the literature. Most research was focused on iron(II) complexes with N-donor ligands as functional materials, such as spin crossover [50-52] and dye-sensitized solar cells [53,54]. Most of these complexes were either square pyramidal or octahedral.

2.3.2 Magnetic properties

Metal ions with d^4-d^7 valence electronic configurations form high-spin (HS) and low-spin (LS) octahedral complexes, depending on the ligands (crystal field splitting energy (Δ_o) and pairing energy (p). In the presence of weak field ligands, such as H_2O and $RCOO^-$ ion, Δ_o is smaller than p. Hence, electrons fill the lower t_{2g} orbitals and higher energy e_g orbitals singly before pairing. This will form a HS complex. In the presence of strong field ligands, such as CO molecule and CN^- ion, Δ_o is larger than p. Hence, electrons fill the lower t_{2g} orbitals before the higher energy e_g orbitals. This will form a LS complex. HS complexes are less stable and form weaker M-L bonds compared to LS complexes.

Iron(II) is a first-row transition metal ion with $3d^6$ valence electronic configuration. Hence, iron(II) forms either paramagnetic HS (4 unpaired electrons; $t_{2g}^4 \rightarrow e_g^2$) or diamagnetic LS (no unpaired electrons; t_{2g}^6) octahedral complexes

(**Figure 2.25**). The *d-d* bands for a LS Fe(II) complexes are found at 545 nm and 377 nm, and are assigned to the $^1A_{1g} \rightarrow {}^1T_{1g}$ and $^1A_{1g} \rightarrow {}^1T_{2g}$ electronic transitions, respectively. On the other hand, the *d-d* bands for HS Fe(II) complexes are normally weak or were not observed as they occur in the near IR region. Hence, the colour of LS complexes was purple, while that of HS iron(II) complexes was usually white.

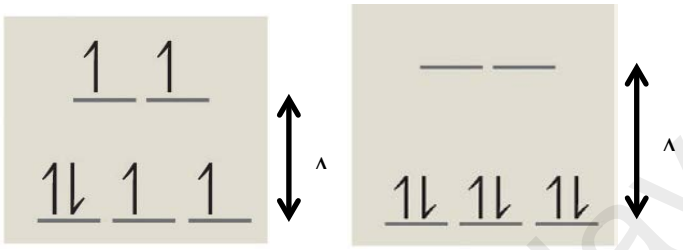

(a) (b)

Figure 2.25 Electronic arrangements in (a) HS, and (b) LS iron(II) octahedral complexes

Theoretically for iron(II) complexes, the $\chi_M^{corr}T$ value for a HS complex (S = 2) is 3.01 cm^3 K mol^{-1}, while the value for a LS complex (S = 0) is 0 [22]. [55].

2.3.3 Complexes of iron(II) carboxylates with N-donor ligands

Reynolds *et al.* reported a dinuclear iron(II) anionic complex, $[Fe_2(\mu\text{-}H_2O)(\mu\text{-}OAc)_2(OAc)_3(Py)_2]^-$, where OAc = CH_3COO^- ion, py = pyridine (**Figure 2.26**) [56,57], formed from the reaction of iron(II) acetate with pyridine. Its molecular structure showed two bridging and three non-bridging CH_3COO^- ligands and an aqua bridge. One pyridine ligand was terminally bound in *syn* orientation to each iron(II) atom. The compound was asymmetric due to differences in the coordination environment of the two iron(II) centre. This is a common feature in dinuclear iron(II) complexes, where hydrogen bonds were observed between two monodentate carboxylato ligands and bridging water molecule. For this molecule, the O(OAc)-O(H_2O) distances (2.62(8) Å and 2.57(7) Å) were within the range reported for strong hydrogen bonds. Its electronic spectrum showed a band at 375 nm (ε_{max} = 4 x 10^3 M^{-1} cm^{-1}), and its μ_{eff}^{corr} value at 250 K and 4 K was 7.62 BM and

4.37 BM, respectively. The *g* value in the dimer was 2.2, which is close to the expected values for 2.8. The very weak anti-ferromagnetic coupling in this complex was as expected for an aqua-bridged dinuclear complex.

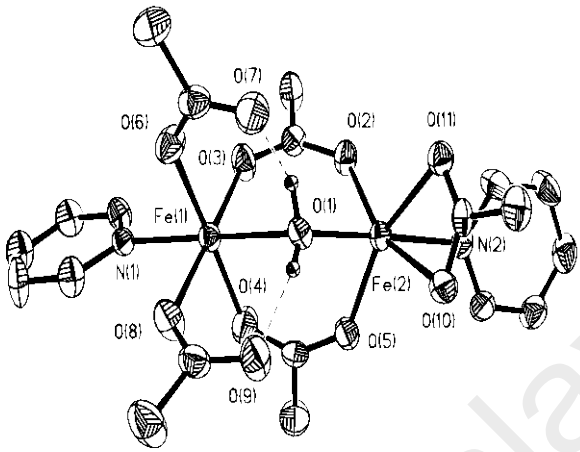

Figure 2.26 Molecular structure of $[Fe_2(\mu\text{-}H_2O)(\mu\text{-}OAc)_2(OAc)_3(py)_2]^-$ [56]

Another dinuclear Fe(II) carboxylate crystalline complex, $[Fe_2(BEAN)(\mu\text{-}O_2CPhCy)_3](OTf)$, where BEAN = 2,7-bis(N,N-diethylaminomethyl)-1,8-naphthyridine (**Figure 2.27**) was reported by He *et al*. [58]. Its molecules crystallised in a monoclinic P_{21}/n space group. Its structure showed a distorted octahedral geometry at each iron(II) centre, pentacoordinated with three bridging bidentate carboxylate ligands (Δ_{COO} = 183 cm^{-1}) and two nitrogen atoms from BEAN ligand.

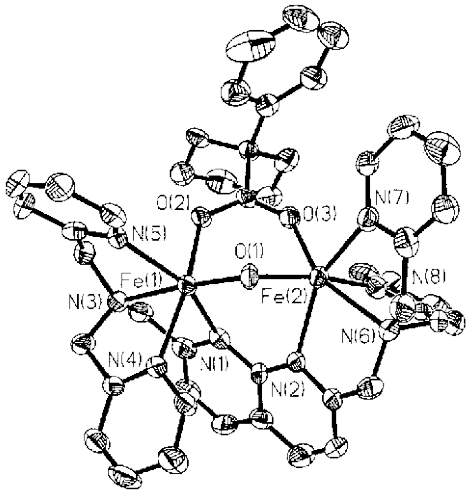

Figure 2.27 Molecular structure of $[Fe_2(BEAN)(\mu\text{-}O_2CPhCy)_3](OTf)$ [58]

Another dinuclear iron(II) complex, $[Fe_2(\mu\text{-}H_2O)(\mu\text{-}O_2CCF_3)_2(\mu\text{-}XDK)(TMEN)_2]$, where XDK = m-xylenediamine Bis(Kemp's triacid imide), and TMEN = N,N,N',N'-tetramethyl-1-diaminoethane, was reported by Edit *et al*. [59]. In this complex, the iron(II) centres have an octahedral coordination (**Figure 2.28**), and were hexacoordinated with two bridging carboxylates ligands, a bridging water molecule, two nitrogen atoms from the TMEN ligand, and the XDK was monodentically bonded to the iron(II) centre.

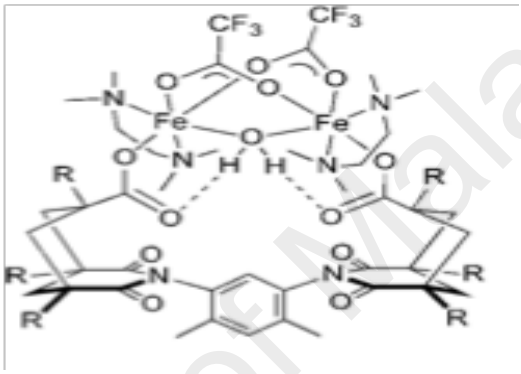

Figure 2.28 Molecular structure of $Fe_2(\mu\text{-}H_2O)(\mu\text{-}O_2CCF_3)_2(\mu\text{-}XDK)(TMEN)_2]$ [59]

In 2014, Abdullah *et al*., reported a dinuclear iron(II) complex, $[Fe_2(CH_3COO)_4(L)_2]$, where L = (4,4'-bis[3,4-bis(tetradecyloxy)stryl-2,2'-bipyridine), formed as dark purple powder from the reaction of $[Fe(CH_3COO)_2]$ with ascorbic acid and L [60]. Its proposed structure (**Figure 2.29**) was based on combined analytical data.

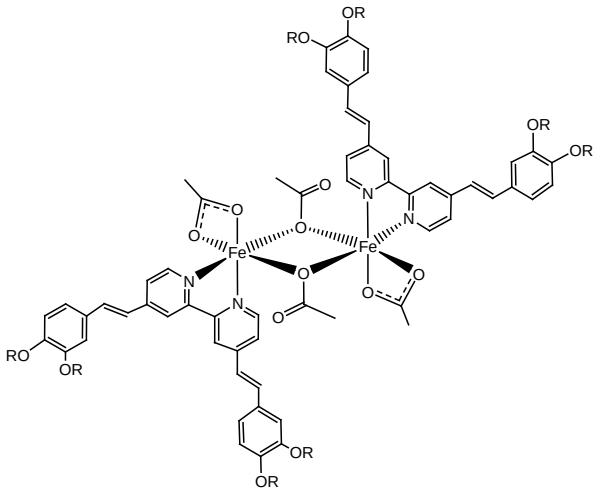

Figure 2.29 Proposed structure of $[Fe_2(CH_3COO)_4(L)_2]$ (R = $CH_3(CH_2)_{13}$) [60]

The results of the CHN elemental analyses for the above complex, C, 74.96%; H, 11.25%; N, 1.84% were in good agreement with the calculated values C, 74.29%; H, 10.48%; N, 2.01%. The Δ_{COO} values from its FTIR spectrum were 130 cm^{-1} and 206 cm^{-1}, suggesting bidentate chelating and monodentate bridging CH_3COO^- ligands, respectively. Its electronic absorption spectrum showed MLCT peak at 544 nm (ε_{max} = 2194 M^{-1} Cm^{-1}), assigned to LS iron(II) (electronic transition, $t_{2g} \rightarrow \pi^*$) [61], and two *d-d* peaks at 1412 nm (ε_{max} = 25.6 M^{-1} cm^{-1}) and 1755 (25.6 M^{-1} cm^{-1}) assigned to HS iron(II) (electronic transition, $^5T_{2g} \rightarrow {}^5E_g$). Weaker Fe-N and Fe-O bonds in the distorted octahedral N_2O_4 coordination to iron(II) centres contributed to the splitting of the d-d peaks for HS iron(II). A d-d peak for LS iron(II) was found as a shoulder on the strong MLCT peak was assigning for $^1A_{1g} \rightarrow {}^1T_{1g}$. The spectral data suggested the presence of HS and LS iron(II) atoms in the complex.

The $\chi_M T$ values for the above dimeric complex decreased from 3.35 cm^3 K mol^{-1} at 294 K to 1.12 cm^3 K mol^{-1} and 0.66 cm^3 K mol^{-1} at 8.1 K and 2 K, respectively. From the data, it was inferred that the complex was made up of 56.8 % HS and 43.2% LS iron(II) atoms at 294 K (the theoretical $\chi_M T$ value for a dinuclear octahedral HS iron(II) at 294 K was 6.0 cm^3 K mol^{-1}). Its *g* value was 1.9, which was lower than the theoretical value (2.0), suggesting an axially distorted octahedral geometry. The *J* value was -81.2 cm^{-1}, indicating an antiferromagnetic interaction between two iron(II) centres, postulated to occur through the carboxylate bridges [60]

The thermal properties of the above complex was later reported by the same authors in 2015 [62]. Its TG trace showed a major weight loss of 97.5% (calcd; 95.6%) from 199 ^oC to 612 ^oC. its DSC scans was done in two cycles (heat-cool-heat-cool) showed two overlapping endotherms at T_{range} = 57.2 – 74.2 ^oC ($\Delta H_{combined}$ = +127.6 kJ mol^{-1}) and a broad exotherm at 48.8 ^oC (ΔH = -189.9 kJ mol^{-1}. These peaks were similar on the second heating indicating reversibility of phase transition. Under the

POM, the sample melted to a dark red liquid at 60 ^{o}C, and on cooling from 100 ^{o}C, at 67 ^{o}C, a mixture of black and pale purple liquids were formed. These liquids solidified to a mixture of orange-red and yellow solids at 60 ^{o}C. The solidified molecules on further cooling at 30 ^{o}C become yellow solid. At 70 ^{o}C (reheating), the orange-solid changed its colour to purple while the yellow solid formed a fan-shaped texture (**Figure 2.30**), and on further heating to 78 ^{o}C, the colour of the texture changed to purple. Combining the DSC and POM results, the authors suggested that the dimeric molecule melted at 61.5 ^{o}C, cleared to I_{iso} at 80 ^{o}C and solidified at 49 ^{o}C. The change in the colour suggested reverse spin crossover (SCO) behavior in the temperature range 30 - 100 ^{o}C.

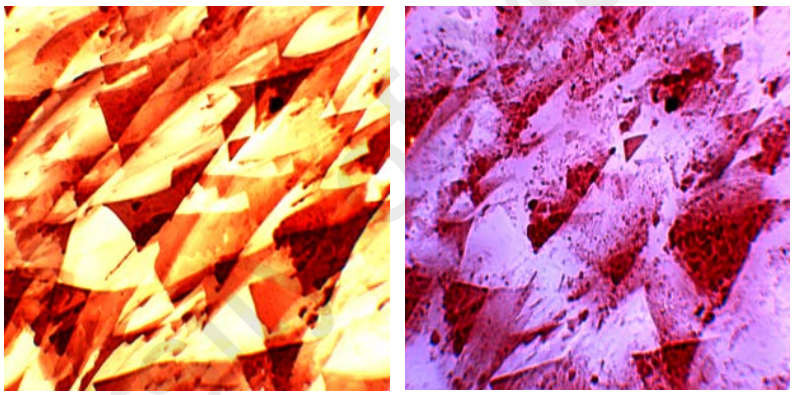

Figure 2.30 Photomicrograph of on heating at (a) 70 ^{o}C and (b) 78 ^{o}C [60]

A polymeric iron(II) complex, [Fe(pyoa)$_2$], where pyoa = 2-(pyridine-3-yloxy)acetate, was reported by Zheng *et al*. (**Figure 2.31**) [63]. Its molecules crystallized in a monoclinic C_2/c space group. Each of its iron(II) atom was in an octahedral coordination with four equatorial carboxylato ligands (Δ_{COO} = 116 cm^{-1}) and two nitrogen atoms from the pyridyl rings. The iron(II) atoms were linked by *syn-anti* bridging carboxylate ligands Its χ_mT value was 4.0 cm^3 K mol^{-1} (μ_{eff} = 5.66 BM), which was larger than the spin-only value of 3.0 cm^3 K mol^{-1} (μ_{eff} = 4.90 BM) for a HS Fe(II) atom.

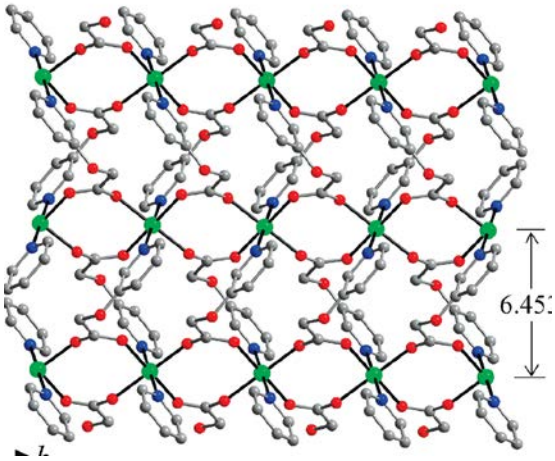

Figure 2.31 Perspective view along b-axis of the *syn-anti* μ-carboxylate bridged iron(II) chain [63]

2.4 Theoretical studies

The goal of the theoretical studies is to predict and understand the initial quantitative description of molecules and their reactions. The knowledge of the exact structural molecule and their bonding as well as the detailed insight into the state-to-state dynamics are required in order to determine the outcome of the reaction. These are essential in order to understand the results from a sophisticated experiment.

Comparison between experimental data with the theoretical allows us to understand more about the structures, bonding and reactions. The theoretical methods are now developed with sufficient accuracy to estimate reliable predictions for molecules and reaction that have not been made or measured in the laboratory.

Vibrational spectroscopy is widely used in structural studies of organic molecules. Quantum-chemical computational may predict the harmonies frequency and spectral intensities essential for the interpretation of experimental spectra. The accuracy of the computational IR intensities is difficult as they are dependent on the dipole moment and polarizability. Hence, this will require the use of large, diffuse basis sets such as aug-cc-pVTZ [64].

For example, in 2009 Sagdinc *et al.* reported the structural and theoretical properties of $[Cu_2(FBF)_4]$, where FBF = (R,S)-[2-(2-fluoro-4-biphenyl)]propanoate ion

(**Figure 2.32**) using DFT calculations, followed by the vibrational properties using Raman and infrared spectroscopy with B3LYP method and 6-31G(d.p) basis set. The investigation was done to better understand the structural and bonding characteristic of the complex. The major characteristic from the FTIR spectrum of this molecule is the frequency of the asymmetric and symmetric COO^-, which were found at 1589 cm^{-1} and 1408 cm^{-1}, respectively. Thus, the Δ_{COO} value was 181 cm^{-1}, consistent with the bridging bidentate of the molecule [65].

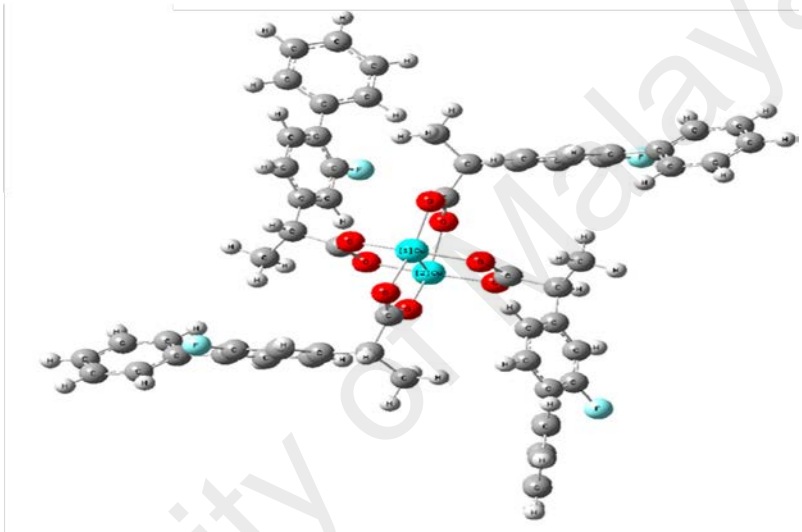

Figure 2.32 Molecular structure of $[Cu_2(FBF)_4]$ [65]

As another example, Abdullah *et al* [60] showed a good match between the experimental FTIR spectrum of a dinuclear iron(II) complex, $[Fe_2(CH_3COO)_4(L)_2]$, where L = (4,4'-bis[3,4-bis(tetradecyloxy)stryl-2,2'-bipyridine), with the simulated spectrum regenerated using the DFT calculation (**Figure 2.33**).

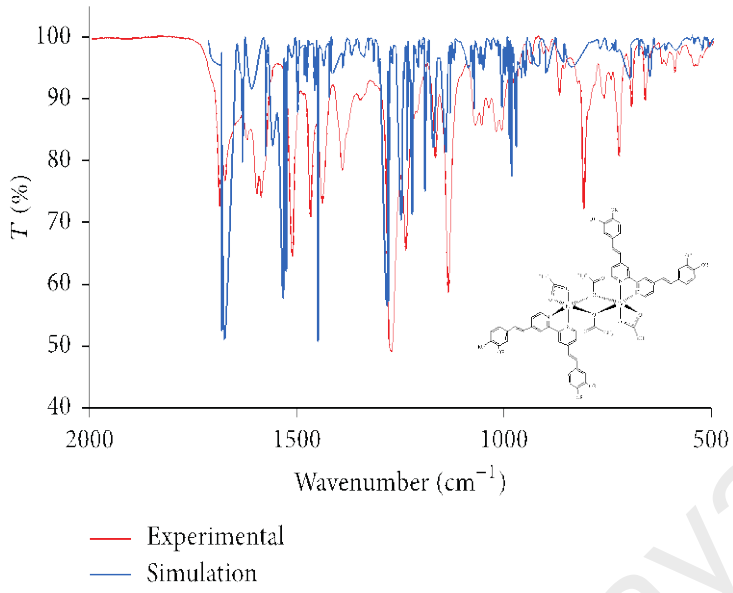

Figure 2.33 The experimental and simulated FTIR spectra of $[Fe_2(CH_3COO)_4(L)_2]$ (R = $CH_3(CH_2)_{13}$) [60]

CHAPTER 3: EXPERIMENTAL

3.1 Materials

All chemicals (**Table 3.1**) used in this research were analytical grade and used as received.

Table 3.1 List of main chemicals used in this research

Name	Chemical formula	Formula weight (g mol^{-1})
1-Bromodecane	$CH_3(CH_2)_9Br$	221.18
1-Bromododecane	$CH_3(CH_2)_{11}Br$	249.23
1-Bromohexadecane	$CH_3(CH_2)_{15}Br$	305.34
1-Bromooctane	$CH_3(CH_2)_7Br$	193.12
1-Bromotetradecane	$CH_3(CH_2)_{13}Br$	277.28
2,2'-Bipyridine	$C_{10}H_8N_2$	156.18
Copper(II) chloride dihydrate	$CuCl_2.2H_2O$	170.48
Copper(II) sulphate pentahydrate	$CuSO_4.5H_2O$	249.68
Decanoic acid	$CH_3(CH_2)_8COOH$	172.27
Dodecanoic acid	$CH_3(CH_2)_{10}COOH$	200.32
Hexadecanoic acid	$CH_3(CH_2)_{14}COOH$	256.42
Iron(II) sulphate heptahydrate	$FeSO_4.7H_2O$	318.01
Magnesium sukphate anhydrous	$MgSO_4$	120.37
Methyl 4-hydroxybenzoate	$4\text{-}HOC_6H_4COOCH_3$	152.15
Octanoic acid	$CH_3(CH_2)_6COOH$	144.22
Potassium carbonate	K_2CO_3	138.21
Potassium iodide	KI	166.00
Sodium carbonate	Na_2CO_3	105.99
Tetradecanoic acid	$CH_3(CH_2)_{12}COOH$	228.37

A total of five $CH_3(CH_2)_{6\text{-}14}COONa$ and four *p*-$CH_3(CH_2)_{9\text{-}15}$OC6H4COOK, 17 metal carboxylates, 17 metal complexes with 2,2'-bipyridine were prepared. These complexes

were analysed by CHN elemental analyses, FTIR spectroscopy, UV-vis spectroscopy, ^{1}H-nuclear magnetic resonance spectroscopy, thermogravimetric analysis (TGA), differential scanning calorimetry (DSC), polarizing optical microscopy (POM) and room-temperature magnetic susceptibility. Crystalline complexes were analysed by single-crystal X-ray crystallography.

All geometry optimization and frequencies calculations were done using Gaussian09W package with DFT B3LYP method with 6-31G basis set. In the calculation, ultrafine integral was used. The frequency calculation calculated from the resultant of the above calculation was done to obtain its IR intensities. The predicted IR intensities from the calculation were compared to the experimental IR. The frequencies were scaled by 0.98 because the overestimates calculation by B3LYP method [66].

3.2 Syntheses

3.2.1 [$Cu_2(RCOO)_4(bpy)_2(H_2O)_2$]

a) [$Cu_2(CH_3(CH_2)_6COO)_4(bpy)_2(H_2O)_2$]

A solution of $CH_3(CH_2)_6COOH$ (14.47 g; 100.3 mmol) in ethanol (100 ml) was added portionwise to a solution of Na_2CO_3 (5.30 g; 50.0 mmol) in water (100 ml). The mixture was magnetically stirred and heated for 30 minutes. The white solid ($CH_3(CH_2)_6COONa.1/2H_2O$) obtained was filtered and washed with water before dried overnight. The yield was 14.23 g (85.6%).

A solution of $CuCl_2.2H_2O$ (1.72 g; 10.1 mmol) in distilled water (20 ml) was added to a solution of $CH_3(CH_2)_6COONa.1/2H_2O$ (3.34 g; 20.1 mmol) in aqueous ethanol (100 ml). The mixture was magnetically stirred and heated for 30 minutes. The reaction mixture was left to cool to room temperature, washed with water, and filtered. The product

was a green powder ($[Cu_6Cl_{10}(CH_3(CH_2)_6COO)_2].3H_2O.2CH_3CH_2OH$), and its yield was 1.21 g (61.6%).

2,2'-Bipyridine (0.24 g; 1.5 mmol) was added to a hot solution of $[Cu_6Cl_{10}(CH_3(CH_2)_6COO)_2].3H_2O.2CH_3CH_2OH$ (0.53 g; 0.5 mmol) in methanol-ethanol (1:2 ratio; 100 ml). The reaction mixture was stirred for about 30 minutes, allowed to cool to room temperature, and filtered. The product was a blue powder, and its yield was 0.06 g (11.9%). On recrystalisation from ethanol, two types of blue crystals were obtained.

b) $[Cu_2(CH_3(CH_2)_8COO)_4(bpy)_2]$

The method was the same as for $[Cu_2(CH_3(CH_2)_6COO)_4(bpy)_2]$ (**Section 3.2.1** (a)), using Na_2CO_3 (5.34 g; 50.3 mmol), $CH_3(CH_2)_8COOH$ (17.76 g; 103.1 mmol), $CH_3(CH_2)_8COONa.2H_2O$ (3.30 g; 18.0 mmol), $CuCl_2.2H_2O$ (1.56 g; 9.0 mmol), $[Cu_2(CH_3(CH_2)_8COO)_4(H_2O)_2]$ (1.15 g; 1.4 mmol), and 2,2'-bipyridine (0.44 g; 2.8 mmol).

The yields of $CH_3(CH_2)_8COONa.2H_2O$ was 14.80 g (74.0%), $[Cu_2(CH_3(CH_2)_8COO)_4(H_2O)_2]$ was 2.99 g (39.2%), and $[Cu_2(CH_3(CH_2)_8COO)_4(bpy)_2]$ (blue semisolid) was 1.54 g (97.9%). On recrystalisation from chloroform-ethanol (1:1 v/v), blue crystals were obtained.

c) $[Cu_2(CH_3(CH_2)_{10}COO)_4(bpy)_2]$

The method was the same as for $[Cu_2(CH_3(CH_2)_6COO)_4(bpy)_2]$ (**Section 3.2.1** (a)), using Na_2CO_3 (5.23 g; 49.3 mmol), $CH_3(CH_2)_{10}COOH$ (20.04 g; 100.0 mmol), $CH_3(CH_2)_{10}COONa.1/2H_2O$ (4.49 g; 20.2 mmol), $CuCl_2.2H_2O$ (1.75 g; 10.3 mmol), $[Cu_2(CH_3(CH_2)_{10}COO)_4(H_2O)_2].2H_2O$ (0.17 g; 0.2 mmol), and 2,2'-bipyridine (0.68 g; 0.4 mmol).

The yields of $CH_3(CH_2)_{10}COONa.1/2H_2O$ was 15.79 g (69.2%), $[Cu_2(CH_3(CH_2)_{10}COO)_4(H_2O)_2].2H_2O$ was 1.01 g (10.2%), and

$[Cu_2(CH_3(CH_2)_{10}COO)_4(bpy)_2]$ (blue solid) was 0.22 g (95.2%). On recrystalisation from ethanol, blue crystals were obtained.

d) $[Cu_2(CH_3(CH_2)_{12}COO)_4(bpy)_2]$

The method was the same as for $[Cu_2(CH_3(CH_2)_6COO)_4(bpy)_2]$ (**Section 3.2.1** (a)), using Na_2CO_3 (5.31 g; 50.1 mmol), $CH_3(CH_2)_{12}COOH$ (22.86 g; 100.1 mmol), $CH_3(CH_2)_{12}COONa$; 5.01 g; 20.0 mmol), $CuCl_2.2H_2O$ (1.71 g; 10.1 mmol), $[Cu_2(CH_3(CH_2)_{12}COO)_4(H_2O)_2].4H_2O$ (0.74 g; 0.70 mmol), and 2,2'-bipyridine (0.24 g; 1.5 mmol).

The yields of $CH_3(CH_2)_{12}COONa$ was 20.73 g (82.8%), $[Cu_2(CH_3(CH_2)_{12}COO)_4(H_2O)_2].4H_2O$ was 2.97 g (23.1%), and $[Cu_2(CH_3(CH_2)_{12}COO)_4(bpy)_2]$ (blue solid) was 0.38 g (43.7%).

e) $[Cu_2(CH_3(CH_2)_{14}COO)_4(bpy)_2]$

The method was the same as for $[Cu_2(CH_3(CH_2)_6COO)_4(bpy)_2]$ (**Section 3.2.1** (a)), using Na_2CO_3 (5.30 g; 50.0 mmol), $CH_3(CH_2)_{14}COOH$ (25.68 g; 100.1 mmol), $CH_3(CH_2)_{14}COONa$ (5.55 g; 0.02 mol), $CuCl_2.2H_2O$ (1.82 g; 0.01 mol), $[Cu_2(CH_3(CH_2)_{14}COO)_4(H_2O)_2]$ (2.67 g; 2.3 mmol), and 2,2'-bipyridine (0.80 g; 5.1 mmol).

The yields of $CH_3(CH_2)_{14}COONa$ was 24.24 g (87.1%), $[Cu_2(CH_3(CH_2)_{14}COO)_4(H_2O)_2]$ was 4.76 g (37.6%), and $[Cu_2(CH_3(CH_2)_{14}COO)_4(bpy)_2]$ (blue crystals) was 2.67 g (81.1%).

3.2.2 [$Fe_2(RCOO)_4(bpy)(H_2O)_2$]

a) [$Fe_2(CH_3(CH_2)_8COO)_4(bpy)(H_2O)_2$]

The method was the same as for [$Cu_2(CH_3(CH_2)_6COO)_4(bpy)_2$] (**Section 3.2.1** (a)), using $CH_3(CH_2)_8COONa.2H_2O$; 4.48 g; 19.5 mmol), $FeSO_4.7H_2O$ (3.58 g; 12.9 mmol), [$Fe_2(\mu\text{-}H_2O)_2(CH_3(CH_2)_8COO)_4].H_2O$ (1.29 g; 1.5 mmol), 2,2'-bipyridine (0.50 g; 3.2 mmol).

The yields of [$Fe_2(\mu\text{-}H_2O)_2(CH_3(CH_2)_8COO)_4].H_2O$ was 5.98 g (36.1%), and [$Fe_2(CH_3(CH_2)_8COO)_4(bpy)(H_2O)_2$] was 0.77 g (49.7%).

b) [$Fe_2(CH_3(CH_2)_{10}COO)_4(bpy)(H_2O)_2$]

The method was the same as for [$Cu_2(CH_3(CH_2)_6COO)_4(bpy)_2$] (**Section 3.2.1** (a)), using $CH_3(CH_2)_{10}COONa$ (2.60 g; 11.2 mmol), $FeSO_4.7H_2O$ (2.13 g; 5.6 mmol), [$Fe_2(\mu\text{-}H_2O)_2(CH_3(CH_2)_{10}COO)_4].2H_2O$ (1.05 g; 1.1 mmol), 2,2'-bipyridine (0.34 g; 2.2 mmol).

The yield of [$Fe_2(\mu\text{-}H_2O)_2(CH_3(CH_2)_{10}COO)_4].2H_2O$ was 1.84 g (33.3%), and [$Fe_2(CH_3(CH_2)_{10}COO)_4(bpy)_2(H_2O)_2].2H_2O$ was 0.85 g (67.9%).

c) [$Fe_2(CH_3(CH_2)_{12}COO)_4(bpy)(H_2O)_2$]

The method was the same as for [$Cu_2(CH_3(CH_2)_6COO)_4(bpy)_2$] (**Section 3.2.1** (a)), using $CH_3(CH_2)_{12}COONa$; 5.71 g; 22.8 mmol), $FeSO_4.7H_2O$ (4.39 g; 11.6 mmol), [$Fe_2(\mu\text{-}H_2O)_2(CH_3(CH_2)_{12}COO)_4].2H_2O$ (0.84 g; 0.8 mmol), 2,2'-bipyridine (0.24 g; 1.5 mmol).

The yield of [$Fe_2(\mu\text{-}H_2O)_2(CH_3(CH_2)_{12}COO)_4].2H_2O$ was 1.72 g (13.8%), and [$Fe_2(CH_3(CH_2)_{12}COO)_4(bpy)(H_2O)_2$] was 0.86 g (90.9%).

d) $[Fe_2(CH_3(CH_2)_{14}COO)_4(bpy)(H_2O)_2]$

The method was the same as for $[Cu_2(CH_3(CH_2)_6COO)_4(bpy)_2]$ (**Section 3.2.1** (a)), using $CH_3(CH_2)_{14}COONa$; 3.83 g; 13.7 mmol), $FeSO_4.7H_2O$ (2.62 g; 6.9 mmol), $[Fe_2(\mu\text{-}H_2O)_2(CH_3(CH_2)_{14}COO)_4]$ (1.23 g; 1.1 mmol), 2,2'-bipyridine (0.34 g; 2.2 mmol).

The yield of $[Fe_2(\mu\text{-}H_2O)_2(CH_3(CH_2)_{14}COO)_4]$ was 3.78 g (47.2%), and $[Fe_2(CH_3(CH_2)_{14}COO)_4(bpy)(H_2O)_2]$ was 0.74 g (50.8%).

3.2.3 $[Cu_2(p\text{-}ROC_6H_4COO)_4(bpy)_2]$

a) $[Cu_2(p\text{-}CH_3(CH_2)_9OC_6H_4COO)_4(bpy)_2]$

p-$HOC_6H_4COOCH_3$ (4.57 g; 30.0 mmol), K_2CO_3 (4.98 g; 36.0 mmol) and KI (0.22 g; 1.3 mmol) were added in 200 ml DMF. The mixture was stirred and heated at 50°C until dissolved. $BrCH_2(CH_2)_8CH_3$ (6.61 g; 29.9 mmol) was added dropwise to the hot solution. The reaction was refluxed for 24 hours. The cool white powder was washed with water (3x100 ml) and ethanol (2x100 ml) until the washing is colourless. The white powder was dissolved in $CHCl_3$ (100 ml) and $MgSO_4$ anhydrous was added to the solution. The $MgSO_4$ anhydrous was filtered. The $CHCl_3$ was evaporated at room temperature and filtered. The product (*p*-$CH_3(CH_2)_9OC_6H_4COOCH_3$) was white solids and its yield was 63.4% (5.54 g).

p-$CH_3(CH_2)_9OC_6H_4COOCH_3$ (3.87 g; 13.2 mmol) was dissolved in 100 ml of hot EtOH. KOH (0.74 g; 13.2 mmol) in 10 ml EtOH was added dropwise to the hot solution. The reaction was reflux for 4 hours. The reaction was cool to room temperature and the white solid (1.46 g) was filtered and its yield was 35.0%.

p-$CH_3(CH_2)_9OC_6H_4COOK$ (0.99 g; 3.1 mmol) was dissolved in ethanol:water (100 ml; 1:1 v/v). The reaction was heated to 50 ^{o}C. $CuSO_4.5H_2O$ (0.40 g; 1.6 mmol) was dissolved in 20 ml water and was added dropwise to the hot solution. The reaction was heated for 30 minutes and blue powder was filtered hot (0.87 g) with 44.2% yield.

$[Cu_2(p\text{-}CH_3(CH_2)_9OC_6H_4COO)_4(H_2O)_2]$ (0.26 g; 0.2 mmol) was immersed in 100 ml ethanol. 2,2'-bipyridine (0.07 g; 0.4 mmol) was dissolved in 10 ml of ethanol was added dropwise to the hot solution above. The reaction was magnetically stirred and heated (50 ^oC) for an hour. The clear solution was left to cool to room temperature overnight. The blue solid, $[Cu_2(p\text{-}CH_3(CH_2)_9OC_6H_4COO)_4(bpy)_2].2H_2O$ was filtered (0.21 g) with 65.4% yield.

b) $[Cu_2(p\text{-}CH_3(CH_2)_{11}OC_6H_4COO)_4(bpy)_2]$

The method was the same as for $[Cu_2(p\text{-}CH_3(CH_2)_9OC_6H_4COO)_4(bpy)_2]$ (**Section 3.2.3** (a)), using p-HO-$C_6H_4COOCH_2CH_3$ (5.01 g; 30.1 mmol), K_2CO_3 (4.9922 g; 36.1 mmol), KI (0.21 g; 1.2 mmol), $CH_3(CH_2)_{11}Br$ (7.47 g; 29.9 mmol), $p\text{-}CH_3(CH_2)_{11}OC_6H_4COOCH_2CH_3$ (2.53 g; 7.1 mmol), KOH (0.55 g; 9.7 mmol), $p\text{-}CH_3(CH_2)_{11}OC_6H_4COOK$ (1.02 g; 2.9 mmol), $CuSO_4.5H_2O$ (1.49 g; 6.0 mmol), $[Cu_2(p\text{-}CH_3(CH_2)_{11}OC_6H_4COO)_4(H_2O)_2].2H_2O$ (0.32 g; 0.2 mmol), and 2,2'-bipyridine (0.06 g; 0.4 mmol).

The yields of $p\text{-}CH_3(CH_2)_{11}OC_6H_4COOCH_2CH_3$ was 5.55 g (52.1%), $p\text{-}CH_3(CH_2)_{11}OC_6H_4COOK$ was 1.20 g (49.1%), $[Cu_2(p\text{-}CH_3(CH_2)_{11}OC_6H_4COO)_4(H_2O)_2].2H_2O$ was 1.03 g (25.1%) and $[Cu_2(p\text{-}CH_3(CH_2)_{11}OC_6H_4COO)_4(bpy)_2]$ (blue solids) was 0.27 g (80.3%).

c) $[Cu_2(p\text{-}CH_3(CH_2)_{13}OC_6H_4COO)_4(bpy)_2]$

The method was the same as for $[Cu_2(p\text{-}CH_3(CH_2)_9OC_6H_4COO)_4(bpy)_2]$ (**Section 3.2.3** (a)), using $p\text{-}HOC_6H_4COOCH_2CH_3$ (5.01 g; 30.2 mmol), K_2CO_3 (5.03 g; 36.4 mmol), KI (0.21 g; 1.3 mmol), $CH_3(CH_2)_{13}Br$ (7.61 g; 27.4 mmol), $p\text{-}CH_3(CH_2)_{13}OC_6H_4COOCH_2CH_3$ (2.79 g; 7.7 mmol), KOH (0.54 g; 9.6 mmol), $p\text{-}CH_3(CH_2)_{13}OC_6H_4COOK$ (0.89 g; 2.4 mmol), $CuSO_4.5H_2O$ (0.31 g; 1.2 mmol),

$[Cu_2(p\text{-}CH_3(CH_2)_{13}OC_6H_4COO)_4(H_2O)_2].2H_2O$ (0.24 g; 0.2 mmol), and 2,2'-bipyridine (0.04 g; 0.3 mmol).

The yields of $p\text{-}CH_3(CH_2)_{13}OC_6H_4COOCH_2CH_3$ was 8.02 g (80.6%), $p\text{-}CH_3(CH_2)_{13}OC_6H_4COOK$ was 1.49 g (51.8%), $[Cu_2(p\text{-}CH_3(CH_2)_{13}OC_6H_4COO)_4(H_2O)_2].2H_2O$ was 0.76 g (39.9%) and $[Cu_2(p\text{-}CH_3(CH_2)_{13}OC_6H_4COO)_4(bpy)_2]$ (blue solids) was 0.04 g (13.4%).

d) $[Cu_2(p\text{-}CH_3(CH_2)_{15}OC_6H_4COO)_4(bpy)_2]$

The method was the same as for $[Cu_2(p\text{-}CH_3(CH_2)_9OC_6H_4COO)_4(bpy)_2]$ (**Section 3.2.3** (a)), using $p\text{-}HOC_6H_4COOCH_3$ (5.51 g; 36.2 mmol), K_2CO_3 (7.07 g; 51.1 mmol), KI (0.21 g; 1.3 mmol), $CH_3(CH_2)_{15}Br$ (10.99 g; 36.0 mmol), $p\text{-}CH_3(CH_2)_{15}OC_6H_4COOCH_3$ (10.57 g; 28.1 mmol), KOH (1.58 g; 28.1 mmol), $p\text{-}CH_3(CH_2)_{15}OC_6H_4COOK.2H_2O$ (3.93 g; 9.0 mmol), $CuCl_2.2H_2O$ (0.84 g; 4.9 mmol), $[Cu_2(p\text{-}CH_3(CH_2)_{13}OC_6H_4COO)_4(H_2O)_2]$ (0.47 g; 0.3 mmol), and 2,2'-bipyridine (0.03 g; 0.2 mmol).

The yields of $p\text{-}CH_3(CH_2)_{15}OC_6H_4COOCH_3$ was 11.91 g (87.8%), $p\text{-}CH_3(CH_2)_{15}OC_6H_4COOK.2H_2O$ was 10.5 g (85.4%), $[Cu_2(p\text{-}CH_3(CH_2)_{15}OC_6H_4COO)_4(H_2O)_2]$ was 3.95 g (54.6%) and $[Cu_2(p\text{-}CH_3(CH_2)_{15}OC_6H_4COO)_4(bpy)_2]$ (blue solids) was 0.28 g (82.7%).

3.2.4 $[Fe_2(\mu\text{-}RCOO)_2(RCOO)_2(bpy)]$

a) $[Fe_2(\mu\text{-}RCOO)_2(RCOO)_2(bpy)]$ ($R = p\text{-}CH_3(CH_2)_9OC_6H_4$)

A solution of $FeSO_4.7H_2O$ (0.44 g; 1.2 mmol) in distilled water (10 ml) was added portionwise to a solution of $p\text{-}CH_3(CH_2)_9OC_6H_4COOK$, (**Section 3.2.3** (a)) (0.73 g; 2.3 mmol) in ethanol:water (100 ml; 1:1 v/v). The reaction mixture was magnetically stirred

and heated for 30 minutes. The brown powder $[Fe_2(\mu\text{-}H_2O)(\mu\text{-}RCOO)_2(RCOO)_2(H_2O)_2]$ formed was filtered hot. The yield was 0.72 g (47.1%).

2,2'-Bipyridine (0.09 g; 0.6 mmol) was added to a hot solution of $[Fe_2(\mu\text{-}H_2O)(\mu\text{-}RCOO)_2(RCOO)_2(H_2O)_2]$ (0.36 g; 0.3 mmol) in chloroform (100 ml). The reaction mixture was stirred for about 30 minutes, allowed to cool to room temperature, and filtered. The yield of $[Fe_2(\mu\text{-}RCOO)_2(RCOO)_2(bpy)]$ was 0.29 g (76.6%).

b) $[Fe_2(\mu\text{-}RCOO)_2(RCOO)_2(bpy)]$ (R = p-$CH_3(CH_2)_{11}OC_6H_4$)

The method was the same as for *$[Fe_2(\mu\text{-}RCOO)_2(RCOO)_2(bpy)]$* (**Section 3.2.4** (a)) using *p*-$CH_3(CH_2)_{11}OC_6H_4COOK$; 2.00 g; 5.8 mmol, $FeSO_4.7H_2O$ (1.10 g; 2.9 mmol), $[Fe_2(\mu\text{-}H_2O)(\mu\text{-}RCOO)_2(RCOO)_2(H_2O)_2].H_2O$ (0.89 g; 0.6 mmol), 2,2'-bipyridine (0.20 g; 1.3 mmol).

The yield of $[Fe_2(\mu\text{-}H_2O)(\mu\text{-}RCOO)_2(RCOO)_2(H_2O)_2].H_2O$ was 1.99 g (48.9%) and $[Fe_2(\mu\text{-}RCOO)_2(RCOO)_2(bpy)]$ was 0.65 g (73.3%).

c) $[Fe(RCOO)_2(bpy)]$(R = p-$CH_3(CH_2)_{13}OC_6H_4$)

The method was the same as for *$[Fe_2(\mu\text{-}RCOO)_2(RCOO)_2(bpy)]$* (**Section 3.2.4** (a)) using $CH_3(CH_2)_{13}OC_6H_4COOK$; 2.17 g; 5.8 mmol, $FeSO_4.7H_2O$ (1.1037 g; 2.9 mmol), $[Fe_2(\mu\text{-}H_2O)(\mu\text{-}RCOO)_2(RCOO)_2(H_2O)_2]$ (0.78 g; 0.5 mmol), 2,2'-bipyridine (0.16 g; 1.0 mmol).

The yield of $[Fe_2(\mu\text{-}H_2O)(\mu\text{-}RCOO)_2(RCOO)_2(H_2O)_2]$ was 2.40 g (55.2%) and $[Fe(RCOO)_2(bpy)]$ was 0.42 g (97.4%).

d) $[Fe(RCOO)_2(bpy)]$ (R = p-$CH_3(CH_2)_{15}OC_6H_4$)

The method was the same as for *$[Fe_2(\mu\text{-}RCOO)_2(RCOO)_2(bpy)]$* (**Section 3.2.4** (a)) using $CH_3(CH_2)_{15}OC_6H_4COOK$; 1.68 g; 3.9 mmol), $FeSO_4.7H_2O$ (0.81 g; 2.1 mmol),

$[Fe_2(\mu\text{-}H_2O)(\mu\text{-}RCOO)_2(RCOO)_2(H_2O)_2]$ (0.66 g; 0.4 mmol), 2,2'-bipyridine (0.13 g; 0.8 mmol).

The yield of $[Fe_2(\mu\text{-}H_2O)(\mu\text{-}RCOO)_2(RCOO)_2(H_2O)_2]$ was 1.32 g (41.9%) and $[Fe(RCOO)_2(bpy)]$ was 0.47 g (79.7%).

3.3 Instrumental Analyses

3.3.1 Single crystal X-ray crystallography

Single crystal X-ray diffraction was performed on a Bruker SMART APEX diffractometer operating with graphite-monochromator Mo Kα radiation (λ = 0.71073Å) at 100 K. The intensities were collected using the ω -2θ scan mode, in the range $2.0^o < \theta < 27.5^o$. The data sets were corrected for absorption based on multiple scans [67] and reduced using standard methods [68]. All structures were solved by direct method using SHELXS-97 [69], and refined by full matrix least-square methods on F^2 with the use of the SHELXL-97 program package [6]. The crystals molecular structures were drawn with 50% displacement ellipsoids using Mercury [70].

3.3.2 Elemental analyses

The elemental analyses were recorded on a Perkin Elmer CHNS/O analyser 2400 Series II. The sample was accurately weighed (1 – 2 mg) in a tin capsule (5 x 8 mm). The capsule containing the sample was folded into a tiny piece and placed inside the analyzer to be heated to a maximum temperature of 1000 ^oC.

3.3.3 Fourier transform infrared spectroscopy

The Fourier Transform Infrared spectra (FTIR) were recorded from 4000 – 450 cm^{-1} on a Perkin Elmer 400 FT-IR/FT-FIR spectrometer with attenuated total reflection (ATR) technique.

3.3.4 Ultraviolet-visible spectroscopy

The ultraviolet-visible spectra (UV-vis), for both solid and solution samples, were recorded from 1000 – 300 nm on a SHIMADZU UV-vis-NIR 3600 spectrophotometer. An exactly known mass of the solid was dissolved in a suitable solvent in a 10-mL volumetric flask. The solution was introduced into a 1-cm quartz cuvette. Then the cuvette was inserted into the sample holder. The spectrum obtained was recorded against the solvent as the background.

3.3.5 ^{1}H-NMR spectroscopy

The proton NMR was recorded on JEOL FT-NMR Lambda 400 MHz spectrometer. The samples were dissolved in $CDCl_3$. The chemical shifts were reported in ppm using the residual protonated solvent as reference.

3.3.6 Room-temperature magnetic susceptibility

Room-temperature magnetic susceptibility was recorded on a Sherwood Auto Magnetic Susceptibility Balance. An empty tube was tared on the analytical balance and then placed in the instrument. The exponent of the reading was changed to 10^{-5} and tared. The finely ground sample was packed into the tube to the calibrated mark (length 5 cm) and the mass was recorded. The tube containing the sample was then placed in the instrument and the χ_g was recorded.

3.3.7 Thermogravimetric analysis

The thermogravimetric analysis (TGA) was recorded from 50–900 ^{o}C on a Pyris Diamond TG/DTA Perkin Elmer instrument with the scan rate of 20 ^{o}C min^{-1}. The sample was analysed under nitrogen at a flow rate of 10 cm^{3} min^{-1}. An empty alumina pan was placed

in the holder and tared. Then the sample (4 - 5 mg) was loaded onto the pan and the weight recorded.

3.3.8 Polarizing optical microscope

The mesophases pictomicrographs were captured using Nikon-H600L Eclipse Miscroscope equipped with Metler Toledo FP90 central processor and Linkam THMS 600 hot stage. The magnification was 50x.

3.3.9 Differential scanning calorimetry

Differential scanning calorimetry (DSC) was recorded from 35–300 ^{o}C on a Perkin Elmer DSC 6 calorimeter. The weight of the sample (3 – 4 mg) was initially recorded on a microbalance. The sample was transferred into an aluminium crucible and placed inside the instrument. The analysis was performed under nitrogen gas at a flow rate of 10 cm^3 min^{-1} and scan rate of 10 ^{o}C min^{-1}.

3.3.10 Molecular modelling

Computational calculation analysis was conducted using density functional theory (DFT), B3LYP method. The calculation was performed on Gaussian 09 program package. In preliminary calculation to determine the lowest energy conformers, the geometry optimization was done using 6-31G basis sets on all atoms. The lowest energy conformers were then individually recalculated their moieties using 6-311G basis sets. The frequency calculation calculated from the resultant of the above calculation was done to obtain its IR intensities. The predicted IR intensities from the calculation were compared to the experimental IR. The frequencies were scaled by 0.98 because the overestimates calculation by B3LYP method [66].

CHAPTER 4: RESULTS AND DISCUSSION

4.1 $[Cu_2(RCOO)_4(bpy)_2]$

The general steps for the syntheses of $[Cu_2(CH_3(CH_2)_nCOO)_4(bpy)_2]$, where n = 6 (**1**), 8 (**2**), 10 (**3**), 12 (**4**) and 14 (**5**), are shown in **Scheme 4.1.**

$$RCOOH \xrightarrow{Na_2CO_3} RCOONa \xrightarrow{CuCl_2.2H_2O} [Cu_2(RCOO)_4] \xrightarrow{bpy} [Cu_2(RCOO)_4(bpy)_2]$$

Scheme 4.1 Synthetic steps for $[Cu_2(RCOO)_4(bpy)_2]$, where R = $CH_3(CH_2)_n$

4.1.1 $[Cu_2(CH_3(CH_2)_6COO)_4(bpy)_2]$ (1)

(a) Synthesis and structural elucidation

The first step in the synthesis $[Cu_2(CH_3(CH_2)_6COO)_4(bpy)_2]$ (**1**) (**Scheme 4.1**) involved the reaction of $CH_3(CH_2)_6COOH$ with Na_2CO_3 to form $CH_3(CH_2)_6COONa.½H_2O$. It was obtained as a white powder in good yield (86 %). Its **elemental analysis** results (C, 54.8%; H, 9.2%) were in good agreement with the calculated values, (C, 55.3%; H, 9.7%; FW 175.198 g mol^{-1}). Its **FTIR** spectrum shown in **Figure 4.1**, and the peak assignments are given in **Table 4.1** (which also include the data for later discussion). It shows two strong peaks at 2924 cm^{-1} and 2858 cm^{-1} for CH_2 asymmetric and symmetric stretching for the alkyl chain, respectively, and two strong peaks at 1559 cm^{-1} and 1418 cm^{-1} for $\nu_{asym}COO$ and $\nu_{sym}COO$, respectively. Hence, the $\Delta\nu_{coo}$ value ($\Delta\nu_{coo} = \nu_{asym}COO^- \nu_{sym}COO$) for $CH_3(CH_2)_6COO^-$ ion was 141 cm^{-1}.

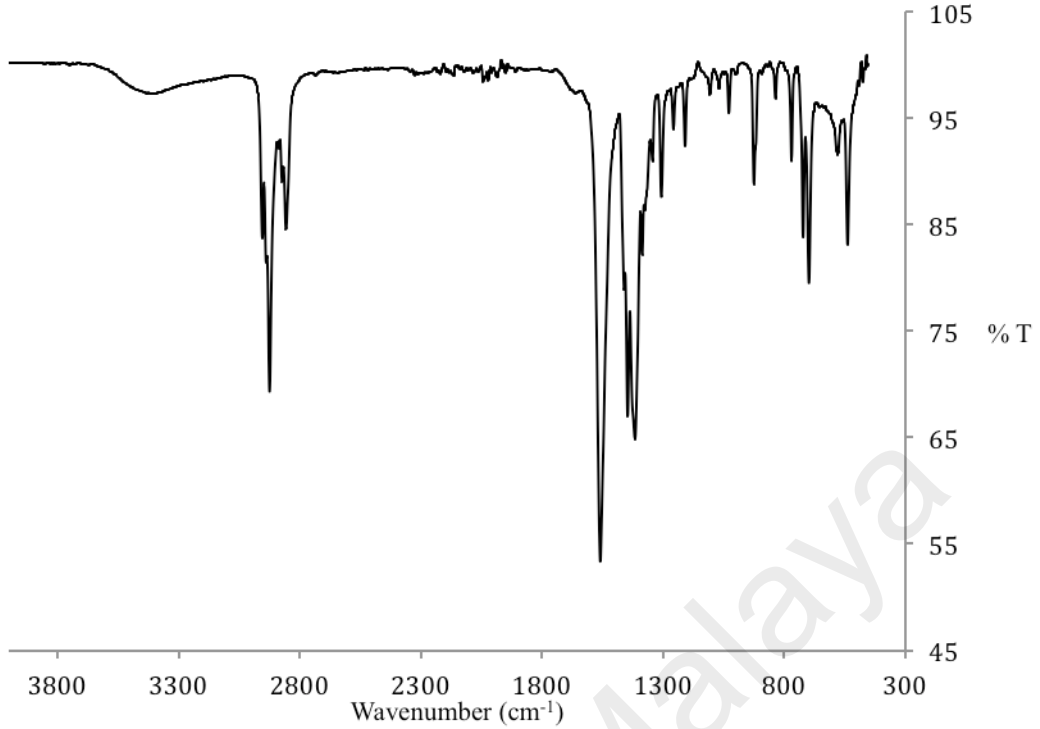

Figure 4.1 FTIR spectrum of $CH_3(CH_2)_6COONa.½H_2O$

Table 4.1 FTIR data (in cm^{-1}) and assignments

Compound	CH_2 (asym)	CH_2 (sym)	COO (asym)	COO (sym)	C=C (aromatic)	C-N
$CH_3(CH_2)_6COONa.½H_2O$	2924	2858	1559	1418	-	-
$CH_3(CH_2)_8COONa.2H_2O$	2922	2853	1558	1425	-	-
$CH_3(CH_2)_{10}COONa.1/2H_2O$	2922	2850	1559	1423	-	-
$CH_3(CH_2)_{12}COONa$	2922	2849	1559	1423	-	-
$CH_3(CH_2)_{14}COONa$	2917	2850	1557	1420	-	-
$[Cu_6Cl_{10}(CH_3(CH_2)_6COO)_2].3H_2O.2CH_3CH_2OH$	2918	2851	1630/1602	1445/1390	-	-
$[Cu_2(CH_3(CH_2)_8COO)_4(H_2O)_2]$	2920	2850	1628	1436	-	-
$[Cu_2(CH_3(CH_2)_{10}COO)_4(H_2O)_2]$	2920	2850	1627	1450	-	-
$[Cu_2(CH_3(CH_2)_{12}COO)_4(H_2O)_2].4H_2O$	2916	2851	1585	1445	-	-
$[Cu_2(CH_3(CH_2)_{14}COO)_4(H_2O)_2].H_2O$	2915	2850	1584	1444	-	-
$[Cu_2(CH_3(CH_2)_6COO)_4(bpy)_2]$; (**1**)	2921	2854	1620	1434/1411	1586	1317
$[Cu_2(CH_3(CH_2)_8COO)_4(bpy)_2]$; (**2**)	2918	2851	1629	1447/1382	1600	1301
$[Cu_2(CH_3(CH_2)_{10}COO)_4(bpy)_2]$; (**3**)	2920	2850	1627	1449/1379	1617	1303
$[Cu_2(CH_3(CH_2)_{12}COO)_4(bpy)_2]$; (**4**)	2918	2851	1602	1444/1382	1630	1302
$[Cu_2(CH_3(CH_2)_{14}COO)_4(bpy)_2]$; (**5**)	2918	2849	1625	1467/1366	1623	1309

The second step involved reacting $CH_3(CH_2)_6COONa.½H_2O$ with $CuCl_2.2H_2O$ to form the precursor complex, $[Cu_2(CH_3(CH_2)_6COO)_4]$. However based on the following data, the product formed was $[Cu_6Cl_{10}(CH_3(CH_2)_6COO)_2].3H_2O.2CH_3CH_2OH$ (green powder; yield = 62%) instead of the expected $[Cu_2(CH_3(CH_2)_6COO)_4]$. The **elemental analysis** results (C, 19.4%; H, 3.2%) were in good agreement with the calculated values (C, 20.6%; H, 4.1%; FW 1168.414 g mol^{-1}). Its **FTIR** data (**Table 4.1**; **Figure 4.2**) shows the presence of the expected functional groups. The $\Delta\nu_{coo}$ values were 157 cm^{-1} and 240 cm^{-1}. These show that the binding modes of $CH_3(CH_2)_6COO^-$ in the complex were bidentate bridging and monodentate, respectively [21, 71].

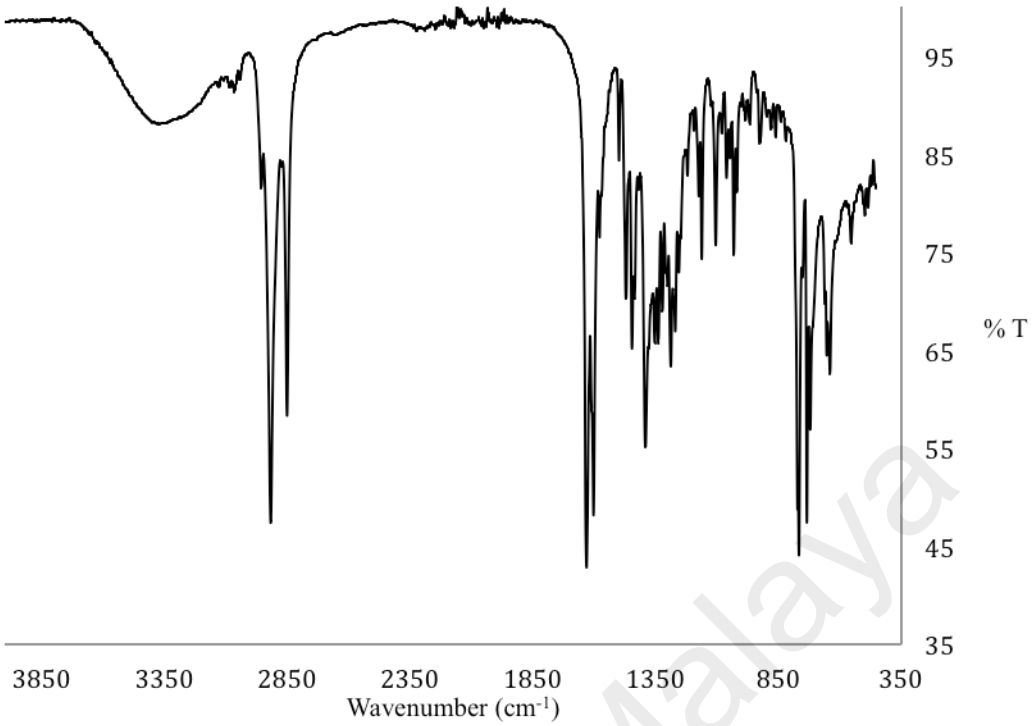

Figure 4.2 FTIR spectrum of $[Cu_6Cl_{10}(CH_3(CH_2)_6COO)_2].3H_2O.2CH_3CH_2OH$

Its **UV-vis** spectrum (**Figure 4.3**) in C_2H_5OH shows a broad *d-d* band at 693 nm (ε_{max} = 104 M^{-1} cm^{-1}). The data suggest a square pyramidal geometry at the Cu(II) centres [72,73].

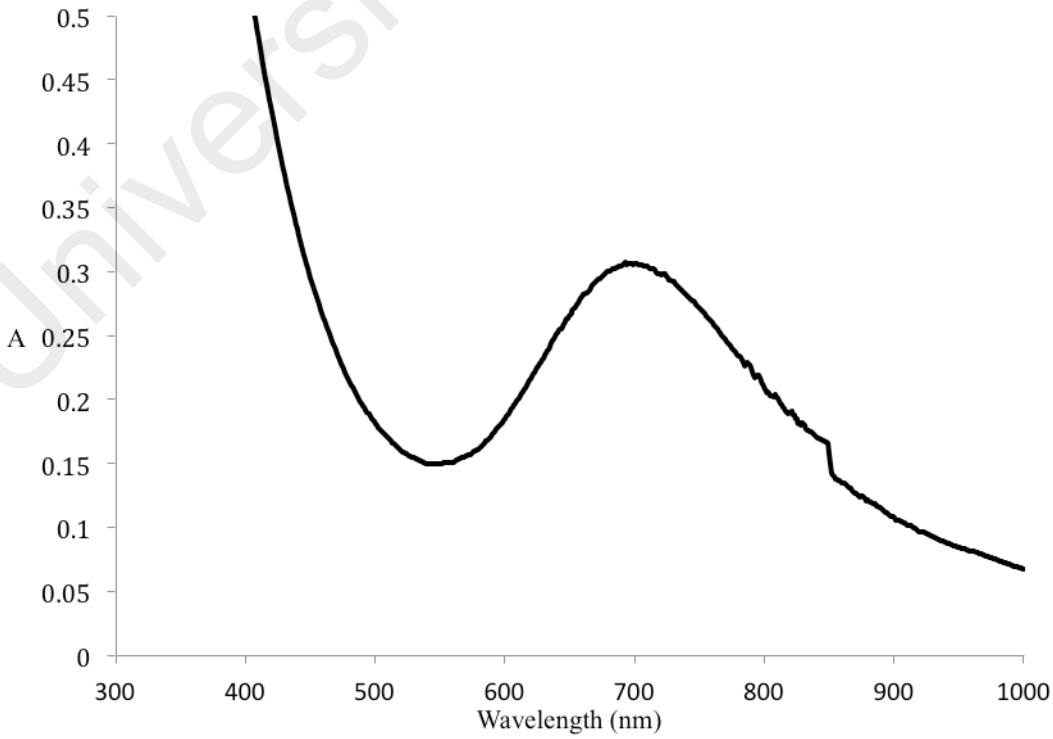

Figure 4.3 UV-vis spectrum of $[Cu_6Cl_{10}(CH_3(CH_2)_6COO)_2].3H_2O.2CH_3CH_2OH$

However, its μ_{eff} value could not be determined due to insufficient amount of sample.

$[Cu_6Cl_{10}(CH_3(CH_2)_6COO)_2].3H_2O.2CH_3CH_2OH$ reacted with bpy to form a blue powder, which on recrystallisation from ethanol, formed two different blue crystals. Single crystal **X-ray crystallographic** data and structure refinement for both crystals are shown in **Table 4.2**, selected bond lengths and angles are shown in **Table 4.3**, and their molecular structure and packing are shown in **Figure 4.4** and **Figure 4.5**. Hence, the structural formulas for these crystals were $[Cu_2(CH_3(CH_2)_6COO)_4(bpy)_2]$ (yield = 12%) (**1**) and $[Cu_2Cl_2(H_2O)_4(bpy)_2]$ (**1a**). These results further support the presence of Cl in the starting complex.

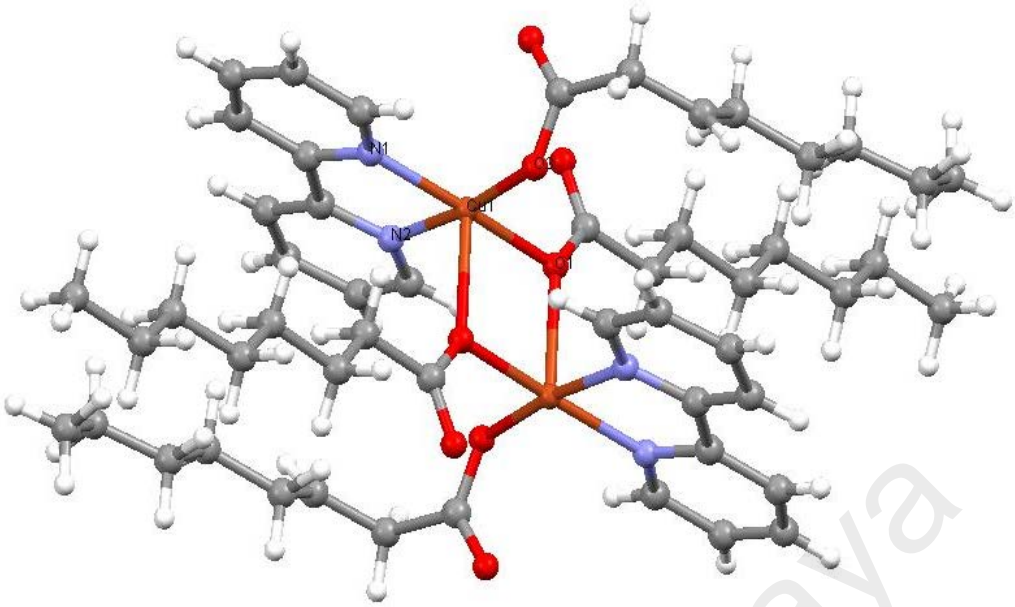

(a)

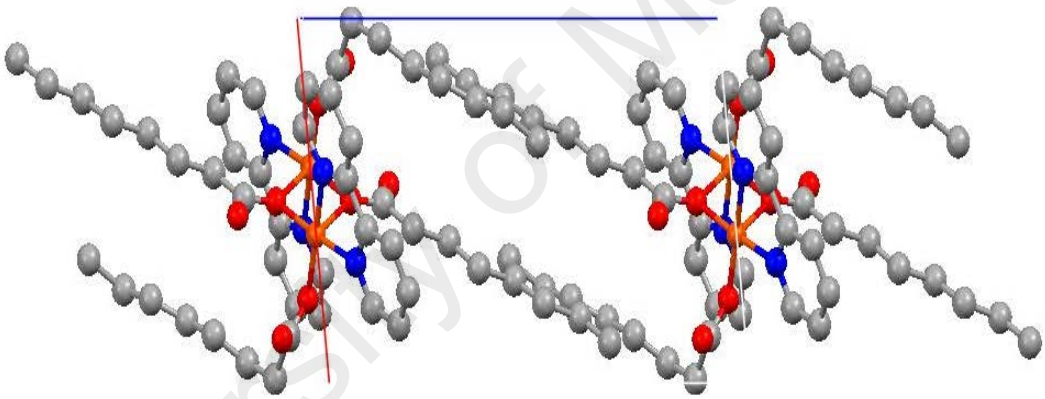

(b)

Figure 4.4 (a) Molecular structure, and (b) the packing diagram of **1** viewed along crystallographic *b*-axis

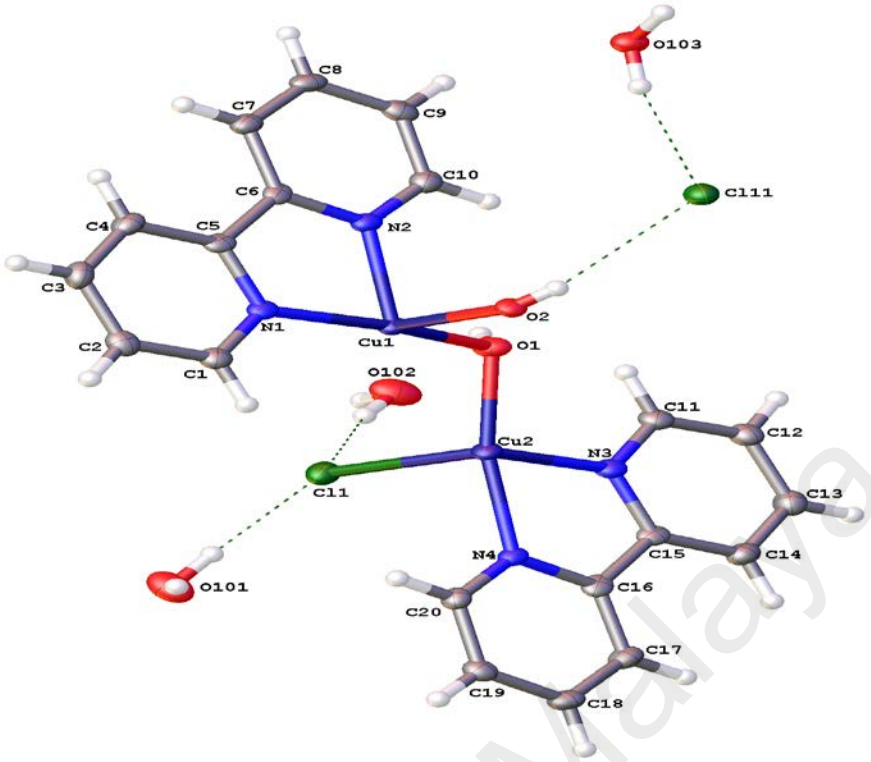

(a)

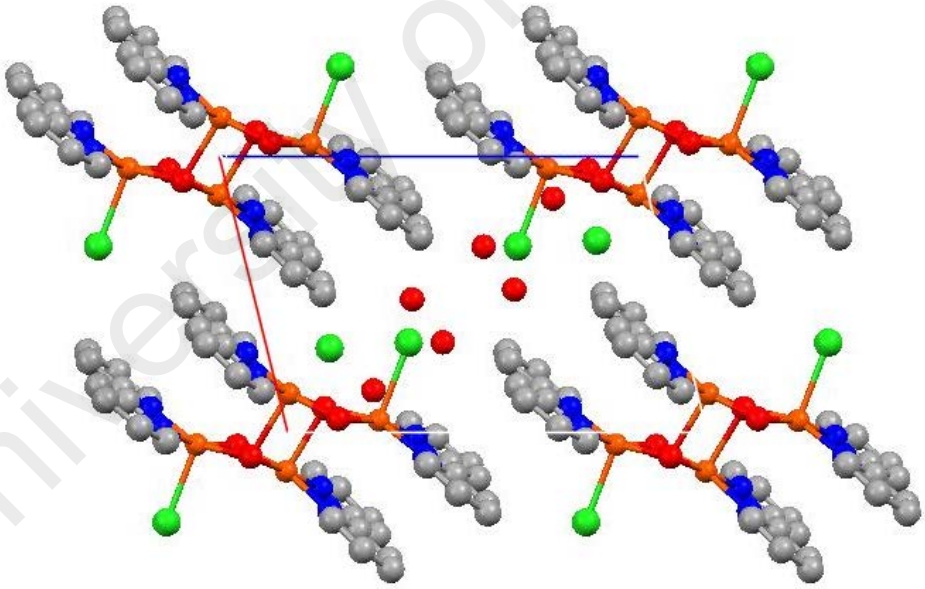

(b)

Figure 4.5 (a) Molecular structure, and (b) the packing diagram of **1a** viewed along crystallographic *b*-axis

From the study of the crystal structure of **1**, the compound was crystallised in the triclinic system with $P\bar{1}$ space group, a = 9.50(11) Å, b = 9.71(11) Å, c = 15.37(2) Å, α = 76.89(3)°, β = 81.96(2)°, γ = 84.33(3)°, Z = 2, V = 1364(3) Å^3 (**Figure 4.4**). Each of its copper(II) centre was penta-coordinated with two N atoms from chelating bpy [Cu-N1 = 2.006 (5) Å and Cu-N2 = 2.048 (5) Å], two O atoms from bridging $CH_3(CH_2)_6COO^-$ ligands (Cu-O1 = 1.968 (5) Å and Cu-O2 = 2.381 (5) Å), and an O atom from monodentate $CH_3(CH_2)_6COO^-$ ligands (Cu-O3 = 1.930 (5) Å), residing in a square pyramidal geometry environment. The Cu-N bond lengths [74-76] and the two equatorial Cu-O bonds lengths were in the expected range [74-76], while the Cu1-O2 bond length at the apical site of copper(II) has a longer length than expected. This is in agreement of the *syn-anti* binding mode of the carboxylato ligand [76], resulting in significantly long Cu-Cu distance (3.374 Å) (the normal Cu-Cu length for copper(II) complexes with the paddle-wheel structure is about 2.6 Å [74,75]. The Cu(II) atom was coplanar with the equatorial donor atoms of O(1)/O(1a) and bpy ring with max deviation of 0.007(5) at N(2) atom from the least square plane.

In contrast, **1a** was a dinuclear copper(I) complex which crystallised in the triclinic $P\bar{1}$ space group (**Figure 4.5**). The two copper(I) centres have distorted tetrahedral geometry and different environments, namely CuN_2O_2 and CuN_2OCl. The coordination at the first Cu(I) centre involved two N atoms from chelating bpy and two O from bridging aqua ligand, while the second Cu(I) involved two N atoms from chelating bpy, an O from bridging aqua ligand, and a Cl atom at the axial position.

The formation of complexes **1** and **1a** suggested that Cu(II) in $[Cu_6Cl_{10}(CH_3(CH_2)_6COO)_2].3H_2O.2CH_3CH_2OH$ was partially reduced to Cu(I) when it reacted with bpy. Similar suggestion was offered by Chisholm *et al*. for $[Mo(OPr^i)_2(bpy)_2]$ [77].

Its **FTIR** data (**Table 4.1**; **Figure 4.6**) shows the presence of the expected functional groups. Hence, the $\Delta\nu_{coo}$ values were 209 and 186 cm^{-1}, in agreement with monodentate nonbridging and *syn-anti* monodentate bridging $CH_3(CH_2)_6COO$ ligands as revealed from its crystal structure, respectively.

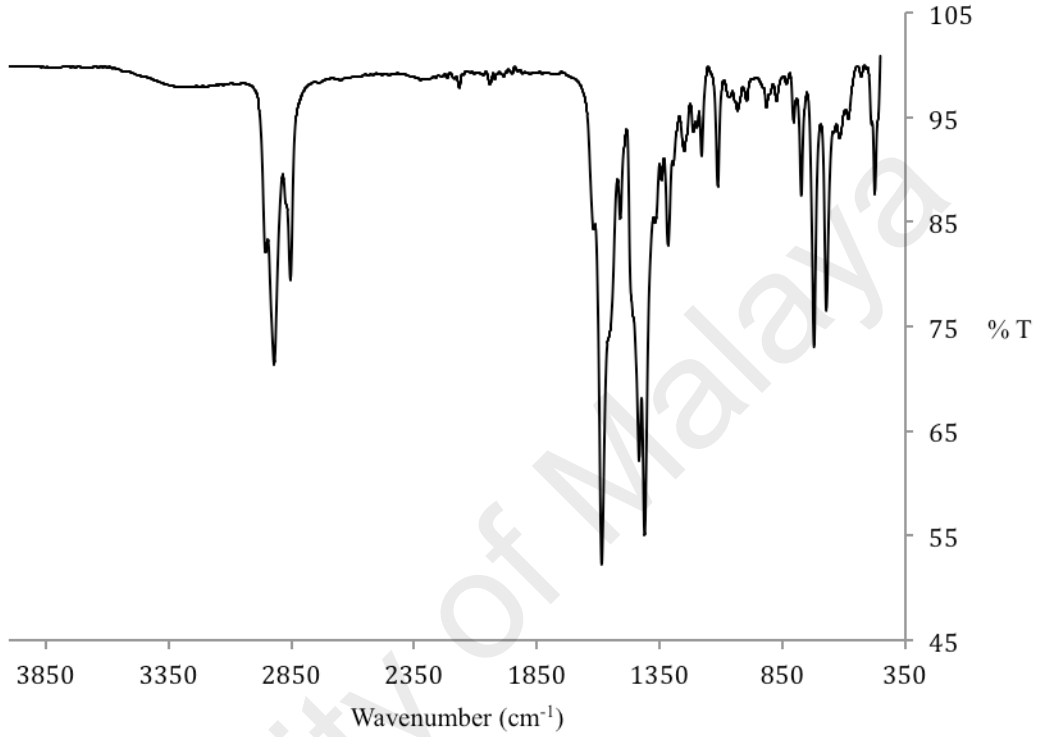

Figure 4.6 FTIR spectrum of **1**

Its **UV-vis spectrum** (**Figure 4.7**) in DMSO-C_2H_5OH shows a broad *d-d* band at 699 nm (ε_{max} = 104 M^{-1} cm^{-1}) and a shoulder on a strong charge transfer band at 370 nm (ε_{max} = 115 M^{-1} cm^{-1}). The data suggest a dinuclear complex with square pyramidal geometry at Cu(II) centres [72, 73]. Hence, the geometry of **1** in the crystals remained intact in these solvents.

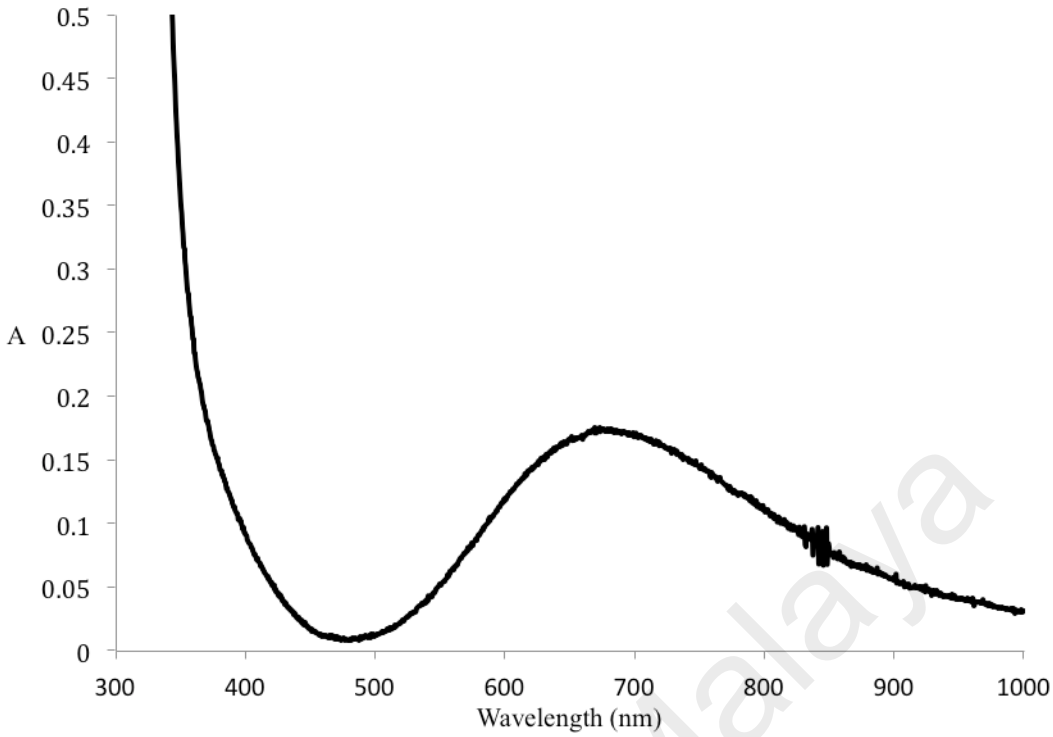

Figure 4.7 UV-vis spectrum of **1** in DMSO-C_2H_5OH

The value of its effective **magnetic moment** (μ_{eff}), obtained by the Gouy method, was 2.36 BM at 298 K. The value was calculated from the values of its formula weight (FW = 506.12 g mol^{-1}), mass susceptibility (χ_g = 1.80 x 10^{-4} cm^3 g^{-1}), molar susceptibility (χ_M = 1.82 x 10^{-4} cm^3 mol^{-1}), diamagnetic correction factor (χ_D = -5.061 x 10^{-4} cm^3 mol^{-1}) and hence corrected molar susceptibility (χ_M^{corr} = 2.33 x 10^{-3} cm^3 mol^{-1}). It is noted that the theoretical value based on the spin-only formula for a dinuclear octahedral copper(II) complex is 2.43 BM (χmT = 0.375 cm^3 K mol^{-1}per Cu(II)) [22]. Thus, there was insignificant communication between the two Cu(II) centres in this complex.

(b) Thermal and mesomorphic studies

The **TG** trace for **1** was measured for the powder (**Figure 4.8**). It shows an initial weight loss of 3.1% at 100.7 ^oC assigned to evaporation of two lattice H_2O (calculated, 3.5%). The next weight loss of 80.6% from 195 ^oC to 659 ^oC were assigned to the decomposition of $CH_3(CH_2)_6COO^-$ ion to CO_2 and other volatiles [32], and bpy

molecule (calculated, 84.4%). The amount of residue at temperatures above 659 ^{o}C was 16.3% (calculated 15.7%, assuming pure CuO [32]). Hence, its decomposition temperature was 195 ^{o}C, which is similar to that of $[Cu(CH_3(CH_2)_6COO)_2(py)_2].H_2O$ (T_{dec} = 210 ^{o}C) [78].

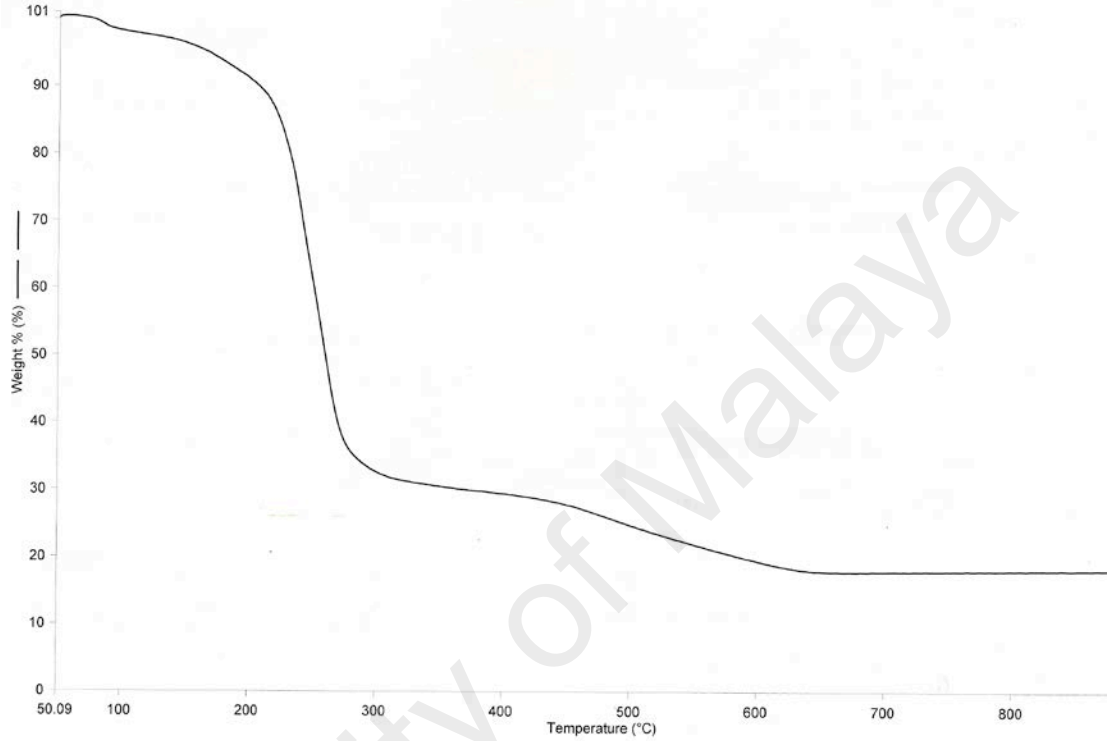

Figure 4.8 TGA trace of **1**

When viewed under **POM**, **1** started to melt at 112 ^{o}C and to clear at about 157 ^{o}C. Upon cooling, an optical texture was observed at 138°C (**Figure 4.9(a)**). In comparison, its precursor complex, $[Cu_2(CH_3(CH_2)_6COO)_4]$, was observed melting at 150 ^{o}C and cleared to an isotropic liquid at 160 ^{o}C. Upon cooling from 160 ^{o}C, a different optical texture was formed at 151 ^{o}C (**Figure 4.9**(**b**)). These observations indicate that both **1** and its precursor complex behaved as different thermotropic metallomesogens.

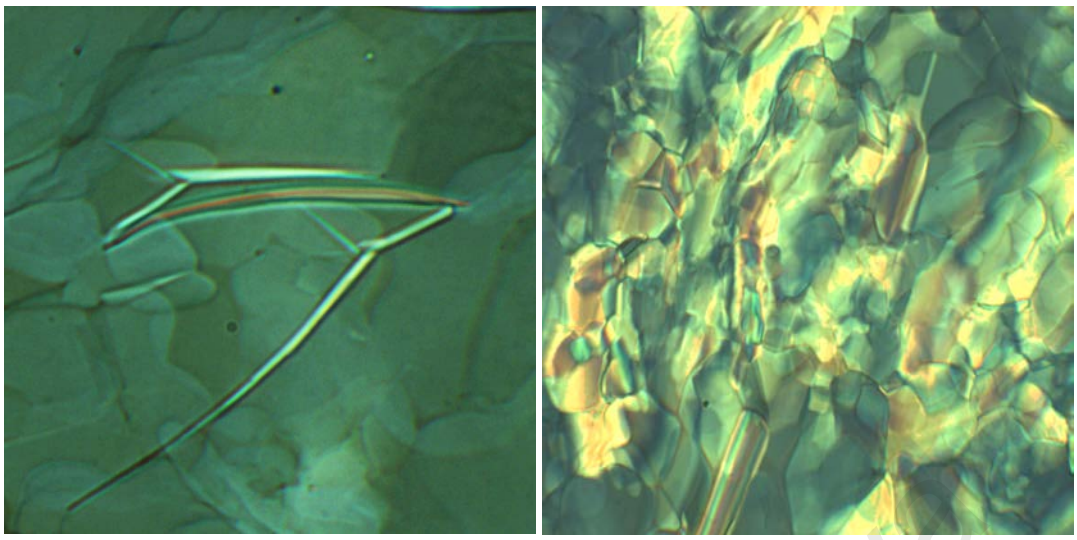

(a) (b)

Figure 4.9 Photomicrographs of: (a) **1** on cooling at 138 ^{o}C; (b) $[Cu_2(CH_3(CH_2)_6COO)_4]$ on cooling at 150 ^{o}C

Its **DSC** traces (**Figure 4.10**) shows two overlapping endothermic peaks on heating at 93 ^{o}C ($\Delta H_{combined}$ = +63 kJ mol^{-1}) assigned to the breaking of the axial Cu-O bonds of the dimeric structure to form two monomers and melting of the monomers, and a broad endothermic peak at 157 ^{o}C (ΔH = +42 kJ mol^{-1}) assigned to its clearing temperature to isotropic liquid (*I*). On cooling, there were two exothermic peaks at 136 ^{o}C (ΔH = -36 kJ mol^{-1}) and 35 ^{o}C (ΔH = -22 kJ mol^{-1}) assigned to the formation of a mesophase (*I-M* transition) and mesophase-to-crystal transition (*M-Cr*), respectively.

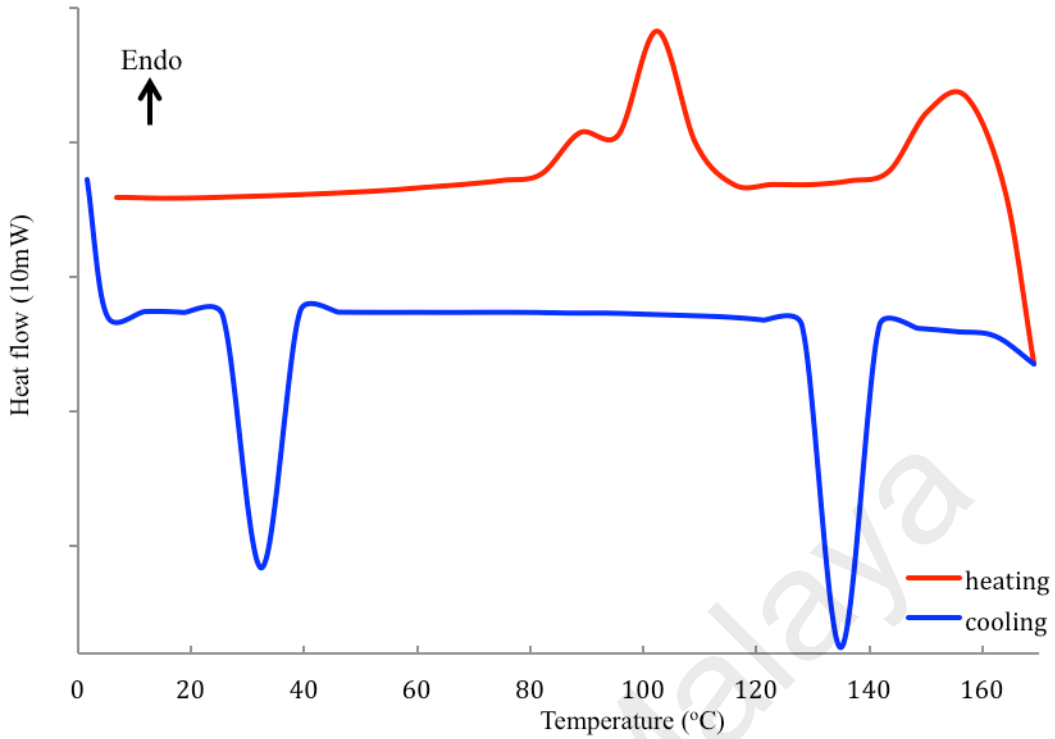

Figure 4.10 DSC scans of **1**

4.1.2 [$Cu_2(CH_3(CH_2)_8COO)_4(bpy)_2$] (2)

(a) Synthesis and structural elucidation

The first step in the synthesis [$Cu_2(CH_3(CH_2)_8COO)_4(bpy)_2$] (**2**) (**Scheme 4.1**) involved the reaction of $CH_3(CH_2)_8COOH$ with Na_2CO_3 to form $CH_3(CH_2)_8COONa.2H_2O$. It was obtained as a white powder in good yield (74%). Its **elemental analysis** results (C, 51.6%; H, 10.2%) were in good agreement with the calculated values (C, 52.2%; H, 10.1%; FW 230.274 g mol^{-1}). Its **FTIR** data (**Table 4.1**; **Figure 4.11**) shows the presence of the expected functional groups. Hence, the $\Delta\nu_{coo}$ value for $CH_3(CH_2)_8COO^-$ ion was 133 cm^{-1}.

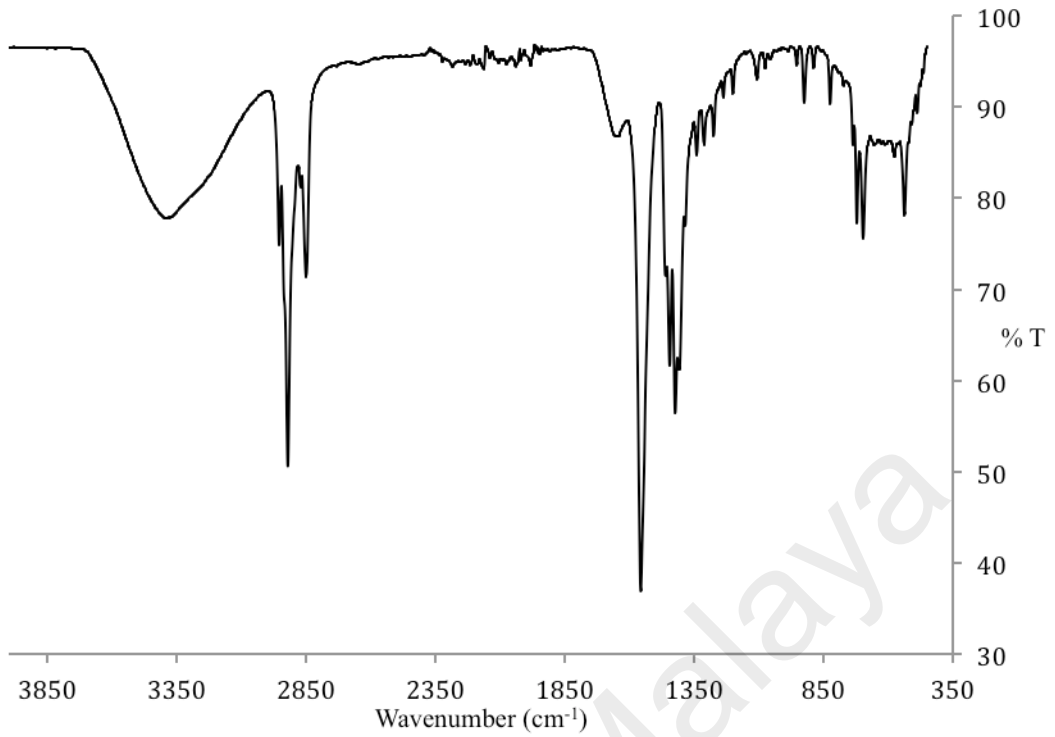

Figure 4.11 FTIR spectrum of $CH_3(CH_2)_8COONa.2H_2O$

The second step involved reacting $CH_3(CH_2)_8COONa.2H_2O$ with $CuCl_2.2H_2O$ to form the precursor complex, $[Cu_2(CH_3(CH_2)_8COO)_4(H_2O)_2]$ (green powder; yield = 39%). Its **elemental analysis** results (C, 57.0%; H, 9.0%) were in good agreement with the calculated values (C, 56.6%; H, 9.5%; FW 848.14 g mol^{-1}). Its **FTIR** data (**Table 4.1**; **Figure 4.12**) shows the presence of the expected functional groups. The $\Delta\nu_{coo}$ value was 192 cm^{-1}, indicating that $CH_3(CH_2)_8COO^-$ was coordinated at a bridging ligand in the complex.

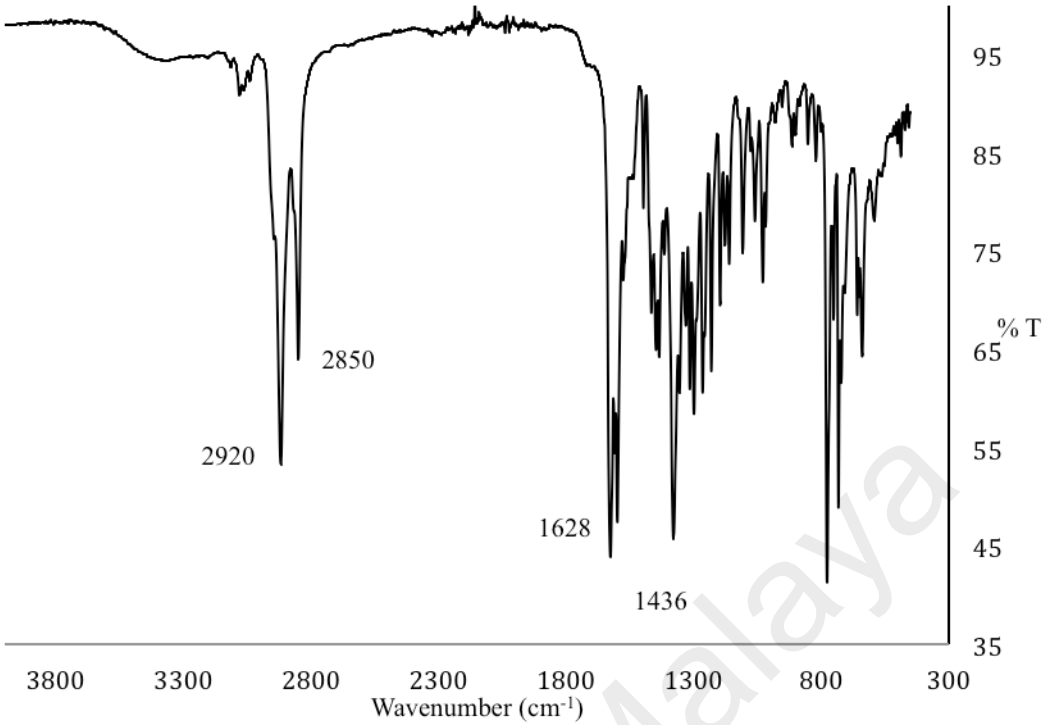

Figure 4.12 FTIR spectrum of $[Cu_2(CH_3(CH_2)_8COO)_4(H_2O)_2]$

Its **UV-vis** spectrum (**Figure 4.13**) in C_2H_5OH shows a broad *d-d* band at 699 nm (ε_{max} = 386 M^{-1} cm^{-1}) and a shoulder to a strong charge transfer band at 366 nm (ε_{max} = 325 M^{-1} cm^{-1}). The data suggest a square pyramidal geometry for both Cu(II) in the dinuclear complex.

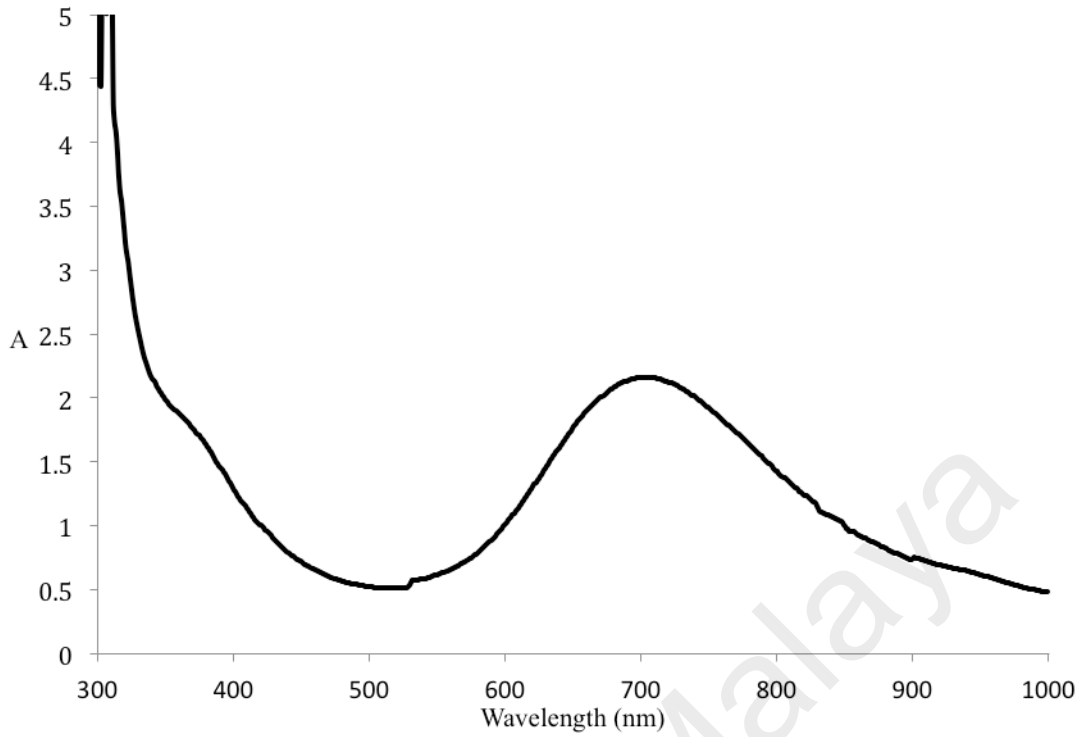

Figure 4.13 UV-vis spectrum of $[Cu_2(CH_3(CH_2)_8COO)_4(H_2O)_2]$ in DMSO-C_2H_5OH

The μ_{eff} value for $[Cu_2(CH_3(CH_2)_8COO)_4(H_2O)_2]$ was 2.2 BM at 298 K. It was calculated from the values of its formula weight (FW = 848.14 g mol^{-1}), mass susceptibility (χ_g = 0.193 x 10^{-5} cm^3 g^{-1}), molar susceptibility (χ_m = 1.637 x 10^{-3} cm^3 mol^{-1}), diamagnetic correction factor (χ_D = -4.24 x 10^{-4} cm^3 mol^{-1}) and corrected molar susceptibility (χ_m^{corr} = 2.06 x 10^{-3} cm^3 mol^{-1}). It is noted that the value was slightly lower than the spin-only value of 2.43 BM for two independent Cu(II) centres (S = ½) [22], but similar with other copper(II) alkylcarboxylates. An example is $[Cu_2(CH_3(CH_2)_5COO)_4]$ (μ_{eff} = 1.6 BM) [30]. Hence, it is proposed that $[Cu_2(CH_3(CH_2)_8COO)_4(H_2O)_2]$ has the paddle-wheel structure, and there were antiferromagnetic interactions between the two Cu(II) centres, postulated to occur through the bridging carboxylate ligands by a mechanism termed the superexchange pathway [26].

$[Cu_2(CH_3(CH_2)_8COO)_4(H_2O)_2]$ reacted with bpy to form a blue semisolid, which on recrystallisation from chloroform-ethanol (1:1 v/v), formed blue crystals (yield = 98%). Single crystal **X-ray crystallographic** data and structure refinement for the

crystal is shown in **Table 4.2**, selected bond lengths and angles are shown in **Table 4.3**, and ORTEP presentations and packing patterns are shown in **Figure 4.14**. Hence, the structural formula for the crystal was $[Cu_2(CH_3(CH_2)_8COO)_4(bpy)_2]$ (**2**).

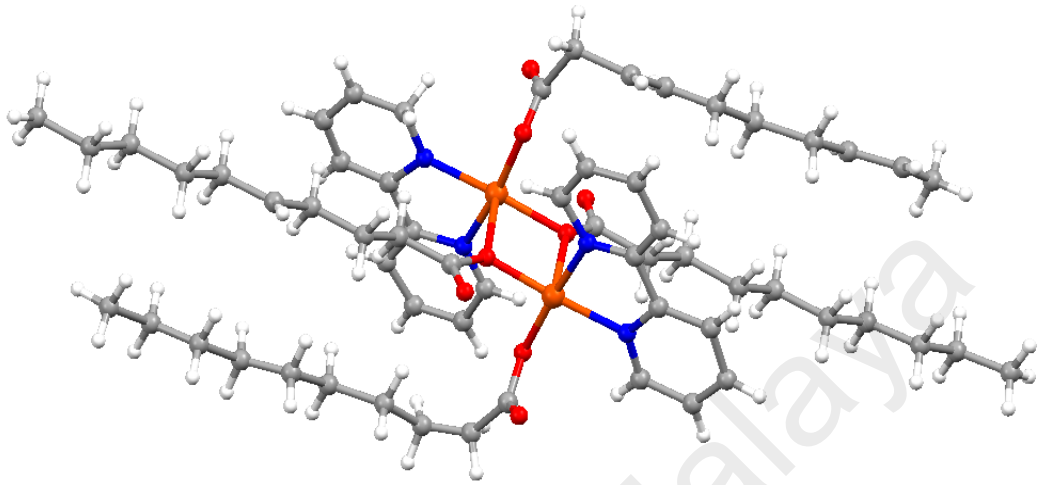

(a)

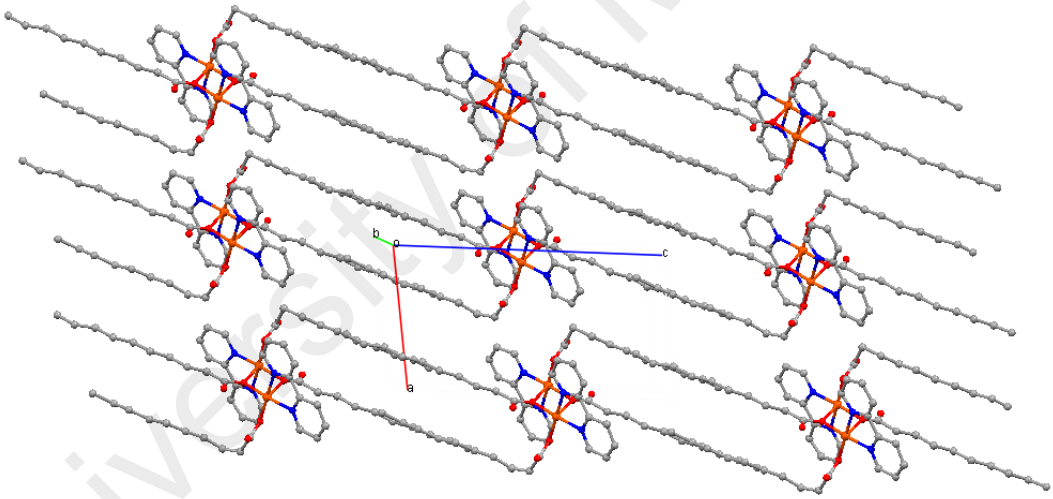

(b)

Figure 4.14 (a) Molecular structure, and (b) packing diagram **2** viewed along crystallographic *b*-axis

The X-ray data shows that **2** has similar structure as **1**. Its crystallised in the triclinic system with *P1* space group, a = 9.39(6) Å, b = 9.59(6) Å, c = 17.59(2) Å, α = 83.34(5)^o, β = 79.60(4)^o, γ = 82.51(5)^o, Z = 1, V = 1536(18) Å^3. Each of its copper(II) centre was penta-coordinated with two N atoms from chelating bpy [Cu-N1 = 2.005 (16) Å and Cu-N2 = 2.059 (19) Å], two O atoms from bridging $CH_3(CH_2)_8COO^-$ ligands (Cu-O1 = 1.919 (19) Å and Cu-O2 = 2.390 (16) Å), and an O

atom from monodentate $CH_3(CH_2)_8COO^-$ ligands (Cu-O3 = 1.901 (15) Å). The Cu(II) atom was coplanar with the equatorial donor atoms of O(1)/O(3) and bpy ring with max deviation of 0.016(5) at N(3) atom from the least square plane.

Its **FTIR** data (**Table 4.1**; **Figure 4.15**) shows the presence of the expected functional groups. Hence, the $\Delta\nu_{coo}$ values were 247 and 182 cm^{-1} in agreement with monodentate nonbridging and *syn-anti* monodentate bridging $CH_3(CH_2)_8COO^-$ ligands, respectively, as observed in its single crystal structure.

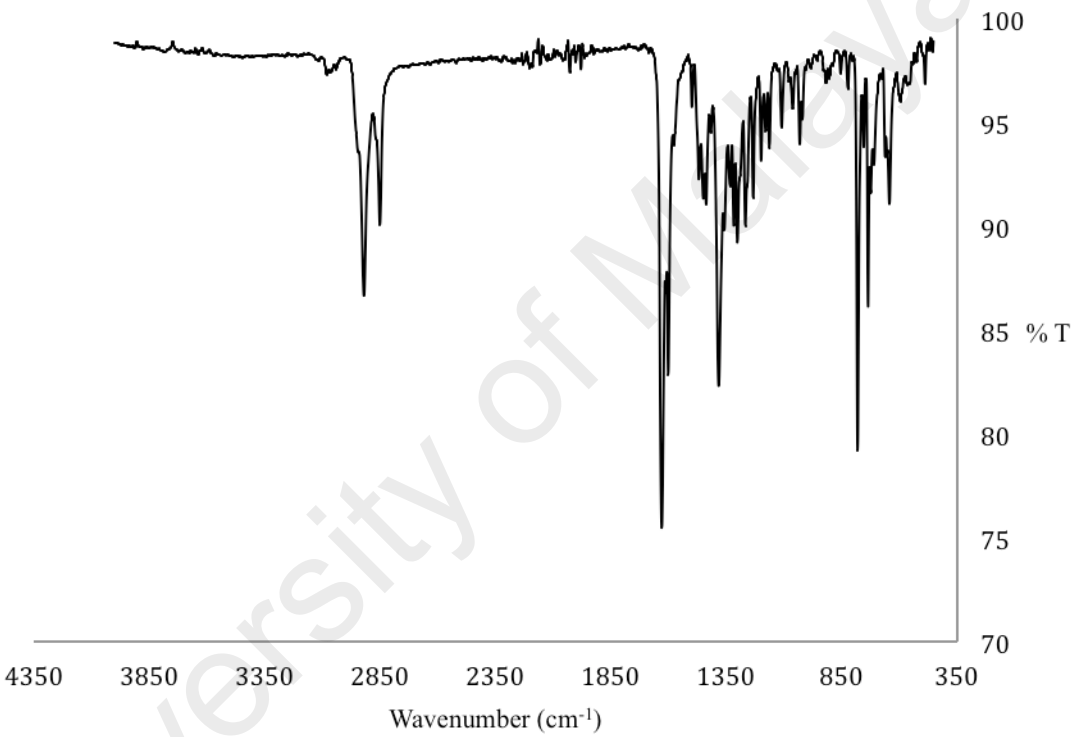

Figure 4.15 FTIR spectrum of **2**

Its **UV-vis spectrum** (**Figure 4.16**) in DMSO-C_2H_5OH shows a broad *d-d* band at 683 nm (ε_{max} = 117 M^{-1} cm^{-1}) and a shoulder to a strong charge transfer band at 388 nm (ε_{max} = 167 M^{-1} cm^{-1}). These data were similar to **1** and may be similarly explained.

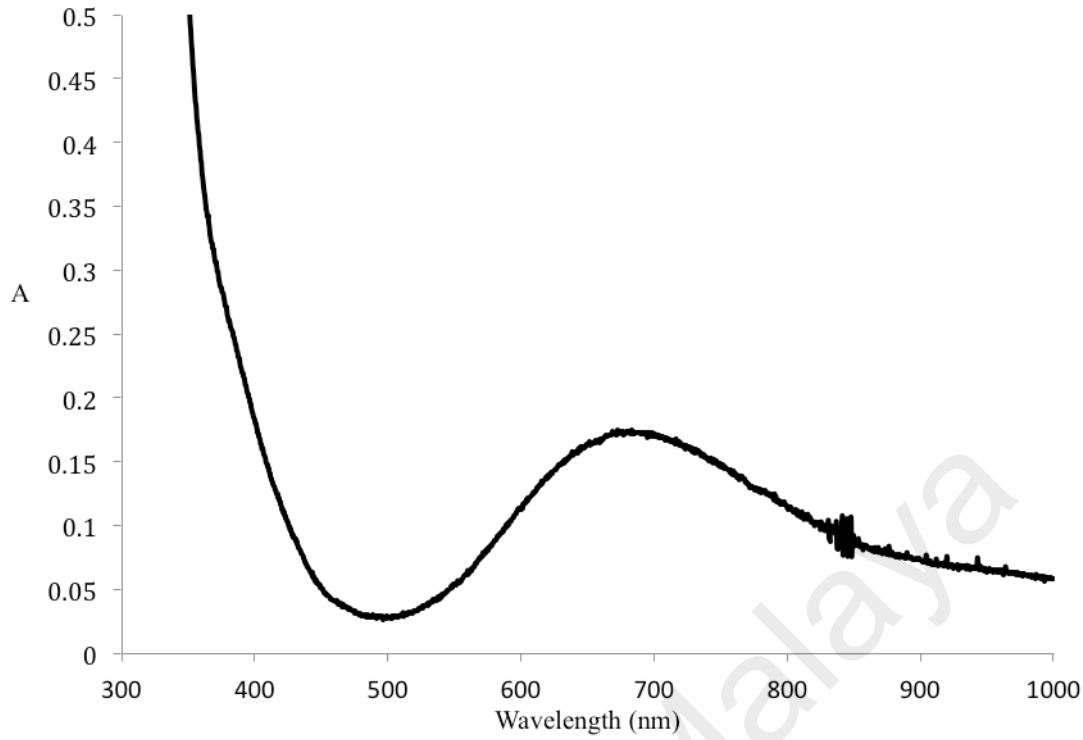

Figure 4.16 UV-vis spectrum of **2** in DMSO-C_2H_5OH

Prior to measuring its magnetic moment, the semisolid was left in an oven for a week when it changed to a blue powder. Its μ_{eff} value, calculated from the values of its formula weight (FW = 1120.42 g mol^{-1}), mass susceptibility (χ_g; 0.207 x 10^{-5} cm^3 g^{-1}), molar susceptibility (χ_m; 2.323 x 10^{-3} cm^3 mol^{-1}), diamagnetic correction factor (χ_D; -5.60 x 10^{-4} cm^3 mol^{-1}) and corrected molar susceptibility (χ_m^{corr}; 2.88 x 10^{-3} cm^3 mol^{-1}), was 2.63 BM at 298 K.

(b) Thermal and mesomorphic studies

The **TG** trace of the semisolid (**Figure 4.17**) shows a total weight loss of 92.9% in the temperature range 177 ^oC to 658 ^oC due to the decomposition of $CH_3(CH_2)_8COO^-$ ion and bpy (calculated, 89.4%). The results are in a good agreement with its structural formula (**Figure 4.14**). The amount of residue was 8.4% (calculated, 13.3% assuming CuO). Hence, its decomposition temperature was 177 ^oC.

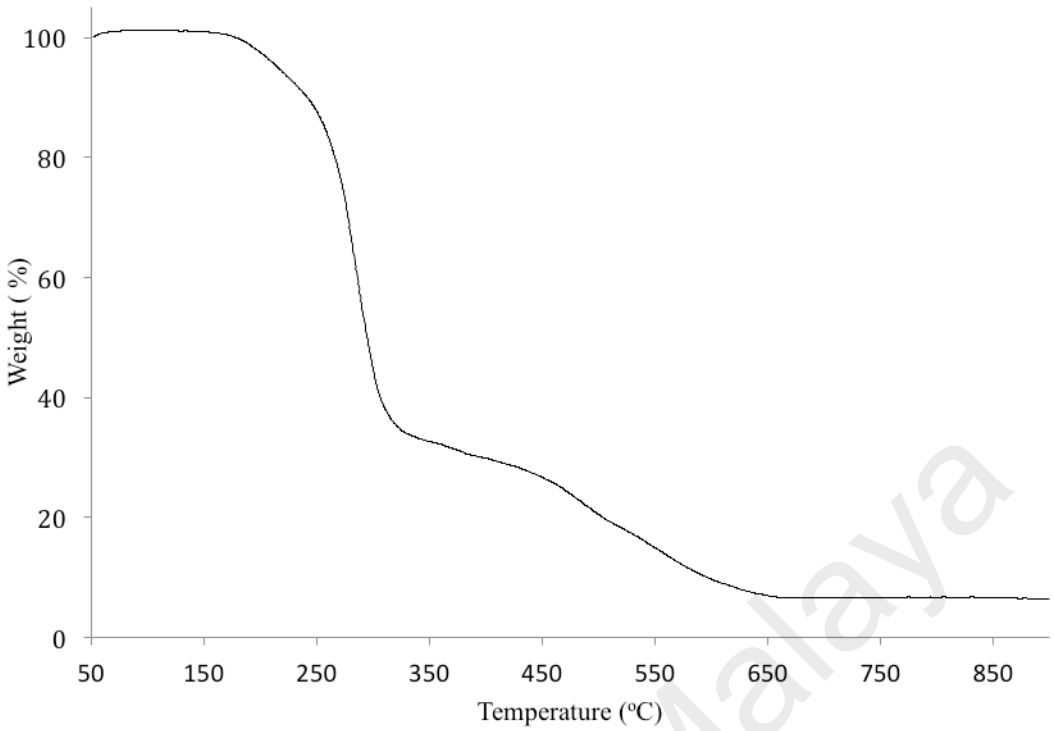

Figure 4.17 TGA trace of **2**

When viewed under **POM**, the semisolid was fluidic at 29.6 ^{o}C and then cleared at about 100 ^{o}C. Upon cooling from *I*, bâtonnet textures were observed at 36 ^{o}C (**Figure 4.18**), indicating the formation of smectic A phase (SmA). In contrast, its precursor complex, $[Cu_2(CH_3(CH_2)_8COO)_4(H_2O)_2]$, did not show any optical structures. Similar observation was reported for crystals of $[Cu_2(CH_3(CH_2)_8COO)_4]$ by Ramos *et al.*, [40]. From these result, it is proposed that the structure of **2** changed to rod-like when the *syn-anti* monodentate bridging $CH_3(CH_2)_8COO^-$ ligand dissociated on heating. Similar thermal effect on the binding modes of carboxylate ligands was suggested for $[Cu_2(CH_3(CH_2)_nCOO)_4]$ (n = 4-8, 10, 12, 14, 16) by Moita *et al.* based on variable-temperature FTIR spectroscopy [79] and by Abdullah *et al.* for $[Cu(R)_2(4,4'\text{-bpy})_2].2RH$ (R = 2-hexydecanoate ion, 4,4'-bpy = 4,4'-bipyridine) [49]. Hence, **2** behaved as a thermotropic metallomesogen (smectogenic).

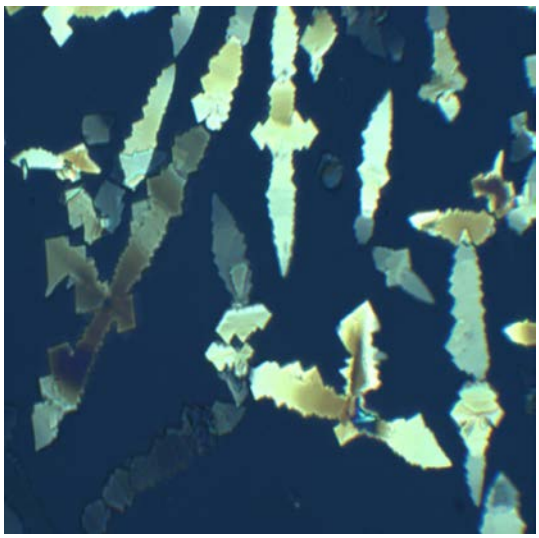

Figure 4.18 Photomicrograph of **2** at 36 ^{o}C on cooling

The **DSC** traces for the semisolid (**Figure 4.19**) shows a broad endothermic peak on heating at 33 ^{o}C (ΔH = +35 kJ mol^{-1}) assigned to breaking of the *syn-anti* bridging bonds of the complex, and a broad peak endothermic peak at 118 ^{o}C (ΔH = +27 x 10^{3} kJ mol^{-1}) assigned to *I*. On cooling, there was an exothermic peak at 32°C (ΔH = -36 kJ mol^{-1}) assigned to *I-M* transition.

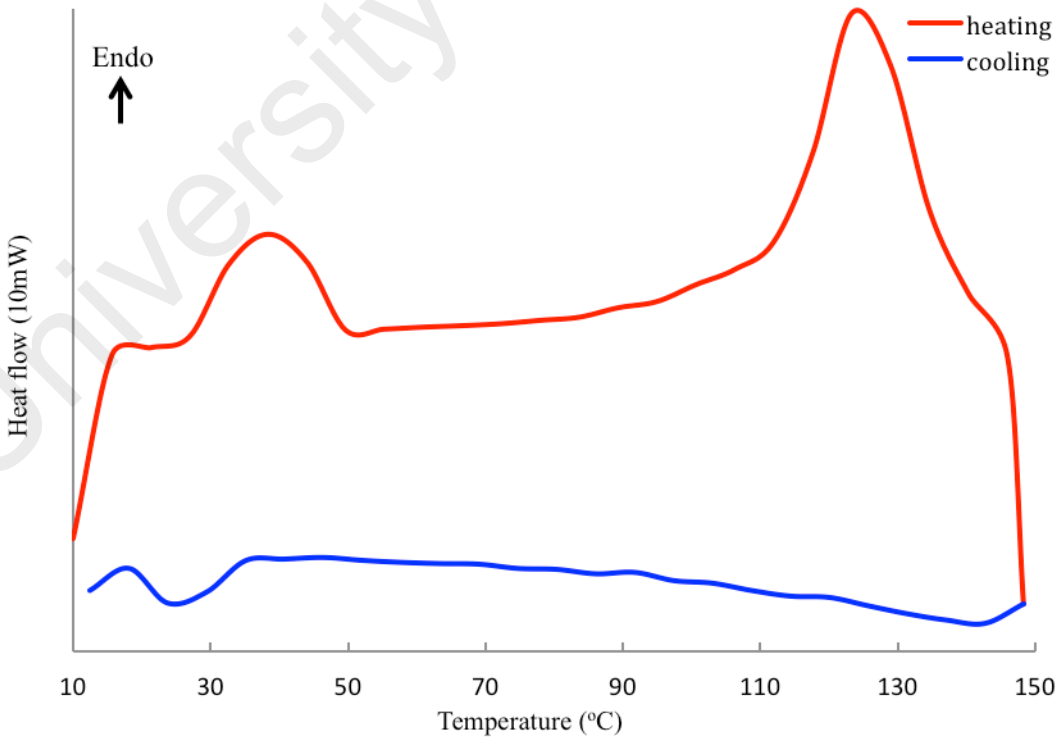

Figure 4.19 DSC scans of **2**

4.1.3 $[Cu_2(CH_3(CH_2)_{10}COO)_4(bpy)_2]$ (3)

(a) Synthesis and structural elucidation

The first step in the synthesis $[Cu_2(CH_3(CH_2)_{10}COO)_4(bpy)_2]$ (**3**) (**Scheme 4.1**) involved the reaction of $CH_3(CH_2)_{10}COOH$ with Na_2CO_3 to form $CH_3(CH_2)_{10}COONa.½H_2O$. It was obtained as a white powder in good yield (69%). Its **elemental analysis** results (C, 62.3%; H, 10.1%) were in good agreement with the calculated values, (C, 61.8%; H, 11.0%; FW 231.302 g mol^{-1}). Its **FTIR** data (**Table 4.1**; **Figure 4.20**) shows the presence of the expected functional groups. Hence, the $\Delta\nu_{coo}$ value for $CH_3(CH_2)_{10}COO^-$ ion was 136 cm^{-1}.

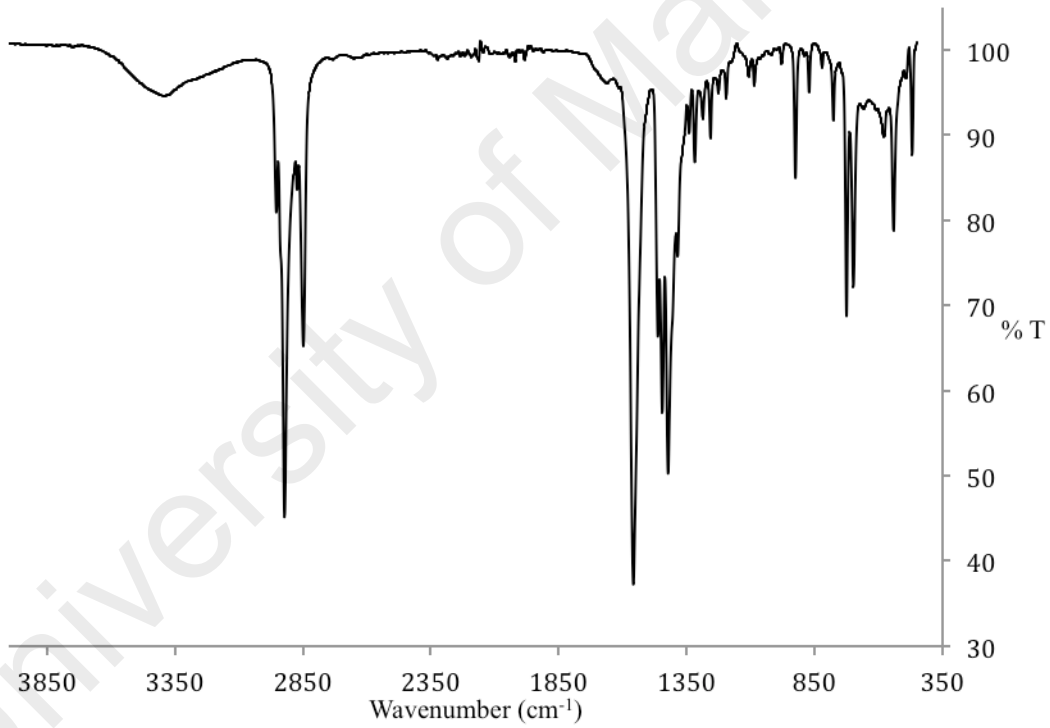

Figure 4.20 FTIR spectrum of $CH_3(CH_2)_{10}COONa.½H_2O$

The second step involved reacting $CH_3(CH_2)_{10}COONa.½H_2O$ with $CuCl_2.2H_2O$ to form the precursor complex, $[Cu_2(CH_3(CH_2)_{10}COO)_4(H_2O)_2].2H_2O$ (blue powder; yield = 10%). Its **elemental analysis** results (C, 58.1%; H, 9.6%) were in good agreement with the calculated values (C, 57.9%; H, 10.1%; FW 996.38 g mol^{-1}). Its **FTIR** data (**Table 4.1**; **Figure 4.21**) shows the presence of the expected functional groups. The

$\Delta\nu_{coo}$ value was 177 cm^{-1}, indicating that $CH_3(CH_2)_{10}COO^-$ was coordinated at a bridging ligand in the complex.

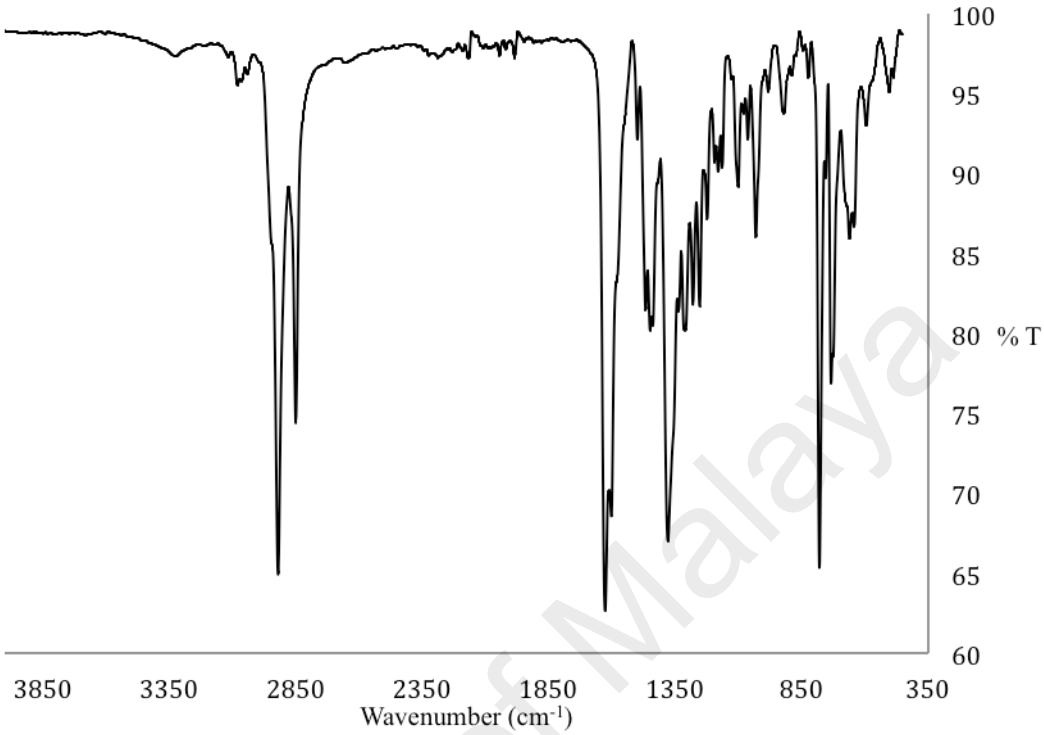

Figure 4.21 FTIR spectrum of $[Cu_2(CH_3(CH_2)_{10}COO)_4(H_2O)_2].2H_2O$

Its **UV-vis** spectrum (**Figure 4.22**) in DMSO-C_2H_5OH shows a broad *d-d* band at 693 nm (ε_{max} = 467 M^{-1} cm^{-1}). The data are similar to previously discussed complexes, and may be similarly explained.

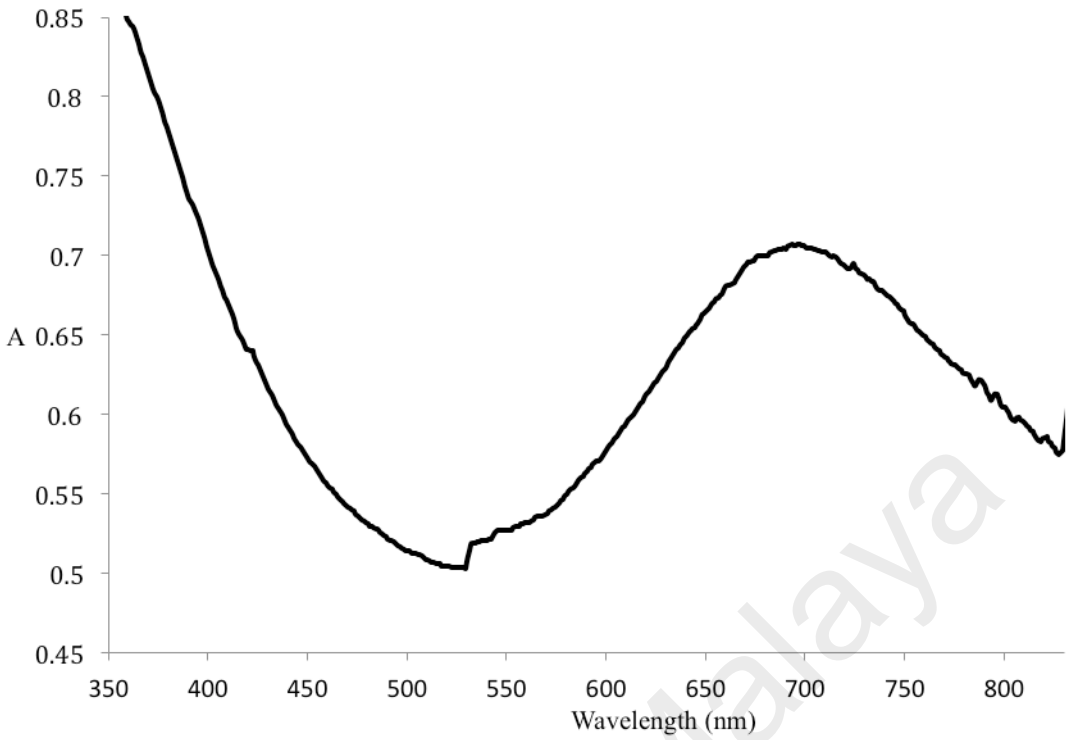

Figure 4.22 UV-vis spectrum of $[Cu_2(CH_3(CH_2)_{10}COO)_4(H_2O)_2].2H_2O$ in DMSO-C_2H_5OH

The μ_{eff} value for $[Cu_2(CH_3(CH_2)_{10}COO)_4(H_2O)_2].2H_2O$ could not determined due to insufficient sample.

$[Cu_2(CH_3(CH_2)_{10}COO)_4(H_2O)_2].2H_2O$ reacted with bpy to form a blue powder (yield = 95%), which on recrystallisation from ethanol, formed blue crystals. Single crystal **X-ray crystallographic** data and structure refinement for the crystal is shown in **Table 4.2**, selected bond lengths and angles are shown in **Table 4.3**, and ORTEP presentations and packing patterns are shown in **Figure 4.23**. Hence, the structural formula for the crystal was $[Cu_2(CH_3(CH_2)_{10}COO)_4(bpy)_2]$ (**3**) which was similar to **1** and **2**.

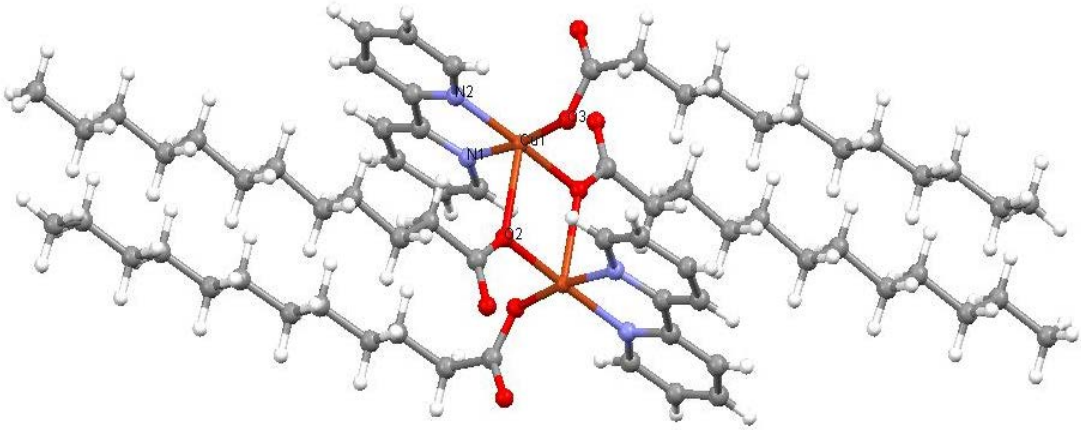

(a)

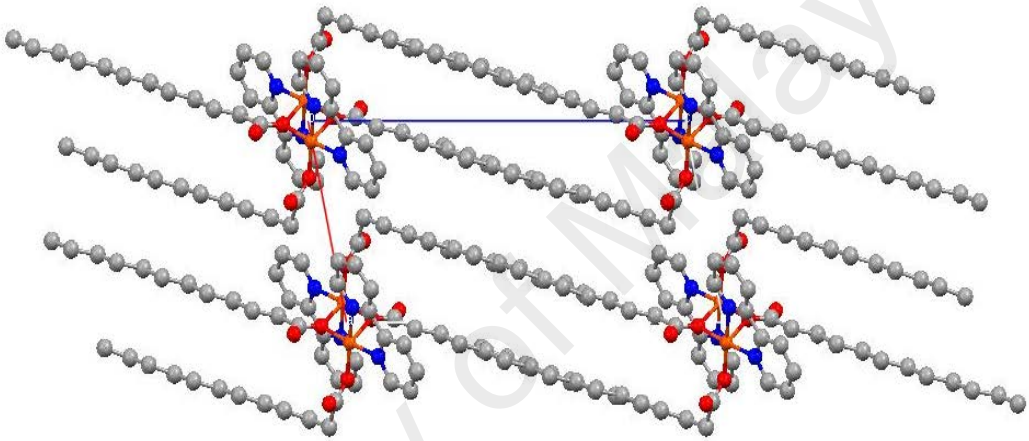

(b)

Figure 4.23 (a) Molecular structure, and (b) packing diagram **3** viewed along crystallographic *b*-axis

The X-ray data shows that **3** has similar structure as **1** and **2**. It crystallised in the triclinic system with *P-1* space group, a = 9.35(7) Å, b = 9.61(6) Å, c = 19.88(13) Å, α = 86.80(5)^o, β = 77.04(4)^o, γ = 81.22(5)^o, Z = 1, V = 1720(19) Å^3. Each of its copper(II) centre was penta-coordinated with two N atoms from chelating bpy [Cu-N1 = 2.016 (2) Å and Cu-N2 = 2.022 (3) Å], two O atoms from bridging $CH_3(CH_2)_{10}COO^-$ ligands (Cu-O1 = 1.952 (2) Å and Cu-O2 = 2.393 (2) Å), and an O atom from monodentate $CH_3(CH_2)_{10}COO^-$ ligands (Cu-O3 = 1.939 (2) Å). The Cu(II) atom was coplanar with the equatorial donor atoms of O(17)/O(17a) and bpy ring with max deviation of 0.007(3) at N(5) atom from the least square plane.

Its **FTIR** data (**Table 4.1**; **Figure 4.24**) shows the presence of the expected functional groups. Hence, the $\Delta\nu_{coo}$ values were 248 and 178 cm^{-1} in agreement with monodentate nonbridging and *syn-anti* monodentate bridging $CH_3(CH_2)_{10}COO^-$ ligands, respectively, as observed in its single crystal structure.

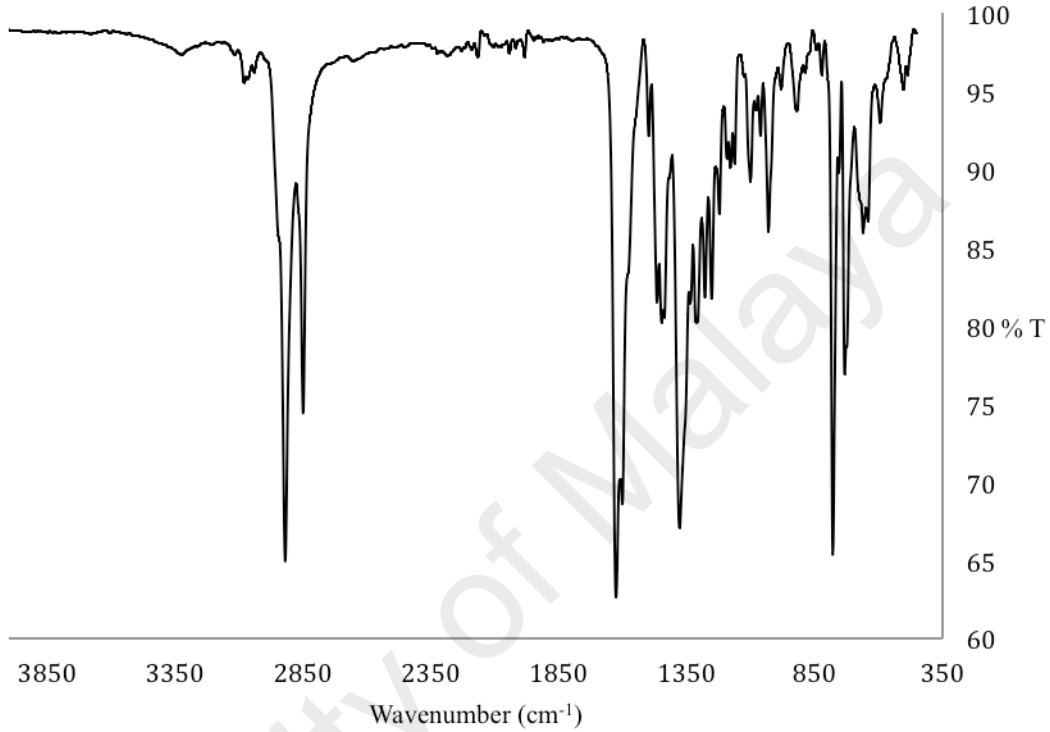

Figure 4.24 FTIR spectrum of **3**

Its **UV-vis spectrum** (**Figure 4.25**) in DMSO-C_2H_5OH shows a broad *d-d* band at 680 nm (ε_{max} = 199 M^{-1} cm^{-1}) and a shoulder to a strong charge transfer band at 369 nm (ε_{max} = 189 M^{-1} cm^{-1}). Hence, the data are similar to **1** and **2**, and may be similarly explained.

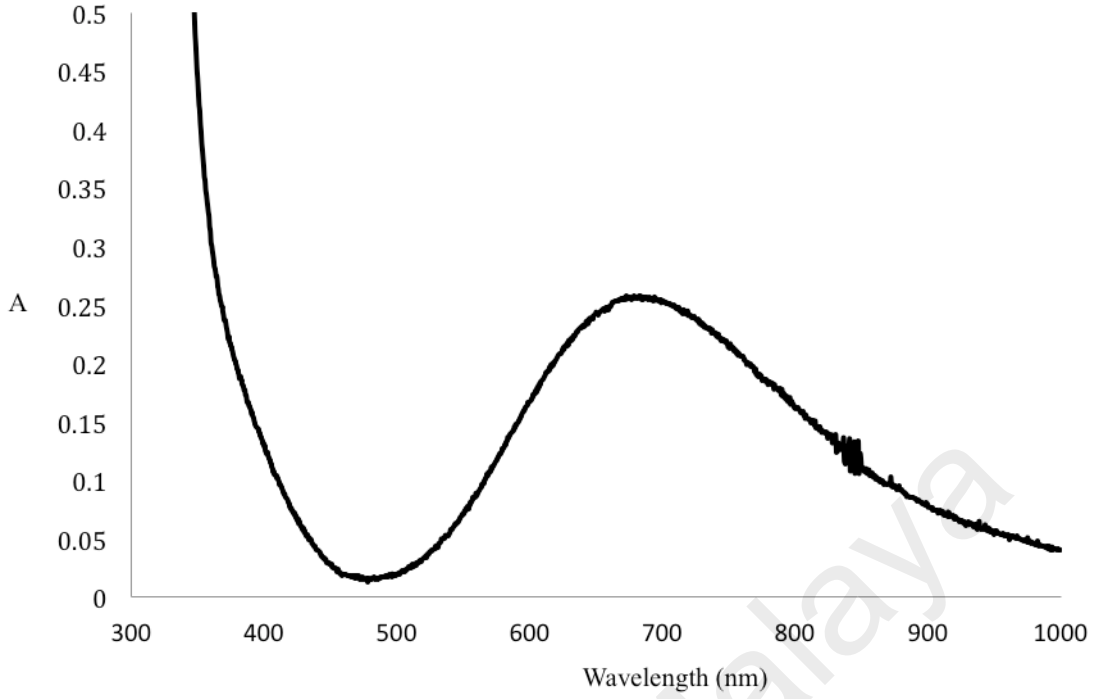

Figure 4.25 UV-vis spectrum of **3**

Its μ_{eff} value, calculated from the values of its formula weight (FW = 1173.12 g mol^{-1}), mass susceptibility (χ_g; 0.193 x 10^{-5} cm^3 g^{-1}), molar susceptibility (χ_M; 2.264 x 10^{-3} cm^3 mol^{-1}), diamagnetic correction factor (χ_D; -5.87 x 10^{-4} cm^3 mol^{-1}) and corrected molar susceptibility (χ_M^{corr}; 2.85 x 10^{-3} cm^3 mol^{-1}), was 2.61 BM at 298 K.

(b) Thermal and mesomorphic studies

Its **TG** trace for **3** (**Figure 4.26**) shows a total weight loss of 89.1% in the temperature range 170 ^oC to 621 ^oC due to the decomposition of $CH_3(CH_2)_{10}COO^-$ ion and bpy (calculated, 89.7%). The results are in a good agreement with its structural formula (**Figure 4.23**). The amount of residue was 11.9% (calculated, 12.9% assuming CuO). Hence, its decomposition temperature was 170 ^oC.

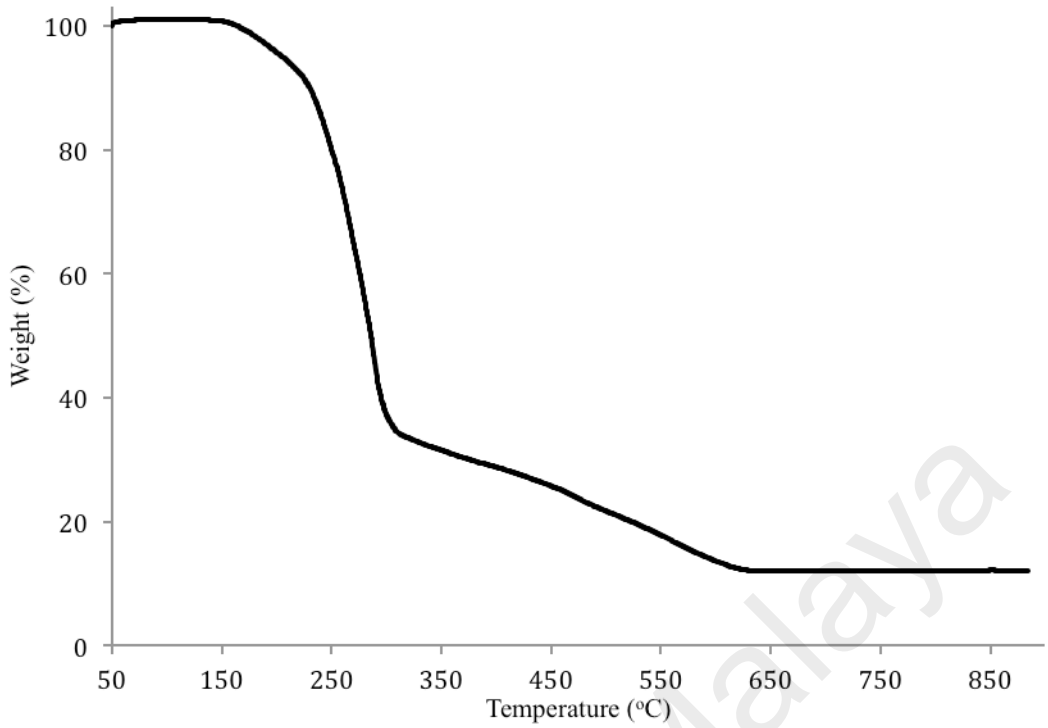

Figure 4.26 TGA trace of **3**

When viewed under **POM**, **3** started to melt at 72 ^{o}C, formed an optical texture on heating at 103 ^{o}C (**Figure 4.27** (**a**)) and cleared at about 151 ^{o}C. On cooling from *I*, an optical texture was observed at 76 ^{o}C (**Figure 4.27** (**b**)). In contrast, its precursor complex, $[Cu_2(CH_3(CH_2)_{10}COO)_4(H_2O)_2]$, did not show any optical structures. Hence, **3** behaved as a thermotropic metallomesogen. The different optical textures observed arose from the thermal effect of the binding mode of the carboxylate ligand, as suggested above for **2.**

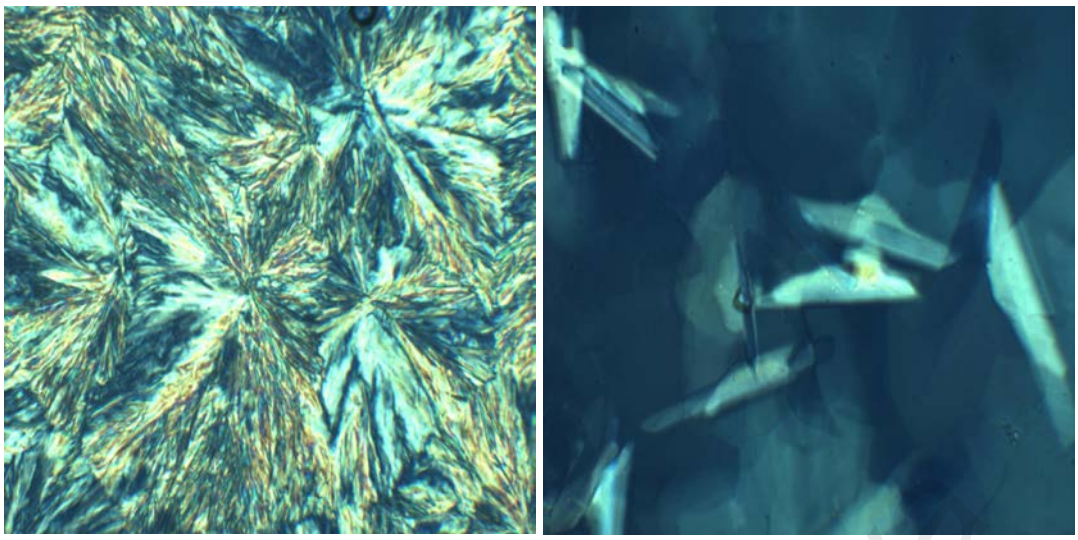

(a) (b)

Figure 4.27 Pictomicrographs of: (a) **3** on heating at 103 °C; (b) **3** on cooling at 76 °C

Its **DSC** traces (**Figure 4.28**) shows overlapping endothermic peaks at 62 °C ($\Delta H_{combined}$ = +87 kJ mol^{-1}) assigned to *Cr1-Cr2* and *Cr2-M* transitions, and a broad endothermic peak at 129 °C (ΔH = +4 kJ mol^{-1}) assigned to *M-I* transition. On cooling, there were two exothermic peaks at 102 °C (ΔH = -10 kJ mol^{-1}) and 67 °C (ΔH = -1 kJ mol^{-1}) assigned to *I-M* transition and *M-Cr2* transitions, respectively.

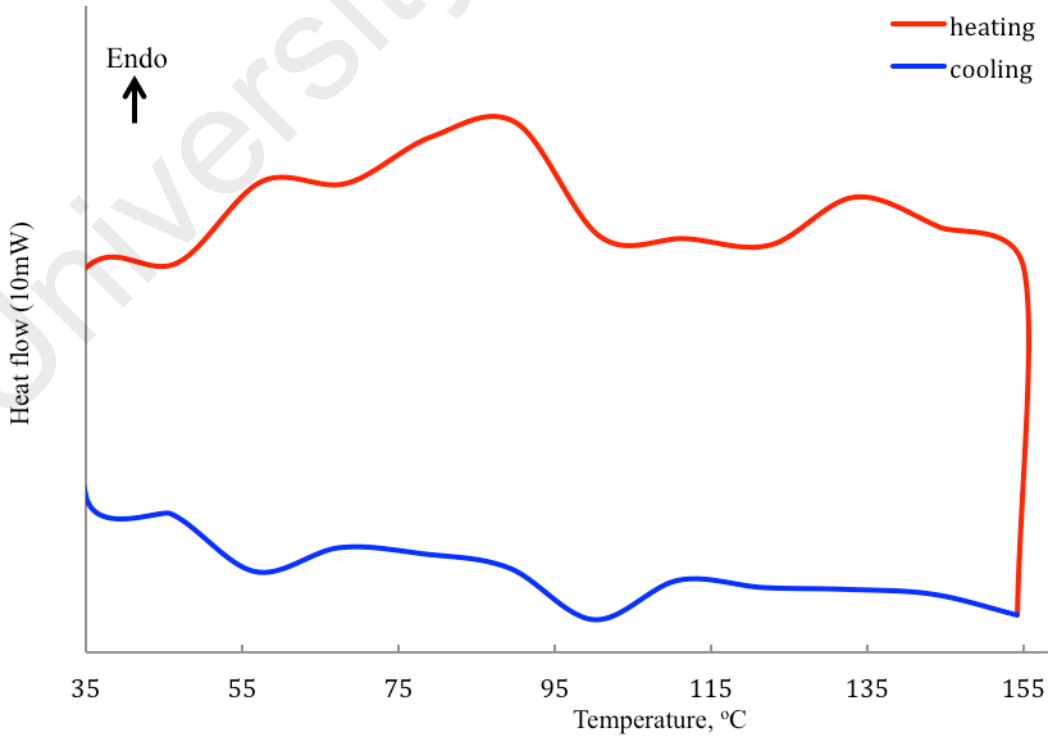

Figure 4.28 DSC scans of **3**

4.1.4 $[Cu_2(CH_3(CH_2)_{12}COO)_4(bpy)_2]$ (4)

(a) Synthesis and structural elucidation

The first step in the synthesis $[Cu_2(CH_3(CH_2)_{12}COO)_4(bpy)_2]$ (**4**) (**Scheme 4.1**) involved the reaction of $CH_3(CH_2)_{12}COOH$ with Na_2CO_3 to form $CH_3(CH_2)_{12}COONa$. It was obtained as a white powder in good yield (83%). The results of its **elemental analyses** (C, 66.1%; H, 11.9%) were in good agreement with the calculated values (C, 67.2%; H, 10.9%; FW 250.346 g mol^{-1}). Its **FTIR** data (**Table 4.1**; **Figure 4.29**) shows the presence of the expected functional groups. Hence, the $\Delta\nu_{coo}$ value for $CH_3(CH_2)_{12}COO^-$ ion was 136 cm^{-1}.

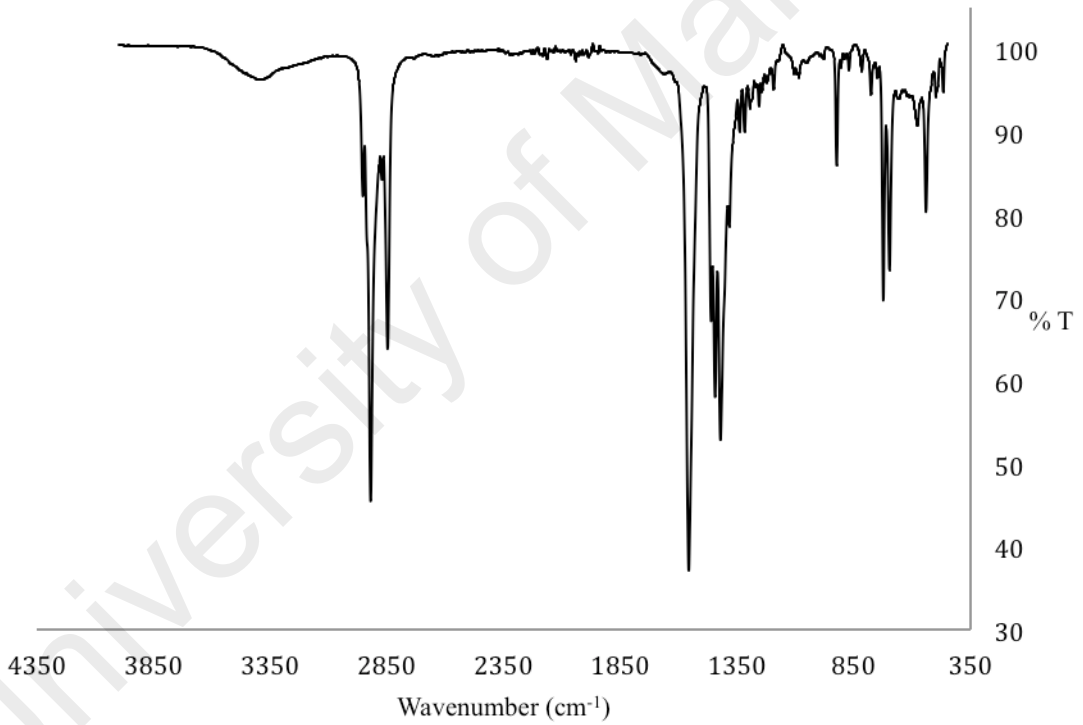

Figure 4.29 FTIR spectrum of $CH_3(CH_2)_{12}COONa$

The second step involved reacting $CH_3(CH_2)_{12}COONa$ with $CuCl_2.2H_2O$ to form the precursor complex, $[Cu_2(CH_3(CH_2)_{12}COO)_4(H_2O)_2].4H_2O$ (blue powder; yield = 23%). The results of its **elemental analyses** (C, 57.3%; H, 10.0%) were in good agreement with the calculated values (C, 58.8%; H, 10.5%); FW 1144.62 g mol^{-1}). Its **FTIR** data (**Table 4.1**; **Figure 4.30**) shows the presence of the expected functional groups. The $\Delta\nu_{coo}$ value was 140 cm^{-1}, indicating that $CH_3(CH_2)_{12}COO^-$ ion was

coordinated as a bridging ligand in the complex as the value was higher than $CH_3(CH_2)_{12}COO^-$ ion (136 cm^{-1}).

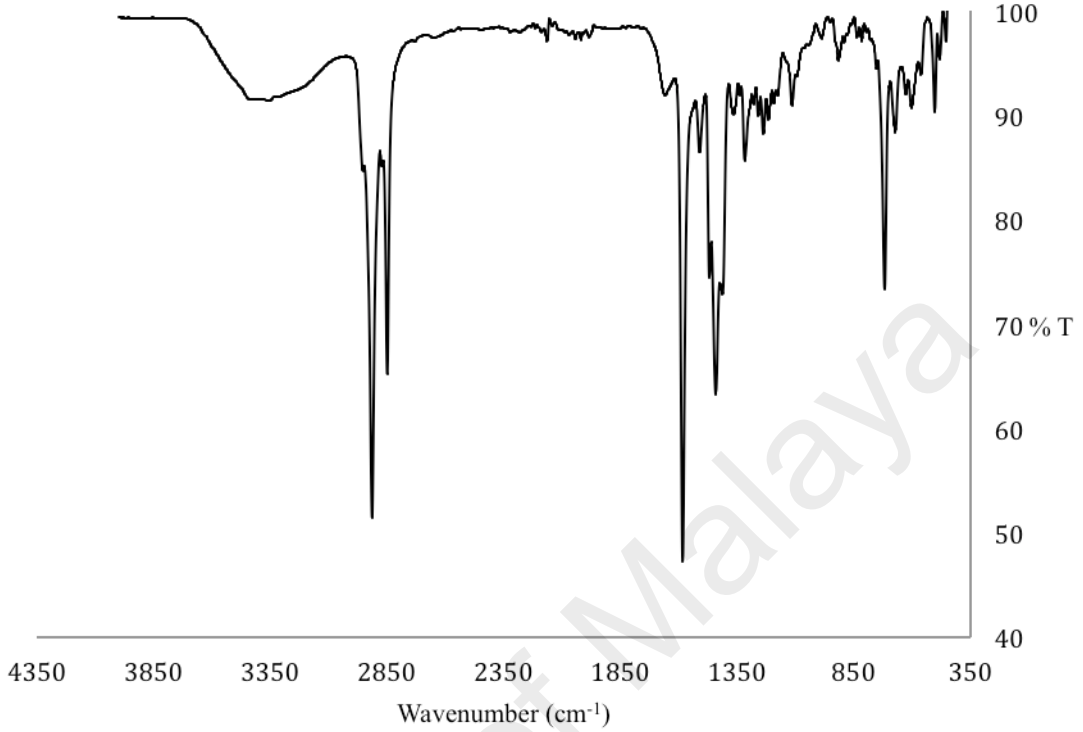

Figure 4.30 FTIR spectrum of $[Cu_2(CH_3(CH_2)_{12}COO)_4(H_2O)_2].4H_2O$

Its **UV-vis** spectrum (**Figure 4.31**) in DMSO-C_2H_5OH shows a broad *d-d* band at 700 nm (ε_{max} = 156 M^{-1} cm^{-1}) and a shoulder to a strong charge transfer band at 357 nm (ε_{max} = 161 M^{-1} cm^{-1}). The results were similar to previously discussed precursors, and may be similarly explained.

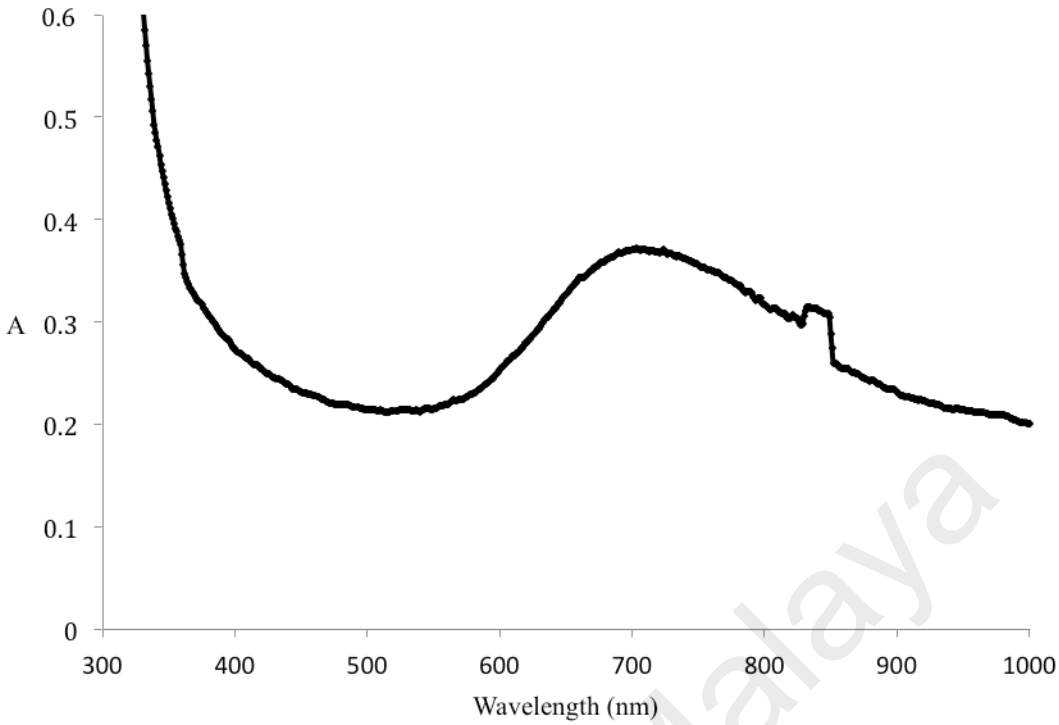

Figure 4.31 UV-vis spectrum of $[Cu_2(CH_3(CH_2)_{12}COO)_4(H_2O)_2].4H_2O$ in DMSO-C_2H_5OH

The μ_{eff} value for $[Cu_2(CH_3(CH_2)_{12}COO)_4(H_2O)_2].4H_2O$, calculated from the values of its formula weight (FW = 1144.62 g mol^{-1}), mass susceptibility (χ_g; 0.124 x 10^{-5} cm^3 g^{-1}), molar susceptibility (χ_m; 1.419 x 10^{-3} cm^3 mol^{-1}), diamagnetic correction factor (χ_D; -5.72 x 10^{-4} cm^3 mol^{-1}), and corrected molar susceptibility (χ_m^{corr}; 1.99 x 10^{-3} cm^3 mol^{-1}), was 1.42 BM at 298 K. Thus, there is a strong antiferromagnetic interaction between the two Cu(II) centres, as similarly reported for other paddle-wheel copper(II) complexes [7,8].

$[Cu_2(CH_3(CH_2)_{12}COO)_4(H_2O)_2].4H_2O$ reacted with bpy to form a blue powder (yield = 44%). The results of the **elemental analyses** (C, 68.6%; H, 9.9%; N, 3.7%)were in good agreement for $[Cu_2(CH_3(CH_2)_{12}COO)_4(bpy)_2]$ (**4**) (C, 67.7%; H, 9.3%; N, 4.2%; FW = 1348.85 g mol^{-1}).

Its **FTIR** data (**Table 4.1**; **Figure 4.32**) shows the presence of the expected functional groups. Hence, the $\Delta\nu_{coo}$ values were 220 and 158 cm^{-1} in agreement with monodentate nonbridging and *syn-anti* monodentate bridging $CH_3(CH_2)_{12}COO^-$ ligands, respectively.

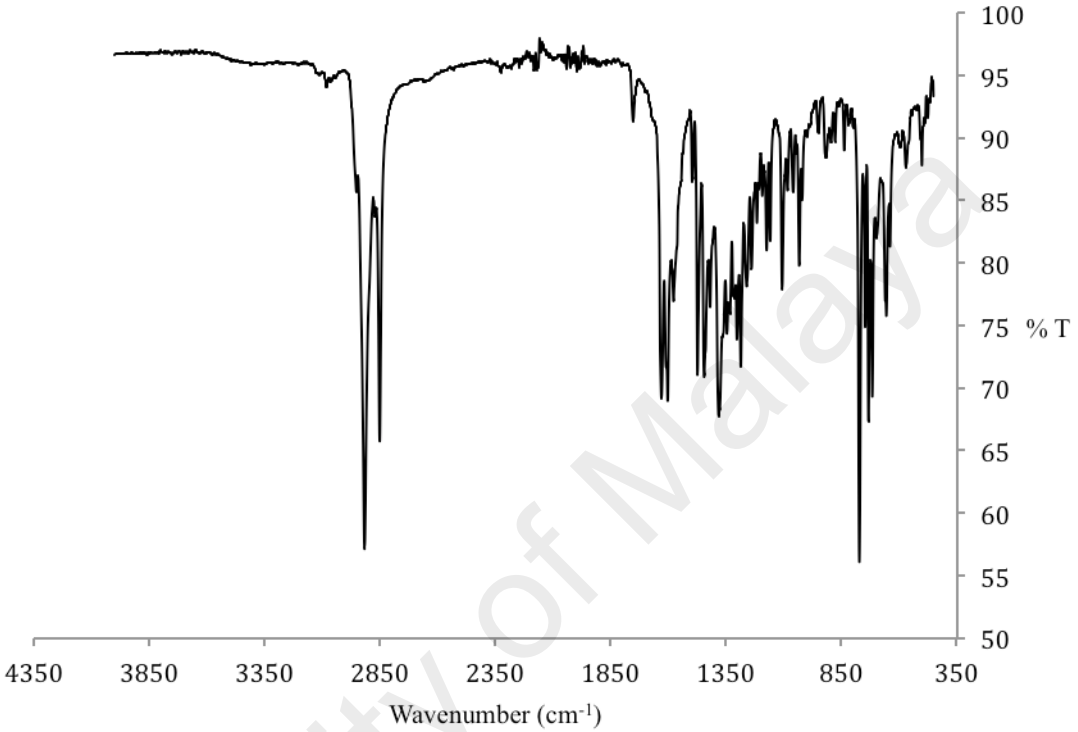

Figure 4.32 FTIR spectrum of **4**

Its **UV-vis spectrum** (**Figure 4.33**) in DMSO-C_2H_5OH shows a broad *d-d* band at 678 nm (ε_{max} = 171 M^{-1} cm^{-1}) and a shoulder to a strong charge transfer band at 367 nm (ε_{max} = 148 M^{-1} cm^{-1}). The data were similar and may be similarly explained.

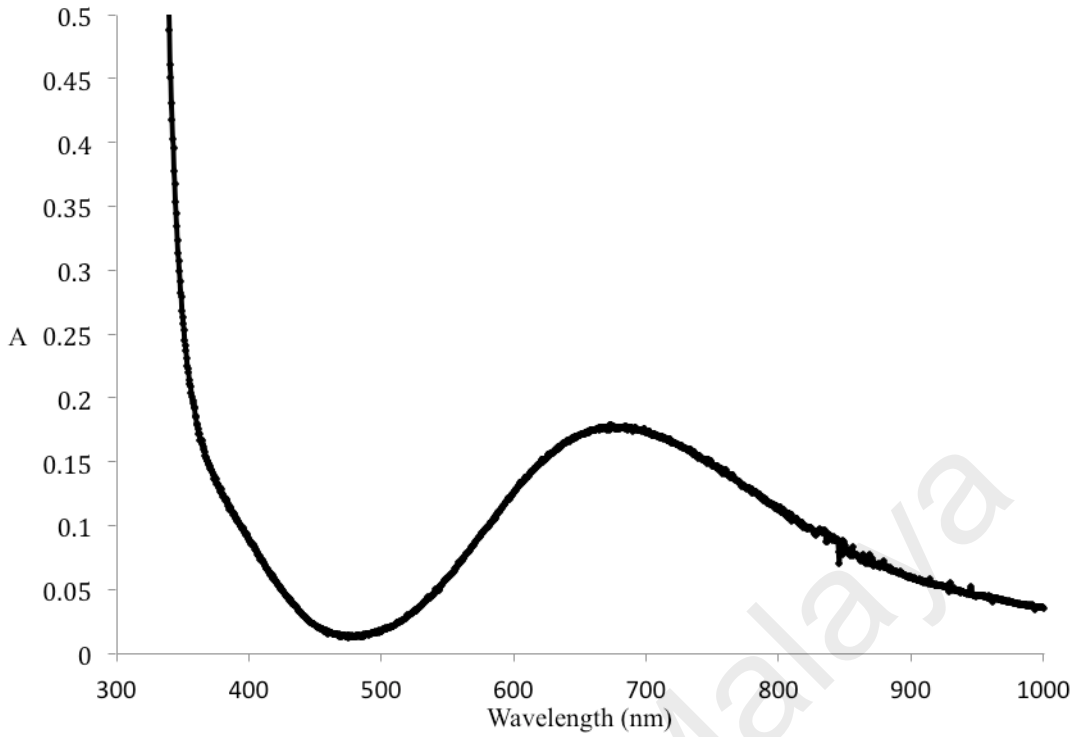

Figure 4.33 UV-vis spectrum of **4**

Combining the above data, it is proposed that **4** has similar structure as **1 - 3**.

Its μ_{eff} value, calculated from the values of its formula weight (FW = 1348.85 g mol^{-1}), mass susceptibility (χ_g; 1.98 x 10^{-6} cm^3 g^{-1}), molar susceptibility (χ_m; 2.671 x 10^{-3} cm^3 mol^{-1}), diamagnetic correction factor (χ_D; -6.74 x 10^{-4} cm^3 mol^{-1}) and corrected molar susceptibility (χ_m^{corr}; 3.35 x 10^{-3} cm^3 mol^{-1}), was 2.83 BM at 298 K.

(b) Thermal and mesomorphic studies

The **TG** trace of **4** (**Figure 4.34**) shows a total weight loss of 89.8% in the temperature range 163 ^oC to 621 ^oC due to the decomposition of $CH_3(CH_2)_{12}COO^-$ ion and bpy (calculated, 90.6%). The results are in a good agreement with its structural formula. The amount of residue was 10.2% (calculated, 9.4% assuming CuO). Hence, its decomposition temperature was 163 ^oC.

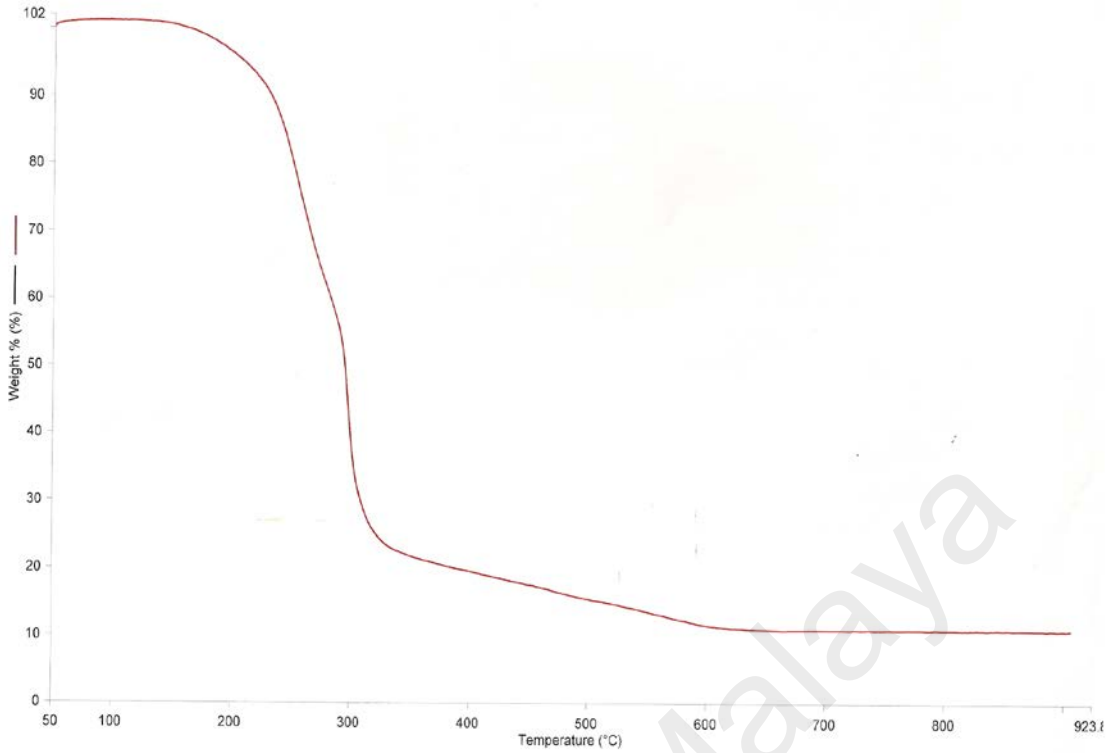

Figure 4.34 TGA trace of **4**

When viewed under **POM**, **4** started to melt at 94 ^{o}C and to clear at about 156 ^{o}C. On cooling from *I*, an optical texture was observed at 152 ^{o}C (**Figure 4.35**(**a**)). In comparison, its precursor complex, $[Cu_2(CH_3(CH_2)_{12}COO)_4(H_2O)_2].4H_2O$, was observed melting at 116 ^{o}C and cleared to an isotropic liquid at 118 ^{o}C. Upon cooling from 120 ^{o}C, a different optical texture was formed at 97 ^{o}C (**Figure 4.35**(**b**)). Its precursor complex showed a typical columnar mesogen. These observations indicate that both **4** and its precursor complex behaved as different thermotropic metallomesogens.

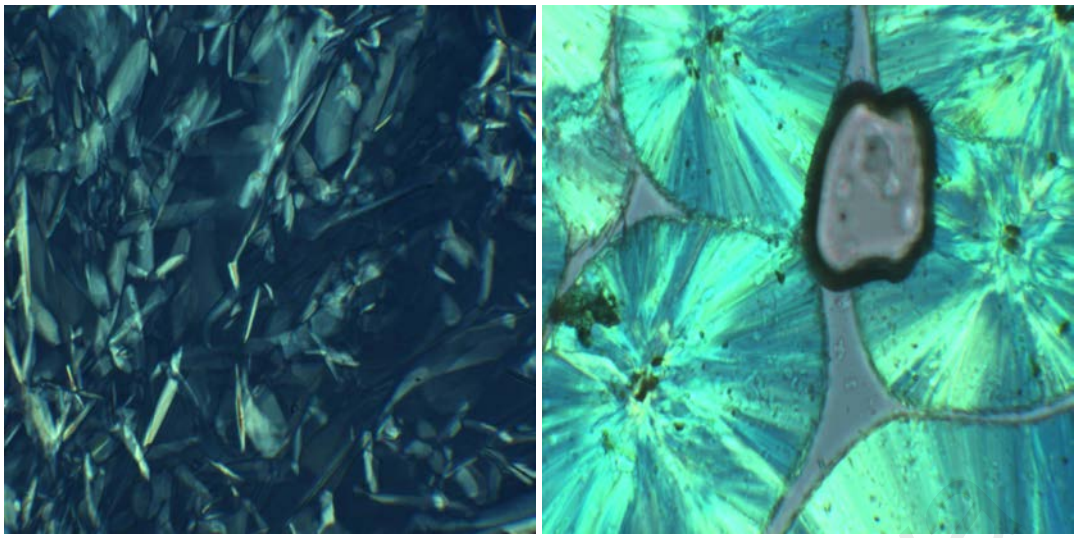

(a) (b)

Figure 4.35 Photomicrographs of: (a) **4** on cooling at 152 ^{o}C; (b) $[Cu_2(CH_3(CH_2)_{12}COO)_4(H_2O)_2].4H_2O$ on cooling at 97 ^{o}C

The **DSC** traces for **3** (**Figure 4.36**) shows two overlapping endothermic peaks at 55 ^{o}C ($\Delta H_{combined}$ = +9 kJ mol^{-1}) assigned to *Cr1-Cr2* transition, a sharp endothermic peak at 105 ^{o}C (ΔH = +47 kJ mol^{-1}) assigned to *Cr2-M* transition, and a broad endothermic peak at 137°C (ΔH = +31 kJ mol^{-1}) assigned to *M-I* transition. On cooling, there were two exothermic peaks at 127 ^{o}C (ΔH = -30 kJ mol^{-1}) and 40 ^{o}C (ΔH = -31 kJ mol^{-1}) assigned to *I-M* and *M-Cr2* transitions, respectively.

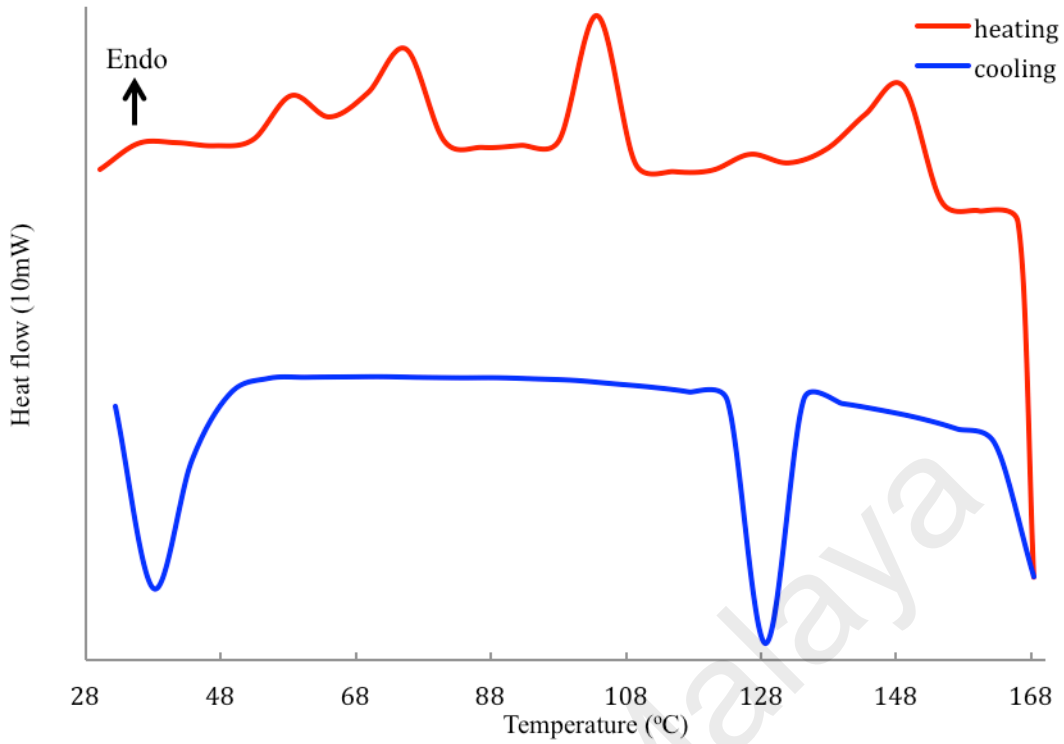

Figure 4.36 DSC scans of **4**

4.1.5 [$Cu_2(CH_3(CH_2)_{14}COO)_4(bpy)_2$] (5)

(a) Synthesis and structural elucidation

The first step in the synthesis [$Cu_2(CH_3(CH_2)_{14}COO)_4(bpy)_2$] (**5**) (**Scheme 4.1**) involved the reaction of $CH_3(CH_2)_{14}COOH$ with Na_2CO_3 to form $CH_3(CH_2)_{14}COONa$. It was obtained as a white powder in good yield (87%). The results of its **elemental analyses** (C, 69.6%; H, 12.9%) were in good agreement with the calculated values (C, 69.0%; H, 11.2%; FW 278.398 g mol^{-1}). Its **FTIR** data (**Table 4.1**; **Figure 4.37**) shows the presence of the expected functional groups. Hence, the $\Delta\nu_{coo}$ value for $CH_3(CH_2)_{14}COO^-$ ion was 137 cm^{-1}.

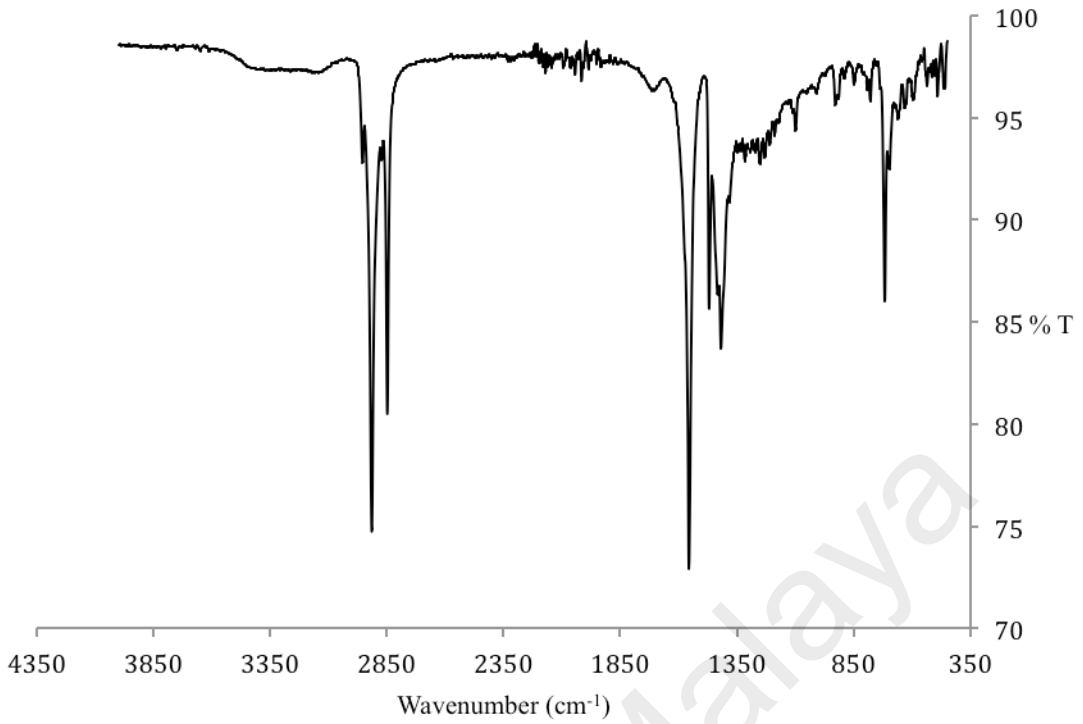

Figure 4.37 FTIR spectrum of $CH_3(CH_2)_{14}COONa$

The second step involved reacting $CH_3(CH_2)_{14}COONa$ with $CuCl_2.2H_2O$ to form the precursor complex, $[Cu_2(CH_3(CH_2)_{14}COO)_4(H_2O)_2]$ (blue powder; yield = 38%). The results of its **elemental analyses** (C, 64.4%; H, 11.3%) were in good agreement with the calculated values (C, 64.9%; H, 10.9%; FW 1184.76 g mol^{-1}). Its **FTIR** data (**Table 4.1**; **Figure 4.38**) shows the presence of the expected functional groups. The $\Delta\nu_{coo}$ value was 140 cm^{-1}, indicating that $CH_3(CH_2)_{14}COO^-$ was coordinated at a bridging ligand in the complex as the value is higher than the $CH_3(CH_2)_{14}COO^-$ ion (137 cm^{-1}).

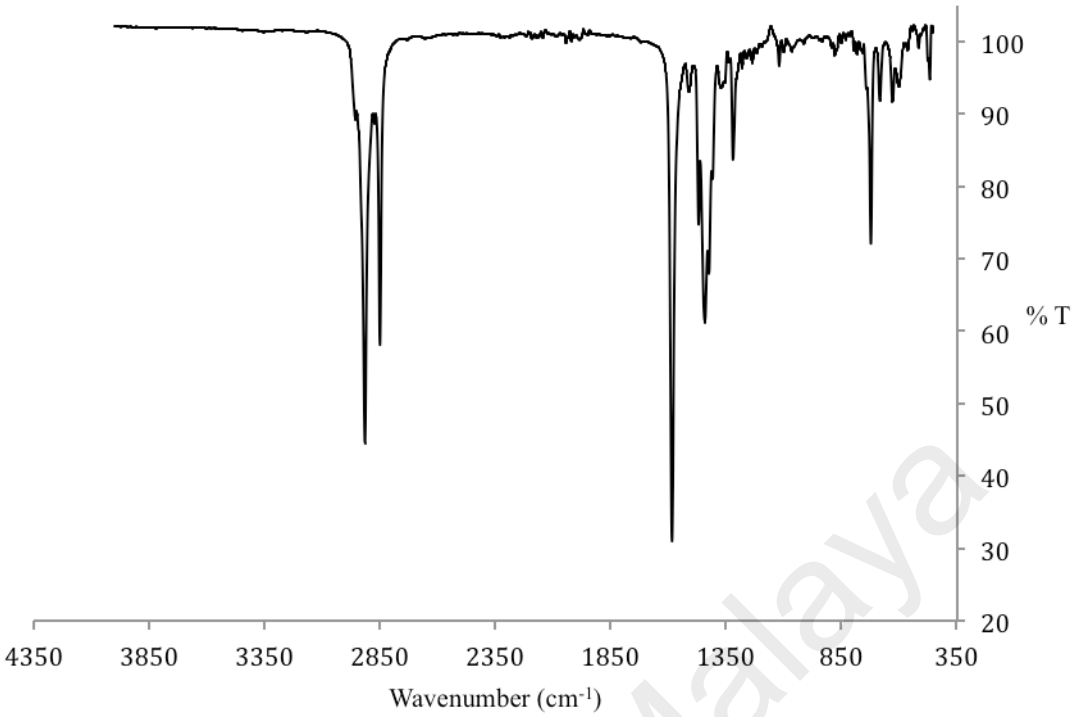

Figure 4.38 FTIR spectrum of $[Cu_2(CH_3(CH_2)_{14}COO)_4(H_2O)_2]$

Its **UV-vis** spectrum (**Figure 4.39**) in DMSO-C_2H_5OH shows a broad *d-d* band at 686 nm (ε_{max} = 161 M^{-1} cm^{-1}). The results were similar to previously discussed precursors, and may be similarly explained.

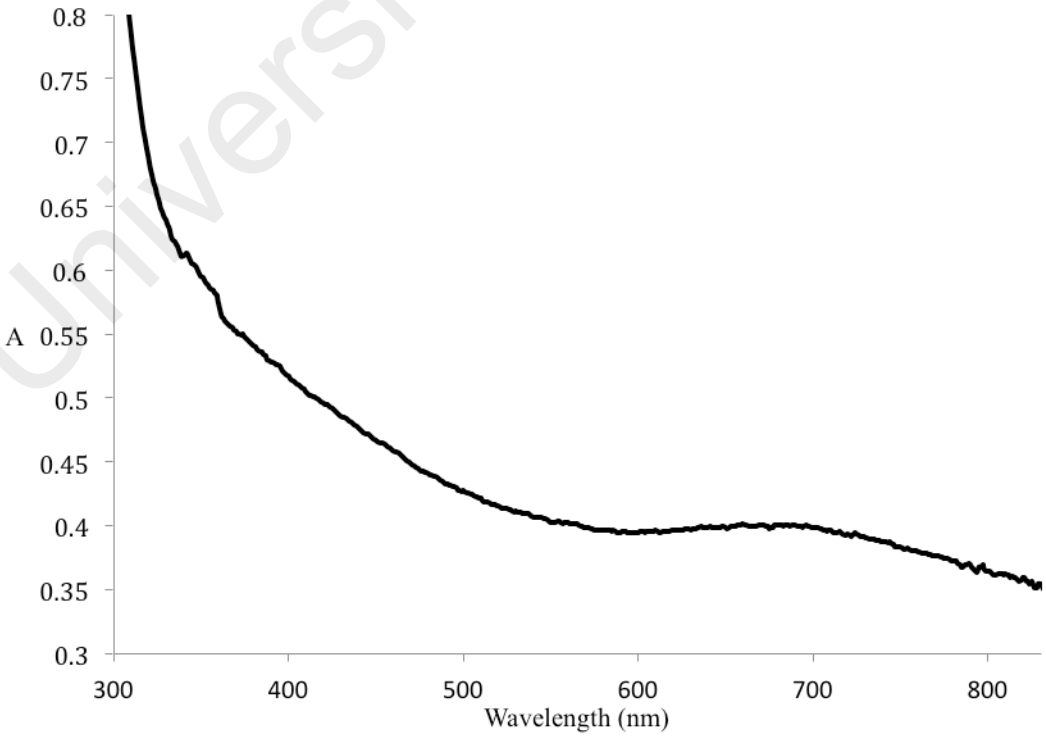

Figure 4.39 UV-vis spectrum of $[Cu_2(CH_3(CH_2)_{14}COO)_4(H_2O)_2].H_2O$ in DMSO-C_2H_5OH

The μ_{eff} value for $[Cu_2(CH_3(CH_2)_{14}COO)_4(H_2O)_2]$, calculated from the values of its formula weight (FW = 1184.76 g mol^{-1}), mass susceptibility (χ_g; 8.30 x 10^{-7} cm^3 g^{-1}), molar susceptibility (χ_m; 9.84 x 10^{-4} cm^3 mol^{-1}), diamagnetic correction factor (χ_D; -5.92 x 10^{-4} cm^3 mol^{-1}) and corrected molar susceptibility (χ_m^{corr}; 1.58 x 10^{-3} cm^3 mol^{-1}), was 1.94 BM at 298 K. Thus, it may be said that there is an antiferromagnetic interaction between the two Cu(II) centres. Hence, the structure of $[Cu_2(CH_3(CH_2)_{14}COO)_4(H_2O)_2].H_2O$ was proposed to have a paddle-wheel structures as similar values were reported.

$[Cu_2(CH_3(CH_2)_{14}COO)_4(H_2O)_2]$ reacted with bpy to form a blue powder, which on recrystallisation from ethanol, formed blue crystals (yield = 81%). Single crystal **X-ray crystallographic** data and structure refinement for the crystal is shown in **Table 4.2**, selected bond lengths and angles are shown in **Table 4.3**, and ORTEP presentations and packing patterns are shown in **Figure 4.40**. Hence, the structural formula for the crystal was $[Cu_2(CH_3(CH_2)_{14}COO)_4(bpy)_2]$ (**5**), which was similar to **1 – 3**.

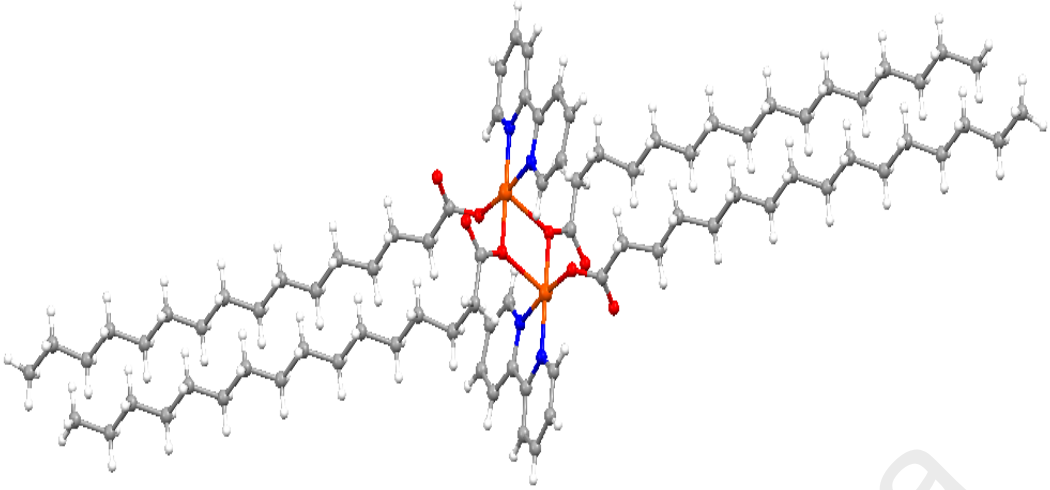

(a)

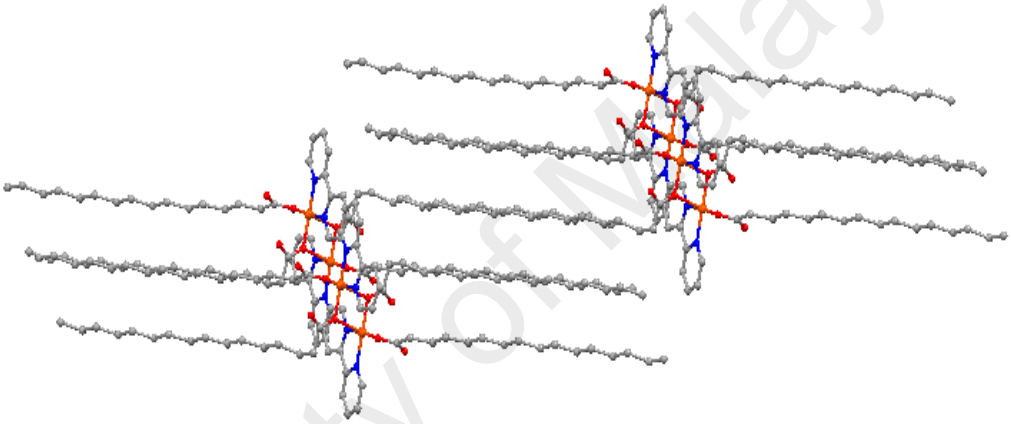

(b)

Figure 4.40 (a) Molecular structure, and (b) packing diagram **5** viewed along crystallographic *b*-axis.

The X-ray data shows that **5** has similar structure as **1** to **3**. It crystallised in the triclinic system with *P-1* space group, a = 9.00(2) Å, b = 9.88(2) Å, c = 23.28(5) Å, α = 92.73(4)^o, β = 98.76(5)^o, γ = 101.51(4)^o, Z = 1, V = 1998.7(7) Å^3. Each of its copper(II) centre was penta-coordinated with two N atoms from chelating bpy [Cu-N1 = 2.011 (16) Å and Cu-N2 = 2.018 (16) Å], two O atoms from bridging $CH_3(CH_2)_{14}COO^-$ ligands (Cu-O1 = 1.964 (13) Å and Cu-O2 = 2.331 (13) Å), and an O atom from monodentate $CH_3(CH_2)_{14}COO^-$ ligands (Cu-O3 = 1.938 (14) Å).

Its **FTIR** data (**Table 4.1**; **Figure 4.41**) shows the presence of the expected functional groups. Hence, the $\Delta\nu_{coo}$ values were 259 and 158 cm^{-1} in agreement with

monodentate nonbridging and *syn-anti* monodentate bridging $CH_3(CH_2)_{14}COO^-$ ligands, respectively, as observed in its single crystal structure.

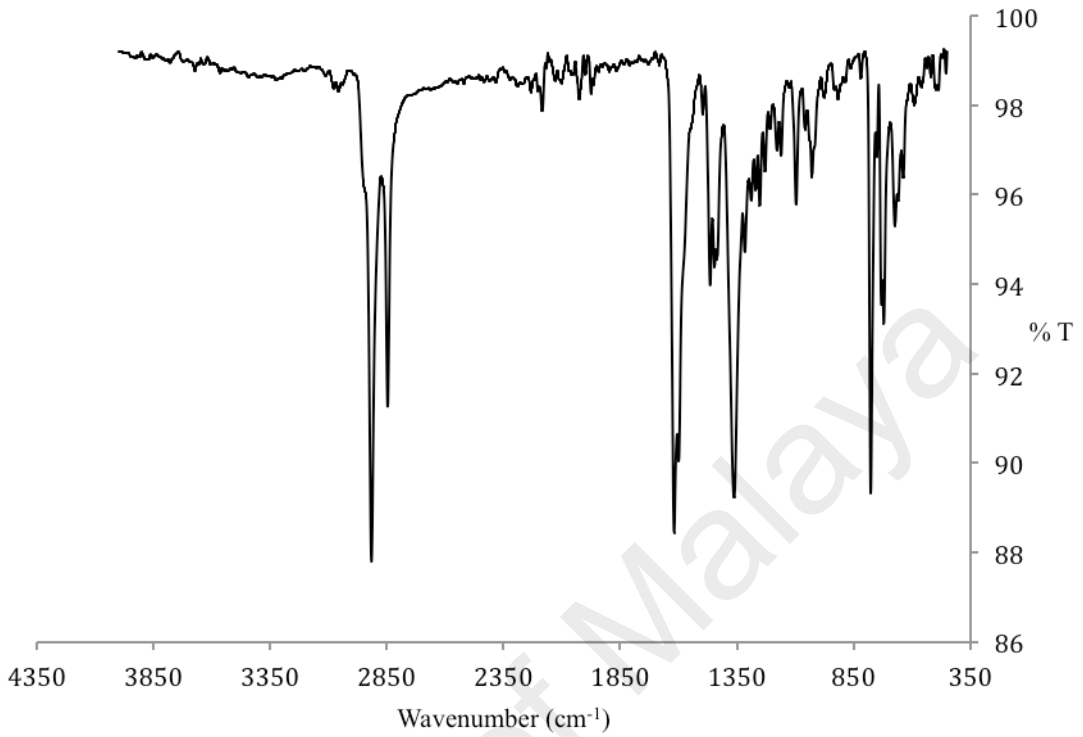

Figure 4.41 FTIR spectrum of **5**

Its **UV-vis spectrum** (**Figure 4.42**) in DMSO-C_2H_5OH shows a broad *d-d* band at 673 nm (ε_{max} = 122 M^{-1} cm^{-1}). The results were similar to previously discussed precursors, and may be similarly explained.

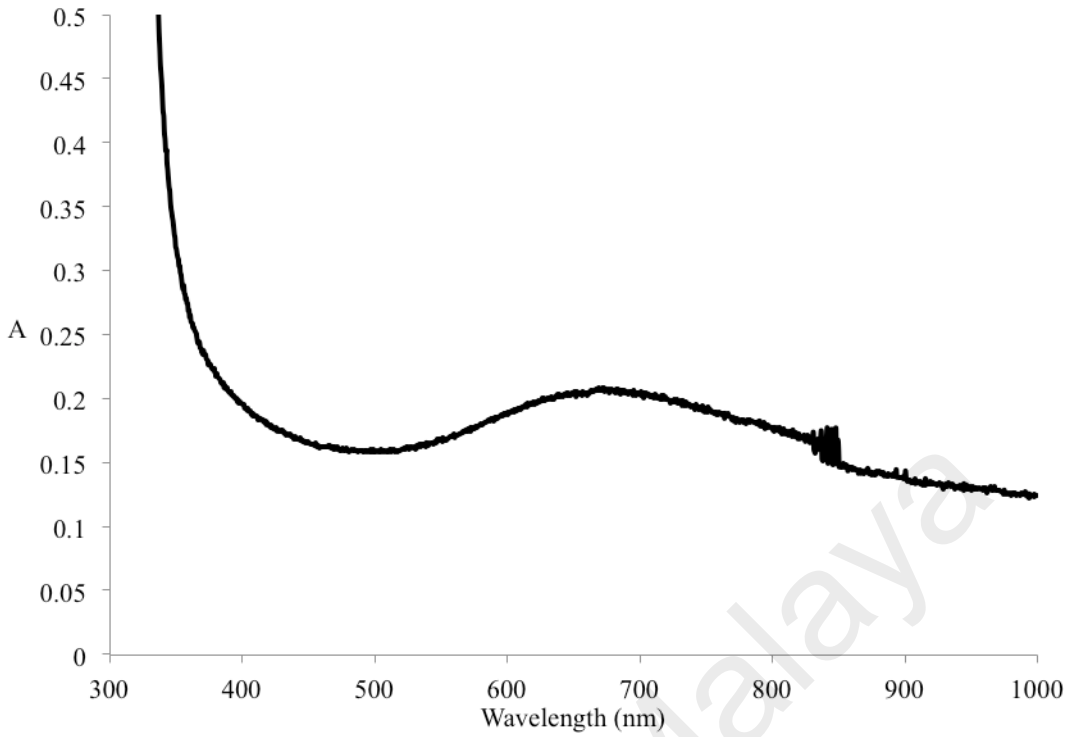

Figure 4.42 UV-vis spectrum of **5**

Its μ_{eff} value, calculated from the values of its formula weight (FW = 1461.14 g mol^{-1}), mass susceptibility (χ_g; 1.38 x 10^{-6} cm^3 g^{-1}), molar susceptibility (χ_m; 2.01 x 10^{-3} cm^3 mol^{-1}), diamagnetic correction factor (χ_D; -7.31 x 10^{-4} cm^3 mol^{-1}) and corrected molar susceptibility (χ_m^{corr}; 2.75 x 10^{-3} cm^3 mol^{-1}), was 2.56 BM at 298 K.

(b) Thermal and mesomorphic studies

The **TG** trace of **5** (**Figure 4.43**) shows a total weight loss of 89.3% in the temperature range 161 ^oC to 596 ^oC due to the decomposition of $CH_3(CH_2)_{14}COO^-$ ion and bpy (calculated, 91.3%). The results are in a good agreement with its structural formula (**Figure 4.40**). The amount of residue was 11.4% (calculated, 10.9% assuming CuO). Hence, its decomposition temperature was 161 ^oC.

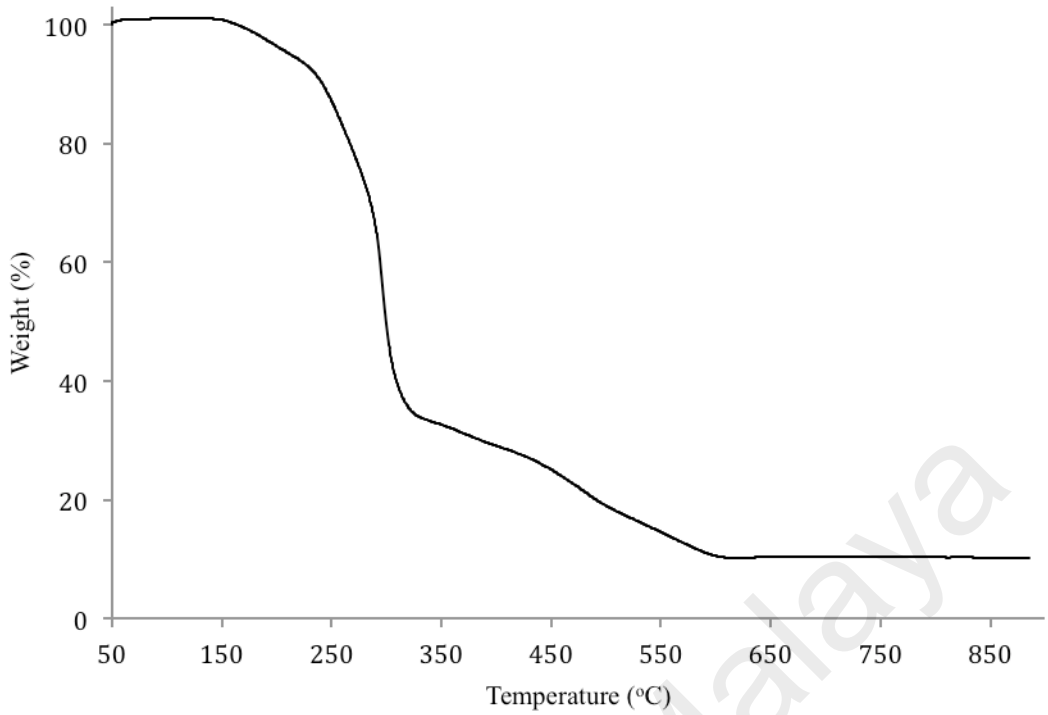

Figure 4.43 TGA trace of **5**

When viewed under **POM**, **5** started to melt at 118 °C and to clear at about 151 °C. Upon cooling from *I*, an optical texture was observed at 140 °C (**Figure 4.44**(**a**)). In comparison, its precursor complex, $[Cu_2(CH_3(CH_2)_{14}COO)_4(H_2O)_2].H_2O$, was observed melting at 117 °C and cleared to an isotropic liquid at 130 °C. Upon cooling from 130 °C, a different optical texture was formed at 85 °C (**Figure 4.44**(**b**)). These observations indicate that both **5** and its precursor complex behaved as different thermotropic metallomesogens.

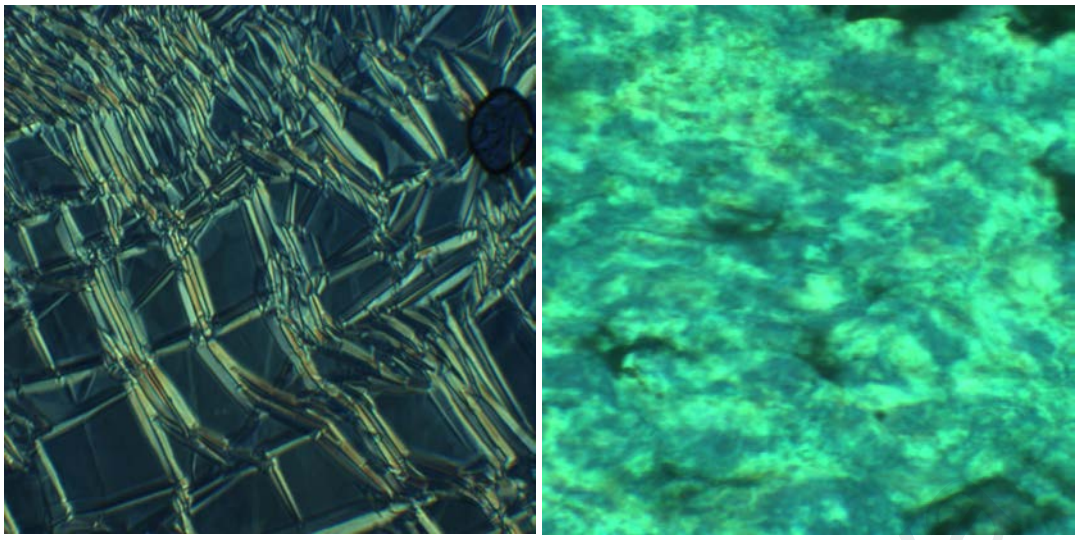

(a) (b)

Figure 4.44 Photomicrographs of: (a) **5** on cooling at 140 ^{o}C; (b) $[Cu_2(CH_3(CH_2)_{14}COO)_4(H_2O)_2].H_2O$ on cooling at 85 ^{o}C

The **DSC** traces for **5** (**Figure 4.45**) shows endothermic peaks at 90 ^{o}C (ΔH = +50 kJ mol^{-1}) assigned to *Cr1-Cr2* transition, 112 ^{o}C (ΔH = +88 kJ mol^{-1}) assigned to *Cr2-M* transition, and 153 ^{o}C (ΔH = +53 kJ mol^{-1}) assigned to *M-I* transition. On cooling, there were two exothermic peaks at 131 ^{o}C (ΔH = -41 kJ mol^{-1}) and 64 ^{o}C (ΔH = -62 kJ mol^{-1}), assigned to *I-M* and *M-Cr2* transitions, respectively.

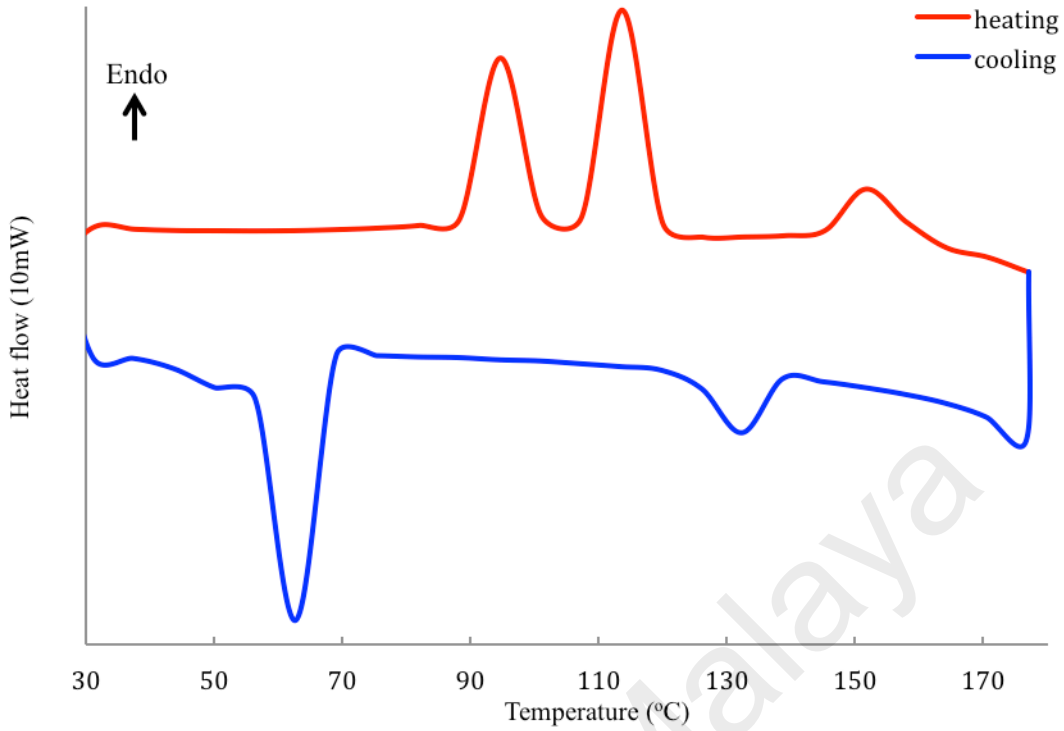

Figure 4.45 DSC scans of **5**

4.1.6 Summary

To summarize, the analytical data for the precursor complexes, $[Cu_2(R)_4]$ (R = $CH_3(CH_2)_{6\text{-}14}COO$) and complexes formed from their reactions with bpy (**1**-**5**) are shown in **Table 4.4** and **Table 4.5**, respectively.

Table 4.4 Precursor complexes of complexes **1 - 5**

Proposed chemical formula	$\Delta\nu_{coo}$ (cm^{-1})	λ_{max}, nm (ε_{max} M^{-1} cm^{-1})	μ_{eff} (BM)	M*
$[Cu_6Cl_{10}(CH_3(CH_2)_6COO)_2].3H_2O.2EtOH$	157, 240	693 (104)	-	Yes
$[Cu_2(CH_3(CH_2)_8COO)_4(H_2O)_2]$	192	699 (386)	2.2	No
$[Cu_2(CH_3(CH_2)_{10}COO)_4(H_2O)_2].2H_2O$	177	693 (467)	-	Yes
$[Cu_2(CH_3(CH_2)_{12}COO)_4(H_2O)_2].4H_2O$	140	700 (156)	1.42	Yes
$[Cu_2(CH_3(CH_2)_{14}COO)_4(H_2O)_2]$	140	686 (161)	1.94	Yes

*M = mesomorphism

$[Cu_6Cl_{10}(CH_3(CH_2)_6COO)_2].3H_2O.2EtOH$ was a hexamer with bidentate bridging and monodentate carboxylates ligand, while the other precursor complexes

were dinuclear with bridging carboxylates ligands. The geometry of copper(II) for all complexes were square pyramidal. The magnetic data (μ_{eff}) indicate that two copper(II) atoms in all complexes experienced antiferromagnetic interactions at room temperature, postulated to occur through the bridging carboxylate ligands by a mechanism termed the superexchange pathway. Finally, except for $[Cu_2(CH_3(CH_2)_8COO)_4(H_2O)_2]$, all other complexes behaved as thermotropic liquid crystals.

Figure 4.5 Complexes **1 - 5**

Chemical formula	$\Delta\nu_{coo}$ (cm^{-1})	λ_{max}, nm (ε_{max}, M^{-1} cm^{-1})	μ_{eff} (BM)	T_{dec} (^oC)	M*
$[Cu_2(CH_3(CH_2)_6COO)_4(bpy)_2]$ (**1**; blue crystal)	209 186	699 (104)	2.36	195	Yes
$[Cu_2(CH_3(CH_2)_8COO)_4(bpy)_2]$ (**2**; blue crystal)	247 182	683 (117)	2.63	177	Yes
$[Cu_2(CH_3(CH_2)_{10}COO)_4(bpy)_2]$ (**3**; blue crystal)	248 178	680 (199)	2.61	170	Yes
$[Cu_2(CH_3(CH_2)_{12}COO)_4(bpy)_2]$ (**4**; blue powder)	220 158	678 (171)	2.83	163	Yes
$[Cu_2(CH_3(CH_2)_{14}COO)_4(bpy)_2]$ (**5**; blue crystal)	259 158	673 (122)	2.56	161	Yes

*M = mesomorphism

Except for **4** which was a powder, the other complexes were single crystals. All complexes were dinuclear with chelating bpy and monodentate nonbridging and *syn-anti* monodentate bridging carboxylato ligands, and square pyramidal copper(II) atoms. Their magnetic data (μ_{eff}) suggest negligible (for **1**) and ferromagnetic interactions (for **2** – **5**) between the two copper(II) atoms. Their decomposition temperatures showed a gradually decreasing trend with increasing number of carbon atoms in the alkyl chain. Since the decomposition of these complexes arose from the decarboxylation of the alkylcarboxylate ligands [32], the lower thermal stability of the longer alkylcarboxylate ion suggests weaker R-COO^- bond. This may be a consequence of a stronger RCOO-Cu bond due to the stronger Lewis basicity of the ion. All complexes, behaved as thermotropic liquid crystal.

Table 4.3 Selected bond lengths (Å) and angles (^{o}) for **1**, **1a**, **2**, **3** and **5**

	1	**1a**	**2**	**3**	**5**
Bond length					
Cu-O(1)	1.930(5)	1.930(2)	1.901(15)	1.939(2)	1.938(14)
Cu-O(3)	1.968(4)	1.966(2)	1.919(19)	1.952(2)	1.964(13)
Cu-O(2)	2.381(5)	2.313(2)	2.390(16)	2.393(2)	2.331(13)
Cu-N(1)	2.006(5)	2.015(3)	2.005(16)	2.016(2)	2.011(16)
Cu-N(2)	2.048(5)	2.001(3)	2.059(19)	2.022(3)	2.018(16)
Cu-Cl	-	2.562(9)	-	-	-
Angle					
O(1)-Cu-O(2)	90.35(19)	81.27(9)	88.4(7)	90.05(9)	89.85(6)
O(1)-Cu-N(1)	95.50(2)	98.01(10)	95.5(7)	95.00(10)	94.58(6)
O(2)-Cu-N(1)	173.60(2)	166.04(10)	174.2(8)	172.75(11)	173.88(6)
O(1)-Cu-N(2)	172.50(2)	177.19(9)	175.1(8)	174.71(9)	174.69(6)
O(2)-Cu-N(2)	93.60(2)	98.92(10)	96.4(8)	94.96(10)	95.29(6)
N(1)-Cu-N(2)	80.20(2)	81.11(11)	79.7(8)	79.86(11)	80.13(6)
O(1)-Cu-O(3)	91.40(2)	99.67(9)	79.6(5)	91.34(10)	90.27(5)
O(2)-Cu-O(3)	78.70(2)	85.57(8)	90.4(7)	79.09(9)	78.13(6)
N(1)-Cu-O(3)	103.60(2)	97.23(9)	94.5(6)	102.42(9)	104.74(6)
N(2)-Cu-O(3)	95.64(19)	94.25(9)	100.9(6)	94.71(9)	94.04(5)

4.2 $[Fe_2(RCOO)_4(bpy)]$

The general steps for the syntheses of $[Fe(CH_3(CH_2)_nCOO)_2(bpy)]$, where n = 8 (**6**), 10 (**7**), 12 (**8**), and 14 (**9**), are shown in **Scheme 4.2.**

$$2\ RCOO^- \xrightarrow{Fe^{2+}} [Fe(RCOO)_2] \xrightarrow{bpy} [Fe(RCOO)_2(bpy)]$$

Scheme 4.2 Synthetic steps for $[Fe(RCOO)_2(bpy)]$, where R = $CH_3(CH_2)_{8\text{-}14}$

4.2.1 $[Fe_2(CH_3(CH_2)_8COO)_4(bpy)(H_2O)_2]$ (6)

(a) Synthesis and structural elucidation

The precursor complex, $[Fe_2(\mu\text{-}H_2O)_2(CH_3(CH_2)_8COO)_4].H_2O$, was obtained as a brown powder in good yield (36%) from the reaction of $CH_3(CH_2)_8COONa.2H_2O$ with $[FeSO_4.7H_2O]$. Its proposed structure (**Figure 4.46**) is based on combined analytical data discussed below, and similar to that reported for $[Fe_2(\mu\text{-}H_2O)(\mu\text{-}OH)(TPA)_2](OTf)_3]$, where TPA = Tri-(2-picolyl)amine and OTf = Trifluoromethanesulfonate by Korendovych [80].

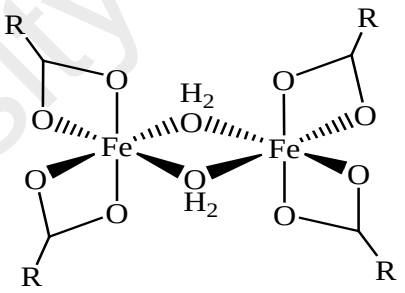

R = $CH_3(CH_2)_6$

Figure 4.46 Proposed structural formula for $[Fe_2(\mu\text{-}H_2O)_2(CH_3(CH_2)_8COO)_4].H_2O$ (lattice H_2O is not shown)

The results of its **elemental analyses** (C, 56.6%; H, 9.2%) were in good agreement with the calculated values (C, 56.5%; H, 9.7%; FW 850.46 g mol^{-1}). Its **FTIR** spectrum is shown in **Figure 4.47**, and the peak assignments are given in **Table 4.6** (which also include the data for other complexes for later discussion). The $\Delta\nu_{coo}$ value was 138 cm^{-1}, which was lower than the value for $CH_3(CH_2)_8COONa$

(133 cm^{-1}), indicating that $CH_3(CH_2)_8COO^-$ ions were coordinated to both Fe(II) centres as chelating ligands [81].

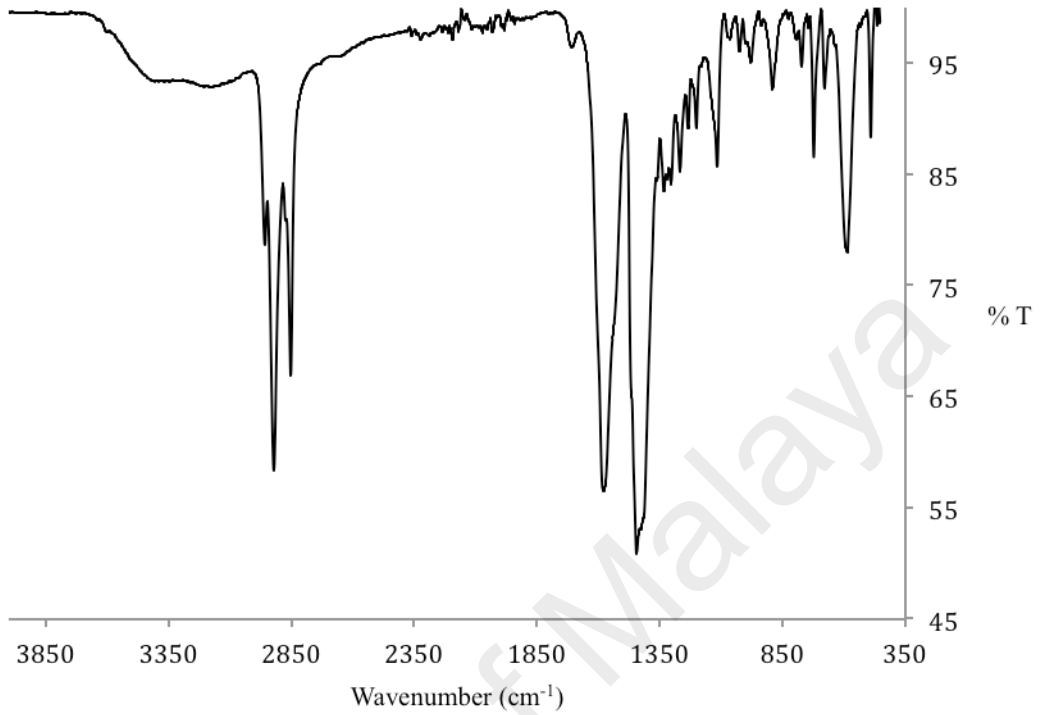

Figure 4.47 FTIR spectrum of $[Fe_2(\mu\text{-}H_2O)_2(CH_3(CH_2)_8COO)_4].H_2O$

Table 4.6 FTIR data in (cm^{-1}) and assignments

Compound	CH_2 (asym)	CH_2 (sym)	COO (asym)	COO (sym)	C=C (aro)	C-N
$[Fe_2(\mu\text{-}H_2O)_2(CH_3(CH_2)_8COO)_4].H_2O$	2924	2854	1584	1446	-	-
$[Fe_2(\mu\text{-}H_2O)_2(CH_3(CH_2)_{10}COO)_4].2H_2O$	2927	2857	1577	1449	-	-
$[Fe_2(\mu\text{-}H_2O)_2(CH_3(CH_2)_{12}COO)_4].2H_2O$	2918	2851	1582/ 1533	1448 1423	-	-
$[Fe_2(\mu\text{-}H_2O)_2(CH_3(CH_2)_{14}COO)_4]$	2919	2851	1573	1449	-	-
$[Fe_2(CH_3(CH_2)_8COO)_4(bpy)(H_2O)_2]$; **(6)**	2923	2854	1549	1442 1411	1580	1318
$[Fe_2(CH_3(CH_2)_{10}COO)_4(bpy)(H_2O)_2].2H_2O$; **(7)**	2917	2850	1605	1472 1433	1605	1304
$[Fe_2(CH_3(CH_2)_{12}COO)_4(bpy)(H_2O)_2]$; **(8)**	2918	2851	1575	1431 1437	1583	1318
$[Fe_2(CH_3(CH_2)_{14}COO)_4(bpy)(H_2O)_2]$; **(9)**	2918	2851	1573	1438 1433	1580	1321

Its **UV-vis** spectrum (**Figure 4.48**) in $CHCl_3$ shows a *d-d* band appearing as a shoulder on the strong CT band at 464 nm (ε = 377 M^{-1} cm^{-1}), assigned to the

$^5E_g \rightarrow {}^5T_{2g}$ electronic transition for a low spin (LS) Fe(II) atom in the complex. The result is consistent with weak field H_2O and $CH_3(CH_2)_8COO^-$ ligands.

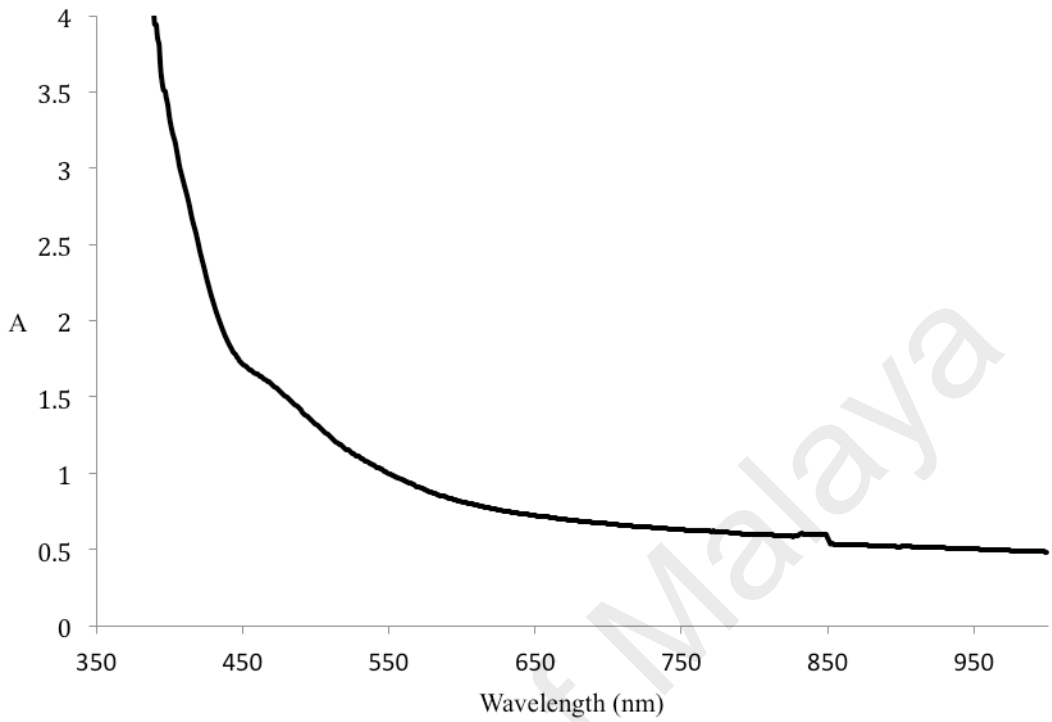

Figure 4.48 UV-vis spectrum of $[Fe_2(\mu\text{-}H_2O)_2(CH_3(CH_2)_8COO)_4].H_2O$ in $CHCl_3$

Its $\chi_M^{corr}T$ value, calculated as before from the values of its formula weight (850.46 g mol^{-1}), mass susceptibility (χ_g = 1.32 x 10^{-5} cm^3 g^{-1}), molar susceptibility (χ_m = 1.12 x 10^{-2} cm^3 mol^{-1}), diamagnetic correction factor (χ_D = -4.25 x 10^{-4} cm^3 mol^{-1}) and corrected molar susceptibility (χ_m^{corr} = 1.17 x 10^{-2} cm^3 mol^{-1}), was 3.47 cm^3 K mol^{-1} at 298 K. Theoretically, the $\chi_M^{corr}T$ value for a high spin (HS) dinuclear Fe(II) complex (S = 2) complex is 6.02 cm^3 K mol^{-1}, while a low spin (LS) Fe(II) (S = 0) complex is diamagnetic ($\chi_M^{corr}T$ = 0) [22]. Accordingly, this complex was made up of 57.8% HS and 42.2% LS Fe(II) atoms at this temperature [82,83].

$[Fe_2(\mu\text{-}H_2O)_2(CH_3(CH_2)_8COO)_4].H_2O$ reacted with bpy to form a brown semi-solid (yield = 50%). The results of the **elemental analyses** (C, 63.0%; H, 8.9%; N, 2.0%) were in good agreement for $[Fe_2(CH_3(CH_2)_8COO)_4(bpy)(H_2O)_2]$ (**6**) (C, 62.5%; H, 8.6%; N, 2.7%; FW = 1036.9 g mol^{-1}).

Its **FTIR** data (**Table 4.6**; **Figure 4.49**) show the presence of the expected functional groups. Hence, the $\Delta\nu_{coo}$ values were 107 cm^{-1} and 138 cm^{-1}, indicating two different chelating $CH_3(CH_2)_8COO^-$ ligands.

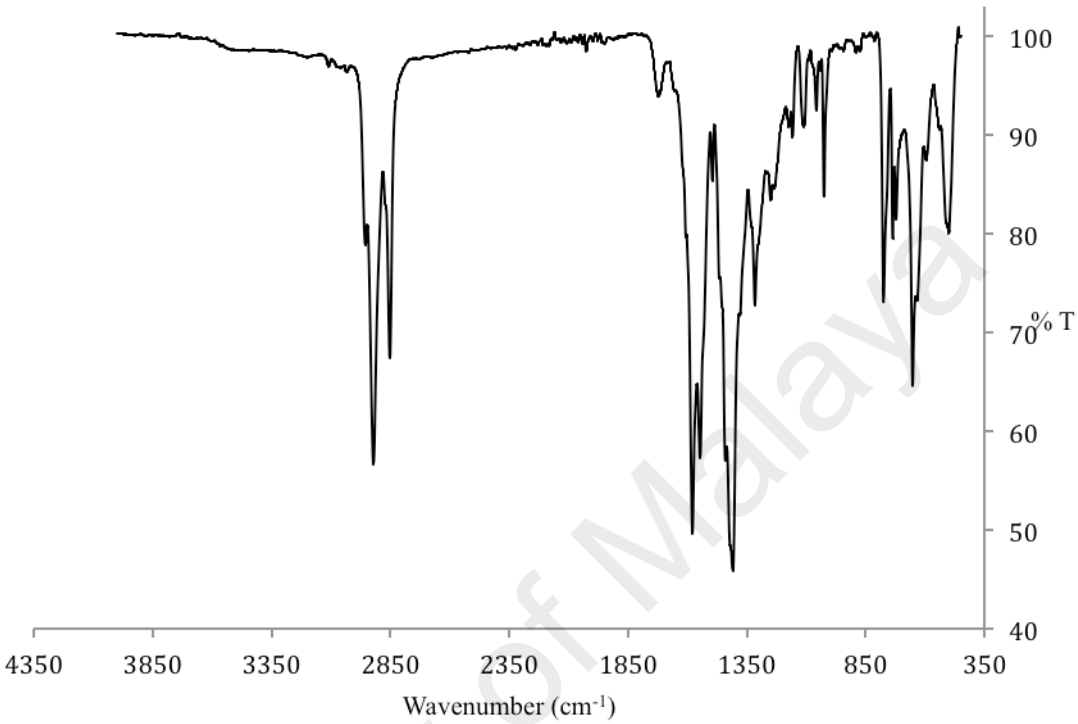

Figure 4.49 FTIR spectrum of **6**

Its **UV-vis** spectrum (**Figure 4.50**) in chloroform shows a *d-d* band appearing as a shoulder at 585 nm (ε = 146 M^{-1} cm^{-1}) and a charge transfer band at 465 nm (ε = 640 M^{-1} cm^{-1}). The *d-d* peak was assigned to the electronic transition for a LS Fe(II) atom, as similarly done for its precursor complex, $[Fe_2(\mu\text{-}H_2O)_2(CH_3(CH_2)_8COO)_4].H_2O$.

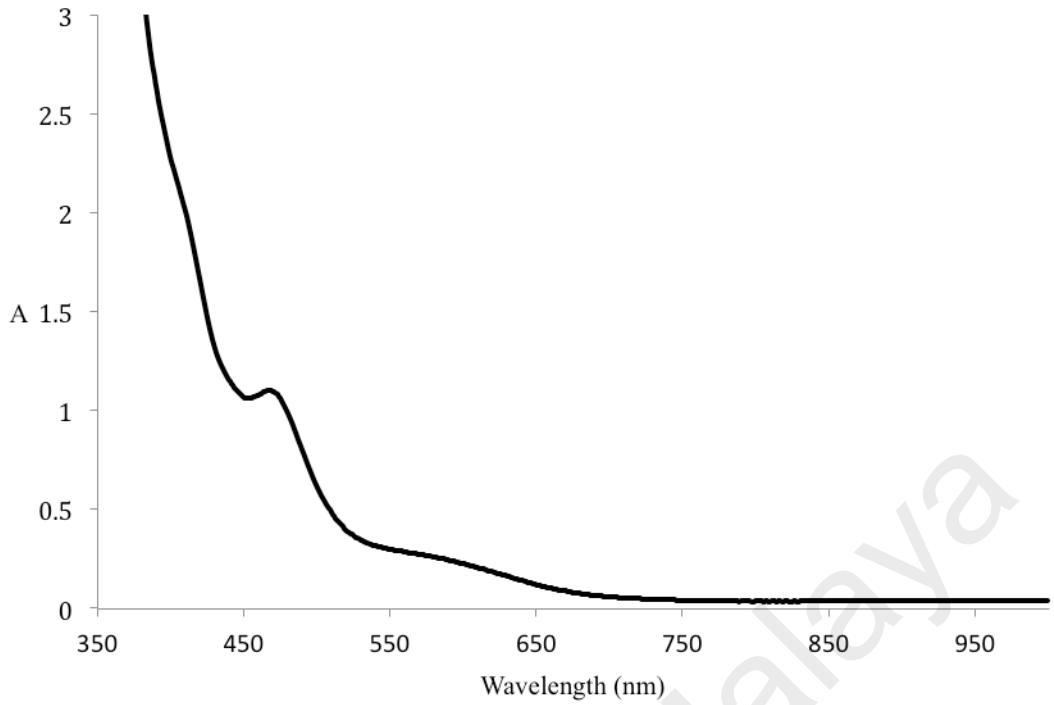

Figure 4.50 UV-vis spectrum of **6** in chloroform

Its magnetic data could not be collected by the Gouy method, as the sample was a semisolid. Hence, its $\chi_M^{corr}T$ value cannot be calculated.

Combining the data above, it is proposed that **6** was dimeric with chelating $CH_3(CH_2)_8COO^-$ ion and bridging bpy ligands (**Figure 4.51**).

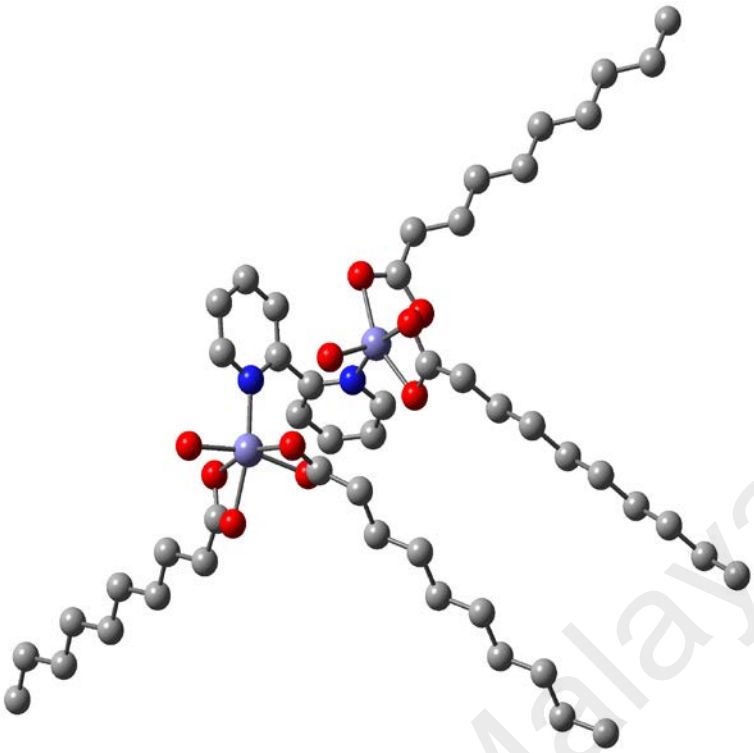

Figure 4.51 Proposed structure of **6** ([$Fe_2(CH_3(CH_2)_8COO)_4(bpy)(H_2O)_2$])

(b) Thermal and mesomorphic studies

TG trace for **6** (**Figure 4.52**) shows a total weight loss of 86.8% in the temperature range 156 ^oC to 436 ^oC due to evaporation of coordinated H_2O and decomposition of $CH_3(CH_2)_8COO^-$ and bpy ligands (calculated, 88.1%). The results are in good agreement with its proposed structural formula. The amount of residue at temperatures above 436 ^oC was 13.2% (calculated, 11.1% assuming FeO). Hence, its decomposition temperature was 156 ^oC, which was lower to the corresponding copper(II) complex ([$Cu_2(CH_3(CH_2)_8COO)_4(bpy)_2$] (**2**); T_{dec} = 177 ^oC).

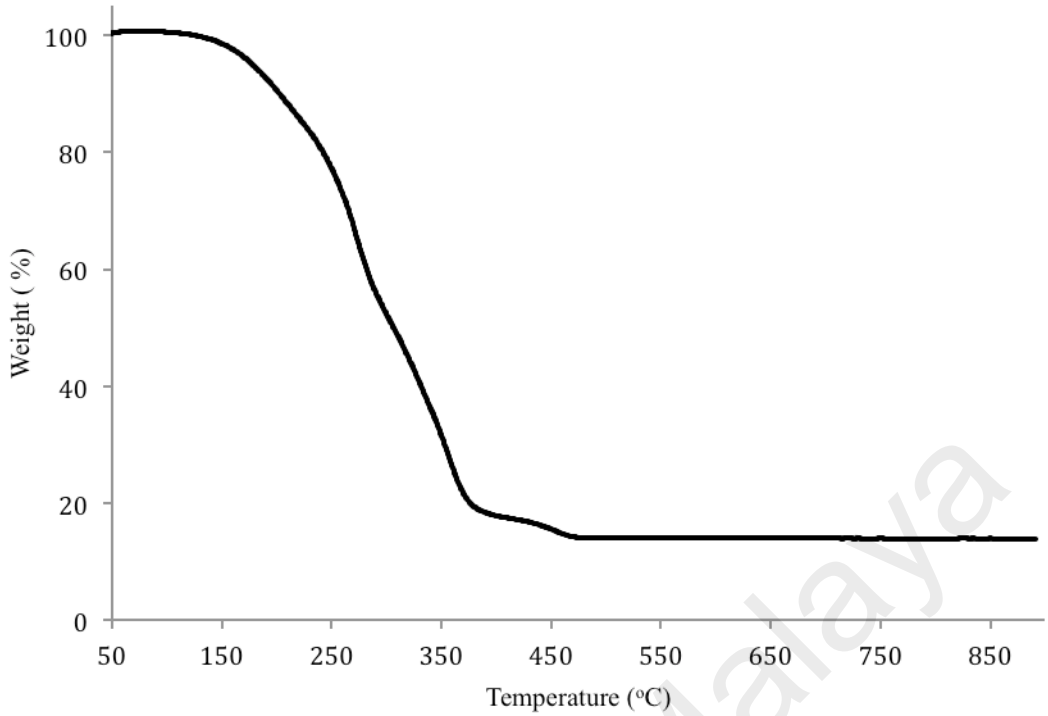

Figure 4.52 TGA trace of **6**

When viewed under **POM**, the semisolid was fluidic and the colour was red at 28 °C (**Figure 4.53**(**a**)). On further heating, it cleared to a paler red liquid at about 49 °C (**Figure 4.53**(**b**)), indicating a lower proportion of LS Fe(II) in the complex. However upon cooling from the liquid phase, there was no optical texture observed. Hence, **6** did not behave as a thermotropic metallomesogen.

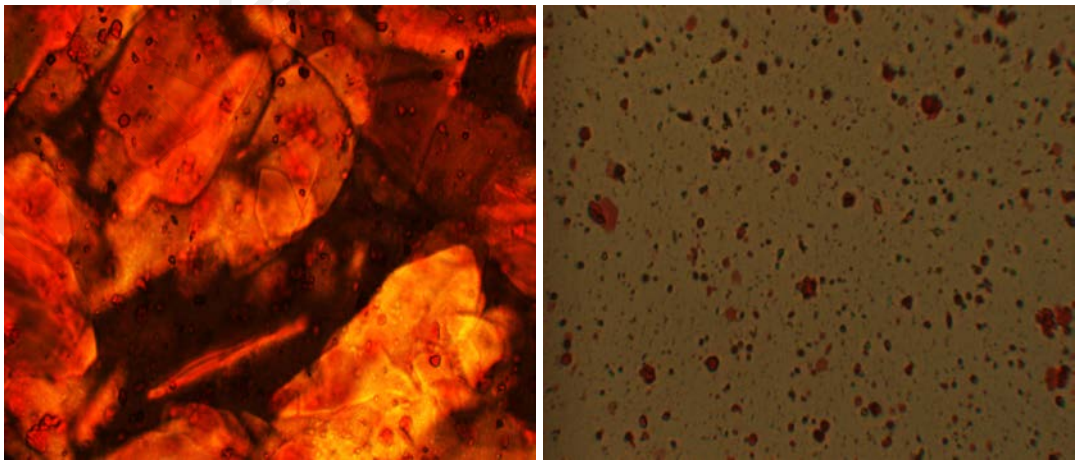

(a) (b)

Figure 4.53 Photomicrographs of **6** on heating at: (a) 28 °C; and (b) 49 °C

Its **DSC** traces (**Figure 4.54**) shows overlapping endothermic peaks in the temperature range of 35.6 ^{o}C to 56.4 ^{o}C ($\Delta H_{combined}$ = +7.0 kJ mol^{-1}) assigned to its melting temperature and LS-HS SCO transition (discussed below). These were followed by several weak overlapping endothermic peaks in the temperature range of 56.5 ^{o}C to 88.6 ^{o}C due to breaking of weak intermolecular forces. However, on cooling from this temperature, there were no peaks observed, in agreement with the results from **POM**.

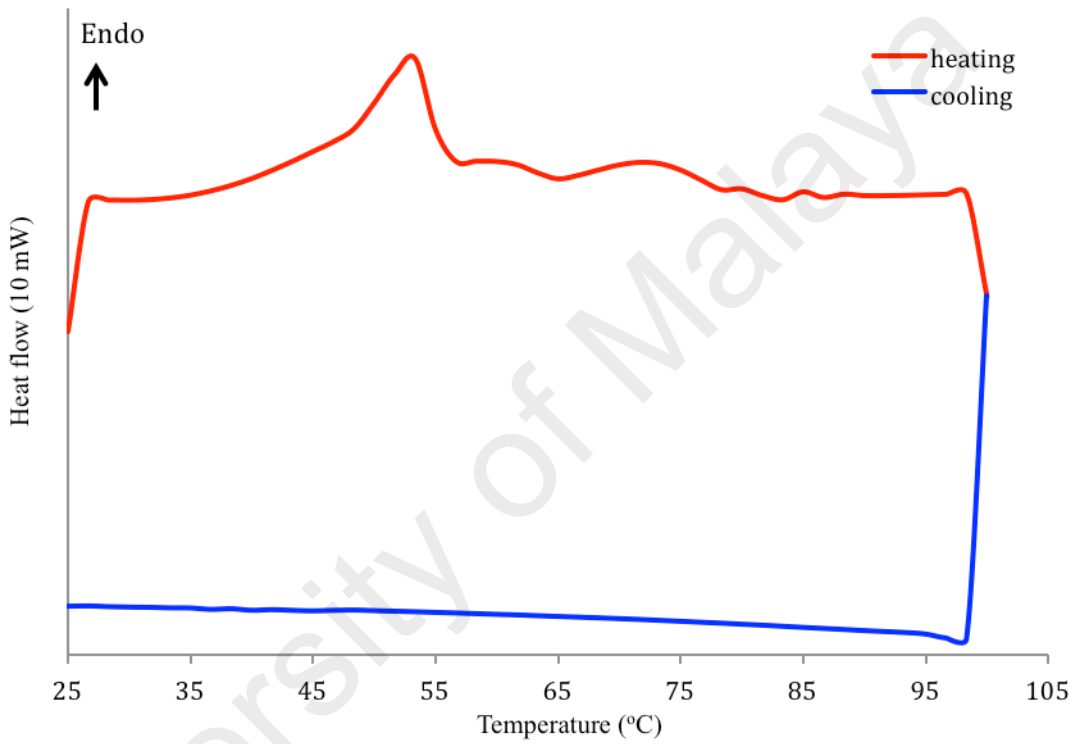

Figure 4.54 DSC scans of **6**

The entropy change for **spin crossover** (SCO; ΔS_{spin}) for spin-labile materials may be theoretically calculated using the formula: $\Delta S_{spin} = R\ln[(2S+1)_{HS}/(2S+1)_{LS}]$, where R = 8.314 J K^{-1} mol^{-1} [84]. The ΔS_{spin} value may then be compared with the experimental value obtained from the DSC, calculated using the formula: $\Delta S_{spin} = \Delta H/T$. The theoretical ΔS_{spin} value for Fe(II) complexes is 13.38 J K^{-1} mol^{-1} since S = 2 for HS Fe(II) atom (electronic configuration = $t_{2g}^{4}e_{g}^{2}$; number of unpaired electrons = 4), while S = 0 for LS Fe(II) (electronic configuration = t_{2g}^{6}; number of unpaired electrons = 0). For **6**, ΔS_{spin} value was 23.5 J K^{-1} mol^{-1} at 46.1 ^{o}C. Hence, it is inferred that the complex showed a LS-HS SCO transition at this temperature.

Combining both POM and DSC data, the effect of heat on the structure and spin state of the complex is shown in **Scheme 4.3**.

$$\underset{\text{LS}}{[Fe_2(R)_4(bpy)(H_2O)_2]} \xrightarrow[49\ ^oC]{\Delta} [Fe(R)_2(bpy)] + \underset{\text{HS}}{[Fe(R)_2(H_2O)_2]}$$

Scheme 4.3 Effect of heat on the structure and spin state of **6** (R = $CH_3(CH_2)_8COO$)

4.2.2 [$Fe_2(CH_3(CH_2)_{10}COO)_4(bpy)(H_2O)_2$] (7)

(a) Synthesis and structural elucidation

The precursor complex, [$Fe_2(\mu\text{-}H_2O)_2(CH_3(CH_2)_{10}COO)_4$].$2H_2O$ was obtained as a brown powder, with 33% yield from the reaction of $CH_3(CH_2)_{10}COONa.½H_2O$ with [$FeSO_4.7H_2O$]. The results of its **elemental analyses** (C, 58.6%; H, 9.2%) were in good agreement with the calculated values (C, 58.7%; H, 10.3%; FW 980.9 g mol^{-1}). Its **FTIR** data (**Table 4.6**; **Figure 4.55**) show the presence of the expected functional groups. Hence, the $\Delta\nu_{coo}$ value was 128 cm^{-1}, which was lower than the value for $CH_3(CH_2)_{10}COONa$ (136 cm^{-1}), indicating that $CH_3(CH_2)_{10}COO^-$ ion was coordinated as a chelating ligand.

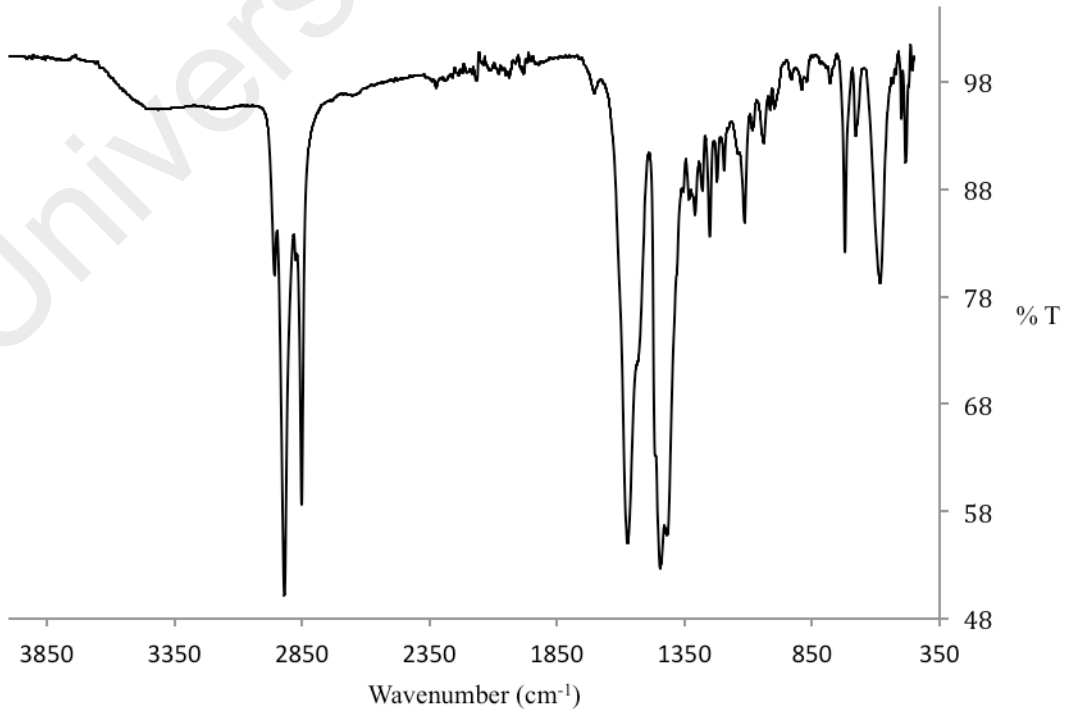

Figure 4.55 FTIR spectrum of [$Fe_2(\mu\text{-}H_2O)_2(CH_3(CH_2)_{10}COO)_4$].$2H_2O$

Its **UV-vis** spectrum (**Figure 4.56**) in $CHCl_3$ shows a continuously increasing absorbance from about 800 nm to about 469 nm (ε = 919 M^{-1} cm^{-1}). These data were similar to $[Fe_2(\mu\text{-}H_2O)_2(CH_3(CH_2)_8COO)_4].H_2O$, and may be similarly explained.

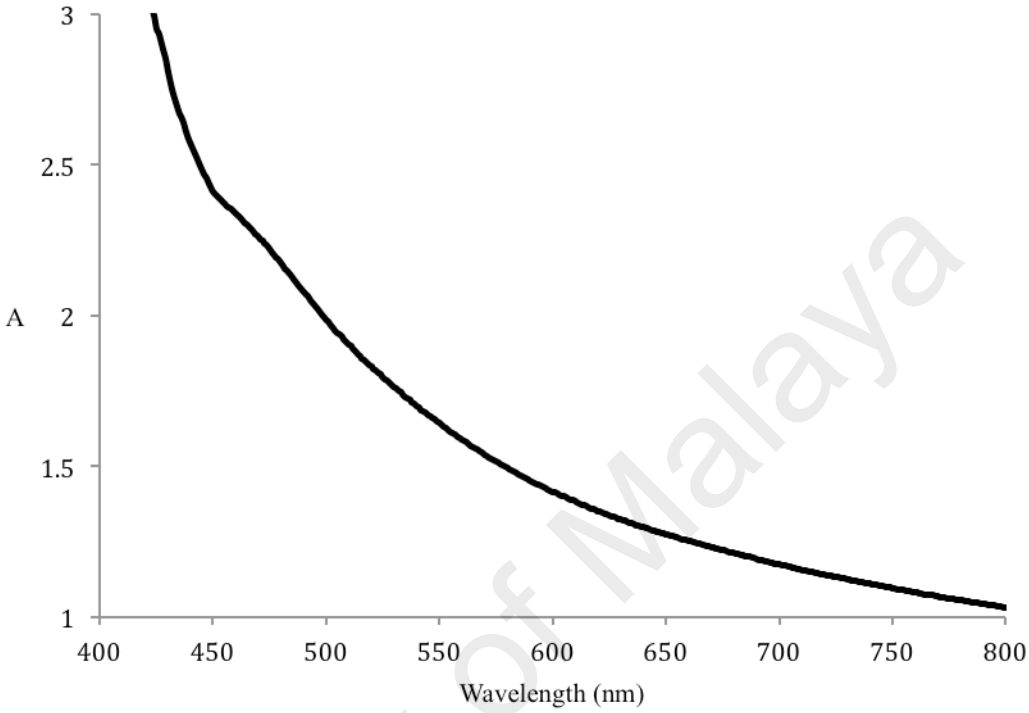

Figure 4.56 UV-vis spectrum of $[Fe_2(\mu\text{-}H_2O)_2(CH_3(CH_2)_{10}COO)_4].2H_2O$ in chloroform

Its $\chi_M^{corr}T$ value, calculated as before from the values of its formula weight (980.9 g mol^{-1}), mass susceptibility (χ_g; 1.02 x 10^{-6} cm^3 g^{-1}), molar susceptibility (χ_m; 1.00 x 10^{-3} cm^3 mol^{-1}), diamagnetic correction factor (χ_D; -4.90 x 10^{-4} cm^3 mol^{-1}) and corrected molar susceptibility (χ_m^{corr}; 1.49 x 10^{-3} cm^3 mol^{-1}), was 0.44 cm^3 K mol^{-1} at 298 K. Accordingly, the complex was made up of 7.4% HS and 92.6% LS Fe(II) atoms at this temperature, indicating strong Fe-O bonds.

$[Fe_2(\mu\text{-}H_2O)_2(CH_3(CH_2)_{10}COO)_4].2H_2O$ reacted with bpy to form red semi-solid (yield = 68%). The results of the **elemental analyses** (C, 60.7%; H, 9.7%; N, 2.8%) were in agreement for $[Fe_2(CH_3(CH_2)_{10}COO)_4(bpy)(H_2O)_2].2H_2O$ (**7**) (C, 61.3%; H, 9.6%; N, 2.5%; FW = 1137.1 g mol^{-1}).

Its **FTIR** data (**Table 4.6**; **Figure 4.57**) show the presence of the expected functional groups. Hence, the $\Delta\nu_{coo}$ values were 133 cm^{-1} and 172 cm^{-1}, indicating two chelating $CH_3(CH_2)_{10}COO^-$ ligands.

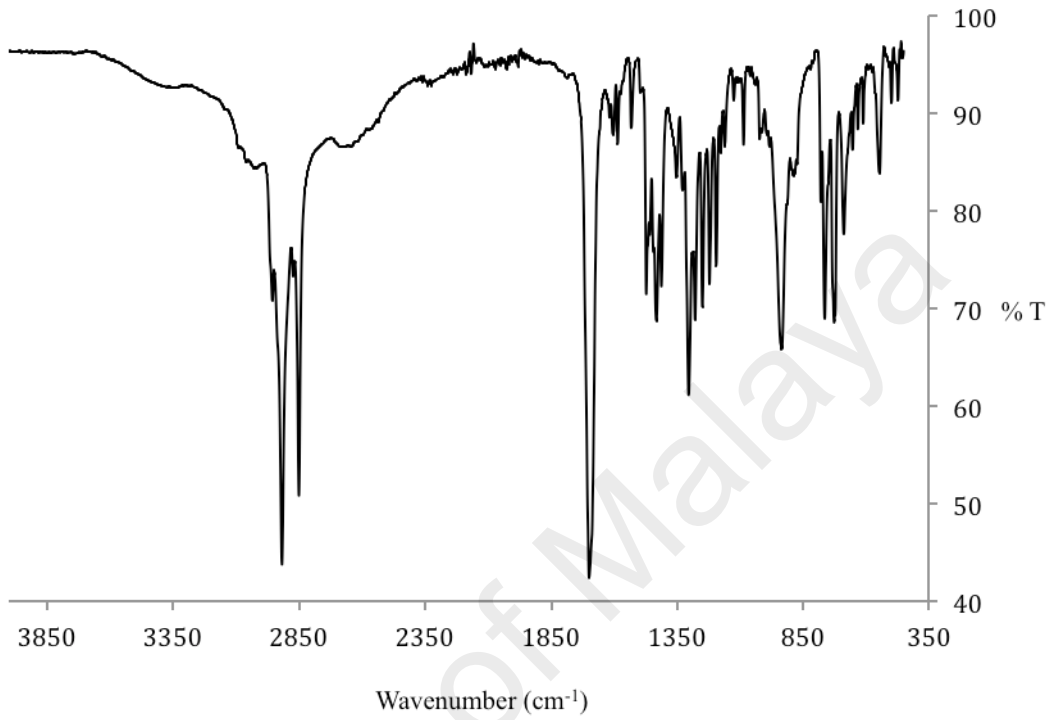

Figure 4.57 FTIR spectrum of **7**

Its **UV-vis** spectrum (**Figure 4.58**) in chloroform shows a *d-d* band appearing as a shoulder at 358 nm (ε = 99 M^{-1} cm^{-1}). The *d-d* peak was assigned to the electronic transition for a LS Fe(II) atom, as explained above.

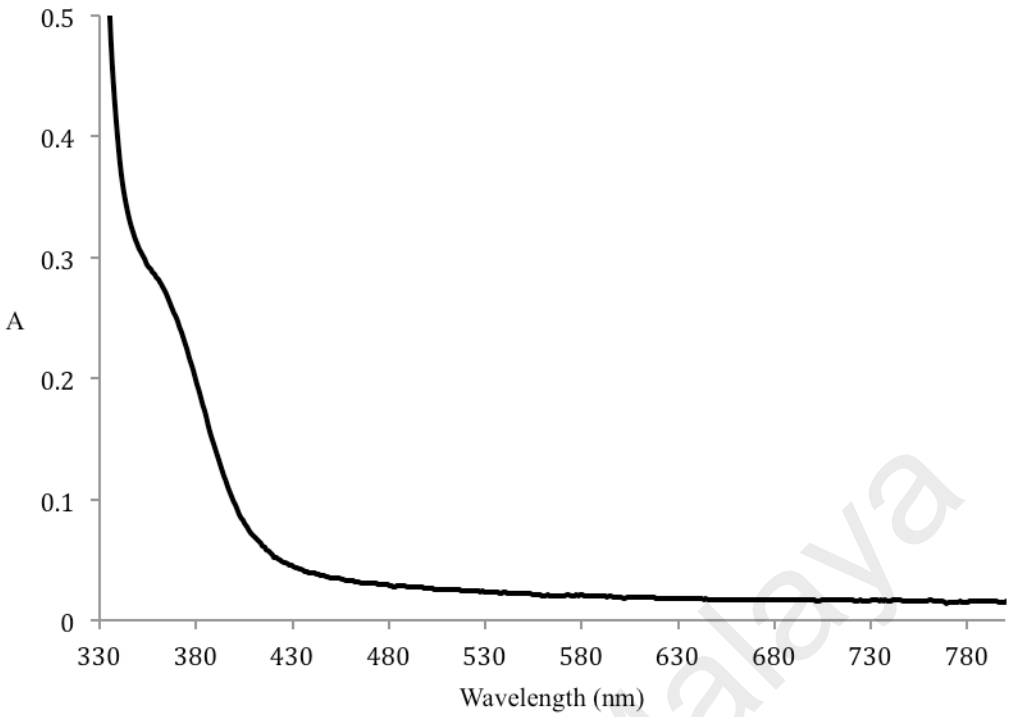

Figure 4.58 UV-vis spectrum of **7** in chloroform

Similar to **6**, its magnetic data could not be collected by the Gouy method as the sample was a semisolid. Hence, its $\chi_M^{corr}T$ value cannot be calculated.

(b) Thermal and mesomorphic studies

TG trace for **7** (**Figure 4.59**) shows a total weight loss of 93.3% in the temperature range 129 ^{o}C to 346 ^{o}C due to evaporation of coordinated and lattice H_2O and decomposition of $CH_3(CH_2)_{10}COO^-$ ion and bpy ligands (calculated, 90.2%). The results were in good agreement with its proposed structural formula. The amount of residue at temperatures above 346 ^{o}C was 6.7% (calculated, 9.8% assuming pure Fe). Hence, its decomposition temperature was 129 ^{o}C.

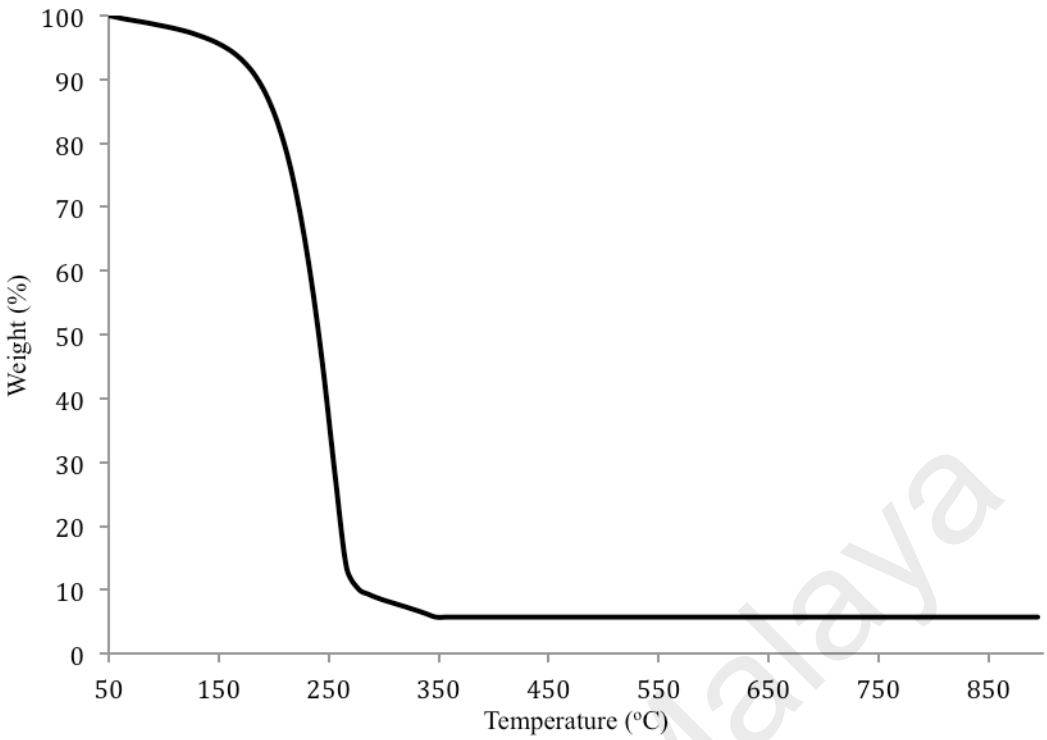

Figure 4.59 TGA traces of **7**

When viewed under **POM**, its colour was red on heating at 40 °C (**Figure 4.60**(**a**)), and on cooling from the isotropic liquid, optical textures were observed at 39 °C (**Figure 4.60**(**b**)). Hence, **7** behave as a thermotropic metallomesogen.

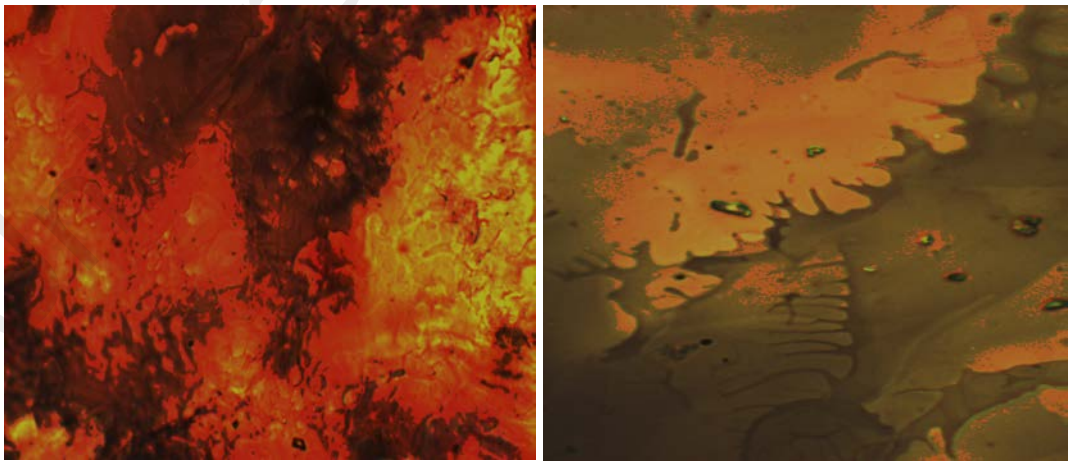

(a) (b)

Figure 4.60 Photomicrographs of **7** on heating at: (a) 40 °C; and on cooling at (b) 39 °C

Its **DSC** traces (**Figure 4.61**) shows overlapping endothermic peaks in the temperature range of 32.1 °C to 45.9 °C ($\Delta H_{combined}$ = +83.9 kJ mol^{-1}) assigned to

combined LS-HS SCO transition, and melting and clearing temperatures. Upon cooling, there is a strong exothermic peak at 29.5 ^{o}C (ΔH = -106.4 kJ mol^{-1}) assigned as formation of a mesophase (*I-M* transition).

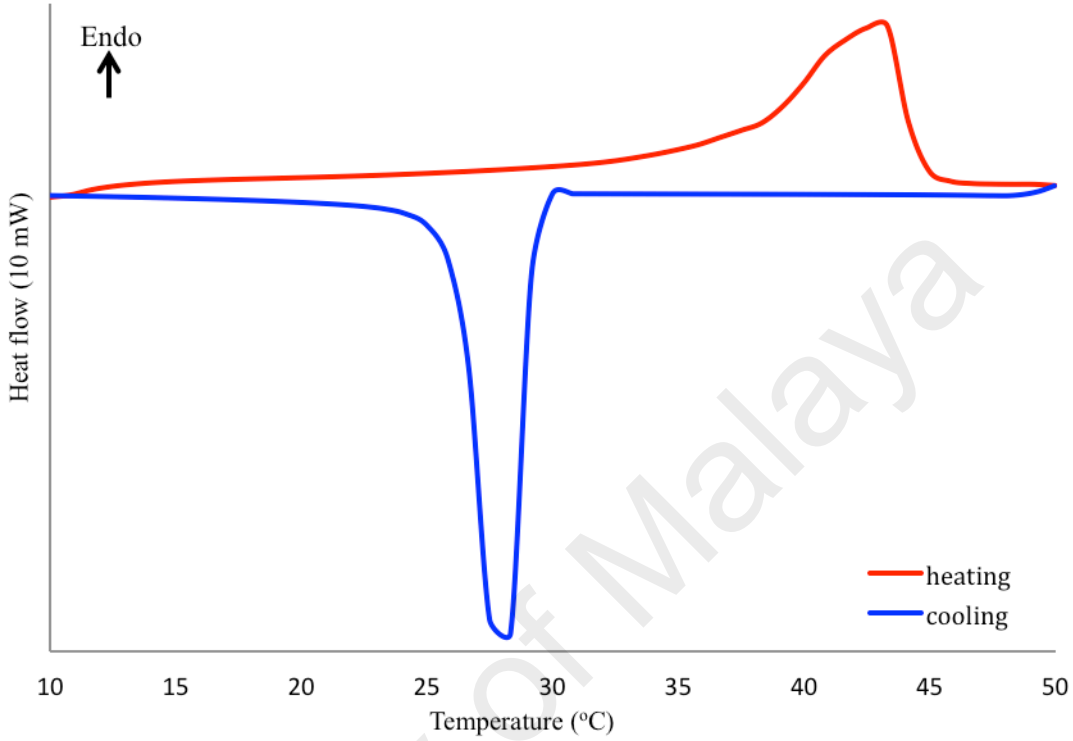

Figure 4.61 DSC scans of **7**

Combining both POM and DSC data, the effect of heat on the structure and spin state of the complex was similar to **6**, and may be similarly explained.

4.2.3 [$Fe_2(CH_3(CH_2)_{12}COO)_4(bpy)(H_2O)_2$] (8)

(a) Synthesis and structural elucidation

The precursor complex, [$Fe_2(\mu\text{-}H_2O)_2(CH_3(CH_2)_{12}COO)_4$].2$H_2O$, was obtained as a brown powder with 14% yield from the reaction of $CH_3(CH_2)_{12}COONa$ with [$FeSO_4.7H_2O$]. The results of its **elemental analyses** (C, 61.6%; H, 11.1%) were in good agreement with the calculated values (C, 61.5%; H, 10.7%; FW 1093.2 g mol^{-1}).

Its **FTIR** data (**Table 4.6**; **Figure 4.62**) show the presence of the expected functional groups. The $\Delta\nu_{coo}$ value was 110 cm^{-1}, which was lower than the value for

$CH_3(CH_2)_{12}COONa$ (136 cm^{-1}), indicating that $CH_3(CH_2)_{12}COO^-$ ion was coordinated as a chelating ligand.

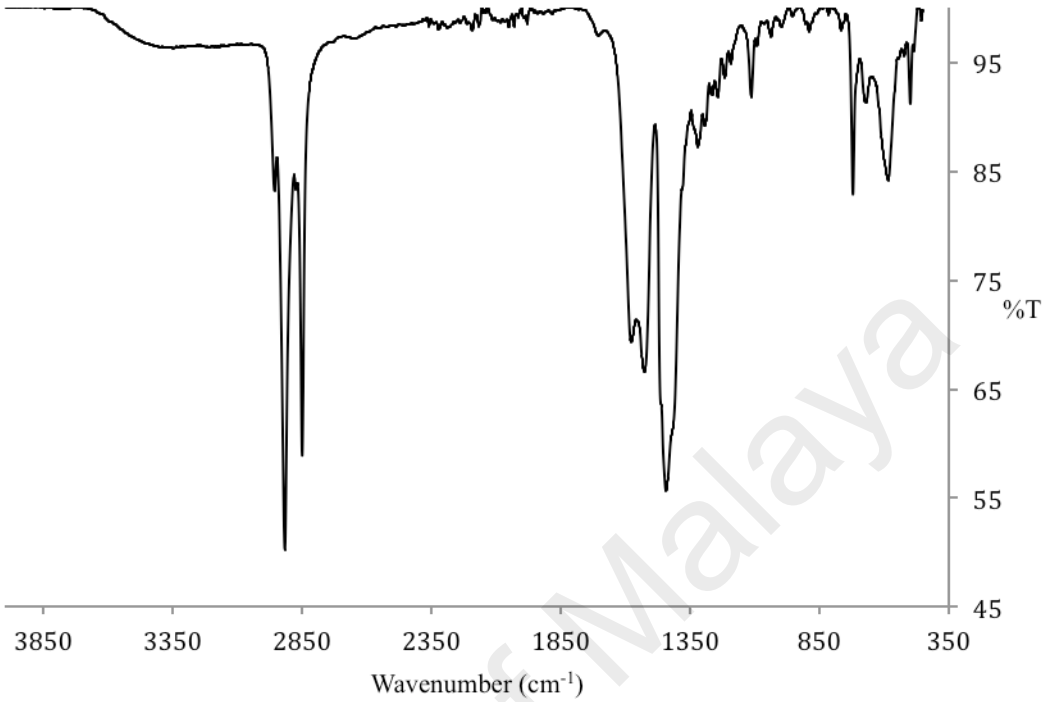

Figure 4.62 FTIR spectrum of $[Fe_2(\mu\text{-}H_2O)_2(CH_3(CH_2)_{12}COO)_4].2H_2O$

Its **UV-vis** spectrum (**Figure 4.63**) in $CHCl_3$ shows a continuously increasing absorbance from about 1000 nm to a shoulder at 591 nm (ε = 774 M^{-1} cm^{-1}). The spectrum was similar to $[Fe_2(\mu\text{-}H_2O)_2(CH_3(CH_2)_8COO)_4].H_2O$, and may be similarly explained.

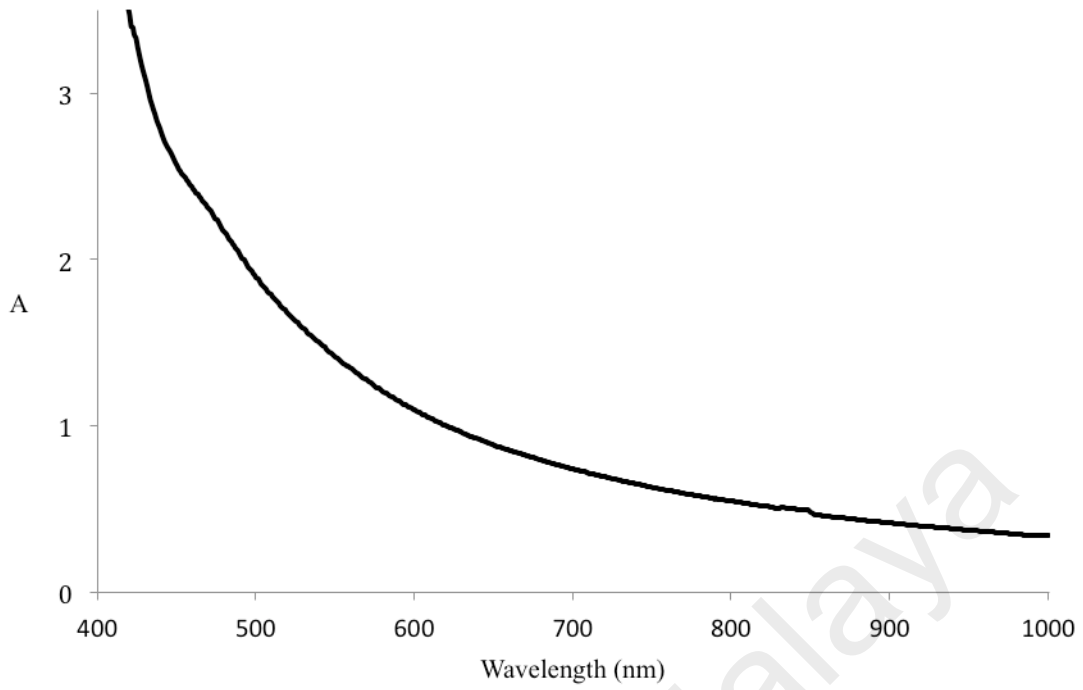

Figure 4.63 UV-vis spectrum of $[Fe_2(\mu\text{-}H_2O)_2(CH_3(CH_2)_{12}COO)_4].2H_2O$ in chloroform

Its $\chi_M^{corr}T$ value, calculated as before from the values of its formula weight (1093.2 g mol^{-1}), mass susceptibility (χ_g; 7.89 x 10^{-6} cm^3 g^{-1}), molar susceptibility (χ_m; 8.63 x 10^{-3} cm^3 mol^{-1}), diamagnetic correction factor (χ_D; -5.47 x 10^{-4} cm^3 mol^{-1}) and corrected molar susceptibility (χ_m^{corr}; 9.17 x 10^{-3} cm^3 mol^{-1}), was 2.73 cm^3 K mol^{-1} at 298 K. Accordingly, the complex was made up of 45.5% HS and 54.5% LS Fe(II) atoms at this temperature.

$[Fe_2(\mu\text{-}H_2O)_2(CH_3(CH_2)_{12}COO)_4].2H_2O$ reacted with bpy to form a reddish solid (yield = 91%). The results of the **elemental analyses** (C, 65.4%; H, 9.4%; N, 2.9%) were in good agreement for $[Fe_2(CH_3(CH_2)_{12}COO)_4(bpy)(H_2O)_2]$ (**8**) (C, 65.3%; H, 10.0%; N, 2.3%; FW = 1213.4 g mol^{-1}). Is it proposed its structure was similar to **6** based on the analytical data discussed below.

Its **FTIR** data (**Table 4.6**; **Figure 4.64**) show the presence of the expected functional groups. Hence, the $\Delta\nu_{coo}$ values were 144 cm^{-1} and 138 cm^{-1}, indicating two chelating $CH_3(CH_2)_8COO^-$ ligands.

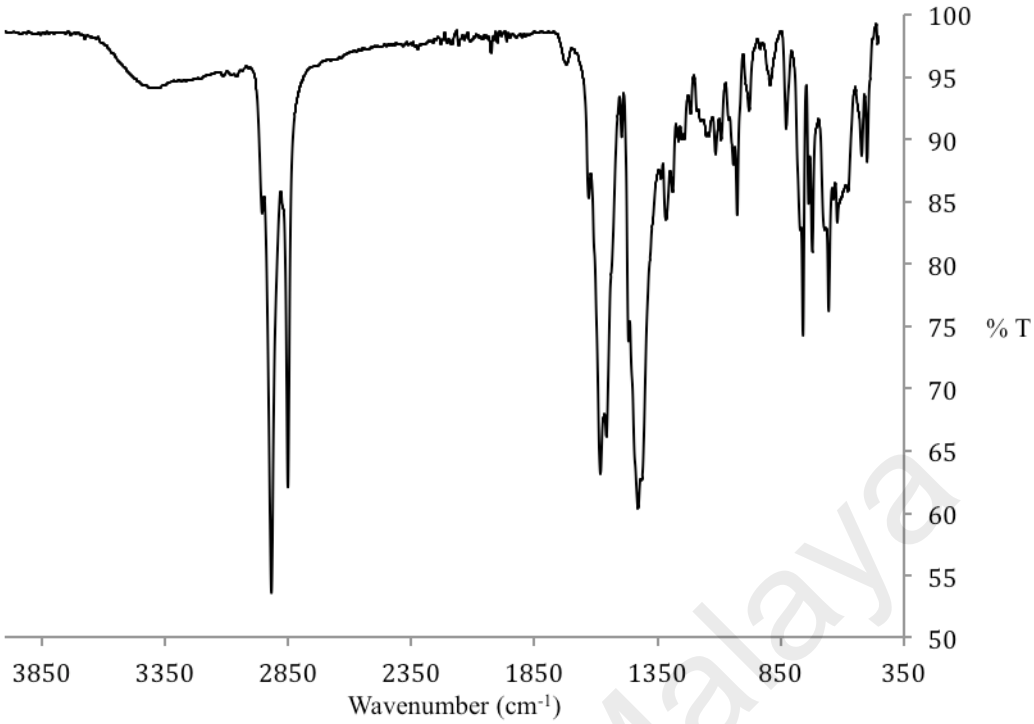

Figure 4.64 FTIR spectrum of **8**

Its **UV-vis** spectrum (**Figure 4.65**) in chloroform shows two band appearing as a shoulder at 575 nm (ε_{max} = 510 M^{-1} cm^{-1}) and at 463 nm (ε_{max} = 931 M^{-1} cm^{-1}). The *d-d* peak was assigned to the electronic transition for a HS Fe(II) atom, as explained above.

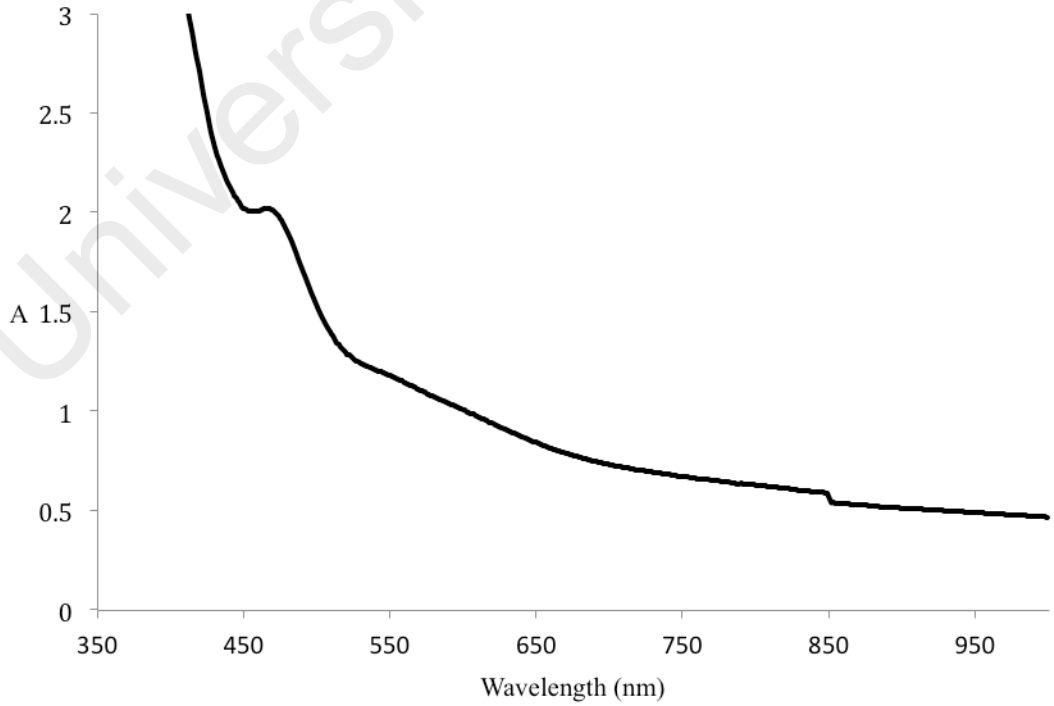

Figure 4.65 UV-vis spectrum of **8** in $CHCl_3$

Its $\chi_M^{corr}T$ value, calculated as before from the values of its formula weight (1213.4 g mol^{-1}), mass susceptibility (χ_g; 3.46 x 10^{-6} cm^3 g^{-1}), molar susceptibility (χ_m; 4.20 x 10^{-3} cm^3 mol^{-1}), diamagnetic correction factor (χ_D; -6.07 x 10^{-4} cm^3 mol^{-1}) and corrected molar susceptibility (χ_m^{corr}; 4.81 x 10^{-3} cm^3 mol^{-1}), was 1.43 cm^3 K mol^{-1} at 298 K. Accordingly, **8** was made up of 23.7% HS and 76.3% LS Fe(II) atoms at this temperature.

(b) Thermal and mesomorphic studies

TG trace for **8** (**Figure 4.66**) shows an initial weight loss of 2.8% at 117 ^oC due to the loss of lattice water (calculated, 1.6%), and a total weight loss of 83.5% in the temperature range 146 ^oC to 483 ^oC due to the decomposition of $CH_3(CH_2)_{12}COO^-$ ion and bpy (calculated, 88.1%). The results are in a good agreement with its proposed structural formula. The amount of residue at temperatures above 483 ^oC was 13.7% (calculated, 13.1% assuming FeO). Hence, its decomposition temperature was 146 ^oC.

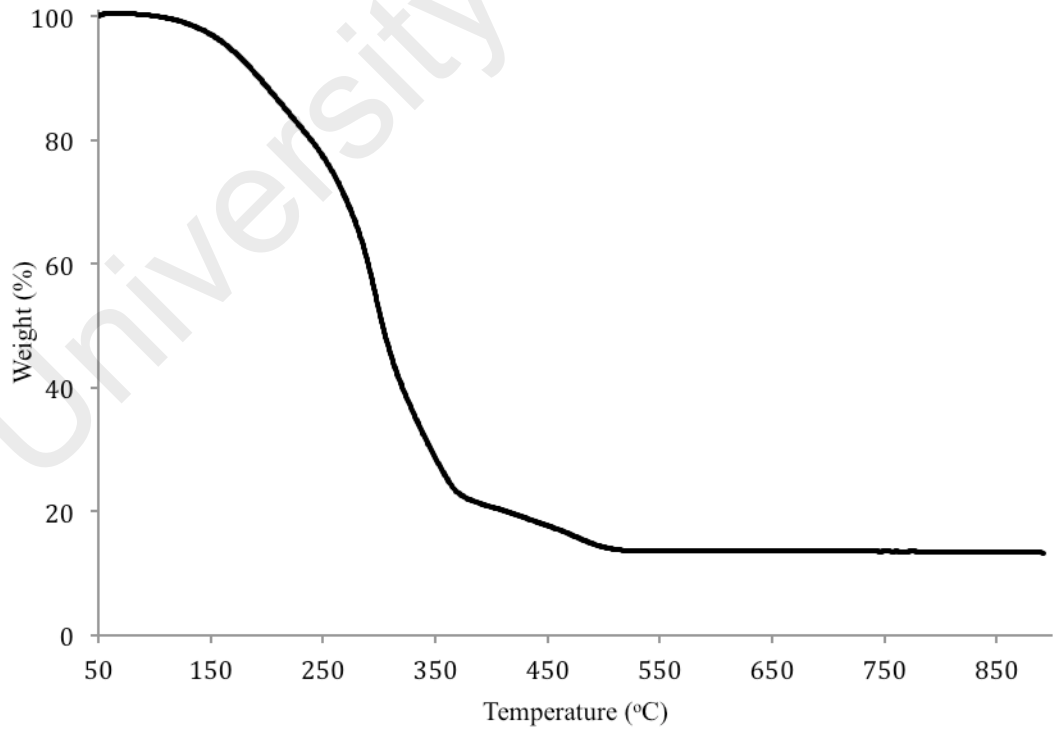

Figure 4.66 TGA trace of **8**

When viewed under **POM**, its colour was dark red at 50 ^{o}C (**Figure 4.67**(**a**)), and on further heating, the intensity of the red colour was reduced and there were orange spots at 56 ^{o}C (**Figure 4.67**(**b**)), and then it cleared to a paler red liquid at about 72 ^{o}C (**Figure 4.67**(**c**)). Upon cooling from the liquid phase, there was no texture observed. Hence, **8** did not behave as a thermotropic metallomesogen.

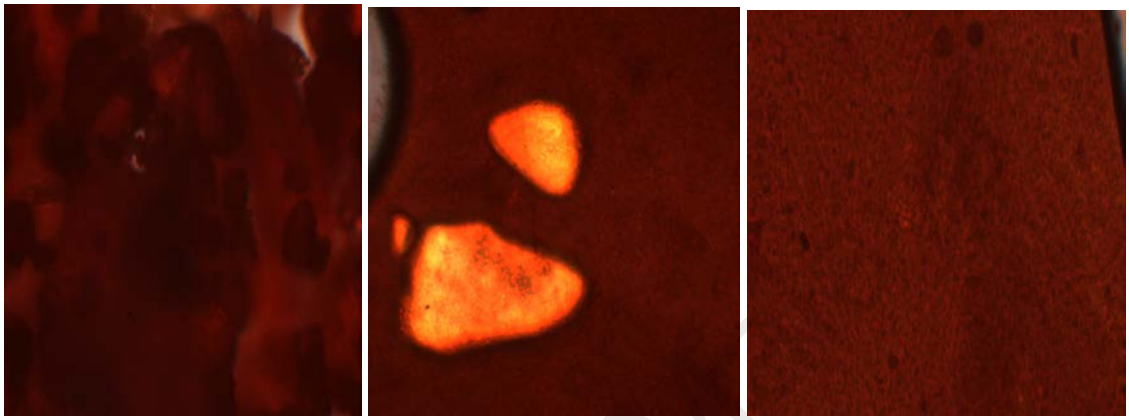

(a) (b) (c)

Figure 4.67 Photomicrographs of **8** on heating at: (a) 50 ^{o}C; (b) 56 ^{o}C; and (c) 72 ^{o}C

Its **DSC** traces (**Figure 4.68**) show overlapping endothermic peaks in the temperature range of 34.7 ^{o}C to 61.7 ^{o}C ($\Delta H_{combined}$ = +49 kJ mol^{-1}) and a broad endothermic peak at 71 ^{o}C (ΔH = +10.0 kJ mol^{-1}). However, there was no peak on cooling from 100 ^{o}C.

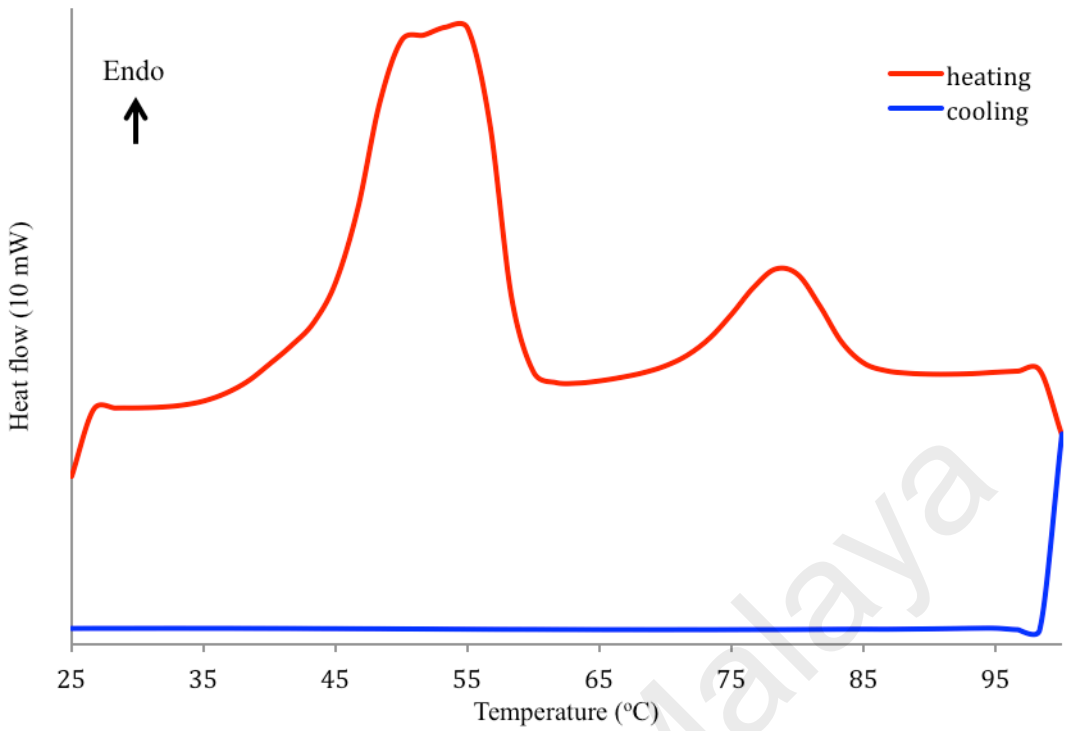

Figure 4.68 DSC scans of **8**

Combining both POM and DSC data, the effect of heat on the structure and spin state of the complex was similar to **6** ([$Fe_2(CH_3(CH_2)_8COO)_4(bpy)(H_2O)_2$], and may be similarly explained.

4.2.4 [$Fe_2(CH_3(CH_2)_{14}COO)_4(bpy)(H_2O)_2$] (9)

(a) Synthesis and structural elucidation

The precursor complex, [$Fe_2(\mu\text{-}H_2O)_2(CH_3(CH_2)_{14}COO)_4$], was obtained as a brown powder in good yield (47%) from the reaction of $CH_3(CH_2)_{14}COONa$ with [$FeSO_4.7H_2O$]. The results of its **elemental analyses** (C, 66.1%; H, 11.4%) were in good agreement with the calculated values (C, 65.7%; H, 11.0%); FW = 1169.4 g mol^{-1}). Its **FTIR** data (**Table 4.6**; **Figure 4.69**) show the presence of the expected functional groups. The $\Delta\nu_{coo}$ value was 124 cm^{-1} which was lower than the value for $CH_3(CH_2)_{14}COONa$ (137 cm^{-1}), indicating that $CH_3(CH_2)_{14}COO^-$ ion was acting as a chelating ligand.

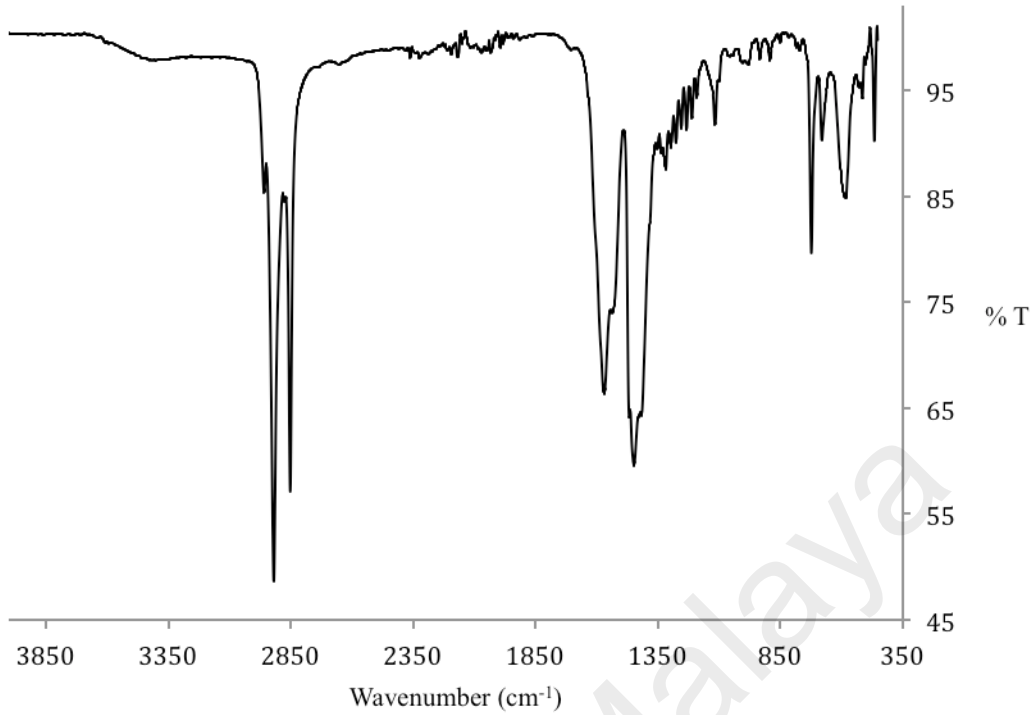

Figure 4.69 FTIR spectrum of $[Fe_2(\mu\text{-}H_2O)_2(CH_3(CH_2)_{14}COO)_4]$

Its **UV-vis** spectrum (**Figure 4.70**) in $CHCl_3$ shows a continuously increasing absorbance with a shoulder at 513 nm (ε = 735 M^{-1} cm^{-1}), similar to the above precursor complexes, and may be similarly explained.

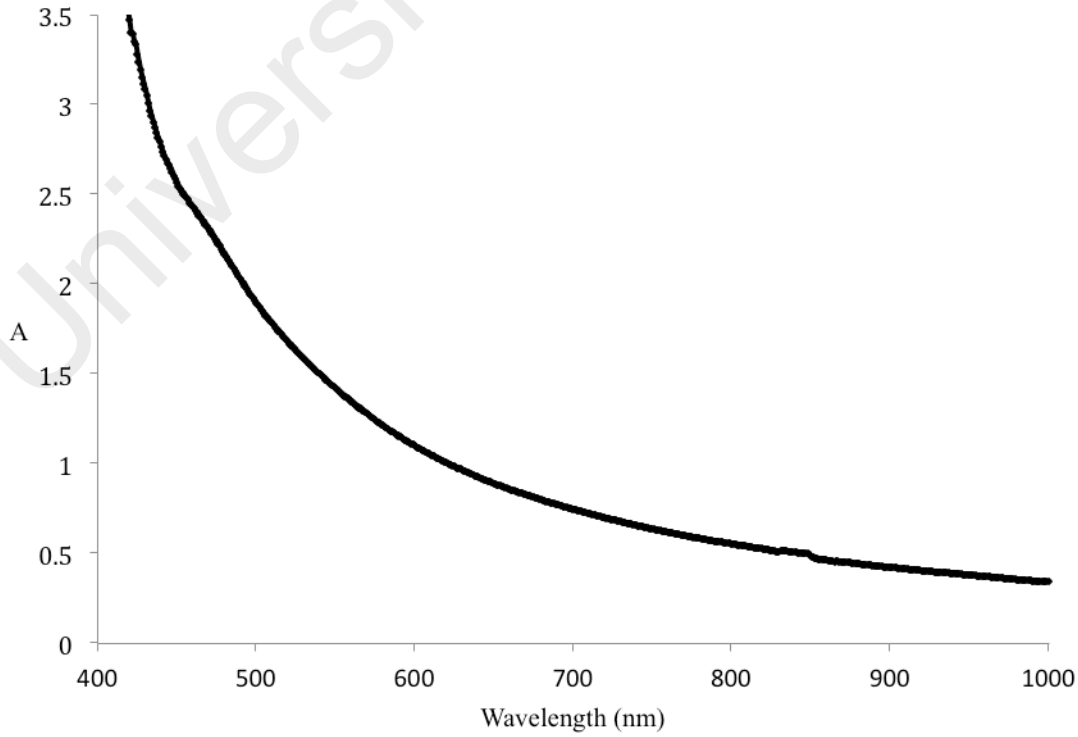

Figure 4.70 UV-vis spectrum of $[Fe_2(\mu\text{-}H_2O)_2(CH_3(CH_2)_{14}COO)_4]$ in $CHCl_3$

Its $\chi_M^{corr}T$ value, calculated as before from the values of its formula weight (1169.4 g mol^{-1}), mass susceptibility (χ_g; 6.78 x 10^{-6} cm^3 g^{-1}), molar susceptibility (χ_m; 7.93 x 10^{-3} cm^3 mol^{-1}), diamagnetic correction factor (χ_D; -5.85 x 10^{-4} cm^3 mol^{-1}) and corrected molar susceptibility (χ_m^{corr}; 8.51 x 10^{-3} cm^3 mol^{-1}), was 2.54 cm^3 K mol^{-1} at 298 K. Accordingly, $[Fe_2(\mu\text{-}H_2O)_2(CH_3(CH_2)_{14}COO)_4]$ was made up of 42.1% HS and 57.9% LS Fe(II) atoms at this temperature.

$[Fe_2(\mu\text{-}H_2O)_2(CH_3(CH_2)_{14}COO)_4]$ reacted with bpy to form a reddish solid (yield = 51%). The results of the **elemental analyses** (C, 66.8%; H, 9.6%; N, 2.8%) were in good agreement for $[Fe_2(CH_3(CH_2)_{14}COO)_4(bpy)(H_2O)_2]$ (**9**) (C, 67.0%; H, 10.3%; N, 2.1%; FW = 1325.5 g mol^{-1}).

Its **FTIR** spectrum (**Table 4.6**; **Figure 4.71**) shows the presence of the expected functional groups. Hence, the $\Delta\nu_{coo}$ values were 135 cm^{-1} and 140 cm^{-1}, indicating two chelating $CH_3(CH_2)_{14}COO^-$ ligands.

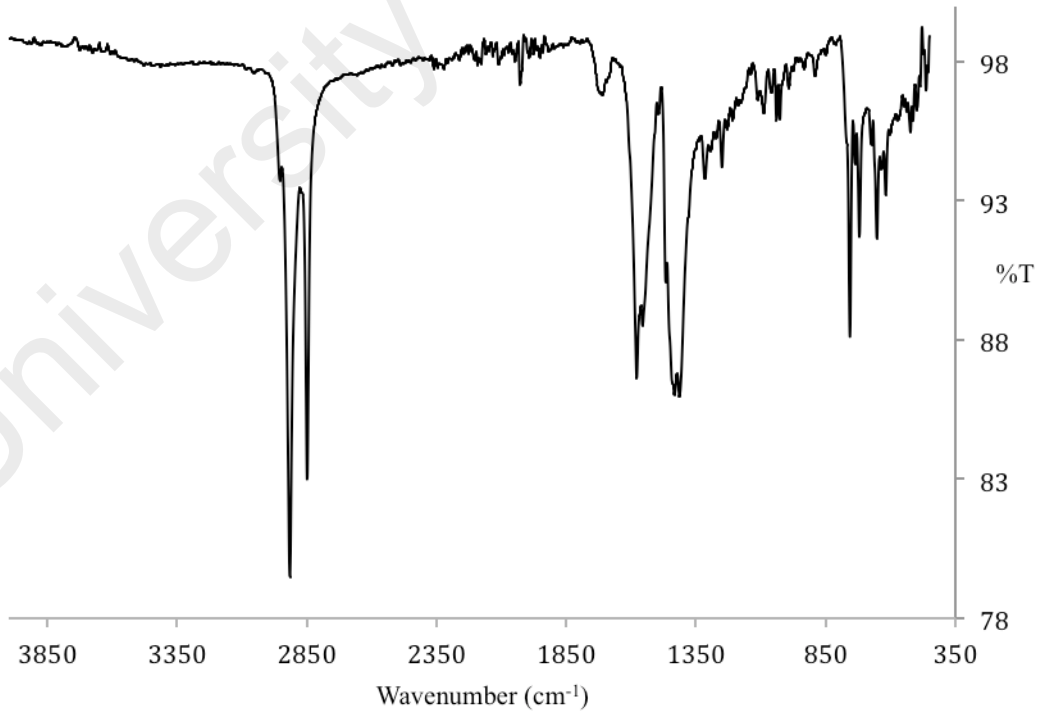

Figure 4.71 FTIR spectrum of **9**

Its **UV-vis** spectrum (**Figure 4.72**) in chloroform shows two bands appearing as shoulders at 585 nm (ε = 234 M^{-1} cm^{-1}) and 461 nm (ε = 662 M^{-1} cm^{-1}). These data were similar to previously discussed complexes, and may be similarly explained.

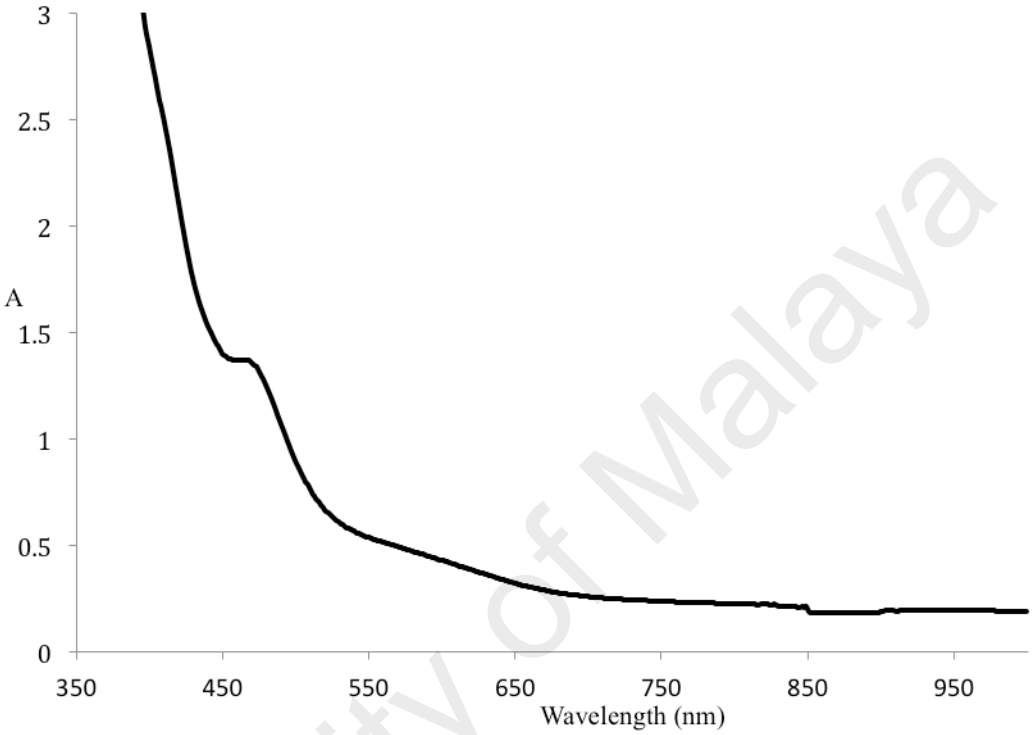

Figure 4.72 UV-vis spectrum of **9**

Its $\chi_M^{corr}T$ value, calculated as before from the values of its formula weight (1325.5 g mol^{-1}), mass susceptibility (χ_g; 3.73 x 10^{-6} cm^3 g^{-1}), molar susceptibility (χ_m; 4.94 x 10^{-3} cm^3 mol^{-1}), diamagnetic correction factor (χ_D; -6.63 x 10^{-4} cm^3 mol^{-1}) and corrected molar susceptibility (χ_m^{corr}; 5.61 x 10^{-3} cm^3 mol^{-1}), was 1.67 cm^3 K mol^{-1} at 298 K. Accordingly, **9** was made up of 27.9% HS and 72.1% LS Fe(II) atoms at this temperature.

(b) Thermal and mesomorphic studies

TG trace for **9** (**Figure 4.73**) shows a total weight loss of 88.3% in the temperature range 121 ^oC to 483 ^oC due to evaporation of coordinated H_2O and decomposition of $CH_3(CH_2)_{14}COO^-$ and bpy ligands (calculated, 91.6%). The results were in good

agreement with its proposed structural formula. The amount of residue at temperatures above 483 ^{o}C was 11.7% (calculated, 10.8% assuming FeO). Hence, its decomposition temperature was 121 ^{o}C.

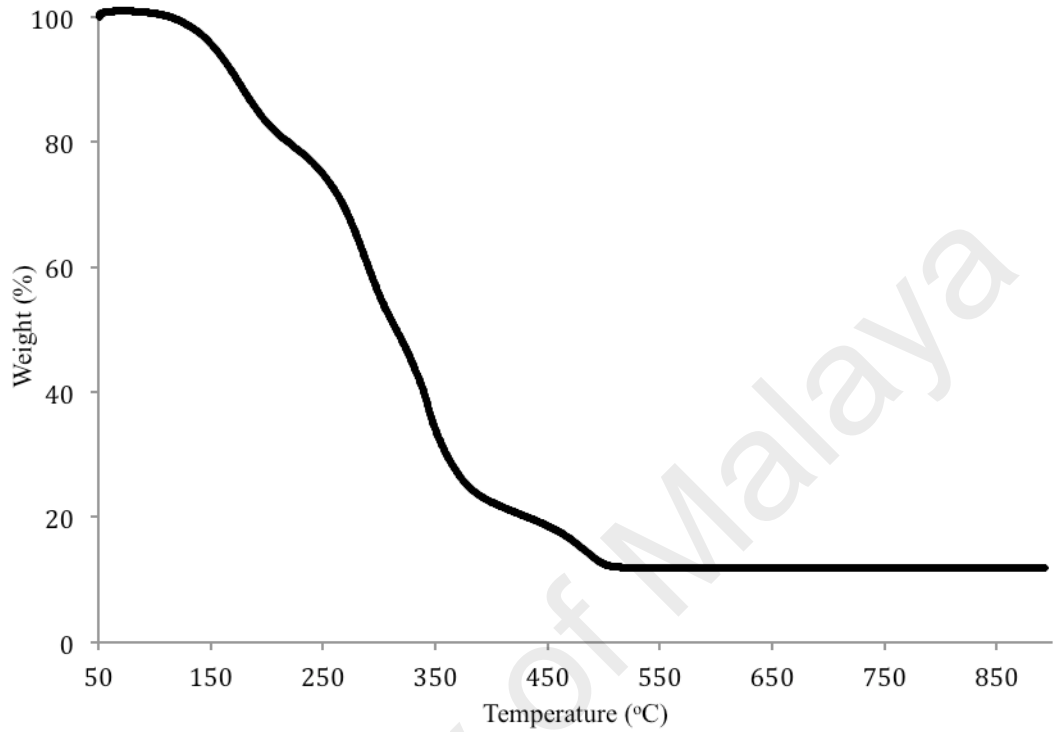

Figure 4.73 TGA trace of **9**

When viewed under **POM**, its colour was red at 45 ^{o}C (**Figure 4.74**(**a**)), and then it cleared to a paler red liquid at about 60 ^{o}C (**Figure 4.74**(**b**)). Upon cooling from the liquid phase, there was no texture observed. Hence, **9** did not behave as a thermotropic metallomesogen.

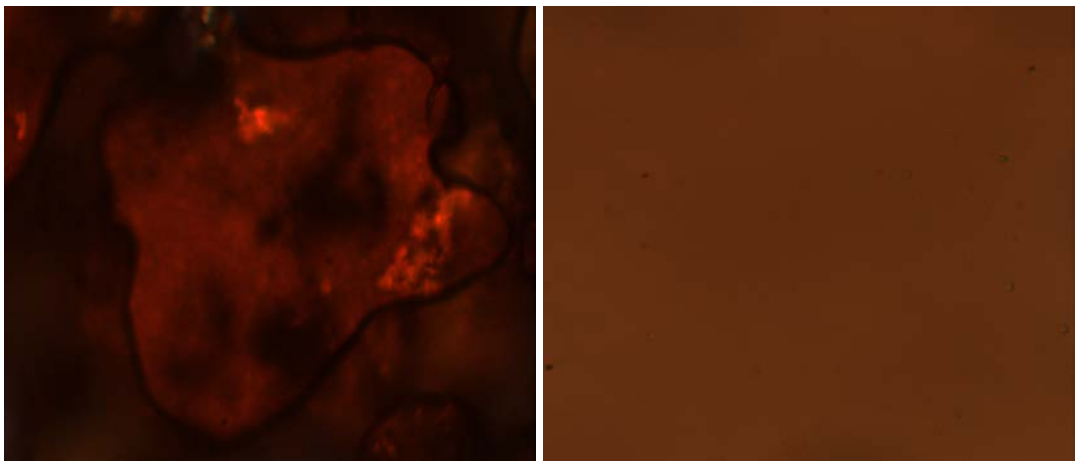

Figure 4.74 Photomicrographs of **9** on heating at: (a) 45 ^{o}C; and (b) 60 ^{o}C

Its **DSC** traces (**Figure 4.75**) shows an endothermic peak at 42 ^{o}C (ΔH = +60.8 kJ mol^{-1}) and a broad endothermic peak at 71°C (ΔH = +5.7 kJ mol^{-1}). However, there was no peak on cooling from 100 ^{o}C.

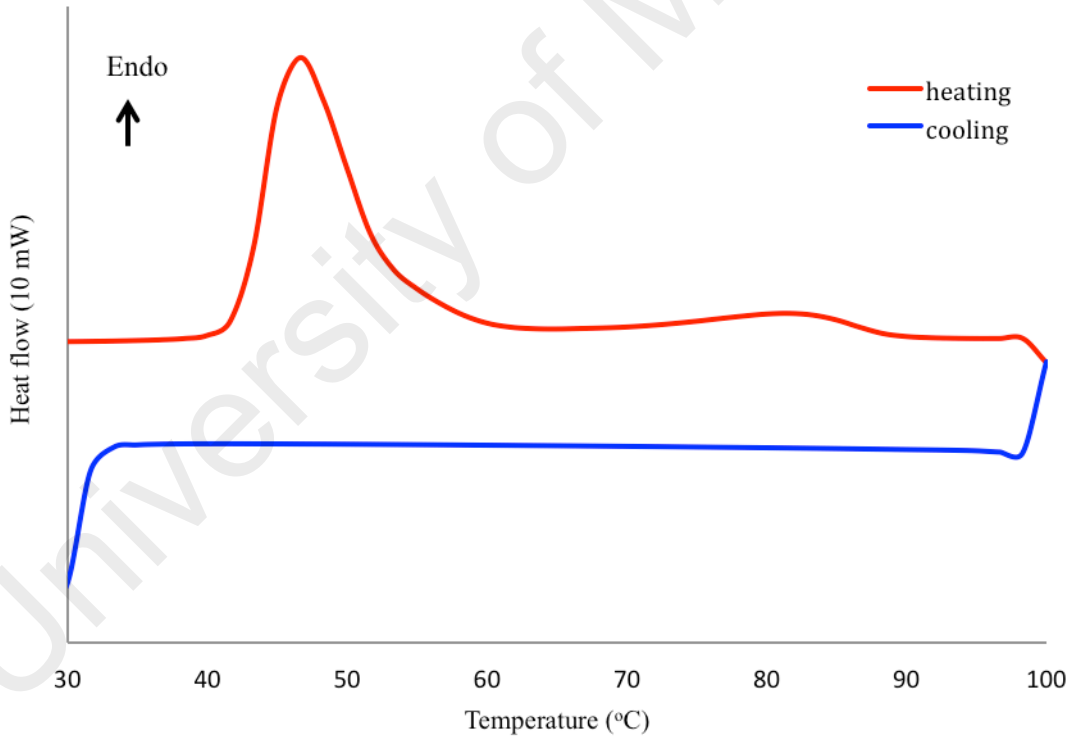

Figure 4.75 DSC scans of **9**

Combining both POM and DSC data, the effect of heat on the structure and spin state of the complex was similar to **6** and **8**, and may be similarly explained.

4.2.5 Summary

To summarize, the analytical data for the precursor complexes, $[Fe_2(\mu\text{-}H_2O)_2(R)_4].xH_2O$ ($R = CH_3(CH_2)_{6\text{-}14}COO$) and the complexes formed from their reactions with bpy (**6-9**) are shown in **Table 4.7** and **Table 4.8**, respectively.

Table 4.7 Precursor complexes of complexes **6 - 9**

Proposed chemical formula	$\Delta\nu_{coo}$ (cm^{-1})	λ_{max}, nm (ε, M^{-1} cm^{-1})	$\chi_M^{corr}T$ (cm^3 K mol^{-1})
$[Fe_2(\mu\text{-}H_2O)_2(CH_3(CH_2)_8COO)_4].H_2O$	138	464 (138)	3.47 (57.8 % HS)
$[Fe_2(\mu\text{-}H_2O)_2(CH_3(CH_2)_{10}COO)_4].2H_2O$	128	469 (919)	0.44 (7.4 % HS)
$[Fe_2(\mu\text{-}H_2O)_2(CH_3(CH_2)_{12}COO)_4].2H_2O$	110	591 (774)	2.73 (45.5 % HS)
$[Fe_2(\mu\text{-}H_2O)_2(CH_3(CH_2)_{14}COO)_4]$	124	513 (735)	2.54 (42.1 % HS)

The precursor complexes were aqua bridged dinuclear molecules with chelating carboxylate ligands, and were made up of both HS and LS Fe(II) atoms at room temperature.

Table 4.8 Complexes **6 - 9**

Proposed chemical formula	$\Delta\nu_{coo}$ (cm^{-1})	λ_{max}, nm (ε, M^{-1} cm^{-1})	$\chi_M^{corr}T$ (cm^3 K mol^{-1})	T_{dec} (^oC)	M*
$[Fe_2(CH_3(CH_2)_8COO)_4(bpy)(H_2O)_2]$ (**6**; red semi-solid)	107 138	585 (375)	-	156	No
$[Fe_2(CH_3(CH_2)_{10}COO)_4(bpy)_2(H_2O)_2].2H_2O$ (**7**; red semi-solid)	133	358 (99)	-	129	Yes
$[Fe_2(CH_3(CH_2)_{12}COO)_4(bpy)(H_2O)_2]$ (**8**; red solid)	144 138	575 (510)	1.43 (23.7 % HS)	146	No
$[Fe_2(CH_3(CH_2)_{14}COO)_4(bpy)(H_2O)_2]$ (**9**; red solid)	135 140	585 (234)	1.67 (27.9% HS)	121	No

*M = mesomorphism

All complexes were dinuclear molecules involving bridging bpy and chelating carboxylate ligands, and have both HS and LS Fe(II) atoms at room temperature. However, compared to their precursor complexes, there were higher percentages of LS Fe(II) atoms, consistent with stronger Fe(II)-N(bpy) bonds. On heating, the colour of all complexes changed from red to paler red, indicating a higher proportion of HS Fe(II) in the complex, proposed to arise from the dissociation of $[Fe_2(R)_4(bpy)(H_2O)_2]$ to

$[Fe(R)_2(bpy)]$ and $[Fe(R)_2(H_2O)_2]$. The complexes were thermally stable in the temperature range of 121 ^oC to 156 ^oC, and their decomposition temperatures decreased with increasing number of carbon atoms in the alkyl chain, as similarly observed for Cu(II) complexes and may be similarly explained. Only **7** behaved as a thermotropic metallomesogen due to its more symmetrical structure.

4.3 $[Cu_2(p\text{-}ROC_6H_4COO)_4(bpy)_2]$

The general steps for the syntheses of $[Cu_2(p\text{-}CH_3(CH_2)_nOC_6H_4COO)_4(bpy)_2]$, where *n* = 9 (**10**), 11 (**11**), 13 (**12**), and 15 (**13**), are shown in **Scheme 4.4.**

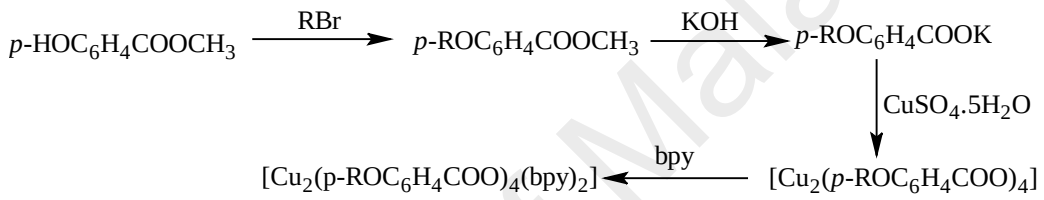

Scheme 4.4 Synthetic steps for $[Cu_2(p\text{-}ROC_6H_4COO)_4(bpy)_2]$, where R = $CH_3(CH_2)_n$

4.3.1 $[Cu_2(p\text{-}CH_3(CH_2)_9OC_6H_4COO)_4(bpy)_2]$ (10)

(a) Synthesis and structural elucidation

The first step in the synthesis of $[Cu_2(p\text{-}CH_3(CH_2)_9OC_6H_4COO)_4(bpy)_2]$ (**10**) (**Scheme 4.3**) involved the synthesis of $p\text{-}CH_3(CH_2)_9OC_6H_4COOCH_3$ from the reaction of $p\text{-}HO\text{-}C_6H_4COOCH_3$ and $BrCH_2(CH_2)_8CH_3$. The ester was obtained as a white powder in good yield (63 %). Its **elemental analytical** results (C, 73.7%; H, 10.3%) were in good agreement with the calculated values (C, 73.9%; H, 9.7%; FW = 292.4 g mol^{-1}). Its chemical formula was further ascertained by **^{1}H-NMR spectroscopy**. The spectrum is shown in **Figure 4.76** and the peak assignments are shown in **Table 4.9**.

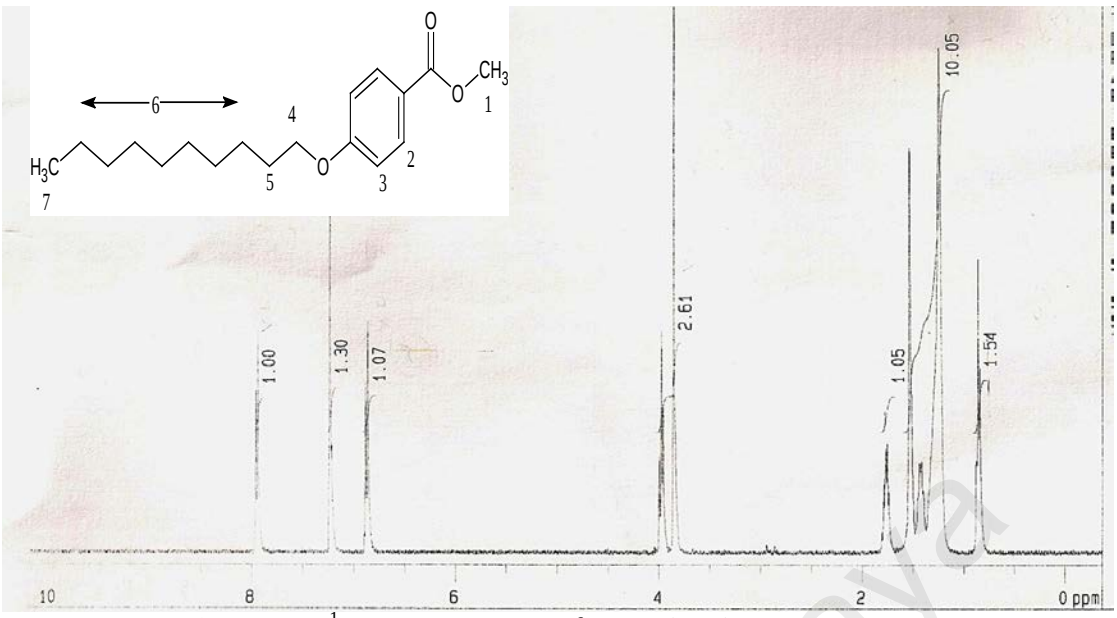

Figure 4.76 ^{1}H-NMR spectrum of *p*-$CH_3(CH_2)_9OC_6H_4COOCH_3$

Table 4.9 ^{1}H-NMR spectral data for *p*-$CH_3(CH_2)_9OC_6H_4COOCH_3$

Chemical shift (ppm)	Ratio	Multiplicity	Assignments
0.84	1.5	triplet	H-7
1.40	10.1	multiplet	H-1, H-6
3.90	2.6	multiplet	H-4, H-5
6.85	1.0	doublet	H-2
7.94	1.0	doublet	H-3

Its **FTIR** spectrum shown in **Figure 4.77**, and the peak assignments are given in **Table 4.10** (which also include the data for later discussion). It shows two strong peaks for CH_2 at 2921 cm^{-1} and 2854 cm^{-1}, a peak for aromatic C=C at 1607 cm^{-1}, and two strong peaks for C=O at 1722 cm^{-1} and C-O at 1255 cm^{-1}.

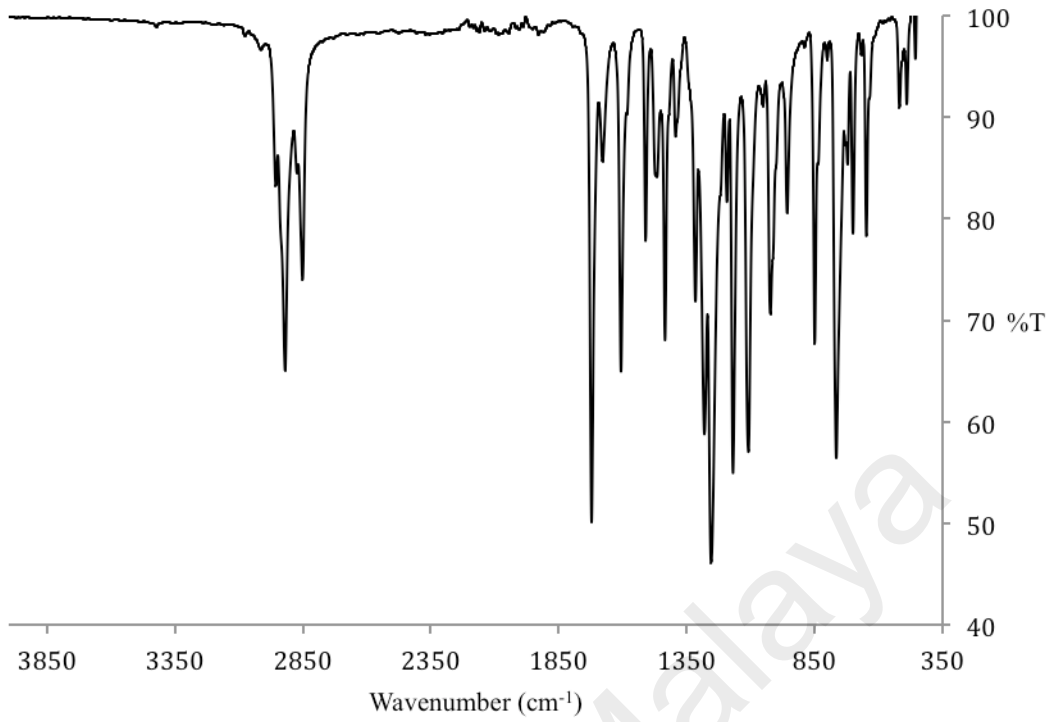

Figure 4.77 FTIR spectrum of *p*-$CH_3(CH_2)_9OC_6H_4COOCH_3$

Table 4.10 FTIR data in (cm^{-1}) and assignments (R = p-$CH_3(CH_2)_nOC_6H_4$)

Compound	CH_2 (asym)	CH_2 (sym)	C=O	C-O	COO (asym)	COO (sym)	C=C (aro)	C-N
$RCOOCH_3$ (n = 9)	2921	2854	1722	1255	-	-	1607	-
$RCOOCH_2CH_3$ (n = 11)	2915	2851	1708	1280	-	-	1608	-
$RCOOCH_2CH_3$(n = 13)	2915	2851	1708	1284	-	-	1609	-
$RCOOCH_3$(n = 15)	2914	2850	1278	1287	-	-	1609	-
RCOOK (n = 9)	2921	2853	-	-	1543	1391	1598	-
RCOOK (n = 11)	2920	2851	-	-	1543	1393	1600	-
RCOOK (n = 13)	2921	2852	-	-	1543	1394	1600	-
RCOOK (n = 15)	2919	2851	-	-	1543	1395	1601	-
$[Cu_2(RCOO)_4(H_2O)_2].2H_2O$ (n = 9)	2921	2853	-	-	1594	1428	1607	-
$[Cu_2(RCOO)_4(H_2O)_2].2H_2O$ (n = 11)	2918	2851	-	-	1608	1431	1609	-
$[Cu_2(RCOO)_4(H_2O)_2].2H_2O$ (n = 13)	2917	2851	-	-	1609	1435	1610	-
$[Cu_2(RCOO)_4(H_2O)_2]$ (n = 15)	2918	2850	-	-	1604	1436	1610	-
$[Cu_2(RCOO)_4(bpy)_2].2H_2O$ (n = 9; complex **10)**	2924	2855	-	-	1590	1384 1373	1601	1304
$[Cu_2(RCOO)_4(bpy)_2]$ (n = 11; complex **11**)	2919	2853	-	-	1593	1417/ 1364	1607	1308
$[Cu_2(RCOO)_4(bpy)_2]$ (n = 13; complex **12**)	2918	2852	-	-	1594	1418/ 1364	1606	1308
$[Cu_2(RCOO)_4(bpy)_2]$ (n = 15; complex **13**)	2917	2851	-	-	1594	1435/ 1370	1609	1310

The second step involved alkaline hydrolysis of p-$CH_3(CH_2)_9OC_6H_4COOCH_3$ using KOH. The product was a white powder and its yield was 35%. The results of the **elemental analyses** (C, 64.3%; H, 7.5%) were in good agreement with those calculated for the salt (C, 64.5%; H, 8.0%; FW 316.5 g mol^{-1}). Its **FTIR** data (**Table 4.10**; **Figure 4.78**) show the presence of the expected functional groups. Hence, the $\Delta\nu_{coo}$ value for p-$CH_3(CH_2)_9OC_6H_4COO^-$ ion was 152 cm^{-1}.

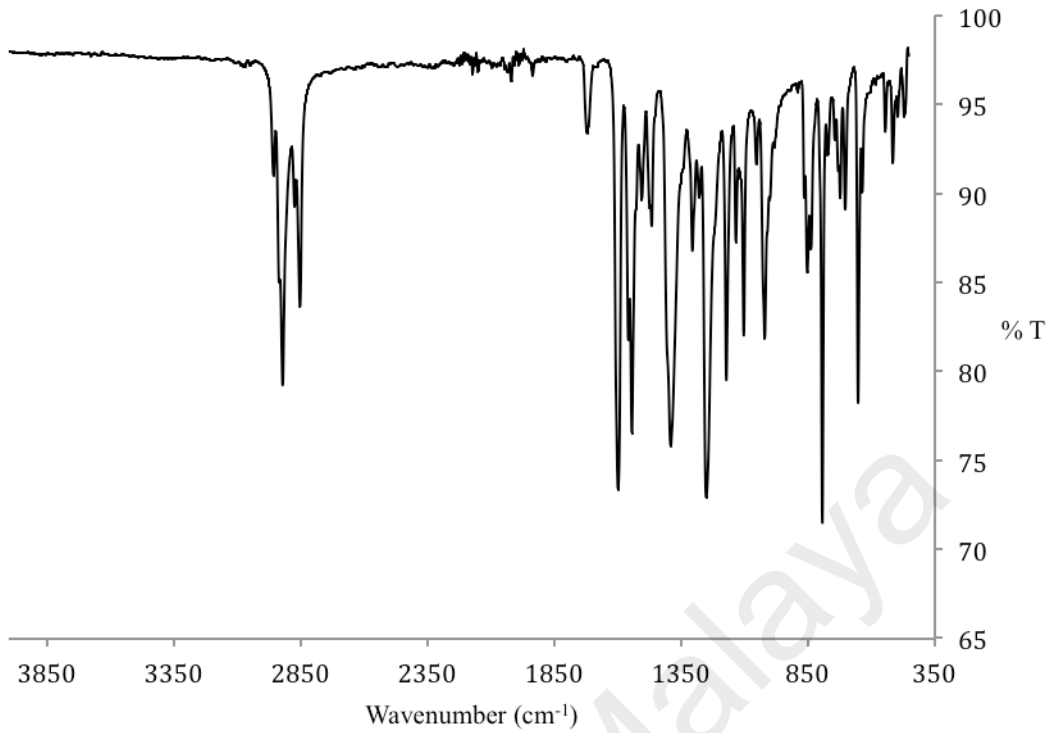

Figure 4.78 FTIR spectrum of *p*-$CH_3(CH_2)_9OC_6H_4COOK$

The third step involved reacting *p*-$CH_3(CH_2)_9OC_6H_4COOK$ with $CuSO_4.5H_2O$ to form the precursor complex, [Cu_2(*p*-$CH_3(CH_2)_9OC_6H_4COO)_4(H_2O)_2$] (yield = 44%). The results of the **elemental analyses** (C, 64.3%; H, 8.8%) were in good agreement with the calculated values (C, 64.2%; H, 8.2%); FW 1272.6 g mol^{-1}). Its **FTIR** data (**Table 4.10**; **Figure 4.79**) show the presence of the expected functional groups. Hence, the $\Delta\nu_{coo}$ value for *p*-$CH_3(CH_2)_9OC_6H_4COO^-$ ion was 166 cm^{-1}, which was higher than the value for *p*-$CH_3(CH_2)_9OC_6H_4COOK$ (152 cm^{-1}), indicating that *p*-$CH_3(CH_2)_9OC_6H_4COO^-$ ion was coordinated to the Cu(II) centre as a bidentate bridging ligand.

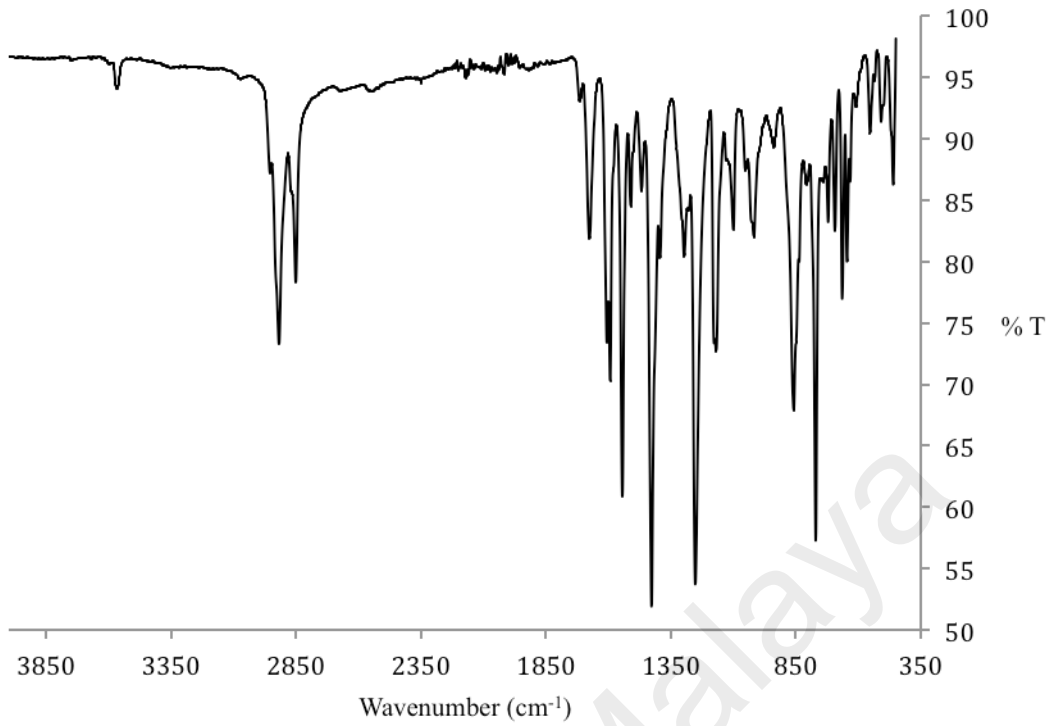

Figure 4.79 FTIR spectrum of $[Cu_2(p\text{-}CH_3(CH_2)_9OC_6H_4COO)_4(H_2O)_2]$

Its **UV-vis** spectrum (**Figure 4.80**) in C_2H_5OH and CH_3COOH (9:1 v/v; molarity = 3.07 x 10^{-3} mol L^{-1}) shows two *d-d* band at 703 nm (ε_{max} = 222 M^{-1} cm^{-1}) and at 361 nm (ε_{max} = 64 M^{-1} cm^{-1}). The data suggest a square pyramidal geometry for both Cu(II) atoms in the dinuclear complex.

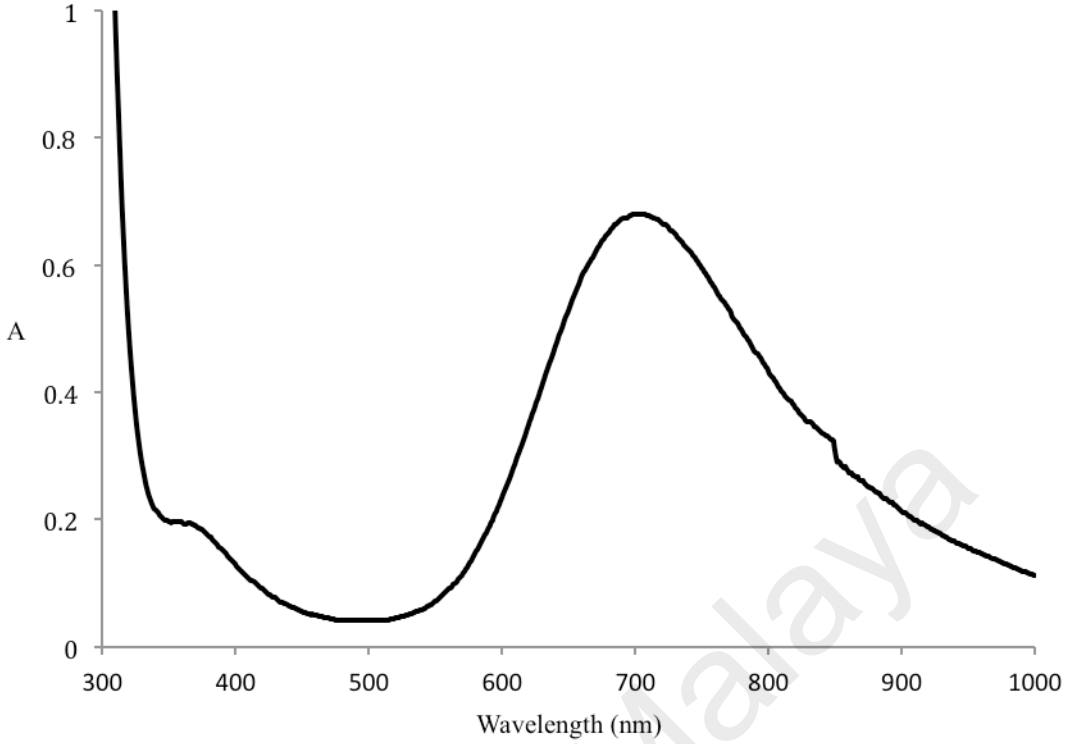

Figure 4.80 UV-vis spectrum of $[Cu_2(p\text{-}CH_3(CH_2)_9OC_6H_4COO)_4(H_2O)_2]$

Its μ_{eff} value, calculated as previously done using its formula weight (1272.6 g mol^{-1}) and the values of mass susceptibility (χ_g; 6.50 x 10^{-7} cm^3 g^{-1}), molar susceptibility (χ_m; 8.27 x 10^{-4} cm^3 mol^{-1}), diamagnetic correction factor (χ_D; -6.36 x 10^{-4} cm^3 mol^{-1}) and corrected molar susceptibility (χ_m^{corr}; 1.46 x 10^{-3} cm^3 mol^{-1}), was 1.87 BM at 298 K. It is noted that value was lower than $[Cu_2(CH_3(CH_2)_8COO)_4(H_2O)_2]$ (2.2 BM), indicating a stronger antiferromagnetic interaction, probably due to less structural distortion and/or the stronger Cu-O bond of the former complex.

$[Cu_2(p\text{-}CH_3(CH_2)_9OC_6H_4COO)_4(H_2O)_2]$ reacted with bpy to form a blue powder (yield = 65%). The results of the **elemental analyses** (C, 66.7%; H, 7.8%; N, 3.3%) were in good agreement with those calculated for $[Cu_2(p\text{-}CH_3(CH_2)_9OC_6H_4COO)_4(bpy)_2].2H_2O$ (**10**) (C, 66.7%; H, 7.6%; N, 3.5%; FW 1584.9 g mol^{-1}).

Its **FTIR** data (**Table 4.10**; **Figure 4.81**) shows the presence of the expected functional groups. Hence, the $\Delta\nu_{coo}$ values were 206 cm^{-1} and 217 cm^{-1}, in agreement

with monodentate nonbridging and *syn-anti* monodentate bridging *p*-$CH_3(CH_2)_9OC_6H_4COO^-$ ligands.

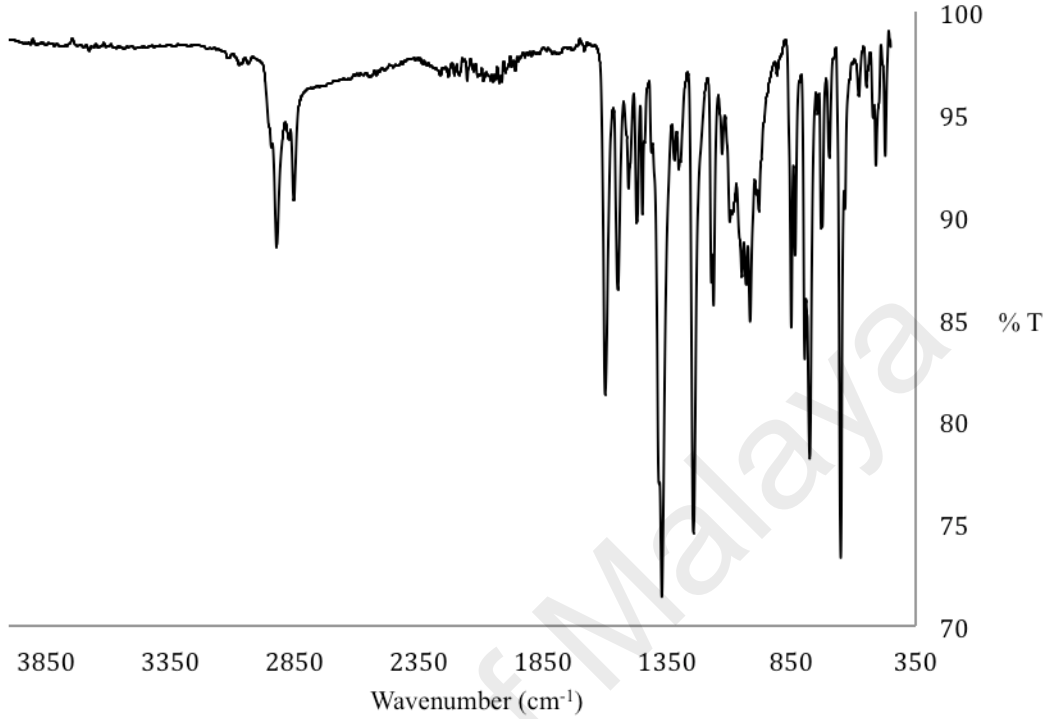

Figure 4.81 FTIR spectrum of **10**

Its **UV-vis** spectrum (**Figure 4.82**) in C_2H_5OH and CH_3COOH (9:1 v/v; molarity = 8.5 x 10^{-4} mol L^{-1}) shows a weak *d-d* band at 679 nm (ε_{max} = 136 M^{-1} cm^{-1}), suggesting a square pyramidal geometry. These data were similar to [Cu_2(*p*-$CH_3(CH_2)_9OC_6H_4COO)_4(H_2O)_2$] and may be similarly explained.

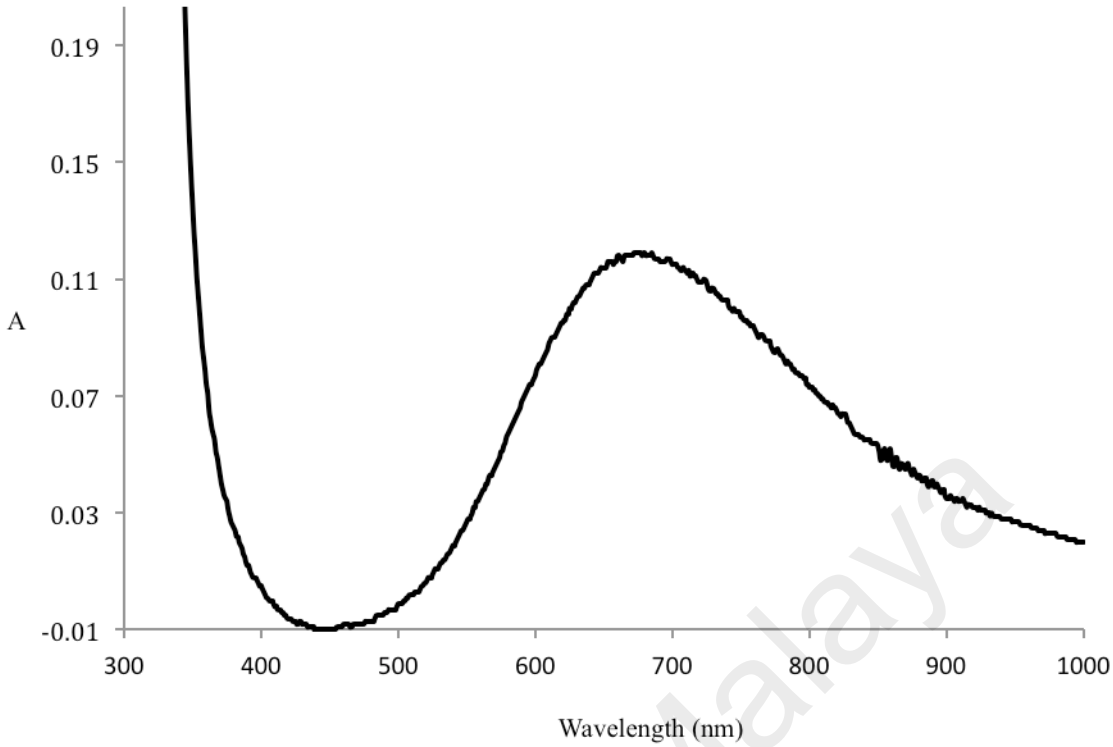

Figure 4.82 UV-vis spectrum of **10**

Its μ_{eff} value, calculated as before from its formula weight (1548.9 g mol^{-1}) and the values of mass susceptibility (χ_g; 1.80 x 10^{-6} cm^3 g^{-1}), molar susceptibility (χ_m; 2.79 x 10^{-3} cm^3 mol^{-1}), diamagnetic correction factor (χ_D; -7.74 x 10^{-4} cm^3 mol^{-1}) and corrected molar susceptibility (χ_m^{corr}; 3.56 x 10^{-3} cm^3 mol^{-1}), was 2.92 BM at 298 K. The value was higher than its precursor; $[Cu_2(p\text{-}CH_3(CH_2)_9OC_6H_4COO)_4(H_2O)_2]$ (1.87 BM) and the expected value for a dinuclear Cu(II) complex (S = ½; g = 2; 2.45 BM [22]. This suggest ferromagnetic interactions between the two Cu(II) centres.

(b) Thermal and mesomorphic studies

TG trace for **10** (**Figure 4.83**) shows an initial weight loss of 2.0% at 79 ^oC due evaporation of lattice H_2O (calculated, 2.3%), followed by a major weight loss of 86.2% in the temperature range 240 ^oC to 568 ^oC due to the decomposition of $p\text{-}CH_3(CH_2)_9OC_6H_4COO^-$ and bpy ligands (calculated, 91.8%). The results are in good agreement with its proposed structural formula. The amount of residue at temperatures

above 568 ^{o}C was 11.8% (calculated, 10.0% assuming CuO). Hence, its decomposition temperature was 240 ^{o}C, which was significantly higher compared to $[Cu_2(CH_3(CH_2)_8COO)_4(bpy)_2]$ (**2**) (T_{dec} = 177 ^{o}C). This is as expected since the R-COO bond is stronger in arylcarboxylates than alkylcarboxylates.

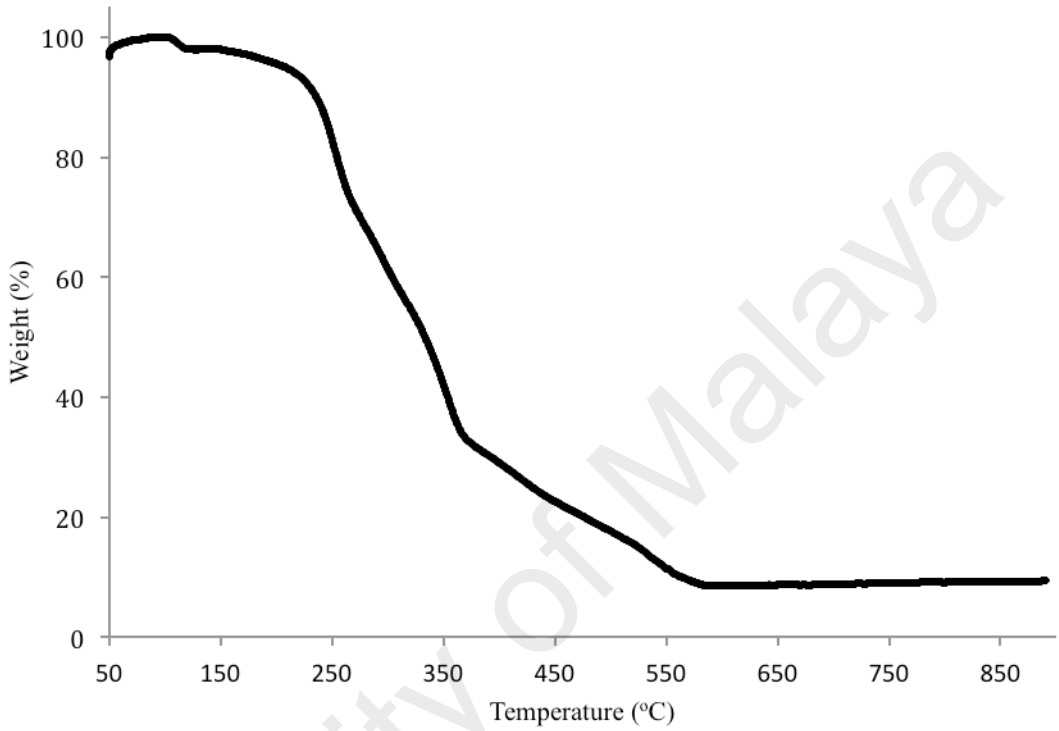

Figure 4.83 TGA trace of **10**

When viewed under **POM**, **10** started to melt at 107 ^{o}C and to clear at about 150 ^{o}C. On cooling from *I*, an optical texture was observed at 121 ^{o}C (**Figure 4.84**(**a**)), which was typical of columnar liquid crystals. In comparison, its precursor complex, $[Cu_2(p\text{-}CH_3(CH_2)_9OC_6H_4COO)_4(H_2O)_2]$, was observed to melt at 130 ^{o}C and clear to an isotropic liquid at 160 ^{o}C. Upon cooling from this temperature, an optical optical texture that was different from **10** was observed at 142 ^{o}C (**Figure 4.84**(**b**)). These observations indicate that both **10** and its precursor complex behaved as different thermotropic metallomesogens.

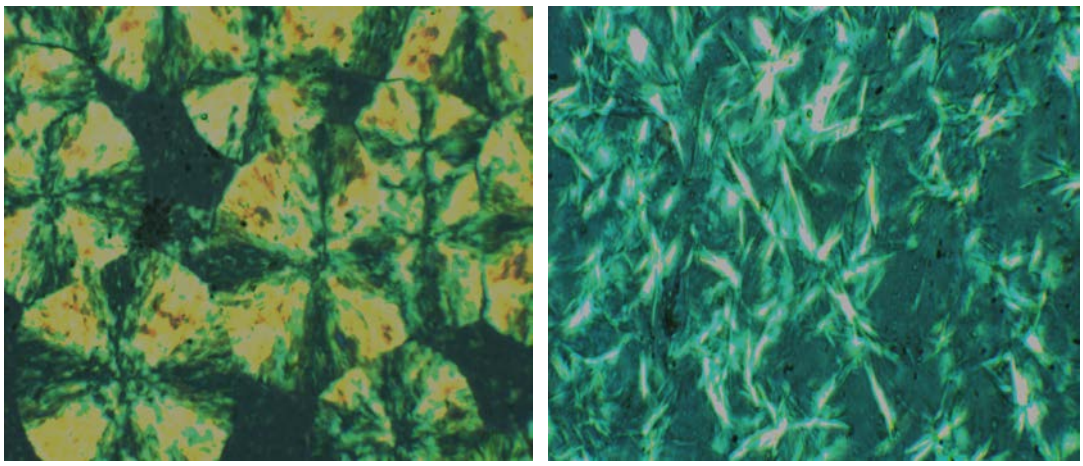

Figure 4.84 Photomicrographs of: (a) **10** on cooling at 121 ^{o}C; and (b) $[Cu_2(p\text{-}CH_3(CH_2)_9OC_6H_4COO)_4(H_2O)_2]$ on cooling at 142 ^{o}C

The **DSC** traces for **10** (**Figure 4.85**) shows a sharp endothermic peaks at 118 ^{o}C (ΔH = +81 kJ mol^{-1}) assigned to *Cr2-M* transition, and two overlapping endothermic peaks at 144 ^{o}C ($\Delta H_{combined}$ = +115 kJ mol^{-1}) assigned to *M-I* transition. On cooling, an exothermic peak at 121 ^{o}C (ΔH = -81 kJ mol^{-1}) and two overlapping endothermic peaks at 92 ^{o}C ($\Delta H_{combined}$ = 27 kJ mol^{-1}) assigned to *I-M* and *M-Cr2* transitions, respectively.

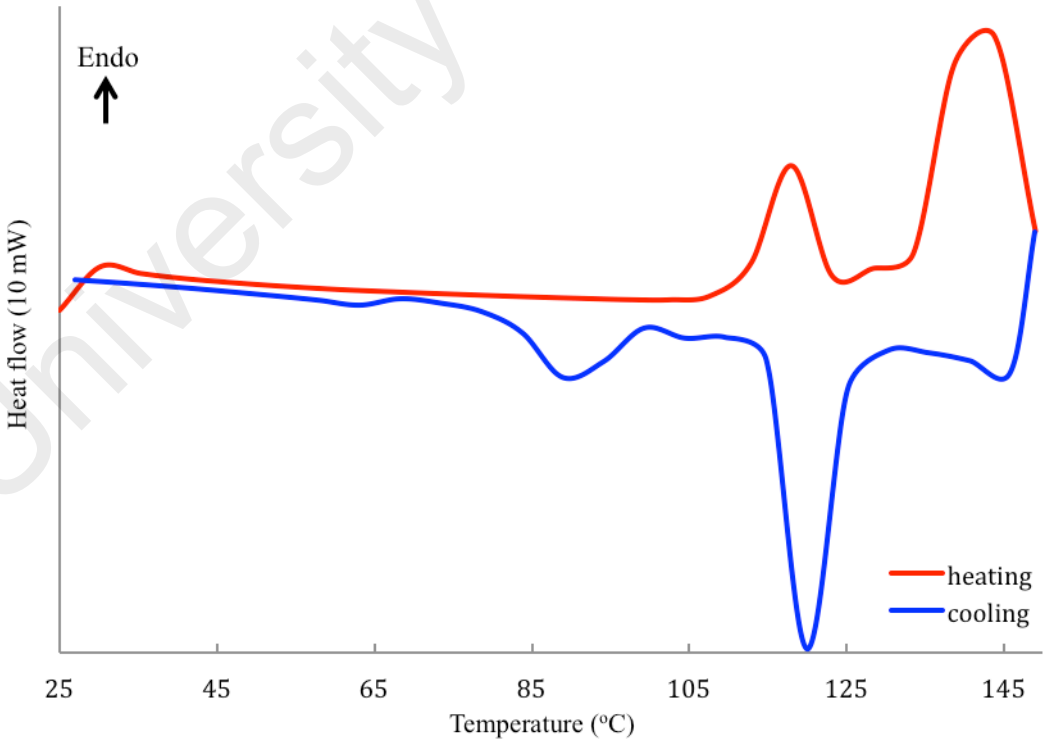

Figure 4.85 DSC scans of **10**

4.3.2 [$Cu_2(p\text{-}CH_3(CH_2)_{11}OC_6H_4COO)_4(bpy)_2$] (11)

(a) Synthesis and structural elucidation

The first step in the synthesis of [$Cu_2(p\text{-}CH_3(CH_2)_{11}OC_6H_4COO)_4(bpy)_2$] (**11**) (**Scheme 4.3**) involved the synthesis of $p\text{-}CH_3(CH_2)_{11}OC_6H_4COOCH_2CH_3$ from the reaction of $p\text{-}HOC_6H_4COOCH_2CH_3$ and $BrCH_2(CH_2)_{10}CH_3$. The ester was obtained as a white powder in good yield (52%). Its **elemental analysis** results (C, 75.6%; H, 11.3%) were in good agreement with the calculated values, (C, 75.1%; H, 10.5%; FW = 355.5 g mol^{-1}). Its chemical formula was further ascertained by **^{1}H-NMR spectroscopy**. The spectrum is shown in **Figure 4.86** and the peak assignments are shown in **Table 4.11**.

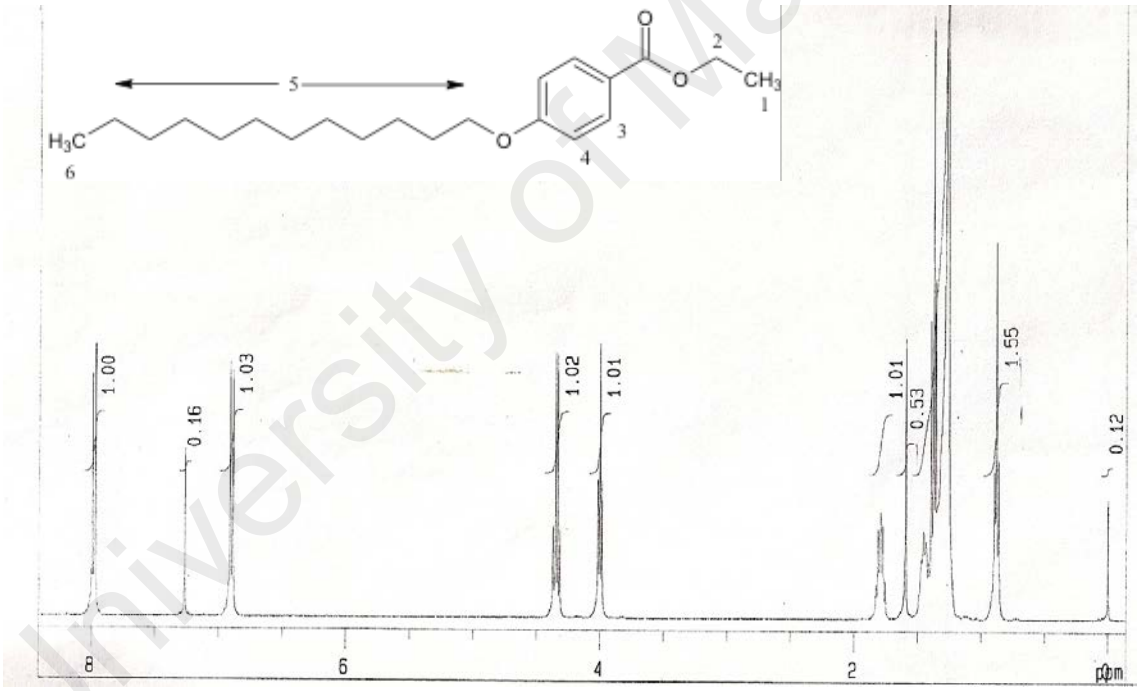

Figure 4.86 ^{1}H-NMR spectrum of $p\text{-}CH_3(CH_2)_{11}OC_6H_4COOCH_2CH_3$

Table 4.11 ^{1}H-NMR spectral data for *p*-$CH_3(CH_2)_{11}OC_6H_4COOCH_2CH_3$

Chemical shift (ppm)	Ratio	Multiplicity	Assignments
0.60	1.5	triplet	H-6
1.2-1.5	10.9	multiplet	H-5
4.00	1.01	triplet	H-1
4.34	1.02	quartet	H-2
6.85	1.0	doublet	H-3
7.98	1.0	doublet	H-4

The ester formed colourless crystals on recrystallisation from chloroform. The single crystal **X-ray crystallographic** data and structure refinement for the crystal are shown in **Table 4.12**, selected bond lengths and angles are shown in **Table 4.13**, and ORTEP presentations and packing patterns are shown in **Figure 4.87**.

Table 4.12 Crystallographic data nd refinement details for *p*-$CH_3(CH_2)_{11}OC_6H_4COOCH_2CH_3$

Empirical formula	$C_{21}H_{34}O_3$	
Formula weight	334.48	
Temperature (K)	296(2)	
Crystal system	Monoclinic	
Space group	P_{21}/C	
Unit cell dimension	a = 23.008(5) Å	α = 90°
	b = 14.532(3) Å	β = 94.409(3)°
	c = 5.8960(12) Å	γ = 90°
V (Å^3)	1965.5(7)	
Z	4	
ρ (calcd) (g cm^{-3})	1.130	
μ (mm^{-1})	0.073	
F(000)	736	
θ range (°)	0.89 – 28.31	
Index ranges	$-30 \leq h \leq 30$; $-19 \leq k \leq 19$; $-7 \leq l \leq 7$	
Reflections collected	25919	
Independent reflections, R_{int}	4849, 0.05251	
Completeness to θ	99.3 %	
Data / restraints / parameters	4849 / 0 / 219	
Goodness-of-fit on F^2	1.177	
Final R indices [I > 2σ(I)]	R_1 = 0.0716; wR_2 = 0.2080	
R indices (all data)	R_1 = 0.0890; wR_2 = 0.2222	
$\Delta\rho_{max}$, $\Delta\rho_{min}$ (e Å^{-3})	0.410, -0.304	

Table 4.13 Selected bond lengths (Å) and angles (°) for *p*-$CH_3(CH_2)_{11}OC_6H_4COOCH_2CH_3$

Bond length		Angle	
C(13)-O(1)	1.367(3)	O-C-O	123.8(2)
C(17)-O(2)	1.338(3)	O-C-C	106.52(19)
C(17)-O(3)	1.212(3)	C-O-C	116.0(2)
C(1)-C(2)	1.531(4)	O-C-H	110.4
C(1)-H(23)	0.9600		

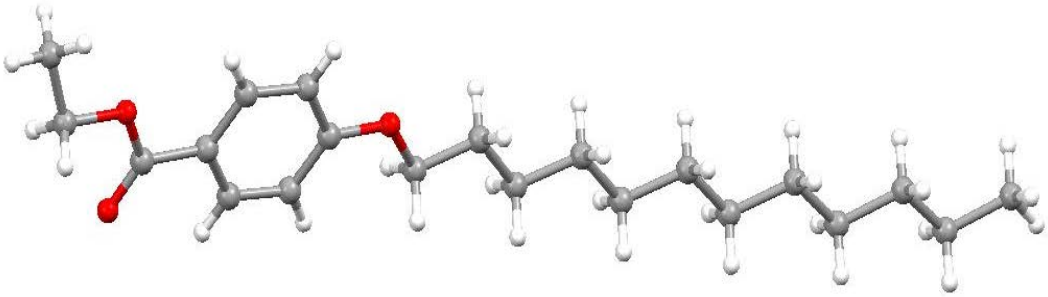

(a)

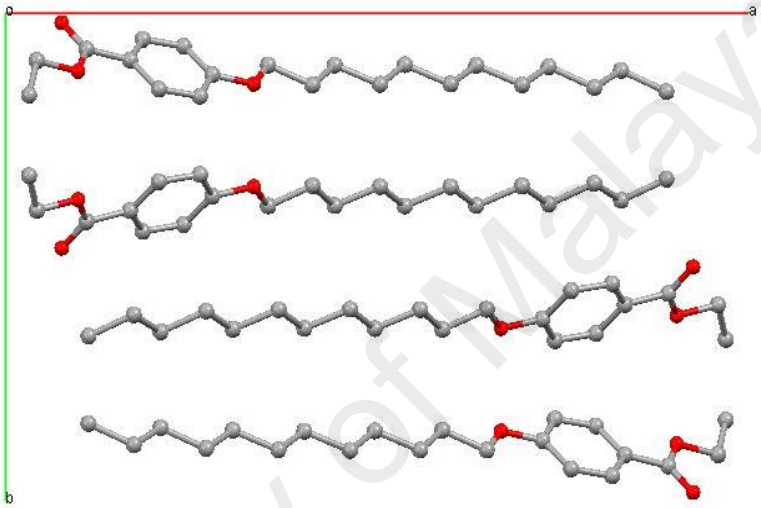

(b)

Figure 4.87 (a) Molecular structure, and (b) packing diagram for *p*-$CH_3(CH_2)_{11}OC_6H_4COOCH_2CH_3$ viewed along crystallographic *c*-axis.

Its **FTIR** data (**Table 4.10**; **Figure 4.88**) shows the presence of the expected functional groups.

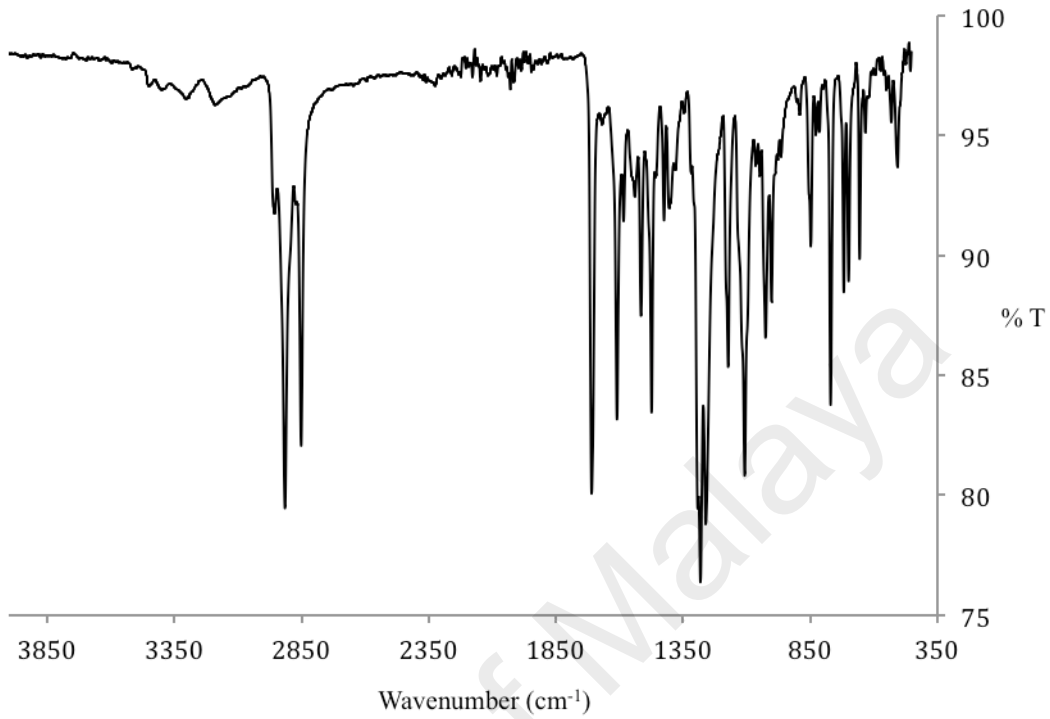

Figure 4.88 FTIR spectrum of p-$CH_3(CH_2)_{11}OC_6H_4COOCH_2CH_3$

The second step involved alkaline hydrolysis of p-$CH_3(CH_2)_{11}OC_6H_4COOCH_2CH_3$ using KOH. The product was a white powder and its yield was 49%. The results of the **elemental analyses** (C, 65.3%; H, 9.0%) were in good agreement with the calculated values for p-$CH_3(CH_2)_{11}OC_6H_4COOK$ (C, 66.2%; H, 8.5%; FW 344.5 g mol^{-1}). Its **FTIR** data (**Table 4.10**; **Figure 4.89**) show the presence of the expected functional groups. Hence, the $\Delta\nu_{coo}$ value for p-$CH_3(CH_2)_{11}OC_6H_4COO^-$ ion was 150 cm^{-1}.

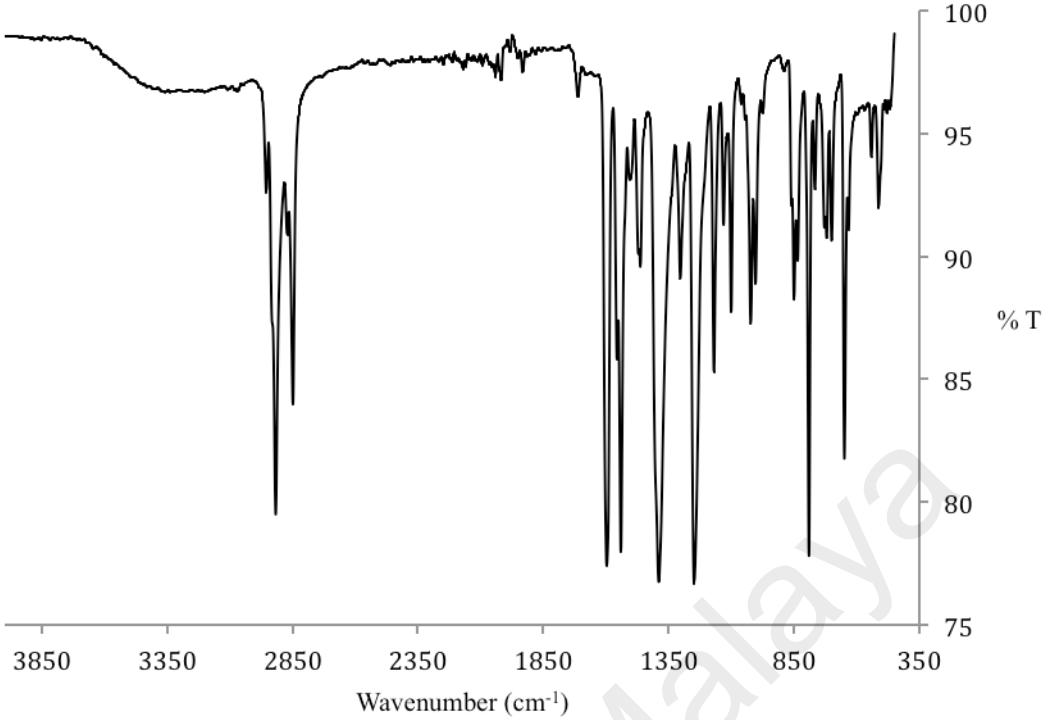

Figure 4.89 FTIR spectrum of p-$CH_3(CH_2)_{11}OC_6H_4COOK$

The third step involved reacting p-$CH_3(CH_2)_{11}OC_6H_4COOK$ with $CuSO_4.5H_2O$ to form the precursor complex, $[Cu_2(p\text{-}CH_3(CH_2)_{11}OC_6H_4COO)_4(H_2O)_2].2H_2O$ (yield = 25%). The results of the **elemental analyses** (C, 64.6%; H, 8.7%) were in good agreement with those calculated (C, 64.2%; H, 8.8%); FW 1420.9 g mol^{-1}). Its **FTIR** data (**Table 4.10**; **Figure 4.90**) show the presence of the expected functional groups. Hence, the $\Delta\nu_{coo}$ value was 177 cm^{-1}, which was higher than the value for p-$CH_3(CH_2)_{11}OC_6H_4COOK$ (150 cm^{-1}), indicating that p-$CH_3(CH_2)_{11}OC_6H_4COO^-$ ion was coordinated as a bridging bidentate ligand.

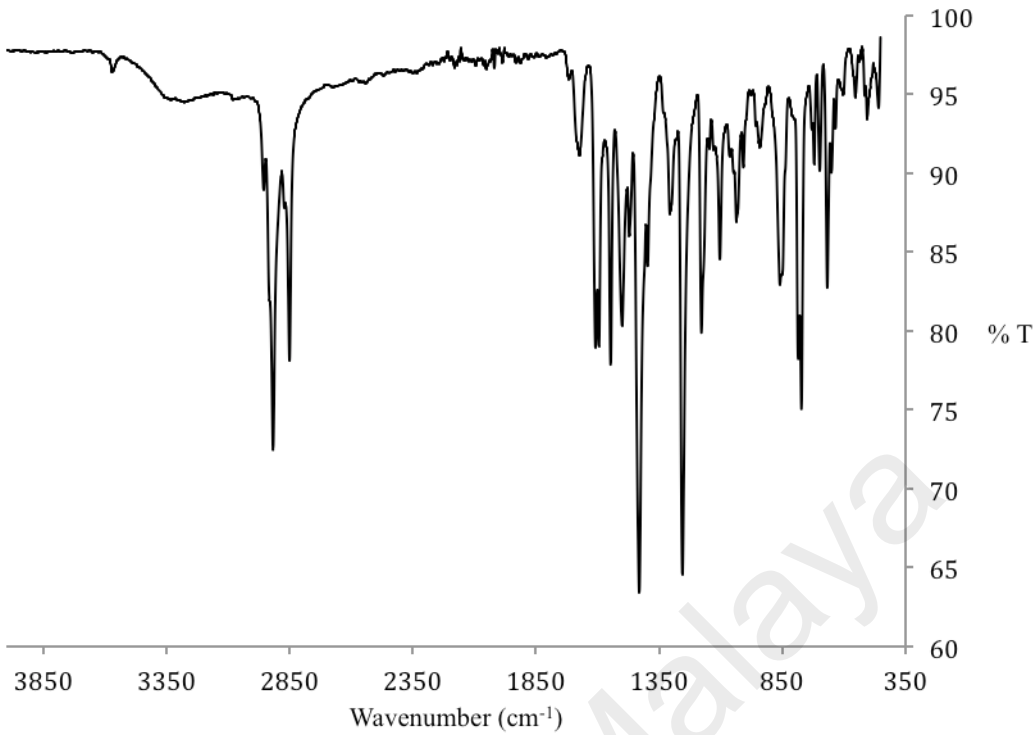

Figure 4.90 FTIR spectrum of $[Cu_2(p\text{-}CH_3(CH_2)_{11}OC_6H_4COO)_4(H_2O)_2].2H_2O$

Its **UV-vis** spectrum (**Figure 4.91**) in C_2H_5OH and CH_3COOH (9:1 v/v; molarity = 2.37 x 10^{-3} mol L^{-1}) shows two weak *d-d* bands at 703 nm (ε_{max} = 330 M^{-1} cm^{-1}) and at 356 nm (ε_{max} = 165 M^{-1} cm^{-1}), suggesting a square pyramidal geometry at both Cu(II) centres. These data were similar to the previous discussed complexes and may be similarly explained.

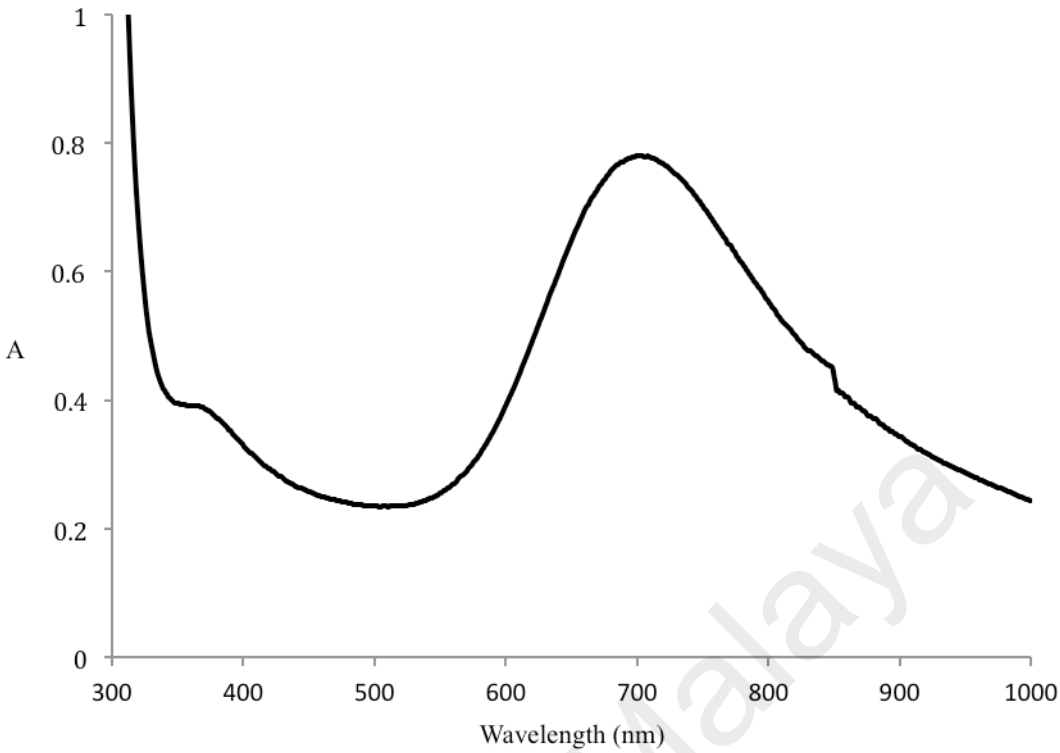

Figure 4.91 UV-vis spectrum of $[Cu_2(p\text{-}CH_3(CH_2)_{11}OC_6H_4COO)_4(H_2O)_2].2H_2O$

Its μ_{eff} value, calculated as previously done using its formula weight (1420.9 g mol^{-1}) and the values of mass susceptibility (χ_g; 2.49 x 10^{-7} cm^3 g^{-1}), molar susceptibility (χ_m; 3.54 x 10^{-4} cm^3 mol^{-1}), diamagnetic correction factor (χ_D; -7.10 x 10^{-4} cm^3 mol^{-1}) and corrected molar susceptibility (χ_m^{corr}; 1.06 x 10^{-3} cm^3 mol^{-1}), was 1.59 BM at 298 K. The value was lower than the shorter alkyloxy chain analog, $[Cu_2(p\text{-}CH_3(CH_2)_9OC_6H_4COO)_4(H_2O)_2]$ (1.87 BM), indicating a strong antiferromagnetic interaction in the former.

$[Cu_2(p\text{-}CH_3(CH_2)_{11}OC_6H_4COO)_4(H_2O)_2].2H_2O$ reacted with bpy to form a blue powder (80%). The results of the **elemental analysis** (C, 68.0%; H, 8.1%; N, 3.3%) were in good agreement with the calculated values for $[Cu_2(p\text{-}CH_3(CH_2)_{11}OC_6H_4COO)_4(bpy)_2]$ (**11**) (C, 69.0%; H, 8.0%; N, 3.4%; FW 1661.1 g mol^{-1}).

Its **FTIR** data (**Table 4.10**; **Figure 4.92**) show the presence of the expected functional groups. Hence, the $\Delta\nu_{coo}$ values were 176 cm^{-1} and 229 cm^{-1}, in agreement

with monodentate nonbridging and *syn-anti* monodentate bridging *p*-$CH_3(CH_2)_{11}OC_6H_4COO^-$ ligands.

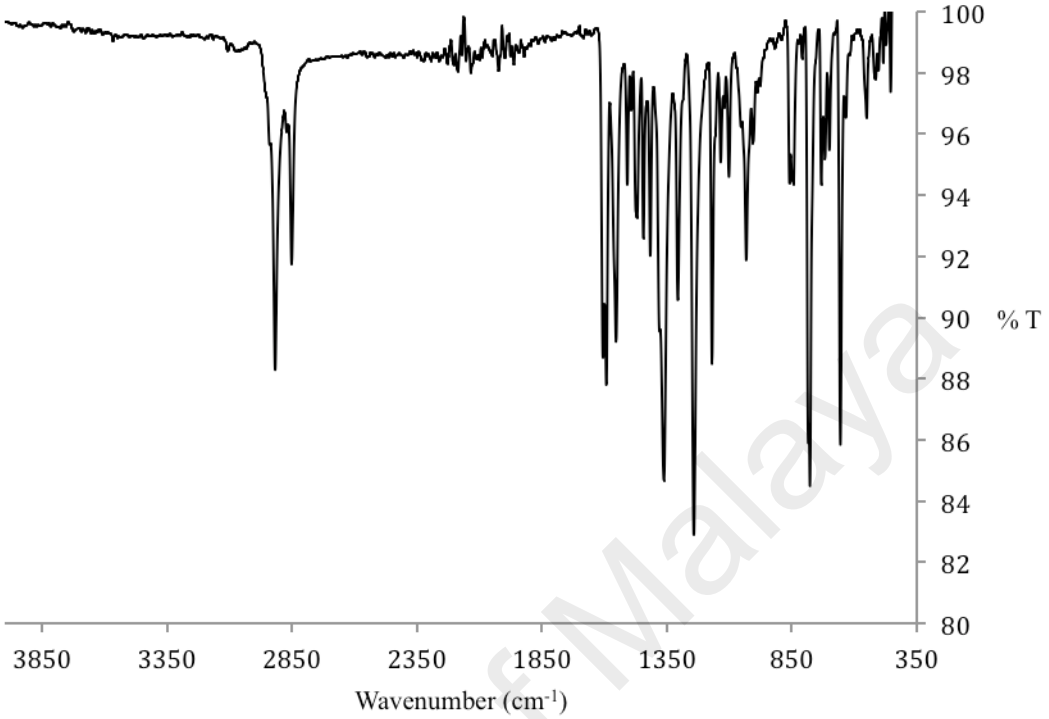

Figure 4.92 FTIR spectrum of **11**

Its **UV-vis** spectrum (**Figure 4.93**) in C_2H_5OH and CH_3COOH (9:1 v/v; molarity = 1.69 x 10^{-3} mol L^{-1}) shows a weak *d-d* band at 675 nm (ε_{max} = 117 M^{-1} cm^{-1}), suggesting a square pyramidal geometry at both Cu(II) centres. These data were similar to the previous discussed complexes.

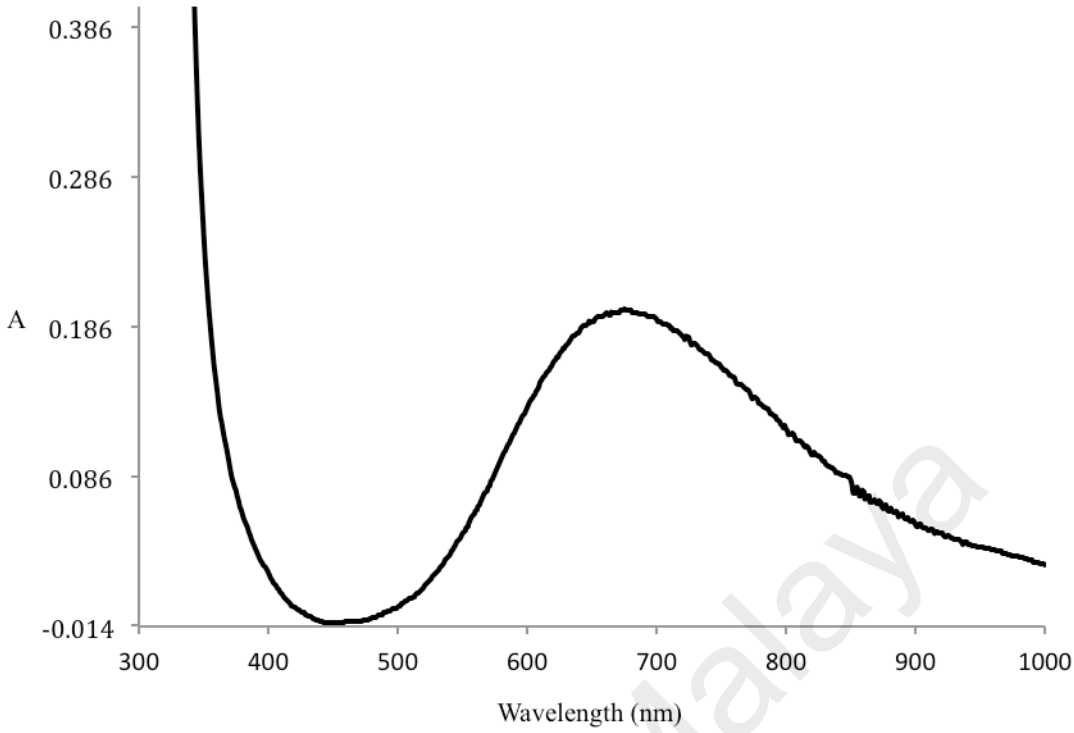

Figure 4.93 UV-vis spectrum of **11**

Its μ_{eff} value, calculated as previously done using its formula weight (1661.1 g mol^{-1}) and the values of mass susceptibility (χ_g; 1.10 x 10^{-6} cm^3 g^{-1}), molar susceptibility (χ_m; 1.83 x 10^{-3} cm^3 mol^{-1}), diamagnetic correction factor (χ_D; -8.31 x 10^{-4} cm^3 mol^{-1}) and corrected molar susceptibility (χ_m^{corr}; 2.66 x 10^{-3} cm^3 mol^{-1}), was 2.52 BM at 298 K.

(b) Thermal and mesomorphic studies

TG trace for **11** (**Figure 4.94**) shows a total weight loss of 89.7% in the temperature range 215 ^oC to 660 ^oC due to decomposition of *p*-$CH_3(CH_2)_{11}OC_6H_4COO^-$ and bpy ligands (calculated, 92.3%). The results are in good agreement with its proposed structural formula. The amount of residue at temperatures above 660 ^oC was 10.3% (calculated, 9.6% assuming CuO). Hence, its decomposition temperature was 215 ^oC.

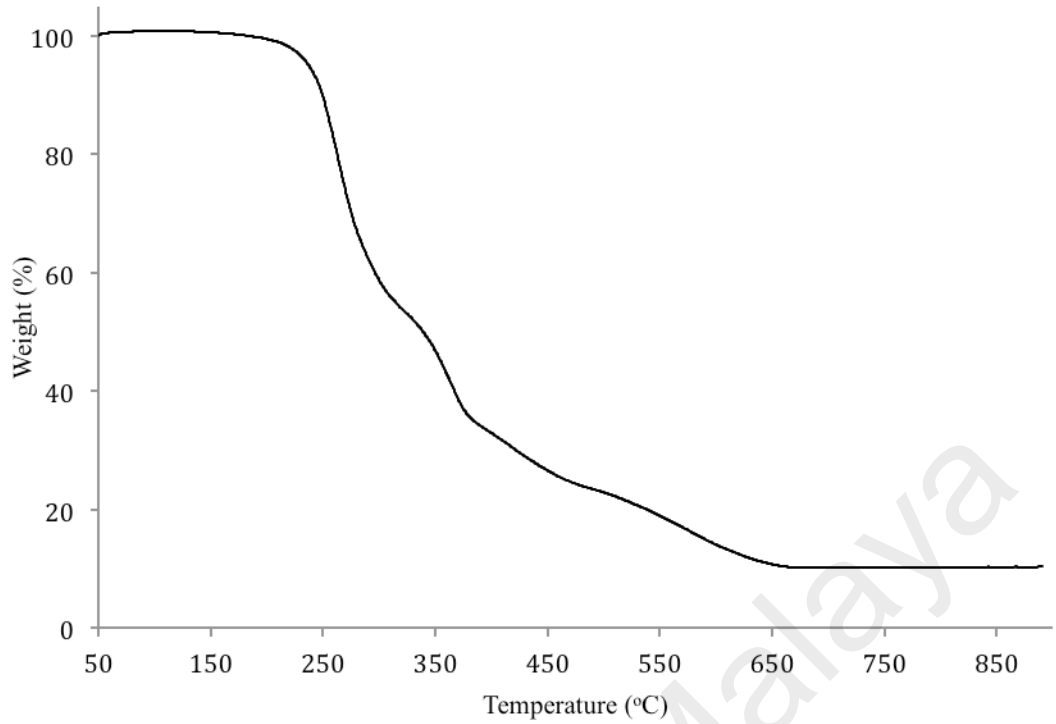

Figure 4.94 TGA trace of **11**

When viewed under **POM**, **11** started to melt at 137 °C and to clear at about 160 °C. On cooling from *I*, optical textures were observed at 145 °C (**Figure 4.95**(**a**)), which was typical of columnar liquid crystals. In comparison, its precursor, $[Cu_2(p\text{-}CH_3(CH_2)_{11}OC_6H_4COO)_4(H_2O)_2].2H_2O$, was observed to melt at 112 °C and clear to an isotropic liquid at 160 °C. Upon cooling from this temperature, optical textures which were different from **11** were observed at 89 °C (**Figure 4.95**(**b**)). These observations indicate that this complex and its precursor behaved as different thermotropic metallomesogens.

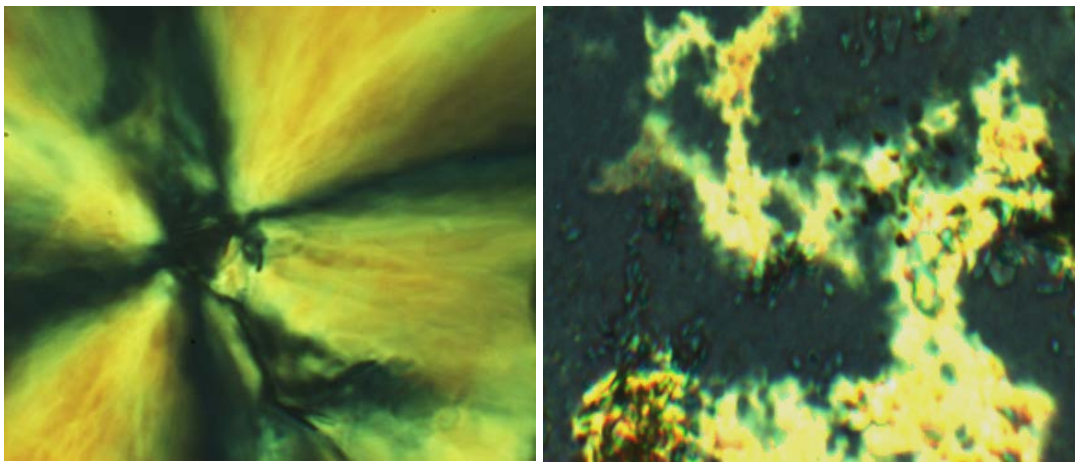

Figure 4.95 Photomicrographs of: (a) **11** on cooling at 145 ^{o}C; and (b) $[Cu_2(p\text{-}CH_3(CH_2)_{11}OC_6H_4COO)_4(H_2O)_2].2H_2O$ on cooling at 89 ^{o}C

The **DSC** traces for **11** (**Figure 4.96**) shows a strong endothermic peak at 132 ^{o}C (ΔH = +266 kJ mol^{-1}) assigned to *Cr2-M* transition and rearranging towards a more stable complex. A broad endothermic peak at 43 ^{o}C (ΔH = +7 kJ mol^{-1}) assigned to *M-I* transition. On cooling, there were three exothermic peaks at 142 ^{o}C (ΔH = -6 kJ mol^{-1}), 137 ^{o}C (ΔH = -2 kJ mol^{-1}) and 101 ^{o}C (ΔH = -3 kJ mol^{-1}) assigned to *I-M1* transition and forming the new stable complex, respectively.

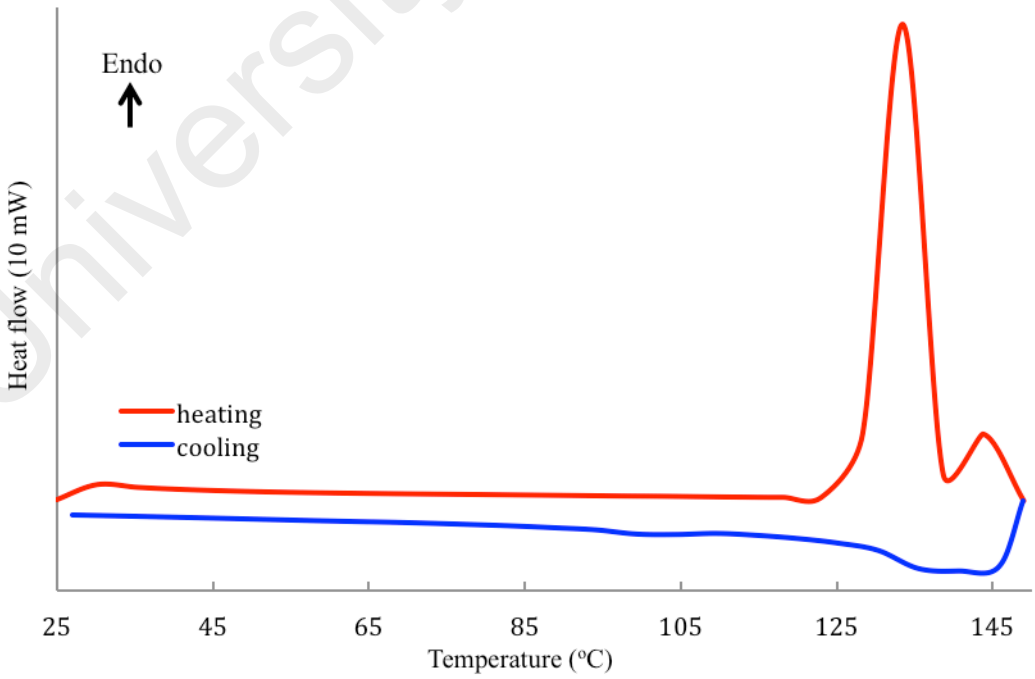

Figure 4.96 DSC scans of **11**

4.3.3 [$Cu_2(p\text{-}CH_3(CH_2)_{13}OC_6H_4COO)_4(bpy)_2$] (12)

(a) Synthesis and structural elucidation

The first step in the synthesis of [$Cu_2(p\text{-}CH_3(CH_2)_{13}OC_6H_4COO)_4(bpy)_2$] (**12**) (**Scheme 4.3**) involved the synthesis of $p\text{-}CH_3(CH_2)_{13}OC_6H_4COOCH_2CH_3$ from the reaction of $p\text{-}HOC_6H_4COOCH_2CH_3$ and $BrCH_2(CH_2)_{12}CH_3$. The ester was obtained as a white powder in good yield (81%). Its **elemental analysis** results (C, 76.2%; H, 10.6%) were in good agreement with the calculated values (C, 76.8%; H, 11.8%; FW = 362.5 g mol^{-1}). Its chemical formula was then ascertained by **^{1}H-NMR spectroscopy**. The spectrum is shown in **Figure 4.97** and the peak assignments are shown in **Table 4.14**.

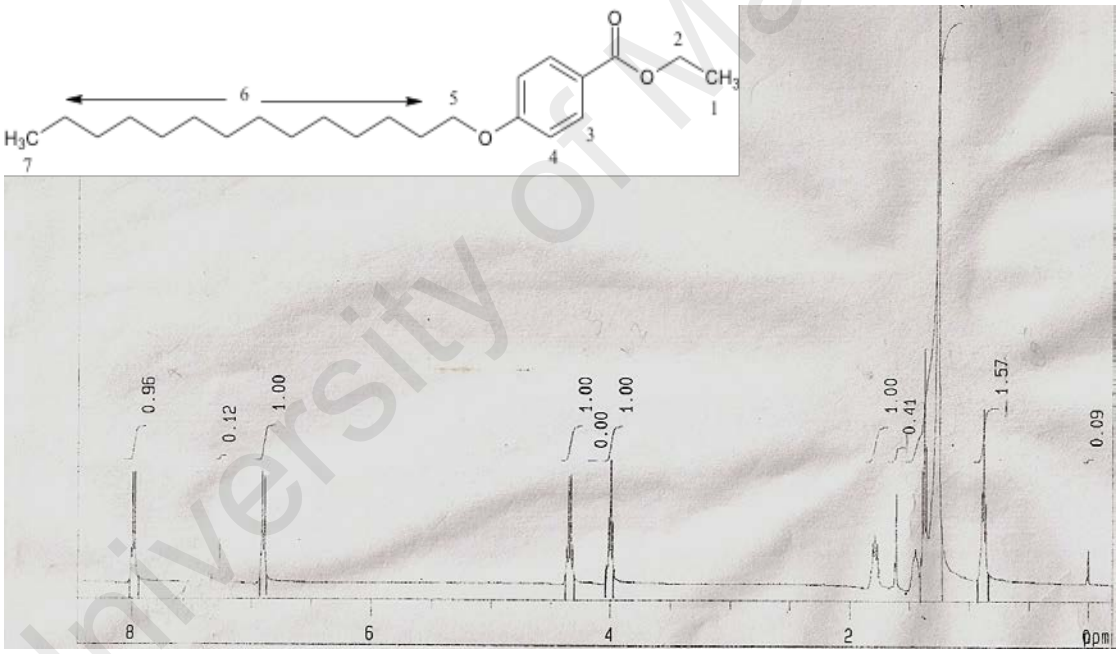

Figure 4.97 Proposed chemical structure of $p\text{-}CH_3(CH_2)_{13}OC_6H_4COOCH_3$

Table 4.14 ^{1}H-NMR data for $p\text{-}CH_3(CH_2)_{13}OC_6H_4COOCH_2CH_3$

Chemical shift (ppm)	Ratio	Multiplicity	Assignment
0.88	1.57	triplet	H-7
1.35	12.82	multiplet	H-1, H-6
4.00	1.00	triplet	H-5
4.34	1.00	triplet	H-2
6.90	1.00	doublet	H-3
7.98	0.96	doublet	H-4

Its **FTIR** data (**Table 4.10**; **Figure 4.98**) show the presence of the expected functional groups.

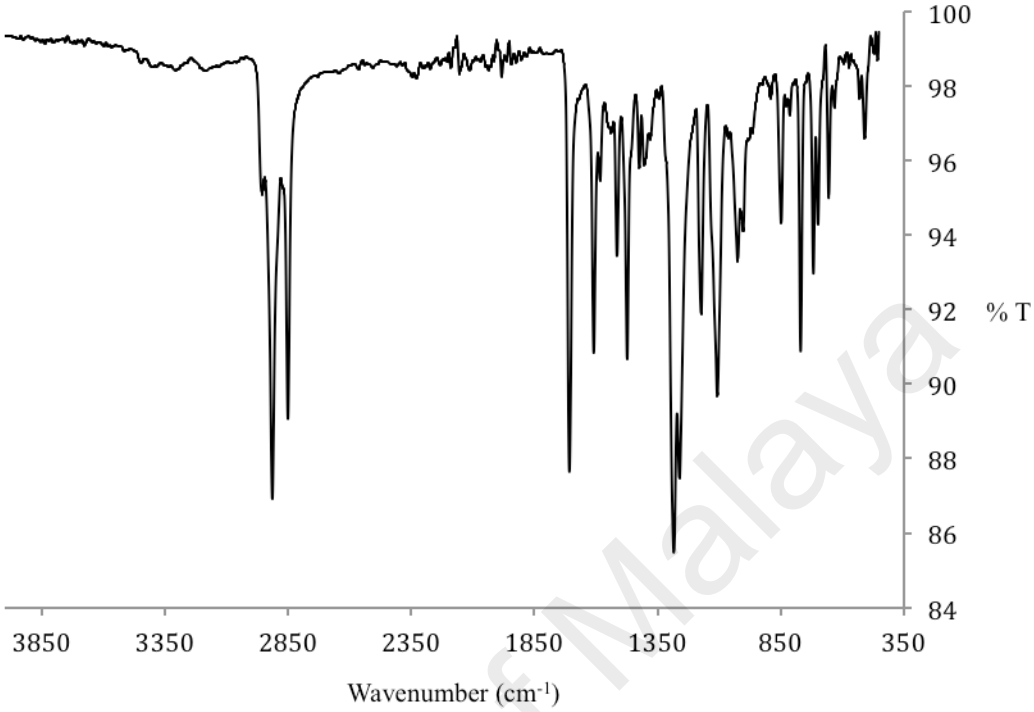

Figure 4.98 FTIR spectrum of *p*-$CH_3(CH_2)_{13}OC_6H_4COOCH_2CH_3$

The second step involved alkaline hydrolysis of *p*-$CH_3(CH_2)_{13}OC_6H_4COOCH_2CH_3$ using KOH. The product was a white powder and its yield was 52%. The results of the **elemental analyses** (C, 67.7%; H, 8.9%) were in good agreement for those calculated for *p*-$CH_3(CH_2)_{13}OC_6H_4COOK$ (C, 66.8%; H, 8.9%; FW 372.6 g mol^{-1}). Its **FTIR** spectrum (**Table 4.10**; **Figure 4.99**) shows the presence of the expected functional groups. Hence, the $\Delta\nu_{coo}$ value for *p*-$CH_3(CH_2)_{13}OC_6H_4COO^-$ ion was 149 cm^{-1}.

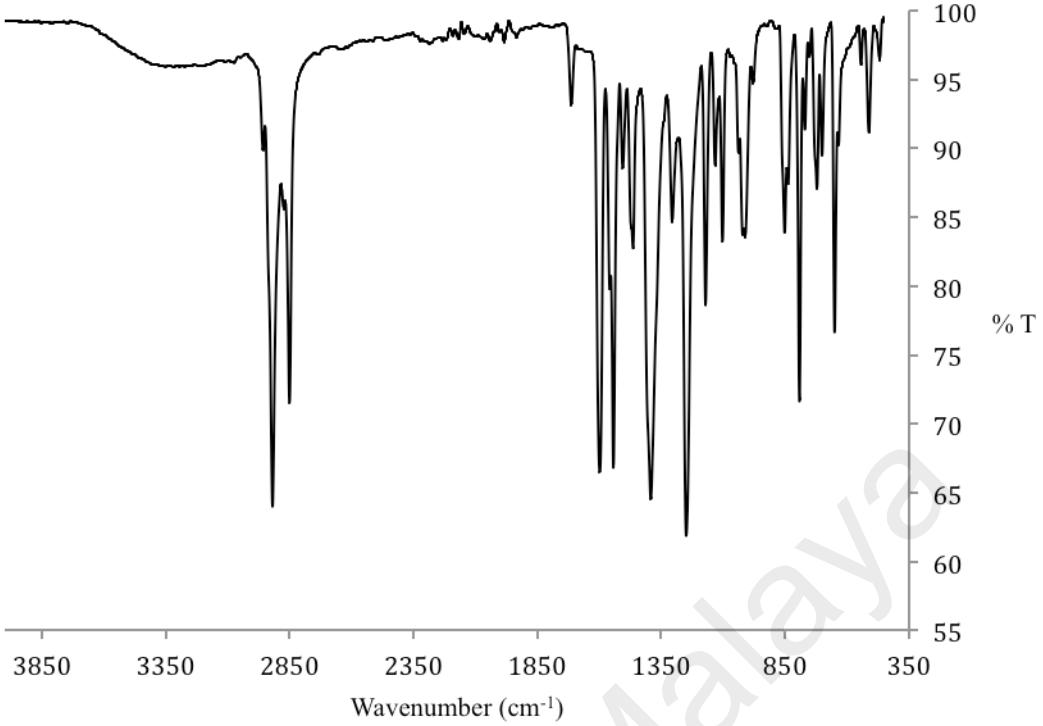

Figure 4.99 FTIR spectrum of $CH_3(CH_2)_{13}OC_6H_4COOK$

The third step involved reacting *p*-$CH_3(CH_2)_{13}OC_6H_4COOK$ with $CuSO_4.5H_2O$ to form the precursor complex, $[Cu_2(p\text{-}CH_3(CH_2)_{13}OC_6H_4COO)_4(H_2O)_2].2H_2O$ (yield = 40%). The results of the **elemental analyses** (C, 65.0%; H, 8.8%) were in good agreement for the stated formula (C, 65.8%; H, 9.2%); FW 1533.1 g mol^{-1}). Its **FTIR** data (**Table 4.10**; **Figure 4.100**) show the presence of the expected functional groups. Hence, the $\Delta\nu_{coo}$ value for *p*-$CH_3(CH_2)_9OC_6H_4COO^-$ ion was 174 cm^{-1}, which was higher than the value for *p*-$CH_3(CH_2)_{13}OC_6H_4COOK$ (149 cm^{-1}) indicating that *p*-$CH_3(CH_2)_9OC_6H_4COO^-$ ion was coordinated as a bridging bidentate ligand.

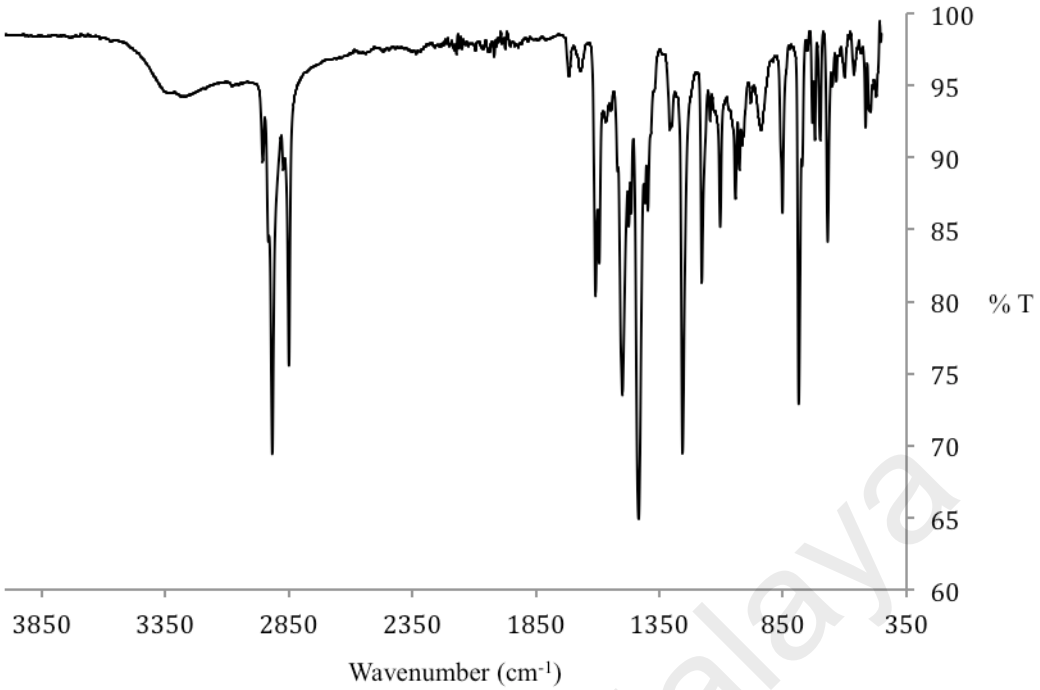

Figure 4.100 FTIR spectrum of $[Cu_2(p\text{-}CH_3(CH_2)_{13}OC_6H_4COO)_4(H_2O)_2].2H_2O$

Its **UV-vis** spectrum (**Figure 4.101**) in C_2H_5OH and CH_3COOH (9:1 v/v; molarity = 1.71 x 10^{-3} mol L^{-1}) shows two *d-d* bands at 705 nm (ε_{max} = 195 M^{-1} cm^{-1}) and 369 nm (ε_{max} = 84 M^{-1} cm^{-1}). The data suggest a square pyramidal geometry for both Cu(II) atoms in the complex.

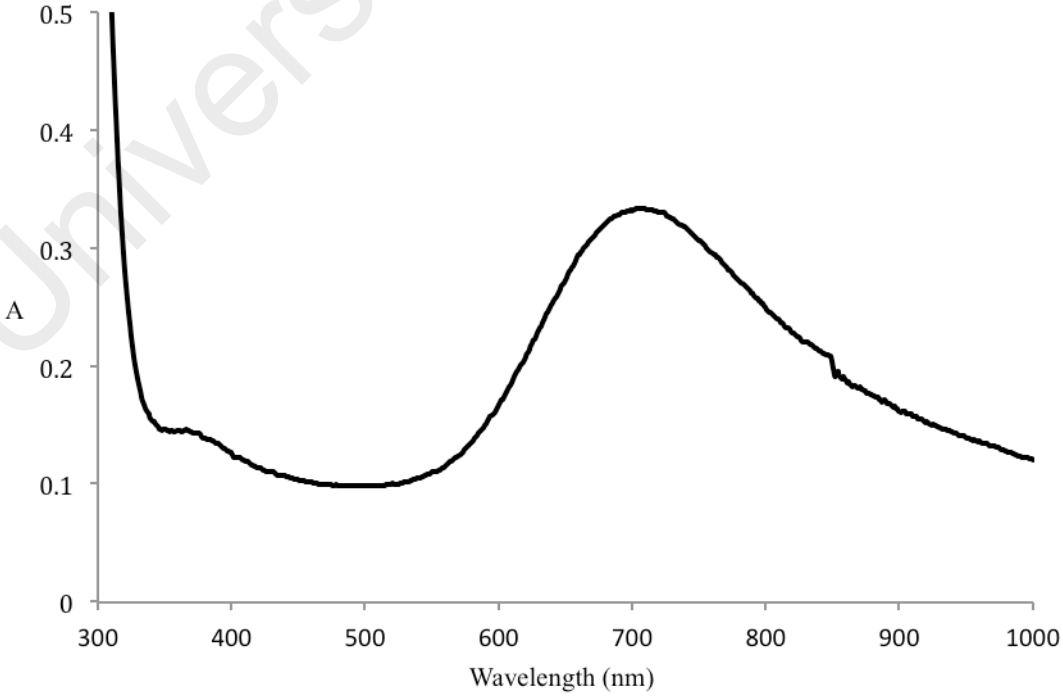

Figure 4.101 UV-vis spectrum of $[Cu_2(p\text{-}CH_3(CH_2)_{13}OC_6H_4COO)_4(H_2O)_2].2H_2O$

Its μ_{eff} value, calculated as previously done using its formula weight (1533.1 g mol^{-1}) and the values of mass susceptibility (χ_g; 2.35 x 10^{-6} cm^3 g^{-1}), molar susceptibility (χ_m; 3.60 x 10^{-4} cm^3 mol^{-1}), diamagnetic correction factor (χ_D; -7.67 x 10^{-4} cm^3 mol^{-1}) and corrected molar susceptibility (χ_m^{corr}; 1.13 x 10^{-3} cm^3 mol^{-1}), was 1.64 BM at 298 K.

$[Cu_2(p\text{-}CH_3(CH_2)_{13}OC_6H_4COO)_4(H_2O)_2].2H_2O$ reacted with bpy to form a blue powder (13%). The results of the **elemental analysis** (C, 69.3%; H, 8.4%; N, 2.8%) were in good agreement for $[Cu_2(CH_3(CH_2)_{13}OC_6H_4COO)_4(bpy)_2]$ (**12**) (C, 70.4%; H, 8.4%; N, 3.1%; FW 1773.3 g mol^{-1}).

Its **FTIR** data (**Table 4.10**; **Figure 4.102**) show the presence of the expected functional groups. Hence, the $\Delta\nu_{coo}$ values were 176 cm^{-1} and 230 cm^{-1}, in agreement with monodentate nonbridging and *syn-anti* monodentate bridging of $p\text{-}CH_3(CH_2)_{13}OC_6H_4COO^-$ ligands.

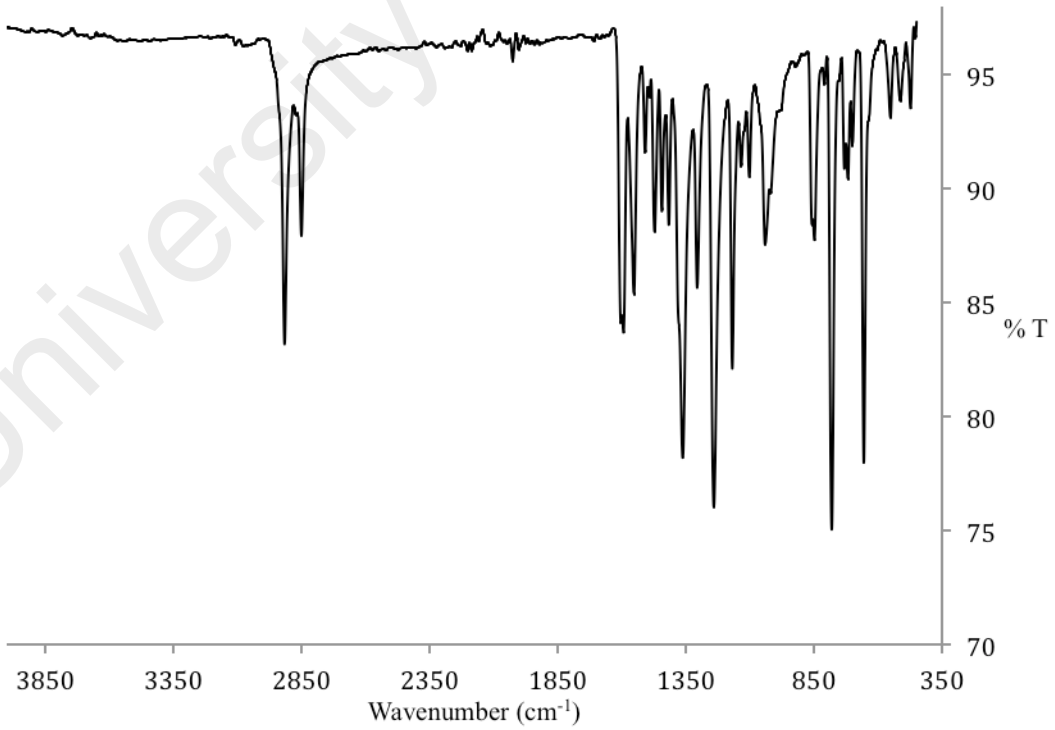

Figure 4.102 FTIR spectrum of **12**

Its **UV-vis** spectrum (**Figure 4.103**) in C_2H_5OH and CH_3COOH (9:1 v/v; molarity = 9.92 x 10^{-4} mol L^{-1}) shows a *d-d* band at 661 nm (ε_{max} = 317 M^{-1} cm^{-1}), suggesting a square pyramidal geometry at both Cu(II) atoms in the complex.

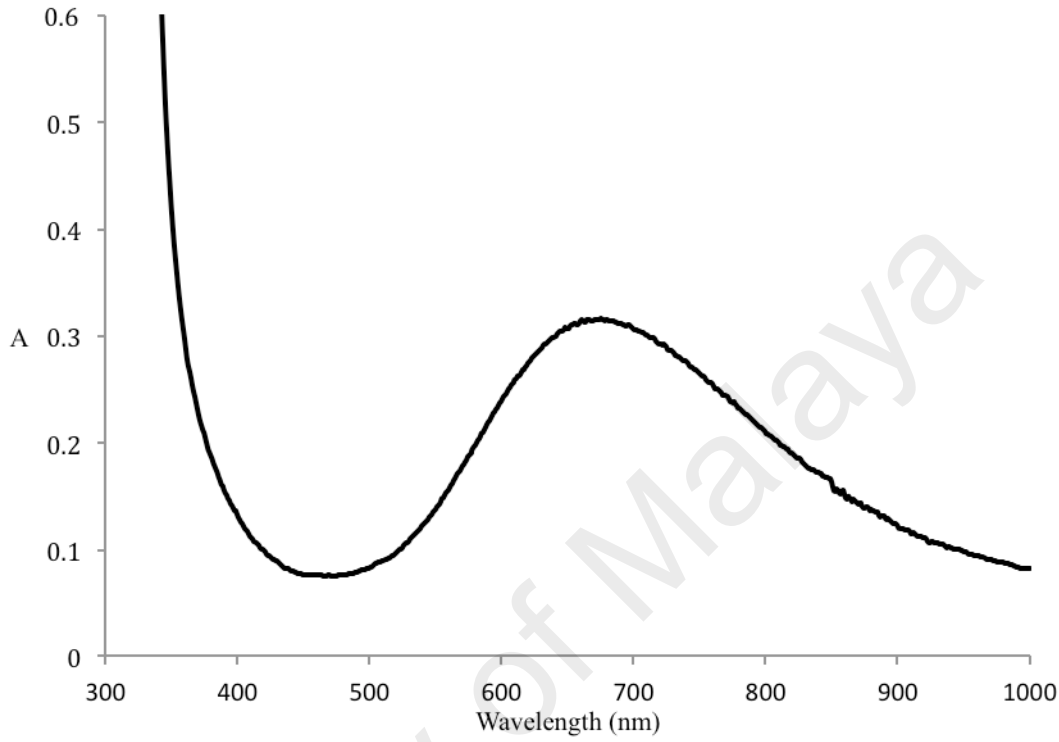

Figure 4.103 UV-vis spectrum of **12**

Its μ_{eff} value, calculated as previously done using its formula weight (1773.3 g mol^{-1}) and the values of mass susceptibility (χ_g; 1.10 x 10^{-6} cm^3 g^{-1}), molar susceptibility (χ_m; 1.95 x 10^{-3} cm^3 mol^{-1}), diamagnetic correction factor (χ_D; -8.87 x 10^{-4} cm^3 mol^{-1}) and corrected molar susceptibility (χ_m^{corr}; 2.84 x 10^{-3} cm^3 mol^{-1}), was 2.61 BM at 298 K.

(b) Thermal and mesomorphic studies

TG trace for **12** (**Figure 4.104**) shows a total weight loss of 80.3% in the temperature range 170 ^oC to 583 ^oC due to decomposition of *p*-$CH_3(CH_2)_{13}OC_6H_4COO^-$ ion and bpy ligands (calculated, 91.1%). The results are in good agreement with its proposed structural formula. The amount of residue at temperatures above 583 ^oC was 19.7%

(calculated, 8.9% assuming CuO). Hence, its decomposition temperature was 170 ^{o}C.

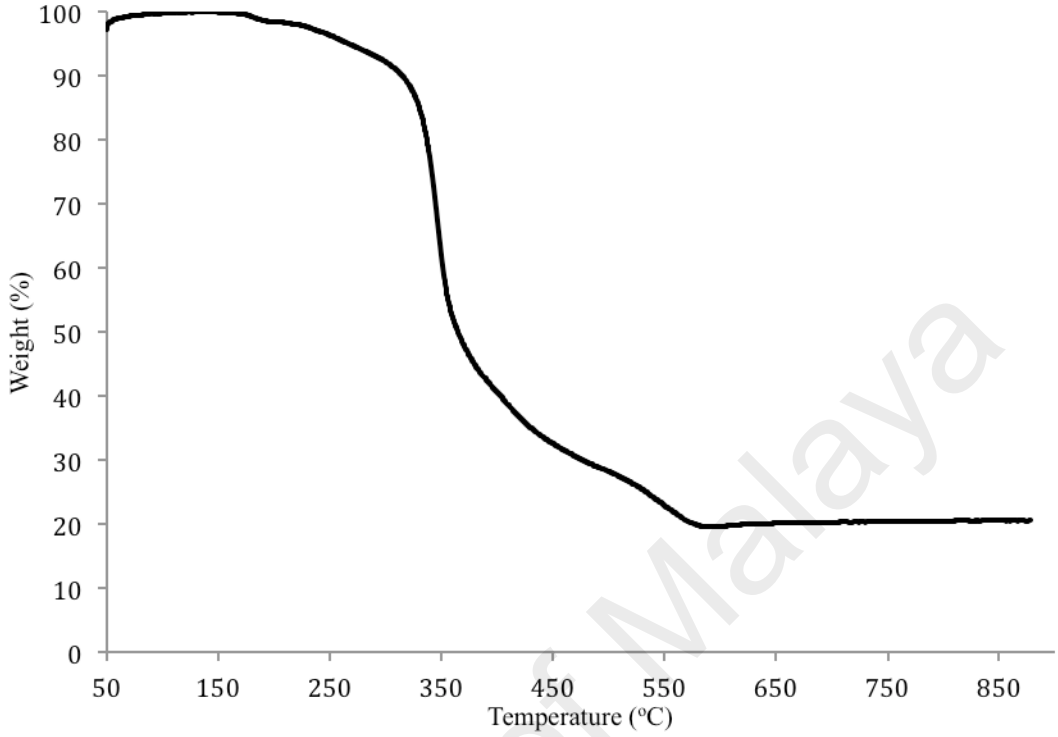

Figure 4.104 TGA trace of **12**

When viewed under **POM**, **12** started to change its colour from green to blue at 128 ^{o}C. On cooling from 150 ^{o}C, there was no optical texture observed. Hence, the complex did not behaved as a thermotropic metallomesogen. As comparison, its precursor ($[Cu_2(p\text{-}CH_3(CH_2)_{13}OC_6H_4COO)_4(H_2O)_2].2H_2O$) was observed to melting at 60 ^{o}C and clear to an isotropic liquid at 70 ^{o}C. Upon cooling from 70 ^{o}C, an optical texture was formed at 65 ^{o}C (**Figure 4.105**).

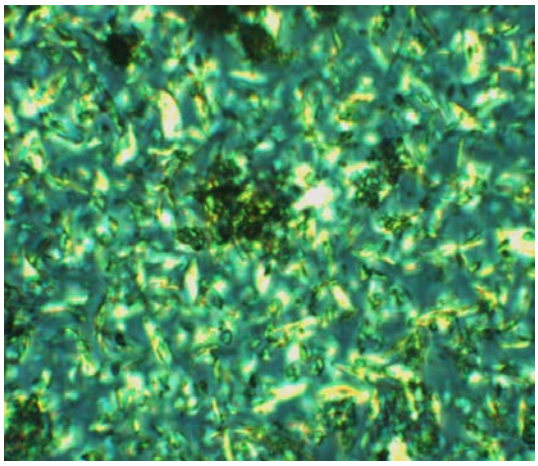

Figure 4.105 Photomicrographs of $[Cu_2(p\text{-}CH_3(CH_2)_{13}OC_6H_4COO)_4(H_2O)_2].2H_2O$ on cooling at 65 ^oC

The **DSC** traces for **12** (**Figure 4.106**) shows an endothermic peak at 133 ^oC (ΔH = +193 kJ mol^{-1}) due to structural rearranging towards a more stable complex. On cooling from 150 ^oC, there were no exothermic peaks observed. On reheating, there was no similar peak observed supporting the structural changes of the complex. This was supported with the POM.

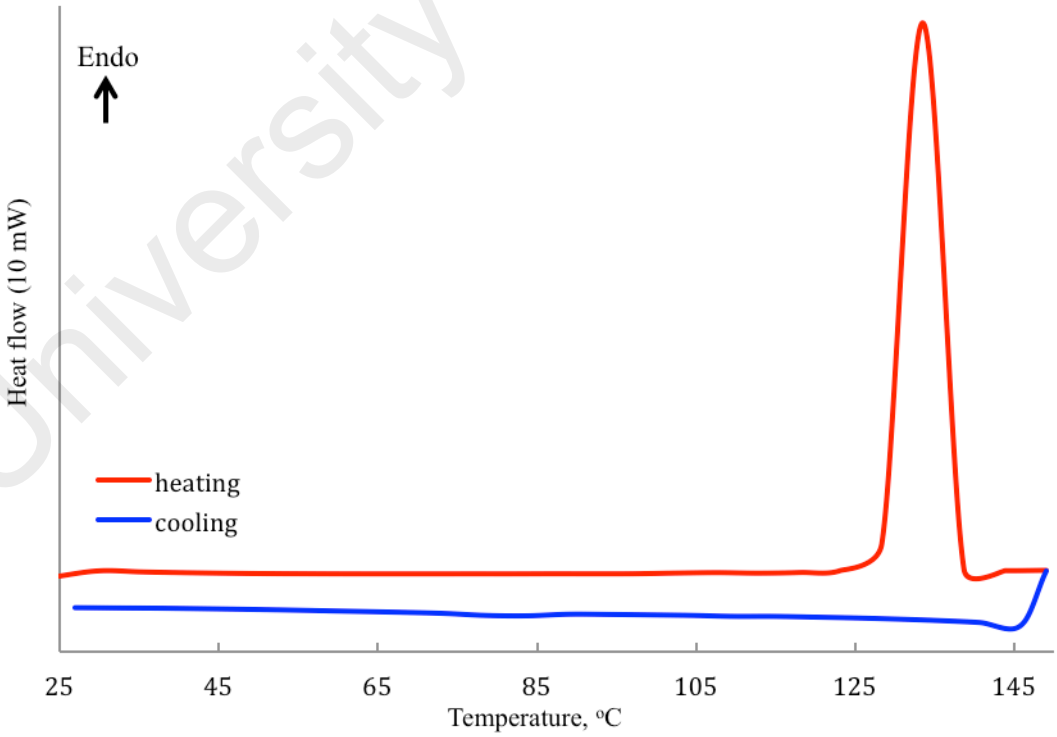

Figure 4.106 DSC scans of **12**

4.3.4 [$Cu_2(p\text{-}CH_3(CH_2)_{15}OC_6H_4COO)_4(bpy)_2$] (13)

(a) Synthesis and structural elucidation

The first step in the synthesis of [$Cu_2(p\text{-}CH_3(CH_2)_{15}OC_6H_4COO)_4(bpy)_2$] (**13**) (**Scheme 4.3**) involved the synthesis of $p\text{-}CH_3(CH_2)_{15}OC_6H_4COOCH_3$, from the reaction of $p\text{-}HO\text{-}C_6H_4COOCH_3$ and $BrCH_2(CH_2)_{14}CH_3$. The ester was obtained as a white powder in good yield (88%). Its **elemental analysis** results (C, 76.6%; H, 11.5%) were in good agreement with the calculated values (C, 76.5%; H, 10.7%; FW = 376.6 g mol^{-1}). Its chemical formula was further ascertained by **^{1}H-NMR spectroscopy**. The spectrum is shown in **Figure 4.107** and the peak assignments are shown in **Table 4.15**.

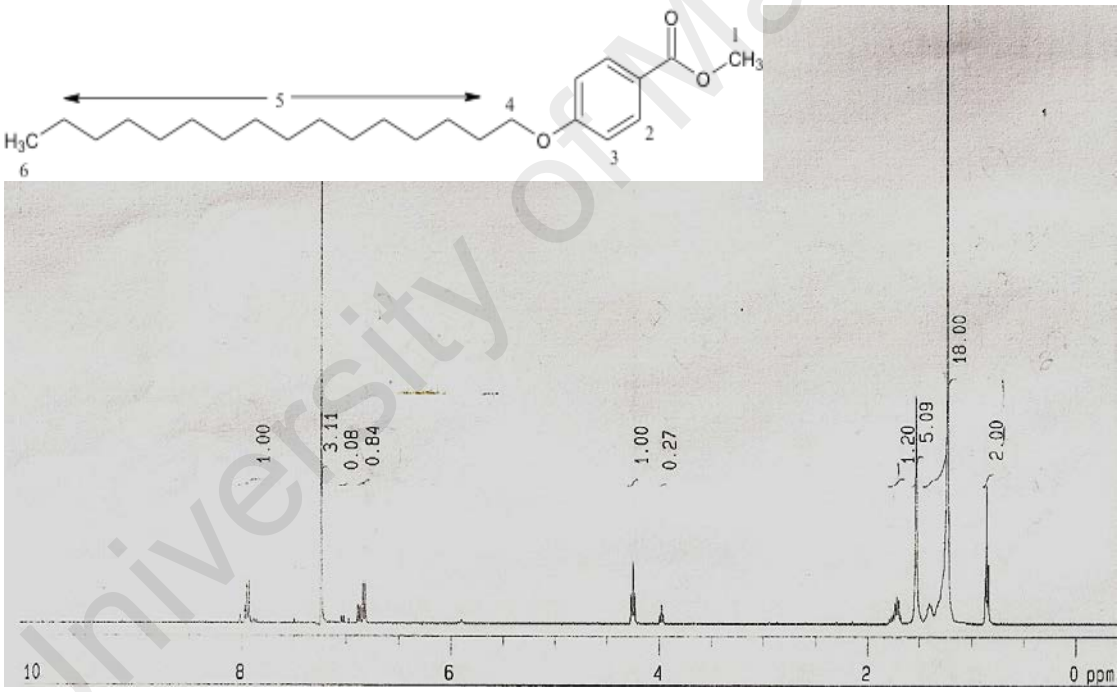

Figure 4.107 H-NMR spectrum $p\text{-}CH_3(CH_2)_{15}OC_6H_4COOCH_3$

Table 4.15 ^{1}H-NMR data for $p\text{-}CH_3(CH_2)_{15}OC_6H_4COOCH_3$

Chemical shift (ppm)	Ratio	Multiplicity	Assignments
0.86	2.00	triplet	H-6
1.33	18.00	multiplet	H-1, H-5
4.26	1.00	triplet	H-4
6.83	0.84	doublet	H-2
7.93	1.00	doublet	H-3

Its **FTIR** data (**Table 4.10**; **Figure 4.108**) show the presence of the expected functional groups.

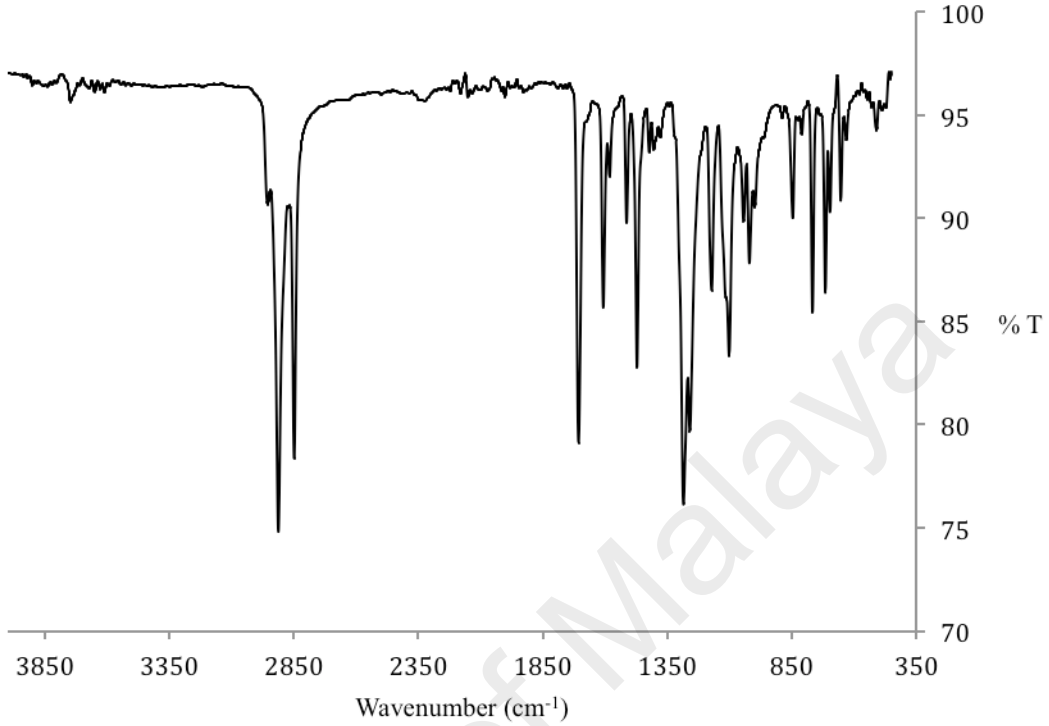

Figure 4.108 FTIR spectrum of *p*-$CH_3(CH_2)_{15}OC_6H_4COOCH_3$

The second step involved alkaline hydrolysis of *p*-$CH_3(CH_2)_{15}OC_6H_4COOCH_3$ using KOH. The product was a white powder and its yield was 85%. The results of the **elemental analyses** (C, 63.7%; H, 9.7%) were in good agreement for *p*-$CH_3(CH_2)_{15}OC_6H_4COOK.2H_2O$ (C, 63.3%; H, 9.5%; FW 436.7 g mol^{-1}). Its **FTIR** data (**Table 4.10**; **Figure 4.109**) show the presence of the expected functional groups. Hence, the $\Delta\nu_{coo}$ value for *p*-$CH_3(CH_2)_{15}OC_6H_4COO^-$ ion was 148 cm^{-1}

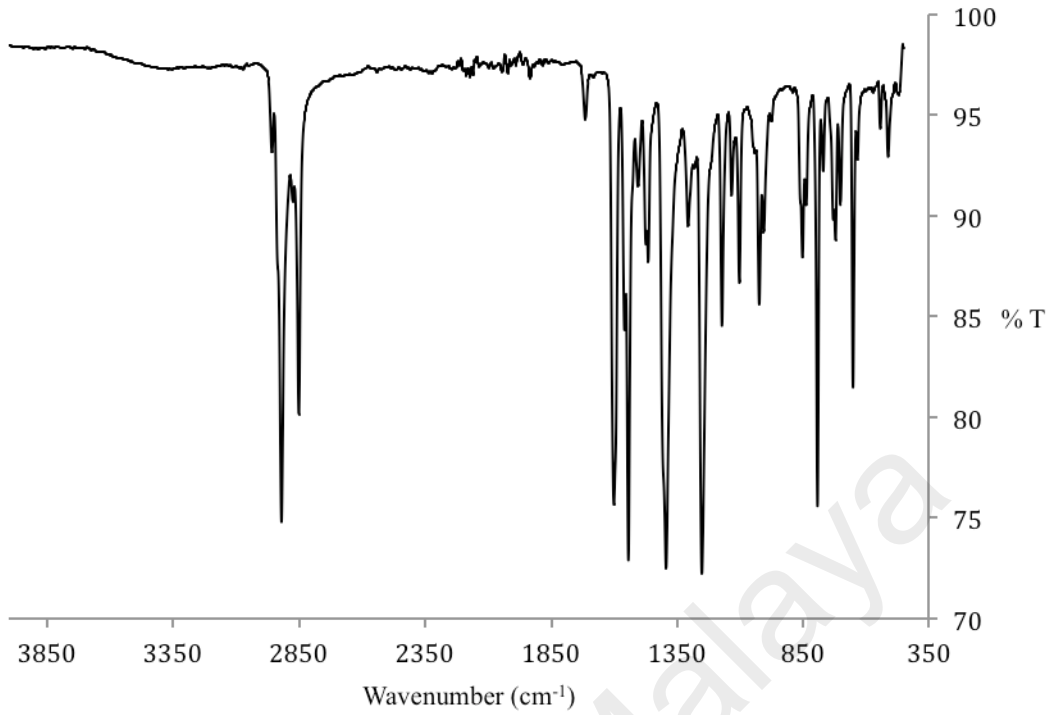

Figure 4.109 FTIR spectrum of p-$CH_3(CH_2)_{15}OC_6H_4COOK$

The third step involved reacting p-$CH_3(CH_2)_{15}OC_6H_4COOK.2H_2O$ with $CuSO_4.5H_2O$ to form the precursor complex, $[Cu_2(p\text{-}CH_3(CH_2)_{15}OC_6H_4COO)_4(H_2O)_2]$ (yield = 55%). The results of the **elemental analyses** (C, 67.8%; H, 10.3%) were in good agreement for the stated formula (C, 68.7%; H, 9.5%; FW 1609.2 g mol^{-1}). Its **FTIR** data (**Table 4.10**; **Figure 4.110**) show the presence of the expected functional groups. Hence, the $\Delta\nu_{coo}$ value for p-$CH_3(CH_2)_9OC_6H_4COO^-$ ion was 168 cm^{-1}, which was higher than the value for p-$CH_3(CH_2)_{15}OC_6H_4COOK.2H_2O$ (152 cm^{-1}) indicating that p-$CH_3(CH_2)_{15}OC_6H_4COO^-$ ion was coordinated as a bridging bidentate ligand.

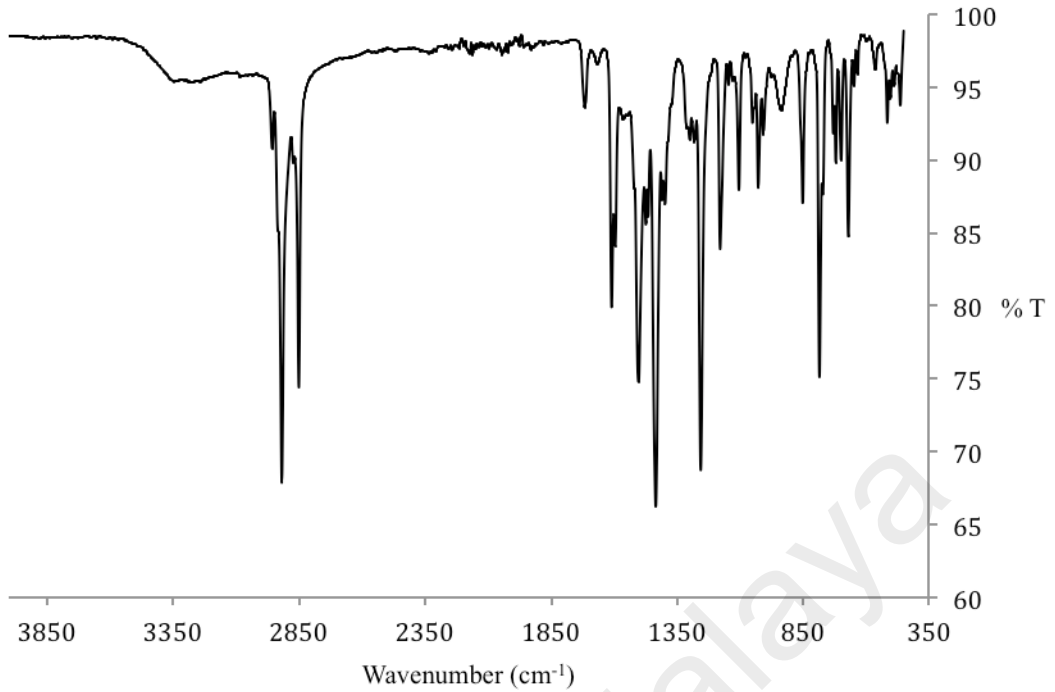

Figure 4.110 FTIR spectrum of $[Cu_2(p\text{-}CH_3(CH_2)_{15}OC_6H_4COO)_4(H_2O)_2]$

Its **UV-vis** spectrum (**Figure 4.111**) in C_2H_5OH and CH_3COOH (9:1 v/v; molarity = 1.51 x 10^{-3} mol L^{-1}) shows two *d-d* bands at 708 nm (ε_{max} = 160 M^{-1} cm^{-1}) and 364 nm (ε_{max} = 140 M^{-1} cm^{-1}). These suggest a square pyramidal geometry for both Cu(II) atoms in the complex.

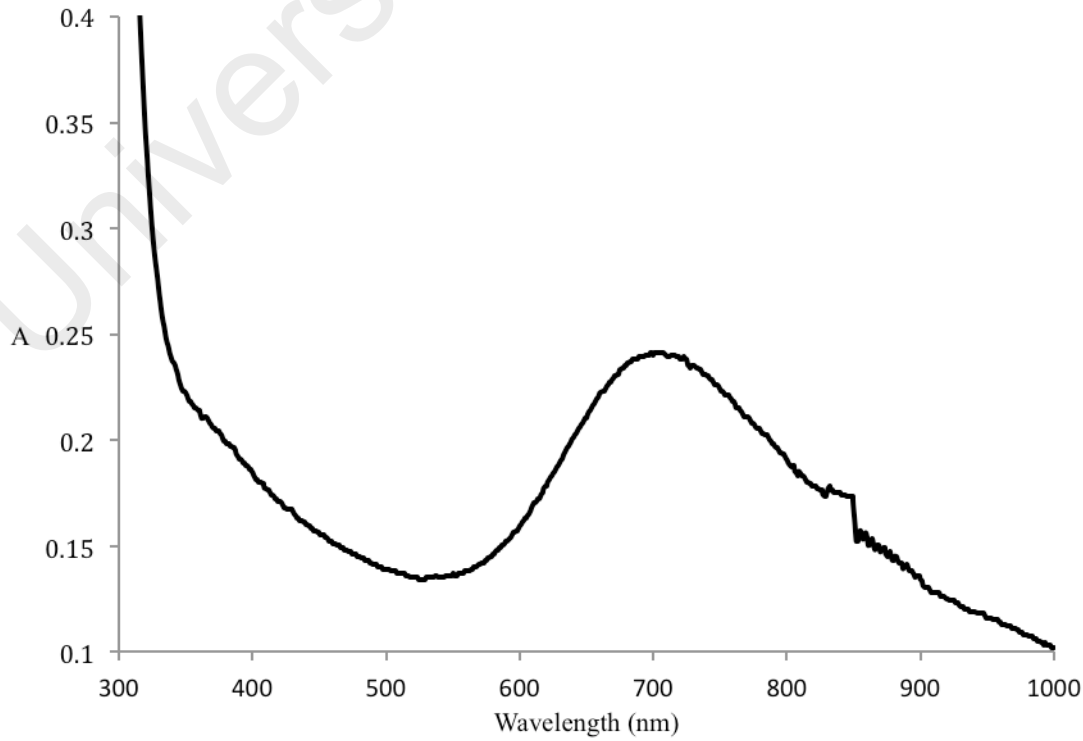

Figure 4.111 UV-vis spectrum of $[Cu_2(p\text{-}CH_3(CH_2)_{15}OC_6H_4COO)_4(H_2O)_2]$

Its μ_{eff} value, calculated as previously done using its formula weight (1609.2 g mol^{-1}) and the values of mass susceptibility (χ_g; 6.90 x 10^{-7} cm^3 g^{-1}), molar susceptibility (χ_m; 1.11 x 10^{-3} cm^3 mol^{-1}), diamagnetic correction factor (χ_D; -8.05 x 10^{-4} cm^3 mol^{-1}) and corrected molar susceptibility (χ_m^{corr}; 1.91 x 10^{-3} cm^3 mol^{-1}), was 2.14 BM at 298 K.

$[Cu_2(p\text{-}CH_3(CH_2)_{15}OC_6H_4COO)_4(H_2O)_2]$ reacted with bpy to form a blue powder (yield = 83%). The results of the **elemental analysis** (C, 70.0%; H, 9.1%; N, 2.0%) were in good agreement for $[Cu_2(p\text{-}CH_3(CH_2)_{15}OC_6H_4COO)_4(bpy)_2]$ (**13**) (C, 71.3%; H, 8.8%; N, 2.8%; FW 1885.5 g mol^{-1}).

Its **FTIR** data (**Table 4.10**; **Figure 4.112**) show the presence of the expected functional groups. Hence, the $\Delta\nu_{coo}$ values were 159 cm^{-1} and 224 cm^{-1}, in agreement with monodentate nonbridging and *syn-anti* monodentate bridging $p\text{-}CH_3(CH_2)_{15}OC_6H_4COO^-$ ligands.

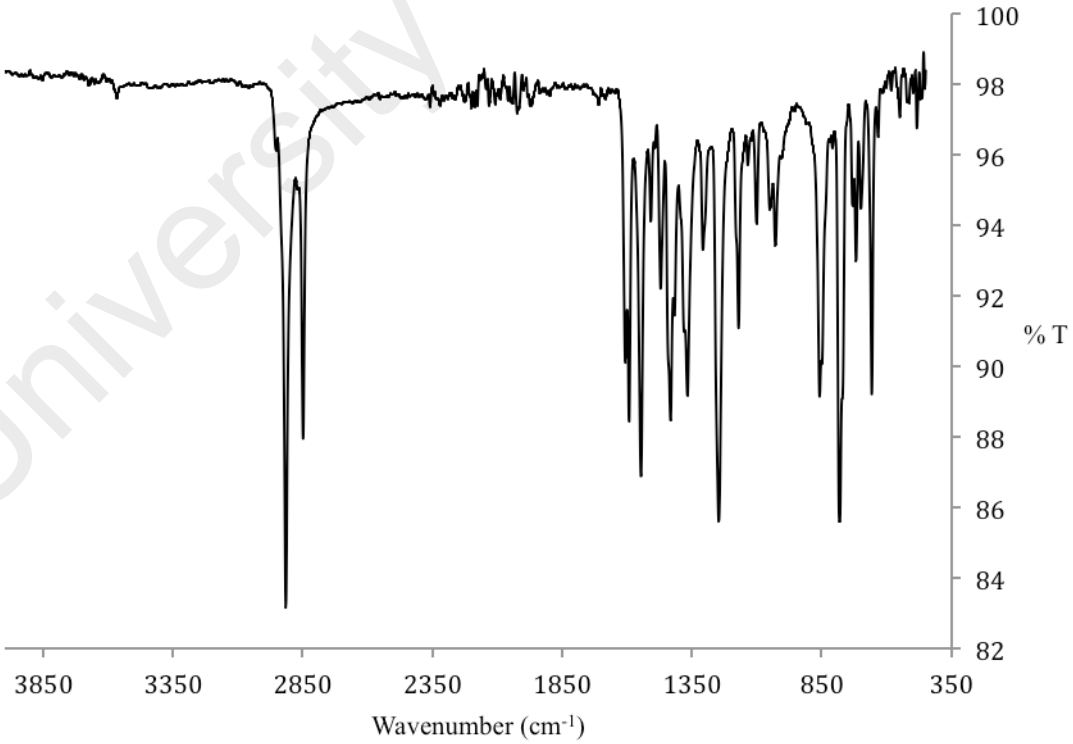

Figure 4.112 FTIR spectrum of **13**

Its **UV-vis** spectrum (**Figure 4.113**) in C_2H_5OH and CH_3COOH (9:1 v/v; molarity = 1.29 x 10^{-3} mol L^{-1}) shows a *d-d* band at 697 nm (ε_{max} = 582 M^{-1} cm^{-1}), suggesting a square pyramidal geometry at both Cu(II) atoms in the complex.

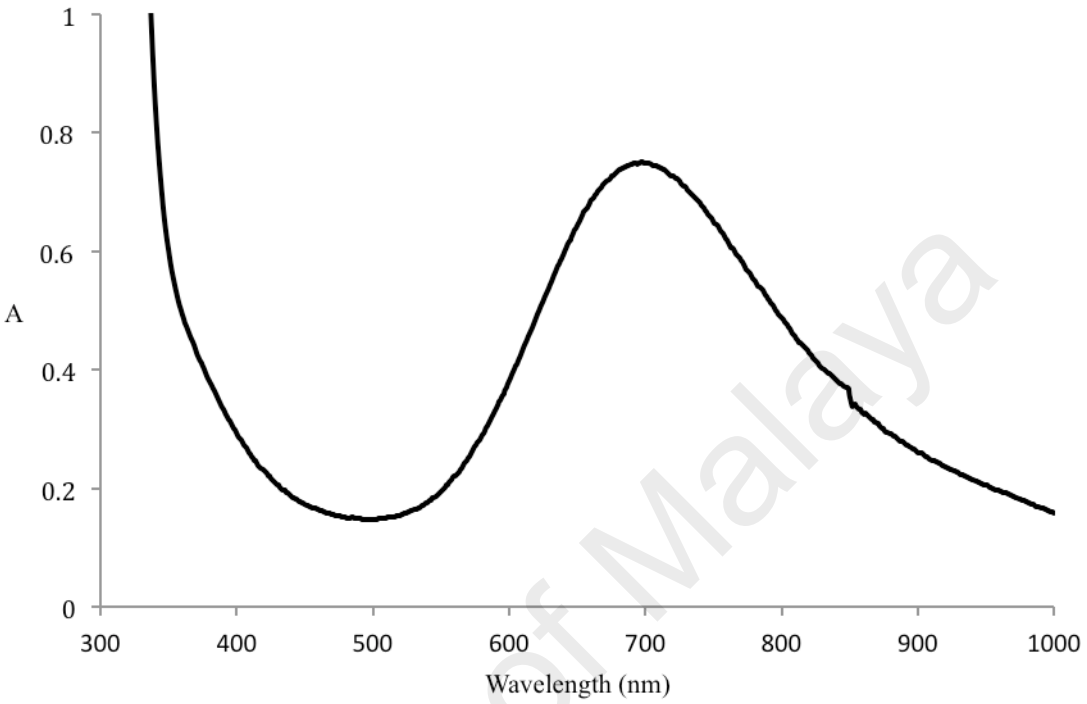

Figure 4.113 UV-vis spectrum of **13**

Its μ_{eff} value, calculated as previously done using its formula weight (1885.5 g mol^{-1}) and the values of mass susceptibility (χ_g; 1.86 x 10^{-6} cm^3 g^{-1}), molar susceptibility (χ_m; 3.51 x 10^{-3} cm^3 mol^{-1}), diamagnetic correction factor (χ_D; -9.43 x 10^{-4} cm^3 mol^{-1}) and corrected molar susceptibility (χ_m^{corr}; 4.45 x 10^{-3} cm^3 mol^{-1}), was 3.26 BM at 298 K.

(b) Thermal and mesomorphic studies

TG trace for **13** (**Figure 4.114**) shows a total weight loss of 87.2% in the temperature range 212 ^oC to 655 ^oC due to decomposition of *p*-$CH_3(CH_2)_{15}OC_6H_4COO^-$ and bpy ligands (calculated, 91.6%). The results are in good agreement with its proposed structural formula. The amount of residue at temperatures above 750 ^oC was 12.8% (calculated, 8.4% assuming CuO). Hence, its decomposition temperature was 212 ^oC.

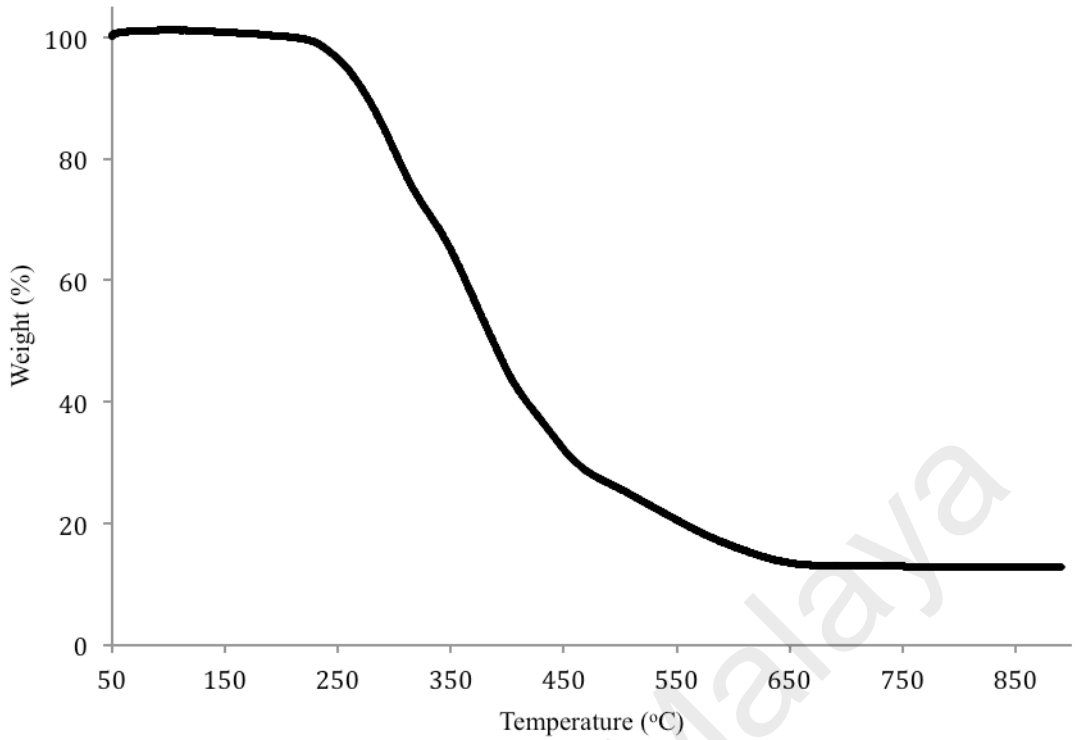

Figure 4.114 TGA trace of **13**

When viewed under **POM**, **13** started to change its colour from green to blue at 130 °C. On cooling from 160 °C, there was no optical texture observed. Hence, the complex did not behave as a thermotropic metallomesogen. In comparison, its precursor ([Cu(*p*-$CH_3(CH_2)_{15}OC_6H_4COO)_2(H_2O)_2$]) was observed to melt at 54 °C and clear to an isotropic liquid at 64 °C. Upon cooling from this temperature, an optical texture was observed at 56 °C (**Figure 4.115**).

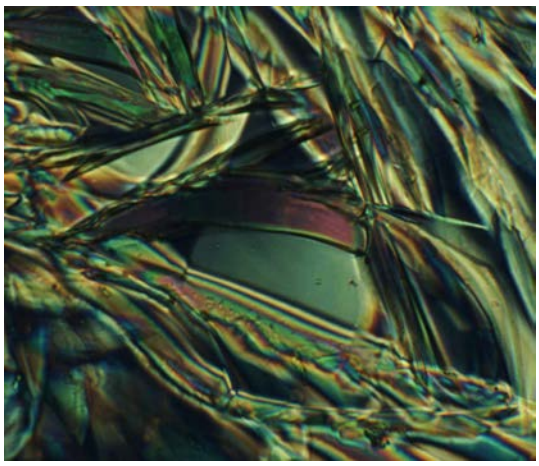

Figure 4.115 Photomicrograph of [$Cu_2(CH_3(CH_2)_{15}OC_6H_4COO)_4(H_2O)_2$] on cooling at 56 °C

The **DSC** traces for **13** (**Figure 4.116**) shows two overlapping endothermic peaks at onset 130 ^{o}C ($\Delta H_{combined}$ = +129 kJ mol^{-1}) assigned to structural rearrangement to form a more stable complex. On cooling from 150 ^{o}C, there were no exothermic peaks observed. On reheating, there was no similar peak observed supporting the structural changes of the complex.

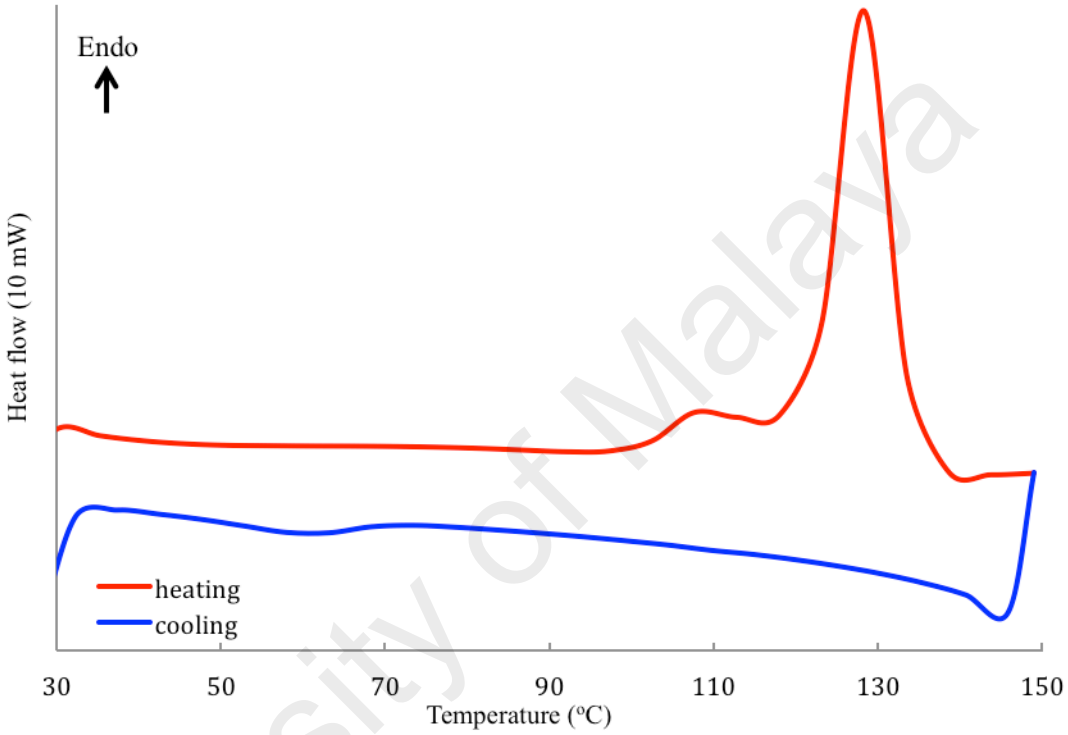

Figure 4.116 DSC scans of **13**

4.3.5 Summary

To summarize, the results for precursor complexes $[Cu_2(R)_4]$ ($R = CH_3(CH_2)_{9\text{-}15}OC_6H_4COO$) and complexes formed from their reactions with bpy (**10 – 13**) are shown in **Table 4.16** and **Table 4.17**, respectively.

Table 4.16 Precursor complexes of complexes **10 -13**

Strutural formula	$\Delta\nu_{coo}$ (cm^{-1})	λ_{max}, nm (ε_{max}, M^{-1} cm^{-1})	μ_{eff} (BM)	M*
$[Cu_2(p\text{-}CH_3(CH_2)_9OC_6H_4COO)_4(H_2O)_2]$	166	703 (222) 361 (64)	1.87	Yes
$[Cu_2(p\text{-}CH_3(CH_2)_{11}OC_6H_4COO)_4(H_2O)_2].2H_2O$	177	703 (330) 356 (165)	1.59	Yes
$[Cu_2(p\text{-}CH_3(CH_2)_{13}OC_6H_4COO)_4(H_2O)_2].2H_2O$	174	705 (195) 369 (84)	1.64	Yes
$[Cu_2(p\text{-}CH_3(CH_2)_{15}OC_6H_4COO)_4(H_2O)_2]$	168	708 (160) 364 (140)	2.14	Yes

*M = mesomorphism

All precursor complexes were dinuclear with bidentate bridging carboxylates ligand and square pyramidal copper(II) atoms. There were antiferromagnetic interactions between the two copper(II) atoms in these complexes at room temperature, postulated to occur through the bridging carboxylate ligands by a mechanism termed the superexchange pathway. Finally, all complexes behaved as thermotropic columnar liquid crystals. These data support the paddle-wheel structure for these complexes, similar to most copper(II) alkylcarboxylates reported in the literature [7,8].

Figure 4.17. Complexes **10 - 13**

Structural formula	$\Delta\nu_{coo}$ (cm^{-1})	λ_{max}, nm (ε_{max})	μ_{eff} (BM)	T_{dec} (^oC)	M*
$[Cu_2(CH_3(CH_2)_9OC_6H_4COO)_4(bpy)_2].2H_2O$ (**10**; blue powder)	206, 217	679 (136)	2.92	240	Yes
$[Cu_2(CH_3(CH_2)_{11}OC_6H_4COO)_4(bpy)_2]$ (**11**; blue powder)	176, 229	675 (117)	2.52	215	Yes
$[Cu_2(CH_3(CH_2)_{13}OC_6H_4COO)_4(bpy)_2]$ (**12** ; blue powder)	176, 230	661 (317)	2.61	170	No
$[Cu_2(CH_3(CH_2)_{15}OC_6H_4COO)_4(bpy)_2]$ (**13**; blue powder)	159, 179	697 (582)	3.26	212	No

*M = mesomorphism

All complexes were dinuclear with chelating bpy and monodentate nonbridging and *syn-anti* monodentate bridging carboxylato ligands, and square pyramidal copper(II) atoms. There were ferromagnetic interactions between the two copper(II) atoms, with the weakest interaction for **11** and strongest interaction for **13**. This trend may correlated with structural distortion and strength of Cu-OOCR bonds. These data suggest similar structures as crystals of $[Cu_2(CH_3(CH_2)_{6,8,10,14}COO)_4(bpy)_2]$ reported in this work.

These complexes were also thermally stable, with decomposition temperatures in the range of 170 ^oC to 240 ^oC. Except for **13**, their decomposition temperatures showed a gradually decreasing trend with increasing number of carbon atoms in the alkyloxy chain. Complexes **10** and **11** behaved as thermotropic liquid crystals, while **12** and **13** were not mesomorphic. This behavior may arose from structural rearrangement proposed for the latter complexes.

4.4 Reactions of $[Fe_2(\mu\text{-}H_2O)(\mu\text{-}RCOO)_2(RCOO)_2(H_2O)_2]$ with bpy

The general equation for the syntheses of the precursor complexes, $[Fe_2(\mu\text{-}H_2O)(\mu\text{-}RCOO)_2(RCOO)_2(H_2O)_2]$ (R = p-$CH_3(CH_2)_{9\text{-}15}OC_6H_4$), is shown below.

$$p\text{-}ROC_6H_4COO^- + Fe^{2+} \longrightarrow [Fe_2(\mu\text{-}H_2O)(\mu\text{-}RCOO)_2(RCOO)_2(H_2O)_2]$$

These precursor complexes were then reacted with bpy to form $[Fe_2(\mu\text{-}RCOO)_2(RCOO)_2(bpy)]$ (**14**), $[Fe_2(\mu\text{-}RCOO)_2(RCOO)_2(bpy)]$ (**15**), $[Fe(RCOO)_2(bpy)]$ (**16**), and $[Fe(RCOO)_2(bpy)]$ (**17**), respectively.

4.4.1 $[Fe_2(\mu\text{-}RCOO)_2(RCOO)_2(bpy)]$ (R = p-$CH_3(CH_2)_9OC_6H_4$) (14)

(a) Synthesis and structural elucidation

The precursor complex, $[Fe_2(\mu\text{-}H_2O)(\mu\text{-}RCOO)_2(RCOO)_2(H_2O)_2]$ (R = p-$CH_3(CH_2)_9OC_6H_4$), was obtained as a brown powder with 47% yield from the reaction of p-$CH_3(CH_2)_9OC_6H_4COOK$ with $[FeSO_4.7H_2O]$. Its proposed structure

(**Figure 4.117**) is based on combined analytical data discussed below, and was similar to that reported by Lippard *et al.* for $[Fe_2(\mu\text{-}H_2O)(\mu\text{-}OAc)_2(OAc)_3(Py)_2]^-$, where OAc = acetate [59].

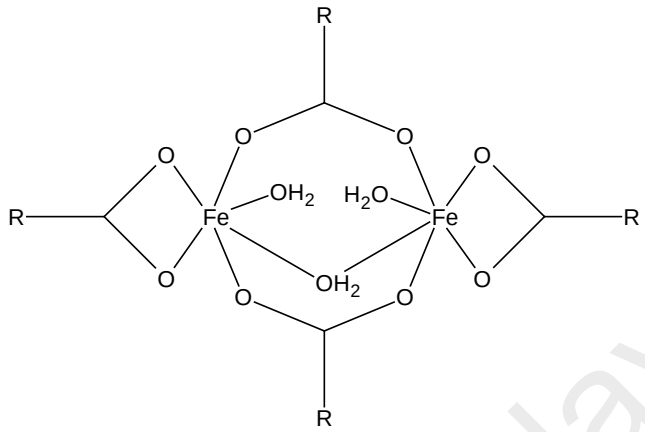

Figure 4.117 Proposed structural formula for $[Fe_2(\mu\text{-}H_2O)(\mu\text{-}RCOO)_2(RCOO)_2(H_2O)_2]$ (R = p-$CH_3(CH_2)_9OC_6H_4$)

The results of its **elemental analyses** (C, 64.0%; H, 9.0%) were in good agreement with the calculated values (C, 64.0%; H, 8.4%; FW 1275.2 g mol^{-1}. Its **FTIR** spectrum is shown in **Figure 4.118**, and the peak assignments are given in **Table 4.18** (which also include the data for other complexes for later discussion). The $\Delta\nu_{coo}$ values were 123 cm^{-1} and 163 cm^{-1}, indicating that p-$CH_3(CH_2)_9OC_6H_4COO^-$ ion was coordinated as a chelating and bridging bidentate ligand, respectively (the Δνcoo value for p-$CH_3(CH_2)_9OC_6H_4COOK$ was 152 cm^{-1}).

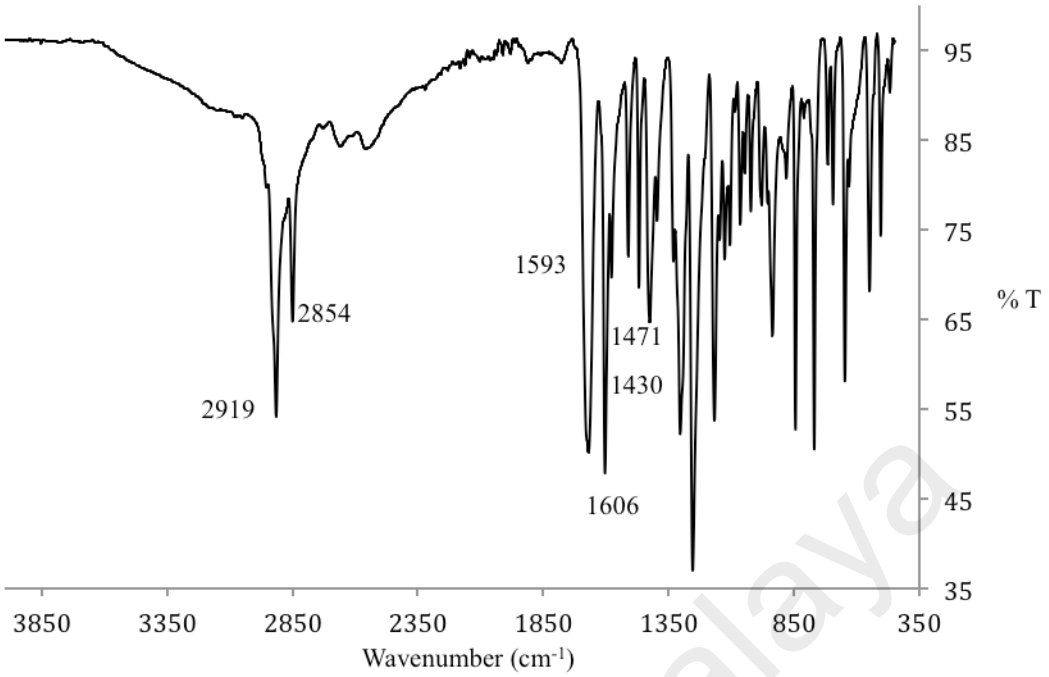

Figure 4.118 FTIR spectrum of $[Fe_2(\mu\text{-}H_2O)(\mu\text{-}RCOO)_2(RCOO)_2(H_2O)_2]$ (R = p-$CH_3(CH_2)_9OC_6H_4$)

Table 4.18 FTIR data in (cm^{-1}) and assignments (R = p-$CH_3(CH_2)_nOC_6H_4$)

Compound	CH_2 (asym)	CH_2 (sym)	COO (asym)	COO (sym)	C=C (aro)	C-N
$[Fe_2(\mu\text{-}H_2O)(\mu\text{-}RCOO)_2(RCOO)_2(H_2O)_2]$ (n = 9)	2919	2854	1593	1471, 1430	1606	-
$[Fe_2(\mu\text{-}H_2O)(\mu\text{-}RCOO)_2(RCOO)_2(H_2O)_2]$ .H_2O (n = 11)	2917	2852	1594	1470, 1431	1605	-
$[Fe_2(\mu\text{-}H_2O)(\mu\text{-}RCOO)_2(RCOO)_2(H_2O)_2]$ (n = 13)	2917	2851	1597	1471, 1433	1606	-
$[Fe_2(\mu\text{-}H_2O)(\mu\text{-}RCOO)_2(RCOO)_2(H_2O)_2]$ (n = 15)	2918	2850	1594	1472, 1429	1606	-
$[Fe_2(\mu\text{-}RCOO)_2(RCOO)_2(bpy)]$; (n = 9; complex **14**)	2919	2853	1595	1470, 1431	1606	1307
$[Fe_2(\mu\text{-}RCOO)_2(RCOO)_2(bpy)]$; (n = 11; complex **15**)	2918	2852	1579	1470, 1418	1606	1307
$[Fe(RCOO)_2(bpy)]$; (n = 13; complex **16**)	2916	2851	1598	1470	1606	1307
$[Fe(RCOO)_2(bpy)]$; (n = 15; complex **17**)	2917	2850	1597	1470	1607	1308

Its **UV-vis** spectrum (**Figure 4.119**) in $CHCl_3$ shows a *d-d* band appearing as a shoulder on the strong CT band at 530 nm (ε = 793 M^{-1} cm^{-1}), assigned to the $^5E_g \rightarrow {}^5T_{2g}$ electronic transition for a low spin (LS) Fe(II) atom in the complex and as similarly done for $[Fe_2(\mu\text{-}H_2O)_2(CH_3(CH_2)_8COO)_4].H_2O$.

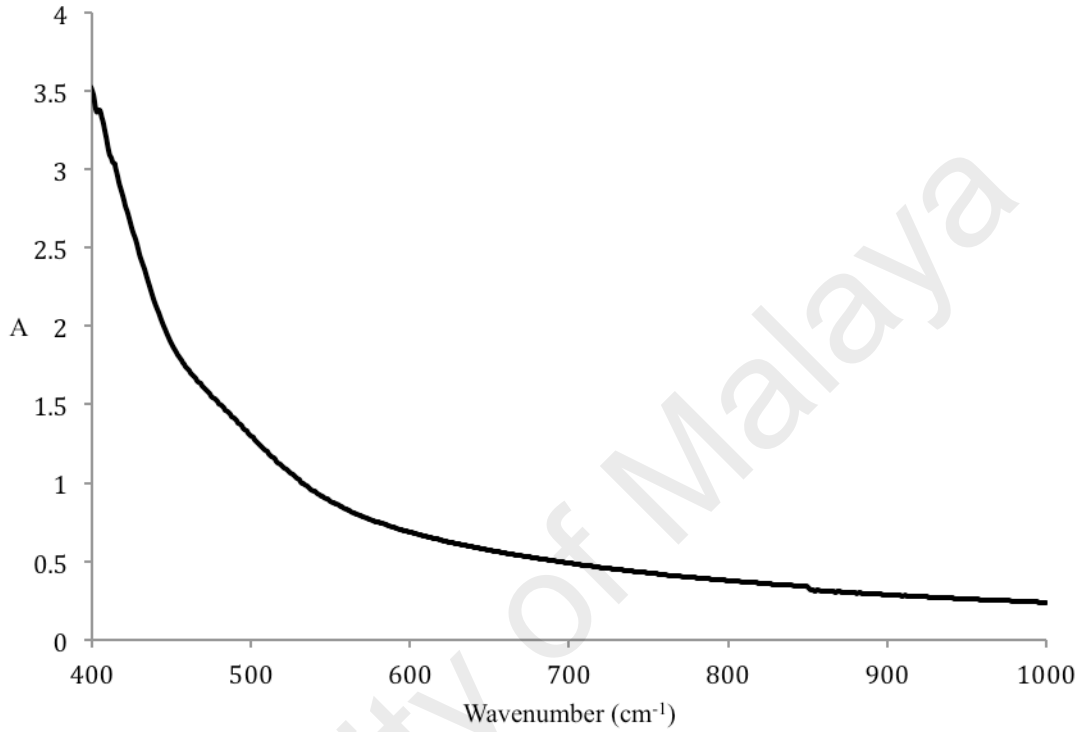

Figure 4.119 UV-vis spectrum of $[Fe_2(\mu\text{-}H_2O)(\mu\text{-}RCOO)_2(RCOO)_2(H_2O)_2]$ (R = *p*-$CH_3(CH_2)_9OC_6H_4$)

Its $\chi_M^{corr}T$ value, calculated from the values of its formula weight (FW = 1275.2 g mol^{-1}), mass susceptibility (χ_g = 9.14 x 10^{-6} cm^3 g^{-1}), molar susceptibility (χ_m = 1.17 x 10^{-2} cm^3 mol^{-1}), diamagnetic correction factor (χ_D = -6.38 x 10^{-4} cm^3 mol^{-1}) and corrected molar susceptibility (χ_m^{corr} = 1.23 x 10^{-2} cm^3 mol^{-1}), was 3.67 cm^3 K mol^{-1} at 298 K. Accordingly, this complex was made up of 61.1% HS and 38.9% LS at this temperature.

$[Fe_2(\mu\text{-}H_2O)(\mu\text{-}RCOO)_2(RCOO)_2(H_2O)_2]$ (R = *p*-$CH_3(CH_2)_9OC_6H_4$) reacted with bpy to form a brownish red solid (yield = 77%). The results of the **elemental analyses** (C, 68.3%; H, 8.0%; N, 2.0%) were in good agreement for $[Fe_2(\mu\text{-}RCOO)_2(RCOO)_2(bpy)]$ (**14**) (C, 68.0%; H, 7.9%; N, 2.0%; FW =

1377.3 g mol^{-1}).

Its **FTIR** data (**Table 4.18**; **Figure 4.120**) show the presence of the expected functional groups and bonds. Hence, the $\Delta\nu_{coo}$ values were 125 cm^{-1} and 164 cm^{-1}, indicating chelating and bridging bidentate *p*-$CH_3(CH_2)_9OC_6H_4COO^-$ ligands.

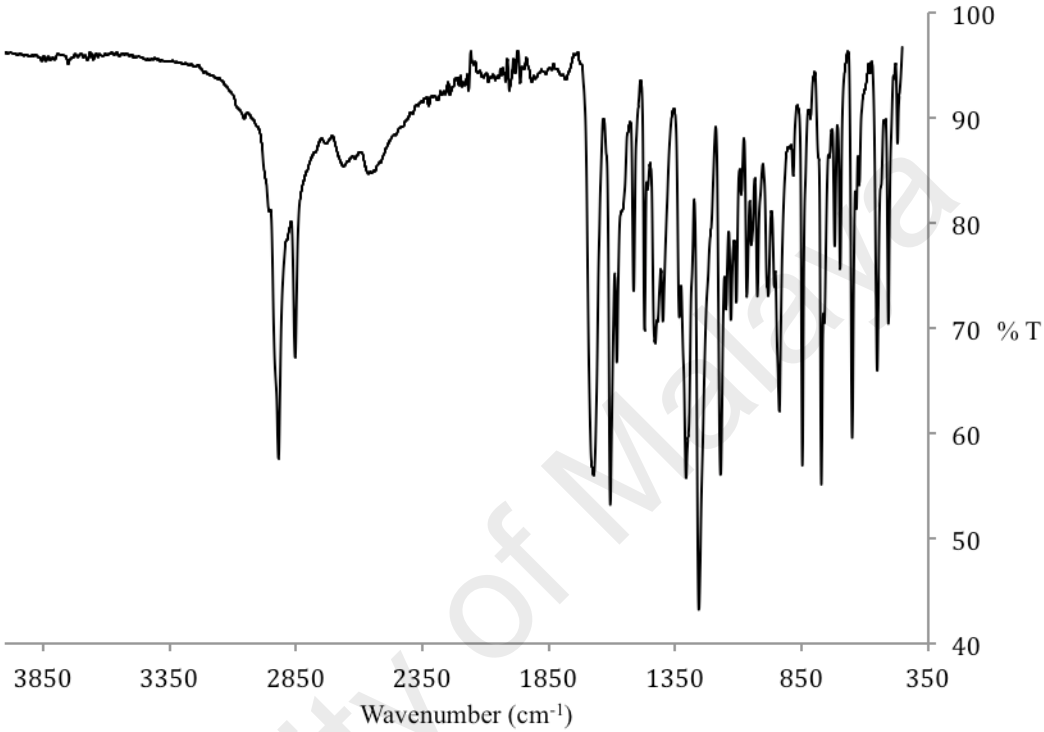

Figure 4.120 FTIR spectrum of **14**

Its **UV-vis** spectrum (**Figure 4.121**) in $CHCl_3$ shows a *d-d* band appearing as a shoulder on the strong CT band at 492 nm (ε = 154 M^{-1} cm^{-1}). The *d-d* peak was assigned to the electronic transition for a LS Fe(II) atom, as explained above.

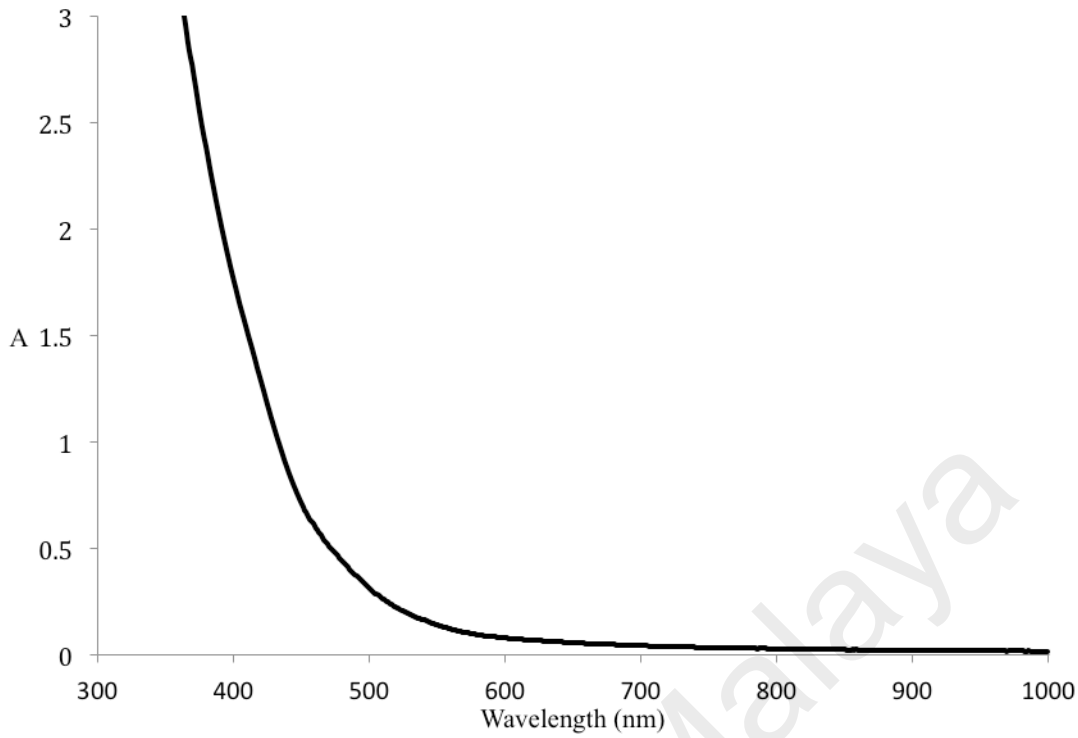

Figure 4.121 UV-vis spectrum of **14**

Its $\chi_M^{corr}T$ value, calculated from the values of its formula weight (FW; 1377.3 g mol^{-1}), mass susceptibility (χ_g; 2.64 x 10^{-6} cm^3 g^{-1}), molar susceptibility (χ_m; 3.64 x 10^{-3} cm^3 mol^{-1}), diamagnetic correction factor (χ_D; -6.89 x 10^{-4} cm^3 mol^{-1}) and corrected molar susceptibility (χ_m^{corr}; 4.32 x 10^{-3} cm^3 mol^{-1}), was 1.29 cm^3 K mol^{-1} at 298 K. Accordingly, **14** was made up of 21.5% HS and 78.5% LS Fe(II) atoms. It is noted that the value of HS was lower than its precursor [$Fe_2(\mu\text{-}H_2O)(\mu\text{-}RCOO)_2(RCOO)_2(H_2O)_2$] (R = *p*-$CH_3(CH_2)_9OC_6H_4$; 61.1% HS and 38.9% LS) at this temperature.

Combining the data above, it is proposed that **14** was dimeric with chelating and bridging bidentate *p*-$CH_3(CH_2)_9OC_6H_4COO^-$ and N-bridging bpy ligands (**Figure 4.122**). Its proposed structure was similar to that reported for [$Fe_2(BEAN)(\mu\text{-}O_2CPhCy)_3$].(OTf), where BEAN = 2,7-bis(*N*,*N*-diethylaminomethyl)-1,8-naphthyridine by He *et al*. [58] and $Fe_2(\mu\text{-}H_2O)(\mu\text{-}O_2CCF_3)_2(\mu\text{-}XDK)(TMEN)_2$], where XDK =

m-xylenediamine Bis(Kemp's triacid imide), and TMEN = *N*,*N*,*N'*,*N'*-tetramethyl-1-diaminoethane by Lippard *et al*. [59], and this may be because the long chain is not directly in the coordination sphere.

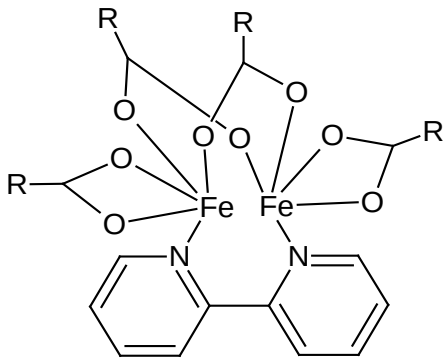

Figure 4.122 Structure of $[Fe_2(\mu\text{-}OOCR)_2(RCOO)_2(bpy)]$ (R = p-$CH_3(CH_2)_9OC_6H_4$)

(b) Thermal and mesomorphic studies

TG trace for **14** (**Figure 4.123**) shows a total weight loss of 91.8% in the temperature range 169 ^oC to 416 ^oC due to decomposition of p-$CH_3(CH_2)_9OC_6H_4COO^-$ ion and bpy ligands (calculated, 91.9%). The results are in good agreement with its proposed structural formula. The amount of residue at temperatures above 416 ^oC was 8.2% (calculated, 8.1% assuming Fe). Hence, its decomposition temperature was 168 ^oC.

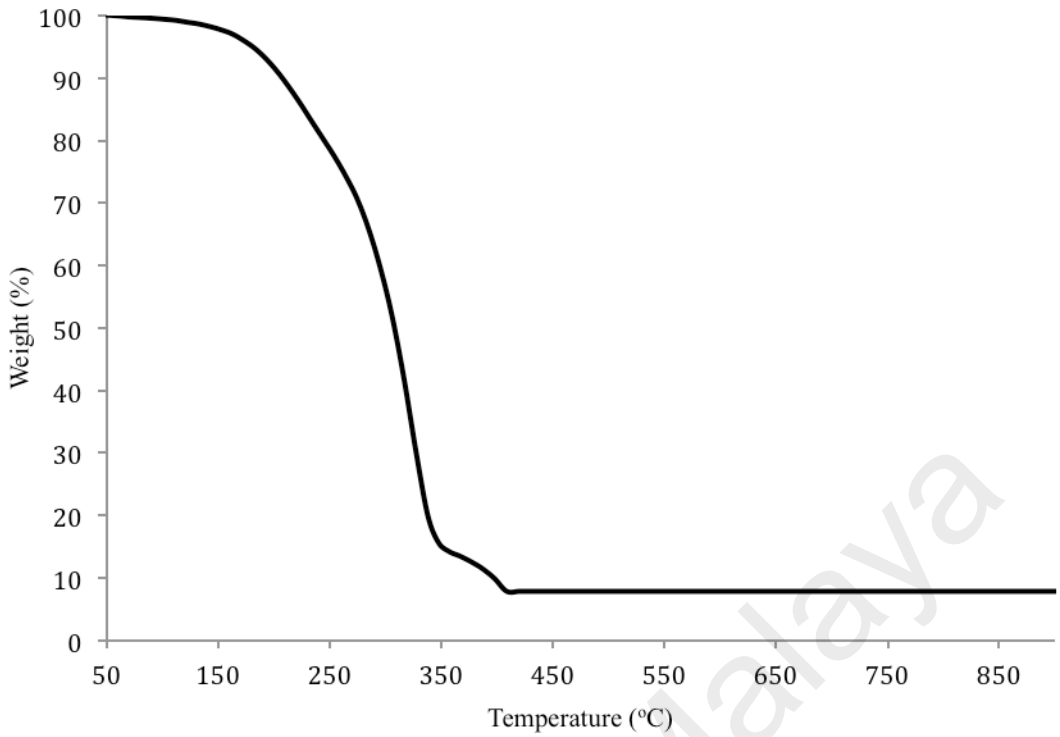

Figure 4.123 TGA trace of **14**

When viewed under **POM**, **14** started to melt at 60 °C, clear at about 94 °C, and then an optical texture was observed on further heating at 101 °C (**Figure 4.124**(**a**)). On cooling from this temperature, different optical textures were observed at 92 °C (**Figure 4.124**(**b**)) and 89 °C (**Figure 4.124**(**c**)). This suggests that on heating, its structure changed to the paddle-wheel structure exhibiting hexagonal columnar mesophase (Col_H) (**Scheme 4.5**). On cooling, the Col_H mesophase coalesced to a mosaic texture with homeotropic region that persisted on further cooling to room temperature. Similar behavior was observed for $[Cu_2(R)_4(bpy)]x$; R = 2- hexyldecanoate ion and bpy = 4,4'-bipyridine [49].

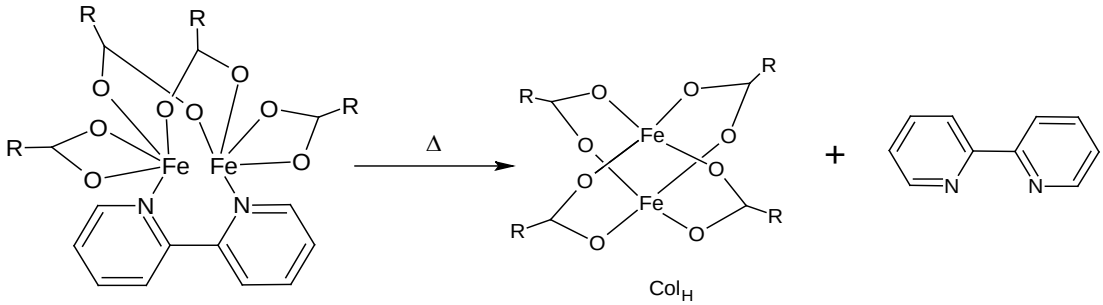

Scheme 4.5 The change in the structure for **14** on heating

For comparison its precursor complex, $[Fe_2(\mu\text{-}H_2O)(\mu\text{-}RCOO)_2(RCOO)_2(H_2O)_2]$ (R = p-$CH_3(CH_2)_9OC_6H_4$), was observed to melt at 130 ^oC and to clear to an isotropic liquid at 160 ^oC. Upon cooling from this temperature, optical textures different from **14** were observed at 127 ^oC (**Figure 4.124**(**d**)). These observations indicate that both **14** and its precursor complex behaved as different thermotropic metallomesogens.

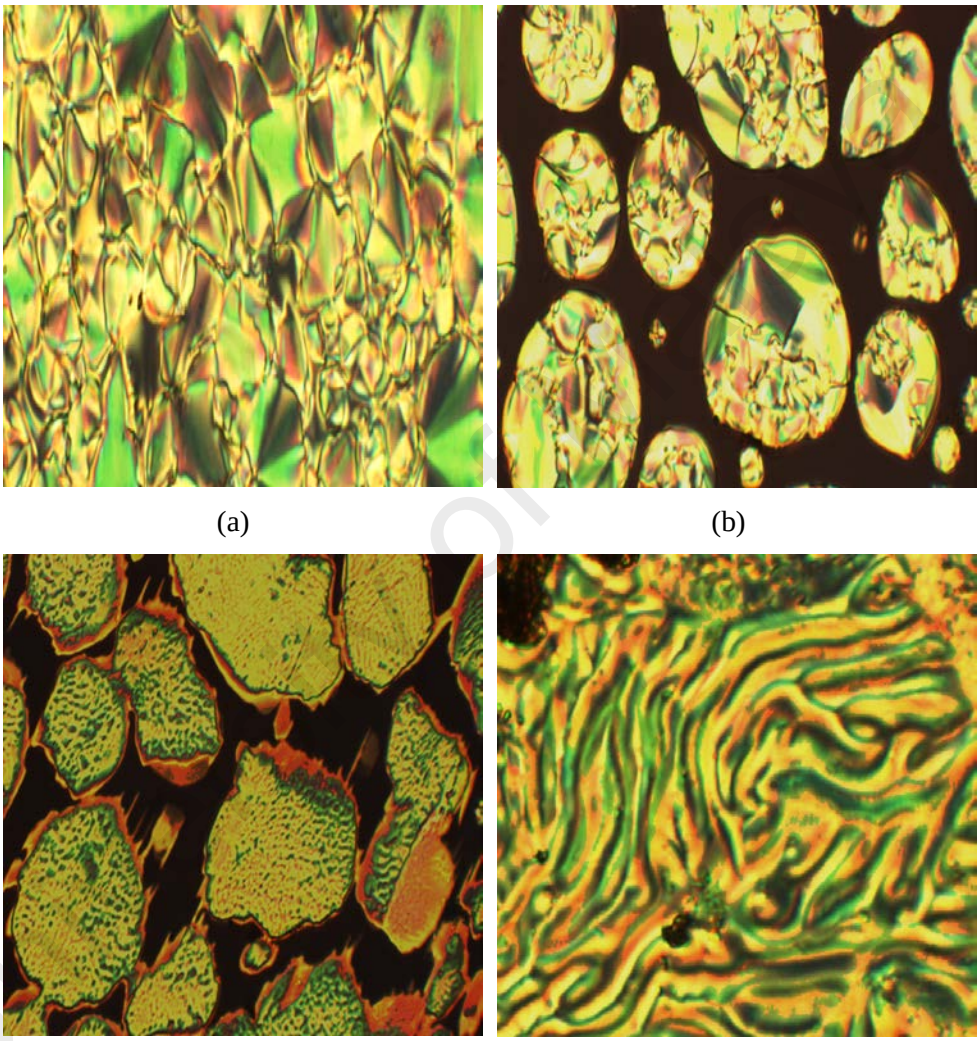

(a) (b) (c) (d)

Figure 4.124 Photomicrographs of: (a) **14** on heating at 101 ^oC; (b) **14** on cooling at 92 ^oC; (c) **14** on cooling at 89 ^oC; and (d) $[Fe_2(\mu\text{-}H_2O)(\mu\text{-}RCOO)_2(RCOO)_2(H_2O)_2]$ (R = p-$CH_3(CH_2)_9OC_6H_4$) on cooling at 127 ^oC

The **DSC** traces for **14** (**Figure 4.125**) shows an endothermic peaks at 59 ^oC (ΔH = +31 kJ mol^{-1}) assigned to its melting temperature, and two overlapping endothermic peaks at 87 ^oC ($\Delta H_{combined}$ = +90 kJ mol^{-1}) assigned to the breaking of the Fe-N(bpy) and Fe-O bridging bonds. On cooling, there were a weak exothermic peak at

100 °C (ΔH = -3 kJ mol^{-1}) and two endothermic peaks at 87 °C (ΔH = -24 kJ mol^{-1}) and 78 °C (ΔH = -23 kJ mol^{-1}) assigned to the formation of the paddle-wheel dimer, Col_H-*M1* and *M1-Cr* transitions, respectively. These results are in agreement with observations from POM.

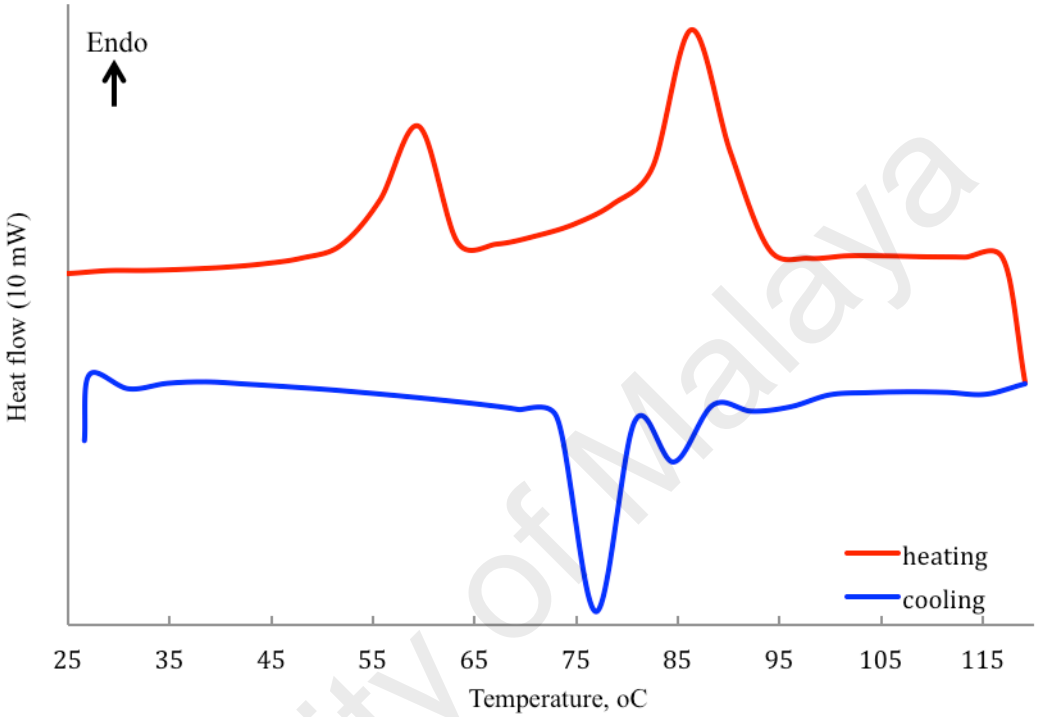

Figure 4.125 DSC scans of **14**

4.4.2 [$Fe_2(\mu$-RCOO$)_2$(RCOO$)_2$(bpy)] (R = p-$CH_3(CH_2)_{11}OC_6H_4$) (15)

(a) Synthesis and structural elucidation

The precursor complex, [$Fe_2(\mu$-$H_2O)(\mu$-RCOO$)_2$(RCOO$)_2(H_2O)_2$].H_2O (R = *p*-$CH_3(CH_2)_{11}OC_6H_4$), was obtained as a brown powder with 49% yield from the reaction of *p*-$CH_3(CH_2)_{11}OC_6H_4COOK$ with $FeSO_4.7H_2O$. The results of its **elemental analyses** (C, 64.6%; H, 9.6%) were in good agreement with the calculated values (C, 64.9%; H, 8.9%; FW 1405.4 g mol^{-1}). Its **FTIR** data (**Table 4.18**; **Figure 4.126**) show the presence of the expected functional groups and bonds. Hence, the $\Delta\nu_{coo}$ values were 124 cm^{-1} and 163 cm^{-1}, indicating that *p*-$CH_3(CH_2)_{11}OC_6H_4COO^-$ ion was coordinated as chelating and bridging bidentate ligands, respectively (The $\Delta\nu_{coo}$ value for *p*-$CH_3(CH_2)_{11}OC_6H_4COO^-$ ion was 150 cm^{-1}).

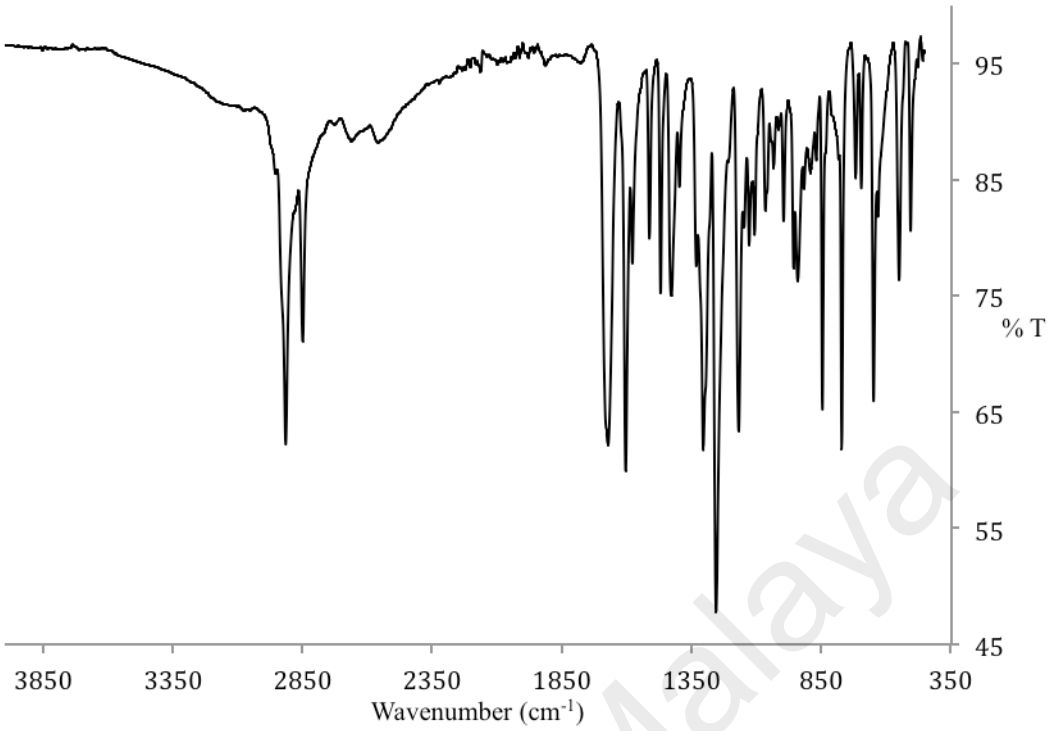

Figure 4.126 FTIR spectrum of $[Fe_2(\mu\text{-}H_2O)(\mu\text{-}RCOO)_2(RCOO)_2(H_2O)_2].H_2O$ ($R = p\text{-}CH_3(CH_2)_{11}OC_6H_4$)

Its **UV-vis** spectrum (**Figure 4.127**) in $CHCl_3$ shows a continuously increasing absorbance from about 800 nm with a *d-d* band appearing as a shoulder on the strong CT band at 486 nm (ε = 1392 M^{-1} cm^{-1}). The *d-d* peak was assigned to the electronic transition for a LS Fe(II) atom, as explained above.

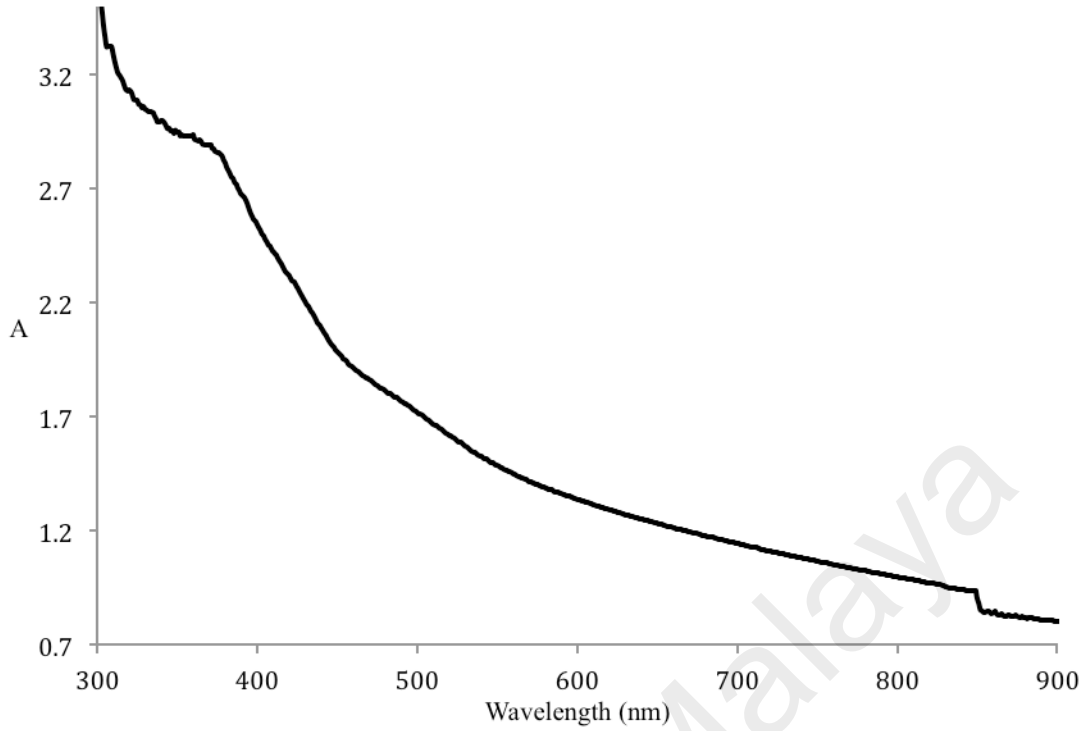

Figure 4.127 UV-vis spectrum of $[Fe_2(\mu\text{-}H_2O)(\mu\text{-}RCOO)_2(RCOO)_2(H_2O)_2].H_2O$ ($R = p\text{-}CH_3(CH_2)_{11}OC_6H_4$)

Its $\chi_M^{corr}T$ value, calculated from the values of its formula weight (FW = 1405.4 g mol^{-1}), mass susceptibility (χ_g = 6.78 x 10^{-6} cm^3 g^{-1}), molar susceptibility (χ_m = 9.53 x 10^{-3} cm^3 mol^{-1}), diamagnetic correction factor (χ_D = -7.03 x 10^{-4} cm^3 mol^{-1}) and corrected molar susceptibility (χ_m^{corr} = 1.02 x 10^{-2} cm^3 mol^{-1}), was 3.04 cm^3 K mol^{-1} at 298 K. Accordingly, this complex was made up of 50.7% HS and 49.3% LS Fe(II) atoms at this temperature.

$[Fe_2(\mu\text{-}H_2O)(\mu\text{-}RCOO)_2)(RCOO)_2(H_2O)_2].H_2O$ ($R = p\text{-}CH_3(CH_2)_{11}OC_6H_4$) reacted with bpy to form a brownish red solid (yield = 74%). The results of the **elemental analyses** (C, 70.0%; H, 8.0%; N, 2.3%) were in good agreement for $[Fe_2(\mu\text{-}RCOO)_2(RCOO)_2(bpy)]$ (**15**) (C, 69.3%; H, 8.4%; N, 1.9%; FW = 1489.5 g mol^{-1}).

Its **FTIR** data (**Table 4.18**; **Figure 4.128**) show the presence of the expected functional groups and bonds. Hence, the $\Delta\nu_{coo}$ values were 109 cm^{-1} and 161 cm^{-1},

indicating chelating and bridging bidentate *p*-$CH_3(CH_2)_{11}OC_6H_4COO^-$ ligands, respectively.

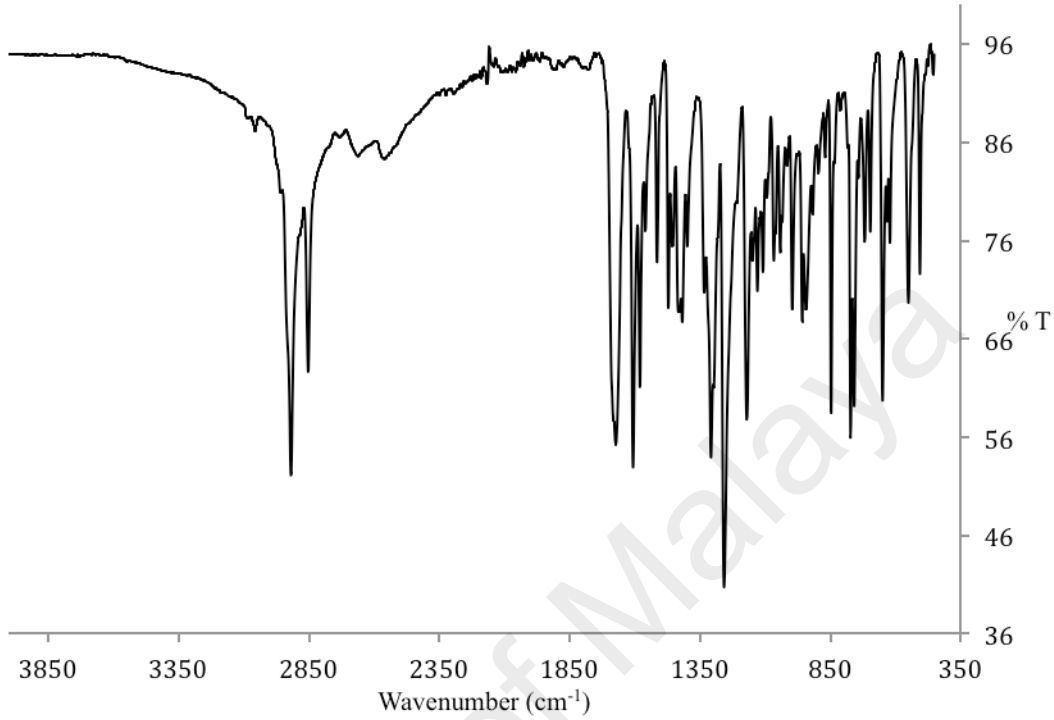

Figure 4.128 FTIR spectrum of **15**

Its **UV-vis** spectrum (**Figure 4.129**) in $CHCl_3$ shows a *d-d* band appearing as a shoulder on the strong CT band at 511 nm (ε = 340 M^{-1} cm^{-1}). The *d-d* peak was assigned to the electronic transition for a LS Fe(II) atom, as explained above.

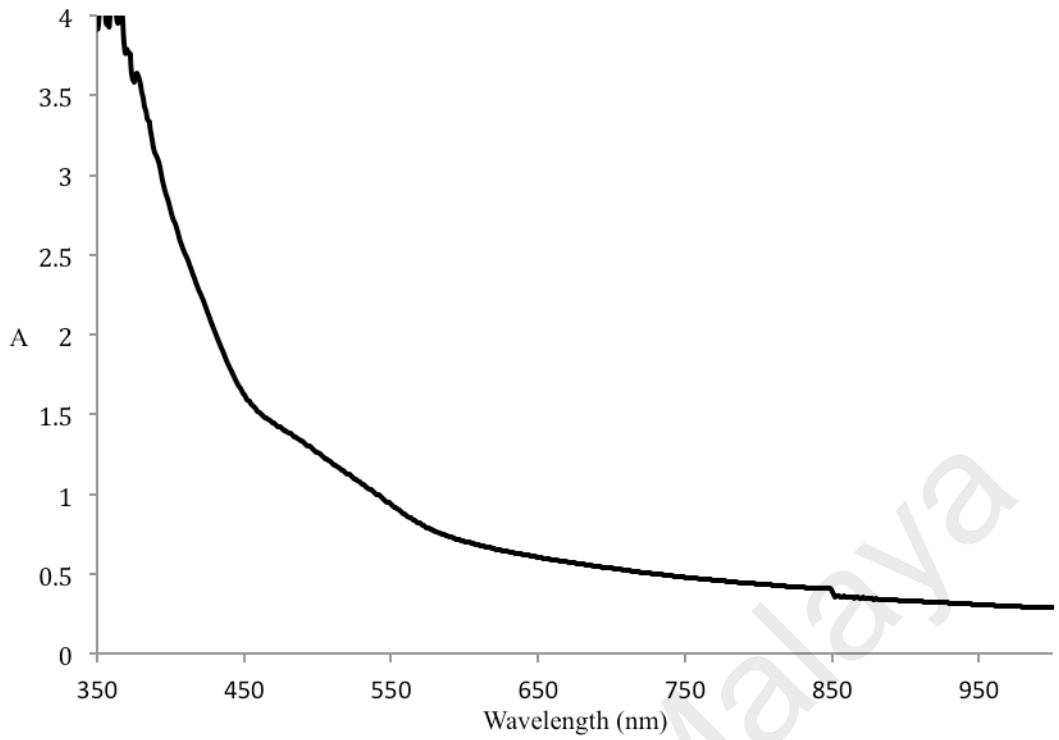

Figure 4.129 UV-vis spectrum of **15**

Its $\chi_M^{corr}T$ value, calculated from the values of its formula weight (FW; 1489.54 g mol^{-1}), mass susceptibility (χ_g; 2.22 x 10^{-6} cm^3 g^{-1}), molar susceptibility (χ_m; 3.30 x 10^{-3} cm^3 mol^{-1}), diamagnetic correction factor (χ_D; -7.45 x 10^{-4} cm^3 mol^{-1}) and corrected molar susceptibility (χ_m^{corr}; 4.05 x 10^{-3} cm^3 mol^{-1}), was 1.21 cm^3 K mol^{-1} at 298 K. Accordingly, **15** was made up of 20.2% HS and 79.8% LS Fe(II) atoms at this temperature.

(b) Thermal and mesomorphic studies

TG trace for **15** (**Figure 4.130**) shows a total weight loss of 93.2% in the temperature range 172 ^oC to 492 ^oC due to decomposition of *p*-$CH_3(CH_2)_{11}OC_6H_4COO^-$ and bpy ligands (calculated, 92.5%). The results are in good agreement with its proposed structural formula. The amount of residue at temperatures above 492 ^oC was 6.8% (calculated, 7.5% assuming pure Fe). Hence, its decomposition temperature was 172 ^oC.

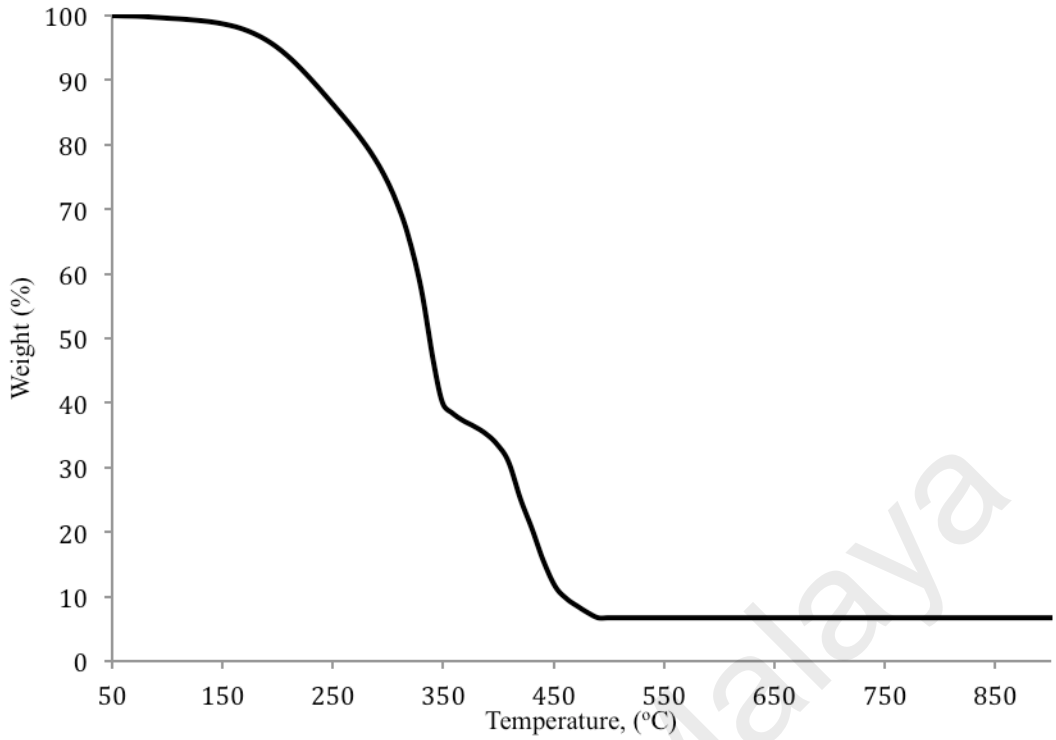

Figure 4.130 TGA trace of **15**

When viewed under **POM**, **15** started to melt at 85 °C and to clear at about 95 °C. On cooling from *I*, different optical textures were observed at 92 °C (**Figure 4.131**(**a**)) and 85 °C (**Figure 4.131**(**b**)), indicating structural rearrangement to form a dimeric paddlewheel structure and a nematic mesophase (N), respectively. This was similar to **14** and may be similarly explained.

For comparison its precursor complex, $[Fe_2(\mu\text{-}H_2O)(\mu\text{-}RCOO)_2(RCOO)_2(H_2O)_2].H_2O$ (R = $p\text{-}CH_3(CH_2)_{11}OC_6H_4$), was observed to melt at 99 °C and to clear to an isotropic liquid at 160 °C. Upon cooling from this temperature, optical textures different from **15** were observed at 100 °C (**Figure 4.131**(**c**)). These observations indicate that both **15** and its precursor complex behaved as different thermotropic metallomesogens.

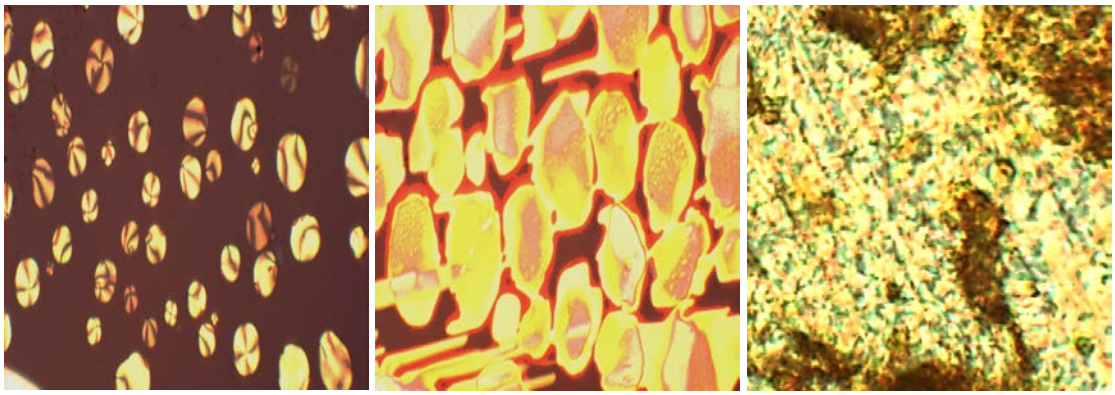

(a) (b) (c)

Figure 4.131 Photomicrographs of: (a) **15** on cooling at 92 ^{o}C; (b) **15** on cooling at 85 ^{o}C; and (c) $[Fe_2(\mu\text{-}H_2O)(\mu\text{-}RCOO)_2(RCOO)_2(H_2O)_2].H_2O$ (R = $p\text{-}CH_3(CH_2)_{11}OC_6H_4$) on cooling at 100 ^{o}C

The **DSC** traces for **15** (**Figure 4.132**) shows two endothermic peaks at 76 ^{o}C (ΔH = +13 kJ mol^{-1}) assigned to *Cr2-M* transition, and at 86 ^{o}C (ΔH = +17 kJ mol^{-1}) assigned to *M-I* transition. On cooling, a weak exothermic peak at 101 ^{o}C (ΔH = -4 kJ mol^{-1}) and two endothermic peaks at 82 ^{o}C (ΔH = -32 kJ mol^{-1}) and at 66 ^{o}C (ΔH = -21 kJ mol^{-1}) assigned to *I-M1*, *M1-M2* and *M2-Cr* transitions, respectively.

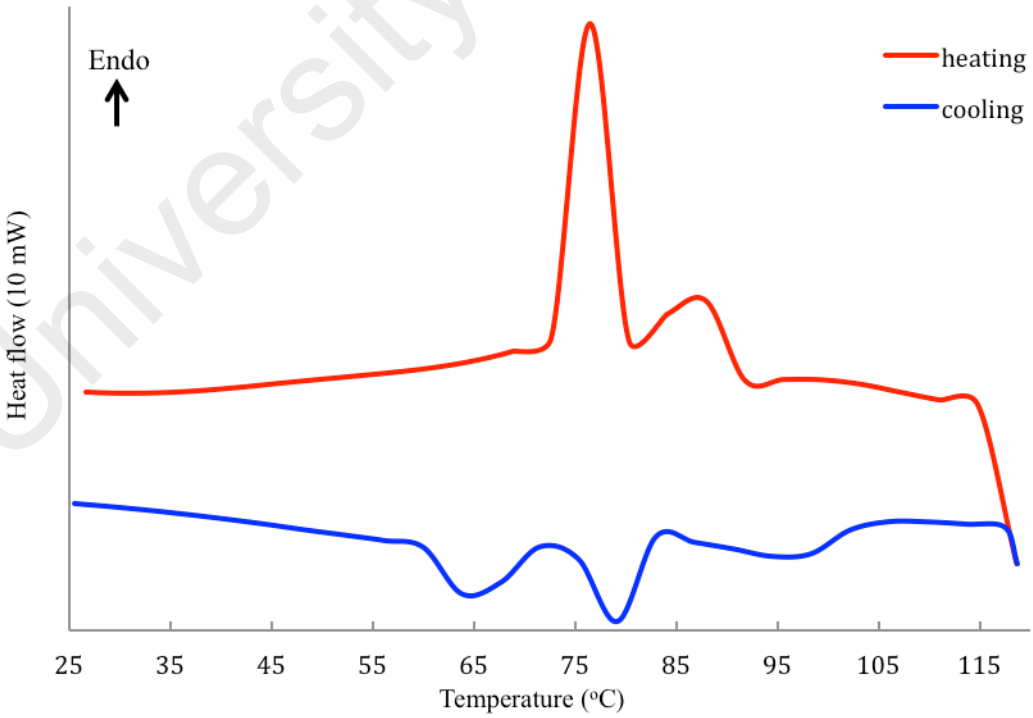

Figure 4.132 DSC scans of **15**

4.4.3 [Fe(p-$CH_3(CH_2)_{13}OC_6H_4COO)_2$(bpy)] (16)

(a) Synthesis and structural elucidation

The precursor complex, $[Fe_2(\mu\text{-}H_2O)(\mu\text{-}RCOO)_2(RCOO)_2(H_2O)_2]$ (R = *p*-$CH_3(CH_2)_{13}OC_6H_4COO$), was obtained as a brown powder in good yield (55%) from the reaction of *p*-$CH_3(CH_2)_{13}OC_6H_4COOK$ with $[FeSO_4.7H_2O]$. The results of its **elemental analyses** (C, 66.6%; H, 9.6%) were in good agreement with the calculated values (C, 67.3%; H, 9.3%; FW 1499.6 g mol^{-1}). Its **FTIR** data (**Table 4.18**; **Figure 4.133**) shows the presence of the expected functional groups. Hence, the $\Delta\nu_{coo}$ values were 126 cm^{-1} and 164 cm^{-1} indicating that *p*-$CH_3(CH_2)_{13}OC_6H_4COO^-$ was coordinated as a chelating and bridging bidentate ligands, respectively (the $\Delta\nu_{coo}$ value for *p*-$CH_3(CH_2)_{13}OC_6H_4COO^-$ ion was 149 cm^{-1}).

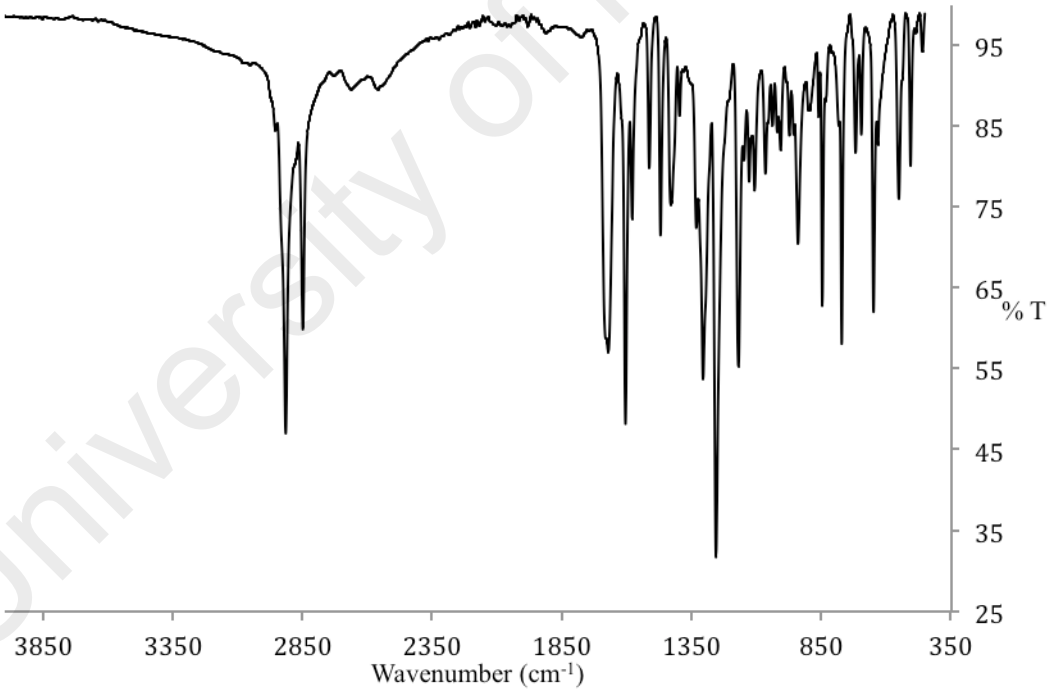

Figure 4.133 FTIR spectrum of $[Fe_2(\mu\text{-}H_2O)(\mu\text{-}RCOO)_2(RCOO)_2(H_2O)_2]$ (R = *p*-$CH_3(CH_2)_{13}OC_6H_4COO$)

Its **UV-vis** spectrum (**Figure 4.134**) in $CHCl_3$ shows a *d-d* band appearing as a shoulder on the strong CT band at 493 nm (ε = 751 M^{-1} cm^{-1}). The *d-d* peak was assigned to the electronic transition for a LS Fe(II) atom, as explained above.

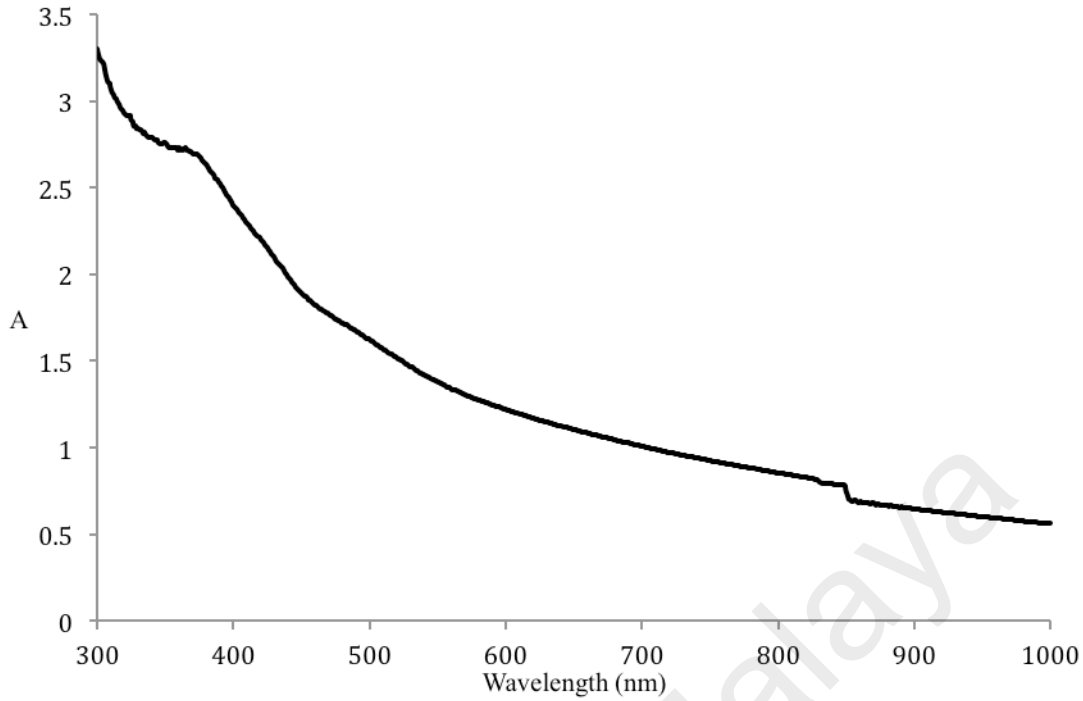

Figure 4.134 UV-vis spectrum of $[Fe_2(\mu\text{-}H_2O)(\mu\text{-}RCOO)_2(RCOO)_2(H_2O)_2]$ (R = p-$CH_3(CH_2)_{13}OC_6H_4COO$)

Its $\chi_M^{corr}T$ value, calculated from the values of its formula weight (FW = 1499.6 g mol^{-1}), mass susceptibility (χ_g = 4.98 x 10^{-6} cm^3 g^{-1}), molar susceptibility (χ_m = 7.47 x 10^{-3} cm^3 mol^{-1}), diamagnetic correction factor (χ_D = -7.50 x 10^{-4} cm^3 mol^{-1}) and corrected molar susceptibility (χ_m^{corr} = 8.22 x 10^{-3} cm^3 mol^{-1}), was 2.45 cm^3 K mol^{-1} at 298 K. Accordingly, this complex was made up of 40.8% HS and 59.2% LS at this temperature.

$[Fe_2(\mu\text{-}H_2O)(\mu\text{-}RCOO)_2(RCOO)_2(H_2O)_2]$ (R = p-$CH_3(CH_2)_{13}OC_6H_4COO$) reacted with bpy to form a red solid (yield = 97%). The results of the **elemental analyses** (C, 70.6%; H, 8.2%; N, 3.4%) were in good agreement for $[Fe(p\text{-}CH_3(CH_2)_{13}OC_6H_4COO)_2(bpy)]$ (**16**) (C, 71.1%; H, 8.5%; N, 3.2%; FW = 878.9 g mol^{-1}).

Its **FTIR** data (**Table 4.18**; **Figure 4.135**) shows the presence of the expected functional groups. Hence, the $\Delta\nu_{coo}$ value was 128 cm^{-1}, indicating chelating p-$CH_3(CH_2)_{13}OC_6H_4COO^-$ ligand.

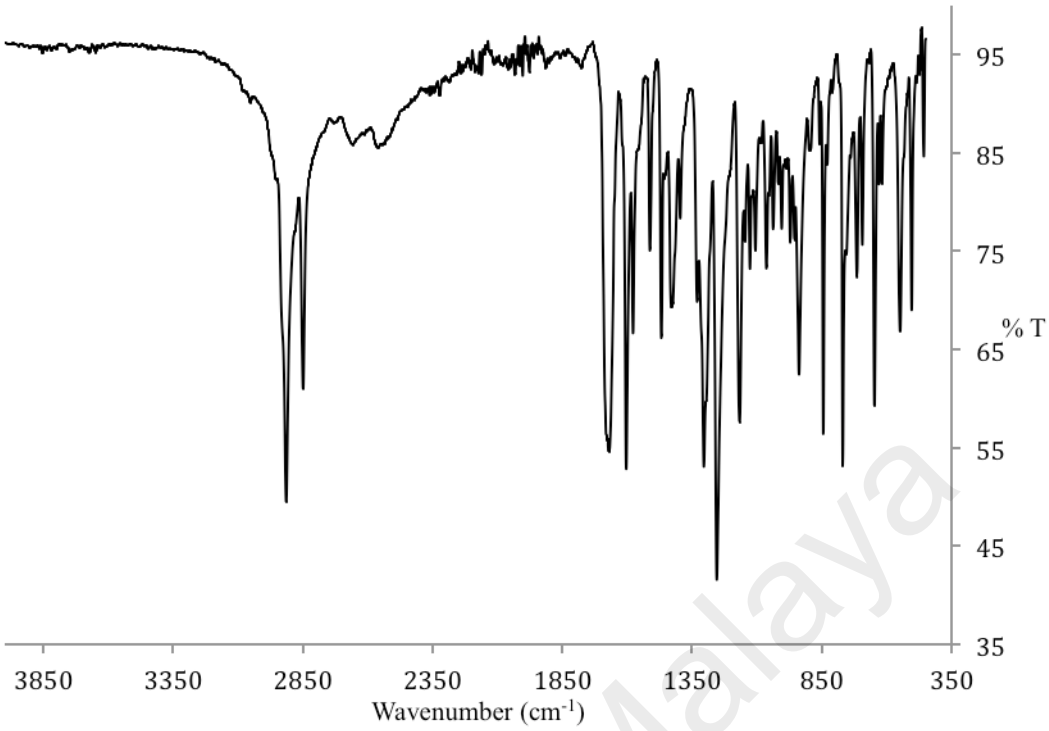

Figure 4.135 FTIR spectrum of **16**

Its **UV-vis** spectrum (**Figure 4.136**) in $CHCl_3$ shows a *d-d* band appearing as a shoulder on the strong CT band at 511 nm ($\varepsilon = 26\ M^{-1}\ cm^{-1}$). The *d-d* peak was assigned to the electronic transition for a LS Fe(II) atom, as explained above.

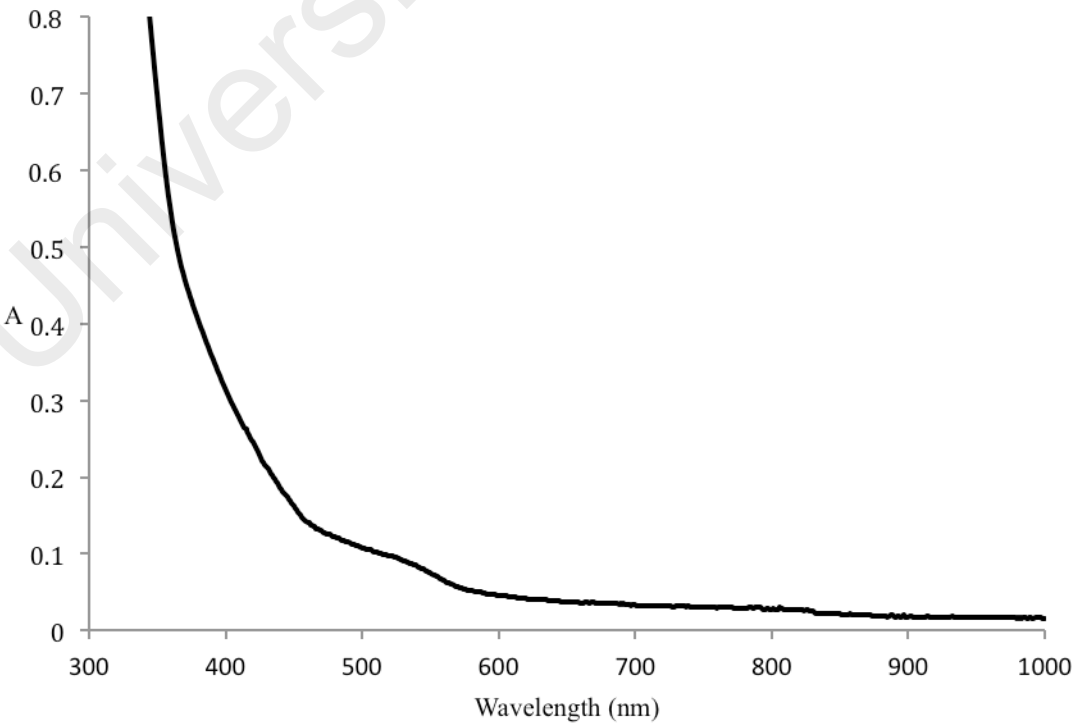

Figure 4.136 UV-vis spectrum of **16**

Its mass susceptibility was 0. Hence, **16** was diamagnetic (made up of 100% LS Fe(II) atoms).

(b) Thermal and mesomorphic studies

TG trace for **16** (**Figure 4.137**) shows a total weight loss of 91.9% in the temperature range 161 ^{o}C to 469 ^{o}C due to decomposition of *p*-$CH_3(CH_2)_{13}OC_6H_4COO^-$ and bpy ligands (calculated, 93.6%). The results are in good agreement with its proposed structural formula. The amount of residue at temperatures above 469 ^{o}C was 8.1% (calculated, 8.2% assuming FeO). Hence, its decomposition temperature was 161 ^{o}C.

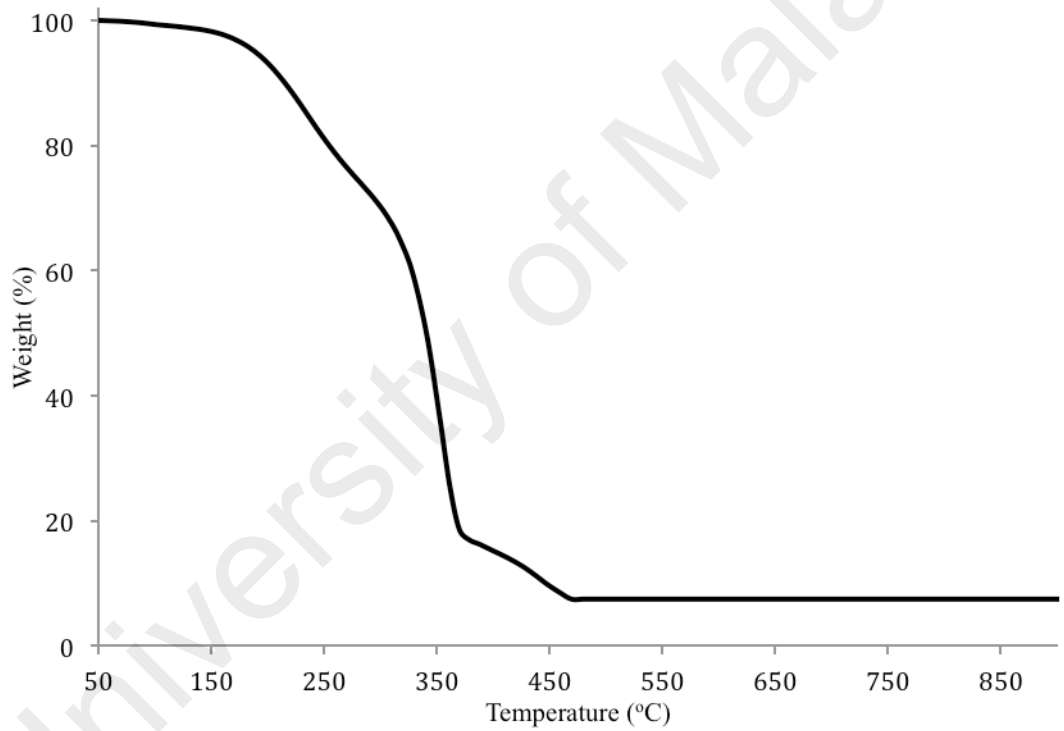

Figure 4.137 TGA trace of **16**

When viewed under **POM**, **16** started to melt at 86 ^{o}C and to clear at about 110 ^{o}C. On cooling from *I*, different optical textures were observed at 100 ^{o}C (**Figure 4.138**(**a**)), and 92 ^{o}C (**Figure 4.138(b))**, indicating formation of nematic globule mesophase (N). This was similarly explained as above.

In comparison, its precursor complex, $[Fe_2(\mu\text{-}H_2O)(\mu\text{-}RCOO)_2(RCOO)_2(H_2O)_2]$ (R = *p*-$CH_3(CH_2)_{13}OC_6H_4COO$) was observed to melt at 102 ^{o}C and to clear to an

isotropic liquid at 135 ^{o}C. Upon cooling from this temperature, optical textures different from **16** were observed at 90 ^{o}C (**Figure 4.138**(**c**)). These observations indicate that both **16** and its precursor complex behaved as different thermotropic metallomesogens.

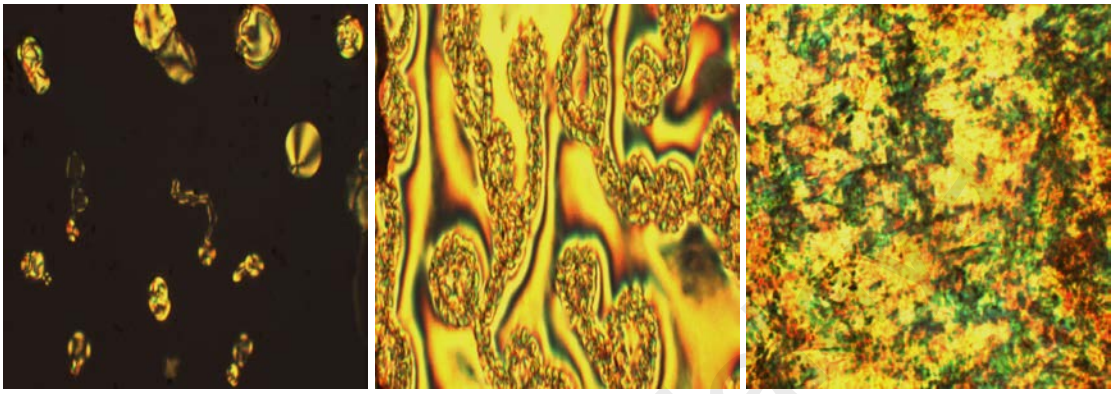

(a) (b) (c)

Figure 4.138 Photomicrographs of: (a) **16** on cooling at 100 ^{o}C; (b) **16** on cooling at 92 ^{o}C; and (c) $[Fe_2(\mu\text{-}H_2O)(\mu\text{-}RCOO)_2(RCOO)_2(H_2O)_2]$ (R = p-$CH_3(CH_2)_{13}OC_6H_4COO$) on cooling at 90 ^{o}C

The **DSC** traces for **16** (**Figure 4.139**) shows an overlapping endothermic peaks at onset 85 ^{o}C ($\Delta H_{combined}$ = +23 kJ mol^{-1}) assigned to *Cr2-M* and *M-I* transitions. On cooling, there was a weak exothermic peak at 101 ^{o}C (ΔH = -4 kJ mol^{-1}) assigned to *I-M1* transition, an endothermic peak at 82 ^{o}C (ΔH = -32 kJ mol^{-1}) assigned to *M1-M2* transition, and an endothermic peak at 31 ^{o}C (ΔH = -30 kJ mol^{-1}) assigned to *M2-Cr* transition.

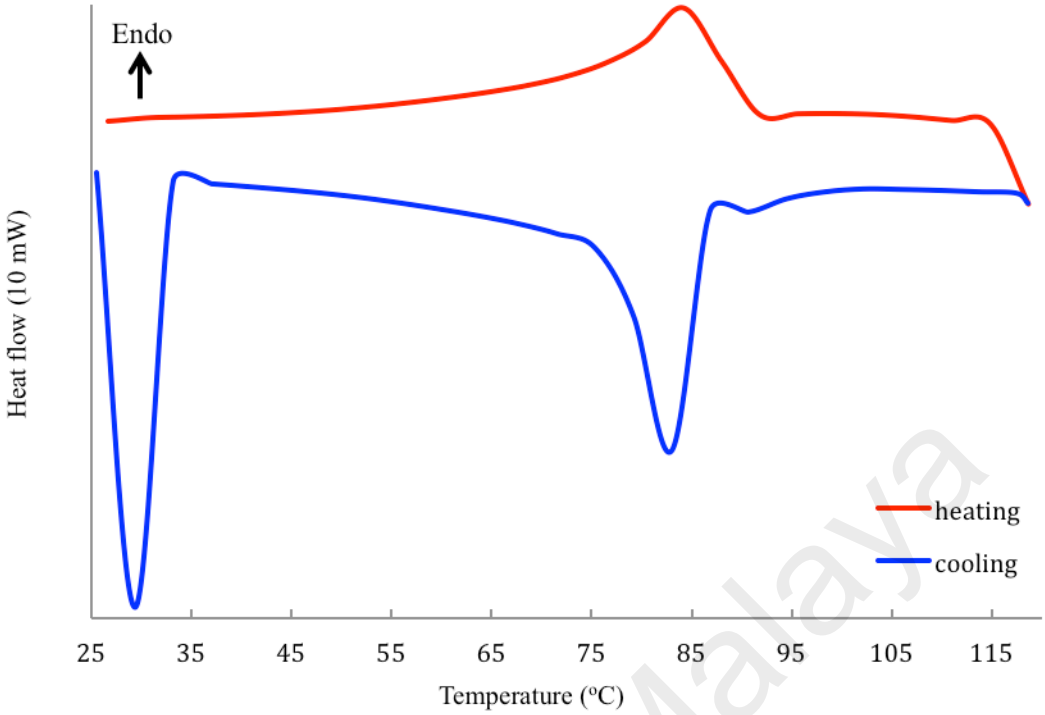

Figure 4.139 DSC scans of **16**

4.4.4 [Fe(p-CH$_3$(CH$_2$)$_{15}$OC$_6$H$_4$COO)$_2$(bpy)] (17)

(a) Synthesis and structural elucidation

The precursor complex, [Fe$_2$(μ-H$_2$O)(μ-RCOO)$_2$(RCOO)$_2$(H$_2$O)$_2$] (R = *p*-CH$_3$(CH$_2$)$_{15}$OC$_6$H$_4$), was obtained as a brown powder with 42% yield from the reaction of *p*-CH$_3$(CH$_2$)$_{15}$OC$_6$H$_4$COOK with FeSO$_4$.7H$_2$O. The results of its **elemental analyses** (C, 68.9%; H, 9.4%) were in good agreement with the calculated values (C, 68.6%; H, 9.6%; FW 1611.8 g mol^{-1}). Its **FTIR** data (**Table 4.18**; **Figure 4.140**) shows the presence of the expected functional groups. Hence, the $\Delta\nu_{coo}$ values were 122 cm^{-1} and 165 cm^{-1}, indicating that *p*-CH$_3$(CH$_2$)$_{15}$OC$_6$H$_4$COO$^-$ ion was coordinated as a chelating and bridging bidentate ligands, respectively (the $\Delta\nu_{coo}$ value for *p*-CH$_3$(CH$_2$)$_{15}$OC$_6$H$_4$COO$^-$ ion was 148 cm^{-1}).

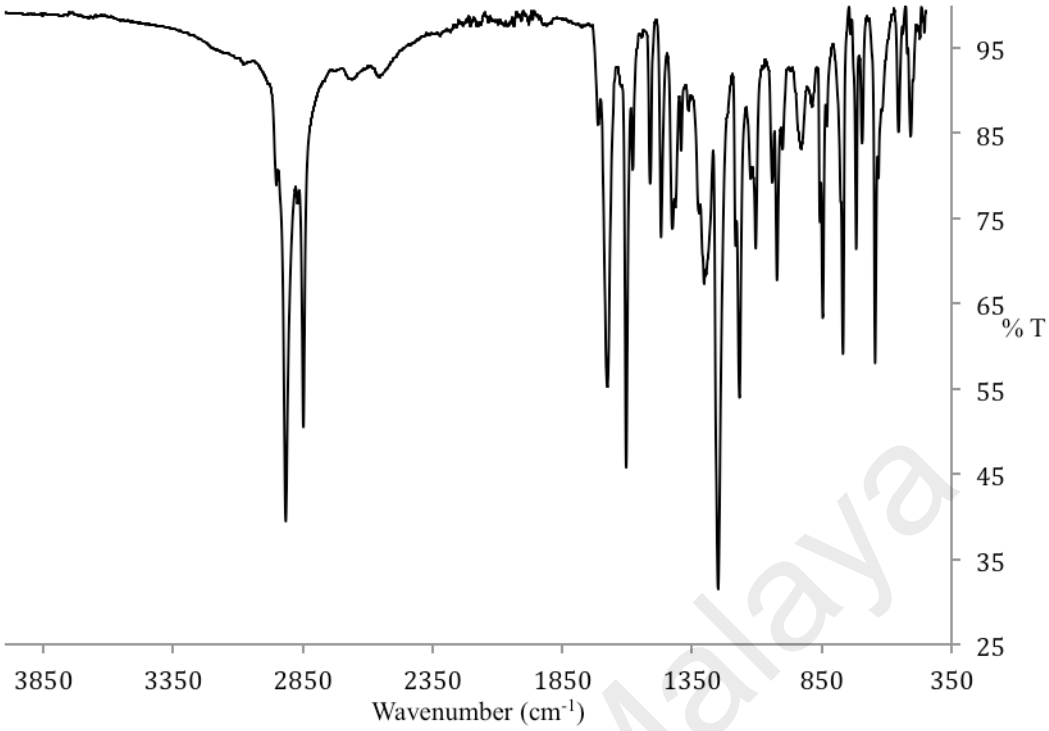

Figure 4.140 FTIR spectrum of $[Fe_2(\mu\text{-}H_2O)(\mu\text{-}RCOO)_2(RCOO)_2(H_2O)_2]$ (R = p-$CH_3(CH_2)_{15}OC_6H_4$)

Its **UV-vis** spectrum (**Figure 4.141**) in $CHCl_3$ shows a *d-d* band appearing as a shoulder on the strong CT band at 594 nm (ε = 751 M^{-1} cm^{-1}). The *d-d* peak was assigned to the electronic transition for a LS Fe(II) atom, as explained above.

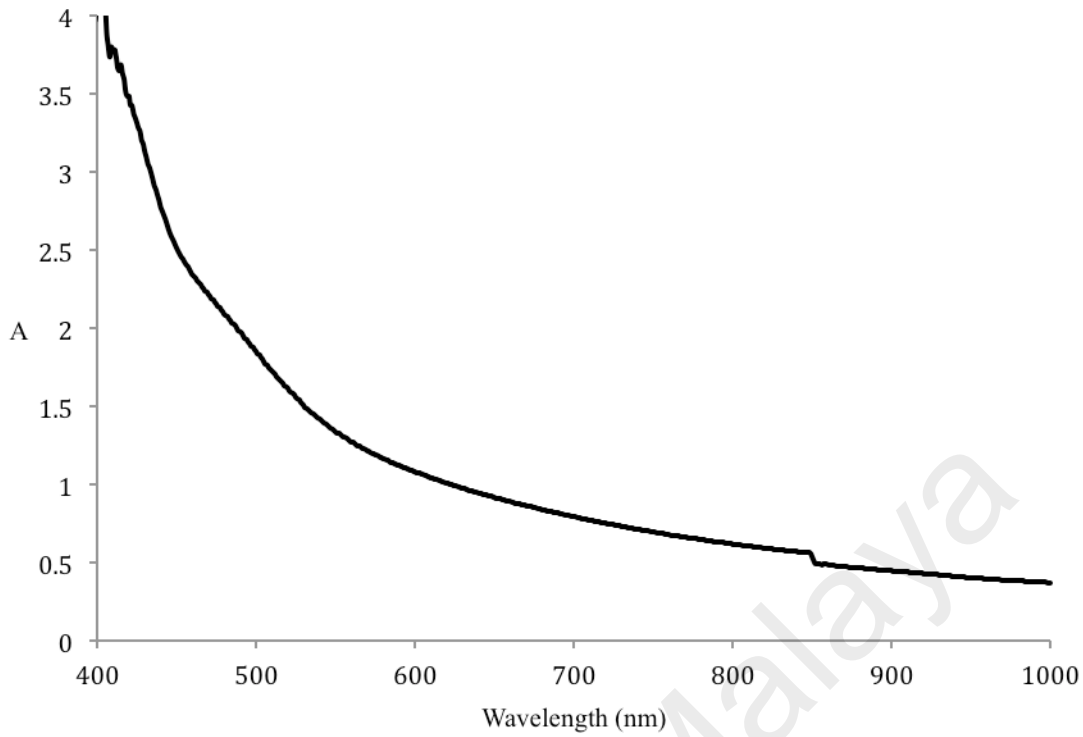

Figure 4.141 UV-vis spectrum of $[Fe_2(\mu\text{-}H_2O)(\mu\text{-}RCOO)_2(RCOO)_2(H_2O)_2]$ (R = p-$CH_3(CH_2)_{15}OC_6H_4$)

Its $\chi_M^{corr}T$ value, calculated from the values of its formula weight (FW = 1611.8 g mol^{-1}), mass susceptibility (χ_g = 3.87 x 10^{-6} cm^3 g^{-1}), molar susceptibility (χ_m = 6.24 x 10^{-3} cm^3 mol^{-1}), diamagnetic correction factor (χ_D = -8.06 x 10^{-4} cm^3 mol^{-1}) and corrected molar susceptibility (χ_m^{corr} = 7.04 x 10^{-3} cm^3 mol^{-1}), was 2.10 cm^3 K mol^{-1} at 298 K. Accordingly, this complex was made up of 34.9% HS and 65.1% LS at this temperature.

$[Fe_2(\mu\text{-}H_2O)(\mu\text{-}RCOO)_2(RCOO)_2(H_2O)_2]$ (R = p-$CH_3(CH_2)_{15}OC_6H_4$) reacted with bpy to form a red solid(yield = 80%). The results of the **elemental analyses** (C, 71.5%; H, 8.1%; N, 2.7%) were in good agreement for $[Fe(R)_2(bpy)]$ (**17**) (C, 71.9%; H, 8.8%; N, 3.0%; FW = 1489.5 g mol^{-1}).

Its **FTIR** data (**Table 4.18**; **Figure 4.142**) shows the presence of the expected functional groups and bonds. Hence, the $\Delta\nu_{coo}$ value was 127 cm^{-1}, indicating chelating p-$CH_3(CH_2)_{15}OC_6H_4COO^-$ ligands.

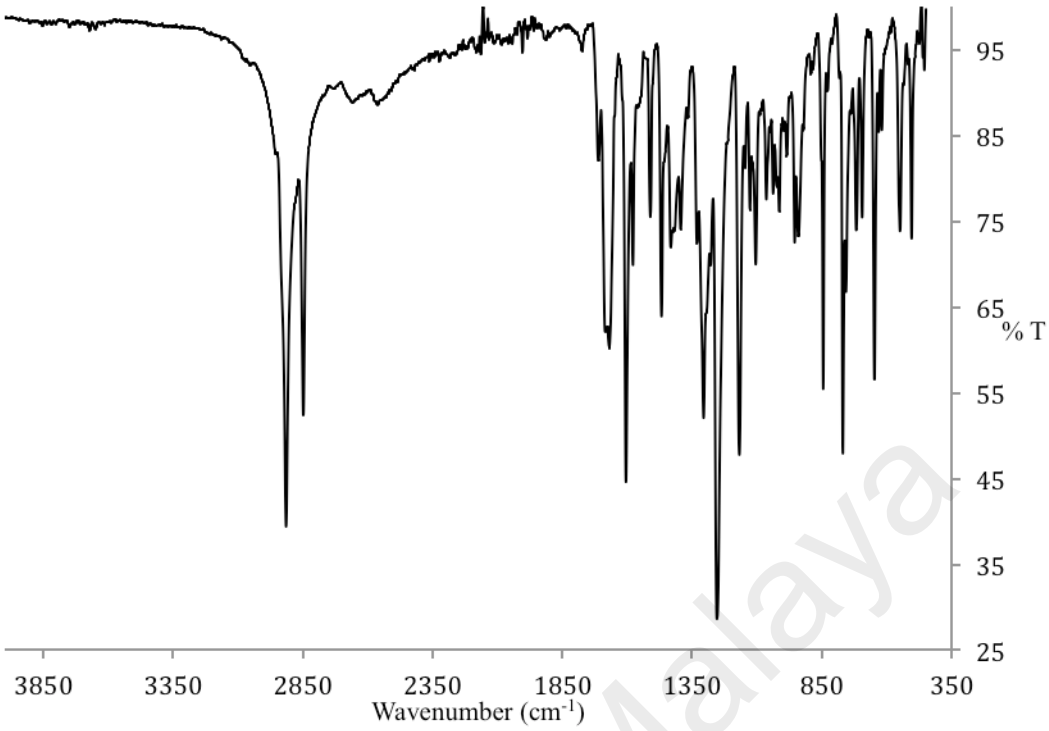

Figure 4.142 FTIR spectrum of **17**

Its **UV-vis** spectrum (**Figure 4.143**) in $CHCl_3$ shows a *d-d* band appearing as a shoulder on the strong CT band at 422 nm (ε = 255 M^{-1} cm^{-1}). The *d-d* peak was assigned to the electronic transition for a LS Fe(II) atom, as explained above.

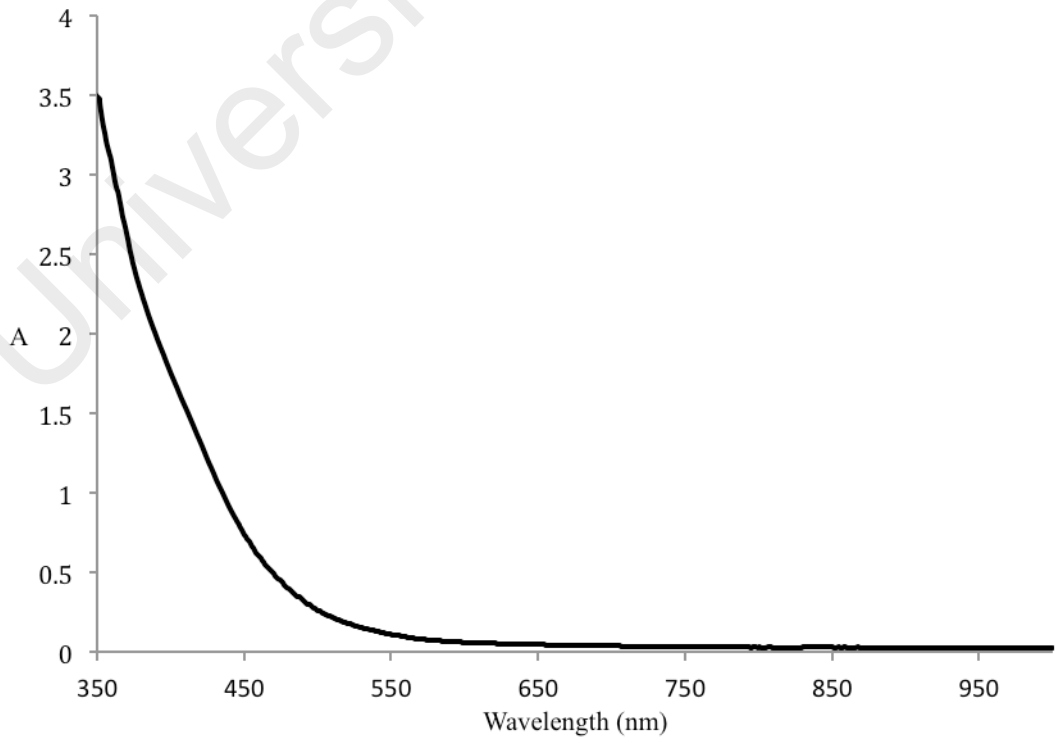

Figure 4.143 UV-vis spectrum of **17**

Its mass susceptibility was 0. Hence, **17** was diamagnetic (made up of 100% LS Fe(II) atoms).

(b) Thermal and mesomorphic studies

TG trace for **17** (**Figure 4.144**) shows a total weight loss of 92.4% in the temperature range 154 ^{o}C to 499 ^{o}C due to decomposition of *p*-$CH_3(CH_2)_{15}OC_6H_4COO^-$ and bpy ligands (calculated, 94.0%). The results are in good agreement with its proposed structural formula. The amount of residue at temperatures above 499 ^{o}C was 7.6% (calculated, 7.7% assuming FeO). Hence, its decomposition temperature was 154 ^{o}C.

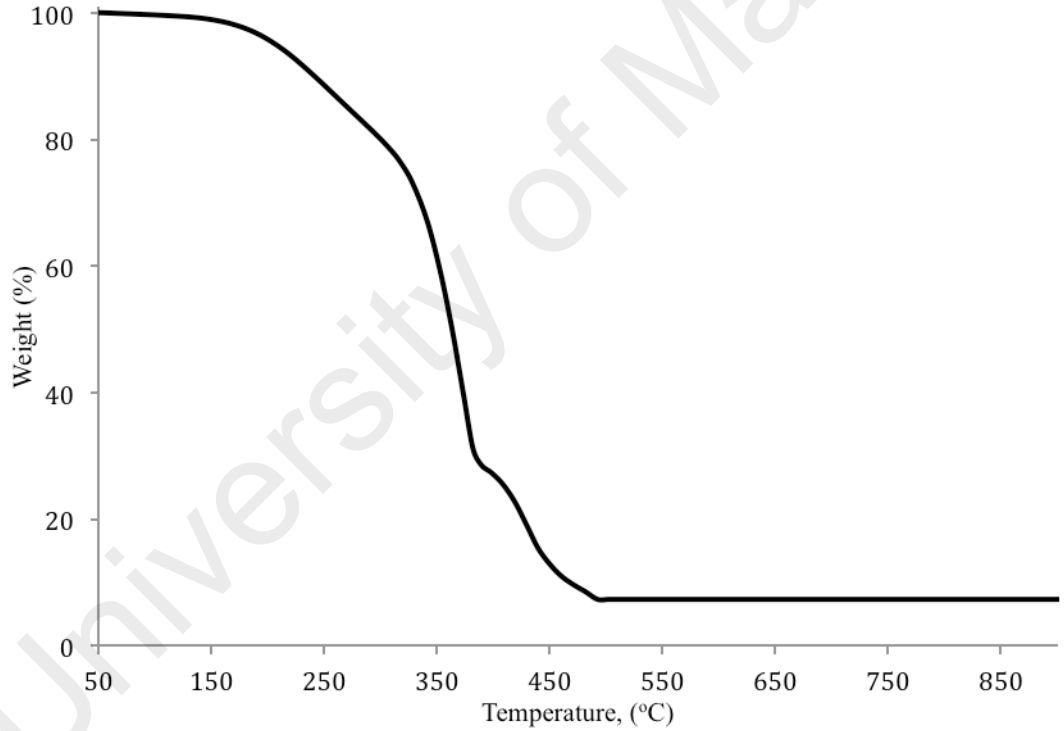

Figure 4.144 TGA trace of **17**

When viewed under **POM**, **17** started to melt at 72 ^{o}C and to clear at about 98 ^{o}C. On cooling from *I*, an optical texture was observed at 92 ^{o}C (**Figure 4.145**(**a**)). For comparison, its precursor complex, $[Fe_2(\mu\text{-}H_2O)(\mu\text{-}RCOO)_2(RCOO)_2(H_2O)_2]$ (R = *p*-$CH_3(CH_2)_{15}OC_6H_4$) was observed to melt at 102 ^{o}C and to clear to an isotropic liquid at 135 ^{o}C. Upon cooling from this temperature, optical textures different from **17**

were observed at 107 °C (**Figure 4.145(b)**). These observations indicate that both **17** and its precursor complex behaved as different thermotropic metallomesogens.

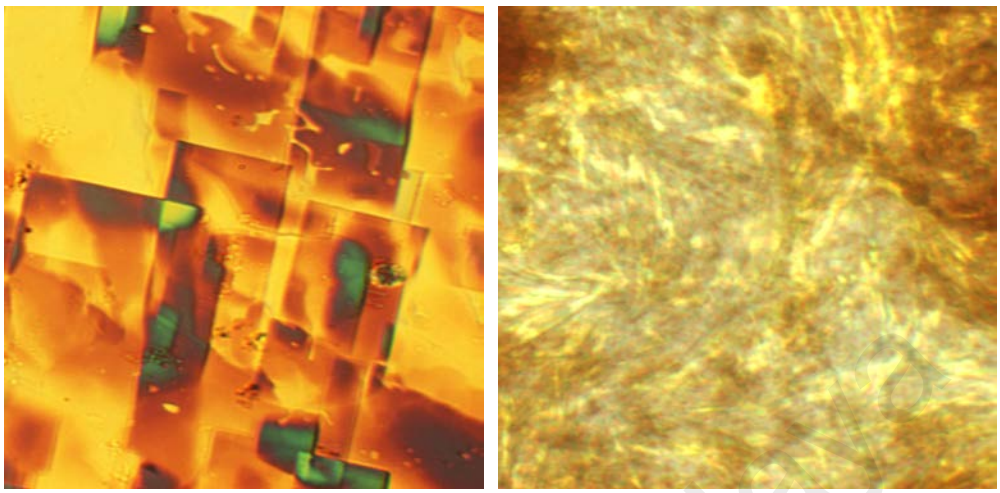

(a) (b)

Figure 4.145 Photomicrographs of: (a) **17** on cooling at 92 °C; and (b) $[Fe_2(\mu\text{-}H_2O)(\mu\text{-}RCOO)_2(RCOO)_2(H_2O)_2]$ (R = $p\text{-}CH_3(CH_2)_{15}OC_6H_4$) on cooling at 107 °C

The **DSC** traces for **17** (**Figure 4.146**) shows an overlapping endothermic peak at onset 75 °C ($\Delta H_{combined}$ = +40 kJ mol^{-1}) assigned to *Cr2-M* and *M-I* transitions. On cooling, an exothermic peak at onset 86 °C (ΔH = -31 kJ mol^{-1}) assigned to *I-M* transition.

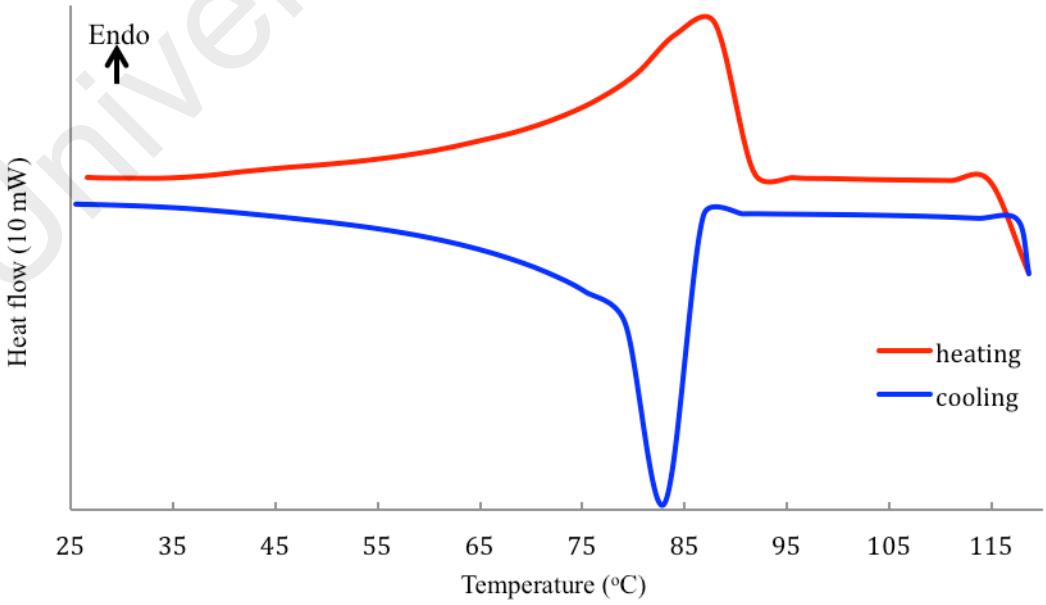

Figure 4.146 DSC scans of **17**

4.4.5 Summary

To summarize, the analytical data for the precursor complexes, $[Fe_2(\mu\text{-}H_2O)(\mu\text{-}RCOO)_2(RCOO)_2(H_2O)_2]$ (R = p-$CH_3(CH_2)_{9\text{-}15}OC_6H_4$) and complexes formed from their reactions with bpy (**14-17**) are shown in **Table 4.19** and **Table 4.20**, respectively.

Table 4.19 Precursor complexes of complexes **14 - 17**

Proposed chemical formula	$\Delta\nu_{coo}$ (cm^{-1})	λ /nm ($\varepsilon/M^{-1}\ cm^{-1}$)	$\chi_M^{corr}T$ ($cm^3\ K\ mol^{-1}$)	M*
$[Fe_2(\mu\text{-}H_2O)(\mu\text{-}RCOO)_2(RCOO)_2(H_2O)_2]$ (n = 9)	123 163	530 (793)	3.67 (61.1% HS)	Yes
$[Fe_2(\mu\text{-}H_2O)(\mu\text{-}RCOO)_2(RCOO)_2(H_2O)_2].H_2O$ (n = 11)	124 163	486 (1392)	3.04 (50.7% HS)	Yes
$[Fe_2(\mu\text{-}H_2O)(\mu\text{-}RCOO)_2(RCOO)_2(H_2O)_2]$ (n = 13)	126 164	493 (751)	2.45 (40.8% HS)	Yes
$[Fe_2(\mu\text{-}H_2O)(\mu\text{-}RCOO)_2(RCOO)_2(H_2O)_2]$ (n = 15)	122 165	594 (751)	2.10 (34.9% HS)	Yes

R = p-$CH_3(CH_2)_nOC_6H_4COO$, *M = mesomorphism

The precursor complexes have similar structural formula. They were aqua bridged dinuclear octahedral molecules with both bridging bidentate and chelating carboxylate ligands, and were made up of both HS and LS Fe(II) atoms at room temperature. All complexes behaved as thermotropic liquid crystals.

Table 4.20 Complexes **14 - 17**

Proposed chemical formula	$\Delta\nu_{coo}$ (cm^{-1})	λ_{max}, nm (ε, M^{-1} cm^{-1})	$\chi_M^{corr}T$ (cm^3 K mol^{-1})	T_{dec} (^oC)	M*
$[Fe_2(\mu\text{-RCOO})_2(RCOO)_2(bpy)]$ (*n* = 9, **14**; brownish red solid)	125 161	492 (154)	1.29 (21.5% HS)	169	Yes
$[Fe_2(\mu\text{-RCOO})_2(RCOO)_2(bpy)]$ (*n* = 11, **15**; brownish red solid)	146 161	511 (340)	1.21 (20.2% HS)	172	Yes
$[Fe(RCOO)_2(bpy)]$ (*n* = 13, **16**; red solid)	147	511 (26)	0 (100 % LS)	161	Yes
$[Fe(RCOO)_2(bpy)]$ (*n* = 15, **17**; red solid)	127	422 (255)	0 (100% LS)	154	Yes

R = *p*-$CH_3(CH_2)_nOC_6H_4COO$, *M = mesomorphism

Complexes **14** and **15** were dinuclear involving bridging bpy, and bridging and chelating carboxylate ligands, and have both HS and LS Fe(II) atoms at room temperature. In contrast, complexes **16** and **17** were mononuclear involving chelating bpy and carboxylate ligands, and have 100% LS Fe(II) atoms at room temperature indicating stronger Fe-N and Fe-O bonds.

The complexes were thermally stable in the temperature range of 154 ^oC to 172 ^oC. Their decomposition temperatures decreased with increasing number of carbon atoms in the alkyl chain, as similarly observed for Cu(II) complexes and may be similarly explained.

All complexes behaved as thermotropic liquid crystals. On heating, it is proposed that the bridging bpy ligands in **15** and **16** dissociated and the molecules formed $[Fe_2(RCOO)_4]$ with the paddle-wheel structure.

4.5 Molecular modelling

Molecular modelling was performed for copper(II) complexes in order to study the magneto-structural correlation, and for iron(II) complexes to ascertain their proposed structures by comparing their simulated FTIR spectra with the experimental spectra.

For the copper(II) complexes series, the geometrical optimization was successful for $[Cu_2(CH_3(CH_2)_8COO)_4(bpy)_2]$ (**1**) only, while for the iron(II) series, the results for $[Fe_2(CH_3(CH_2)_8COO)_4(bpy)(H_2O)_2]$ (**6**) and $[Fe(p\text{-}CH_3(CH_2)_{13}OC_6H_4COO)_2(bpy)]$) (**16**) only will be discussed since the results for the other complexes were similar since these complexes differ only in the carbon chain lengths, and because of insufficient space for calculation, and for some complexes, difficulties in optimization.

The main objective of the modelling was to determine the lowest energy conformations of these complexes. The wave functions from the equilibrium geometries were then used to determine the Mulliken charges, molecular electrostatic potential map and theoretical FTIR intensities (for iron(II) complexes). The energy was in Hartree atomic unit (a.u), which was then converted to the SI unit (kJ mol^{-1}) using the relationship: 1 a.u = 2625.5 kJ mol^{-1}.

Computational analyses were conducted through differential functional theory (DFT) with the three-parameter hybrid functional (B3) [85] for the exchange part and the Lee-Yang-Parr (LYP) correlation functional [86] using 6-31G basis set for copper(II) and iron(II), and in addition for **1**, self-consistent field (SCF) theory known as Hartree-Fork (HF) method using 3-21G basis set for the rest of the atoms.

4.5.1 Magneto-structural correlation and computational results for copper(II) complexes

The first step in the magneto-structural correlation study was determining the magnitude of the magnetic interaction $2J$, which can be calculated using the formula: $2J$ (cm^{-1}) = $-74.53\alpha + 7270$ [87], where α (in degree) was the Cu-O-Cu bond angle obtained from the molecular structures of single crystals. The value is negative if the interaction is antiferromagnetic, and positive if the interaction is ferromagnetic. From the J values, the Neél temperatures (T_N) were calculated using the equation: $J = -1.6\ kT_N$, where k = 0.69535 $cm^{-1}\ K^{-1}$ [88].

For copper(II) crystalline complexes (**1**, **2**, **3** and **5**), the Cu-O-Cu bond angles are shown in **Figure 4.147**, and the results of the calculation are shown in **Table 4.21**. It shows that all of these complexes have large negative 2J values, indicating strong antiferromagnetic interactions. The interaction in **2** was the weakest while that in **5** was the highest. The Neel temperatures were in a range -131.2 to -197.7 ^{o}C.

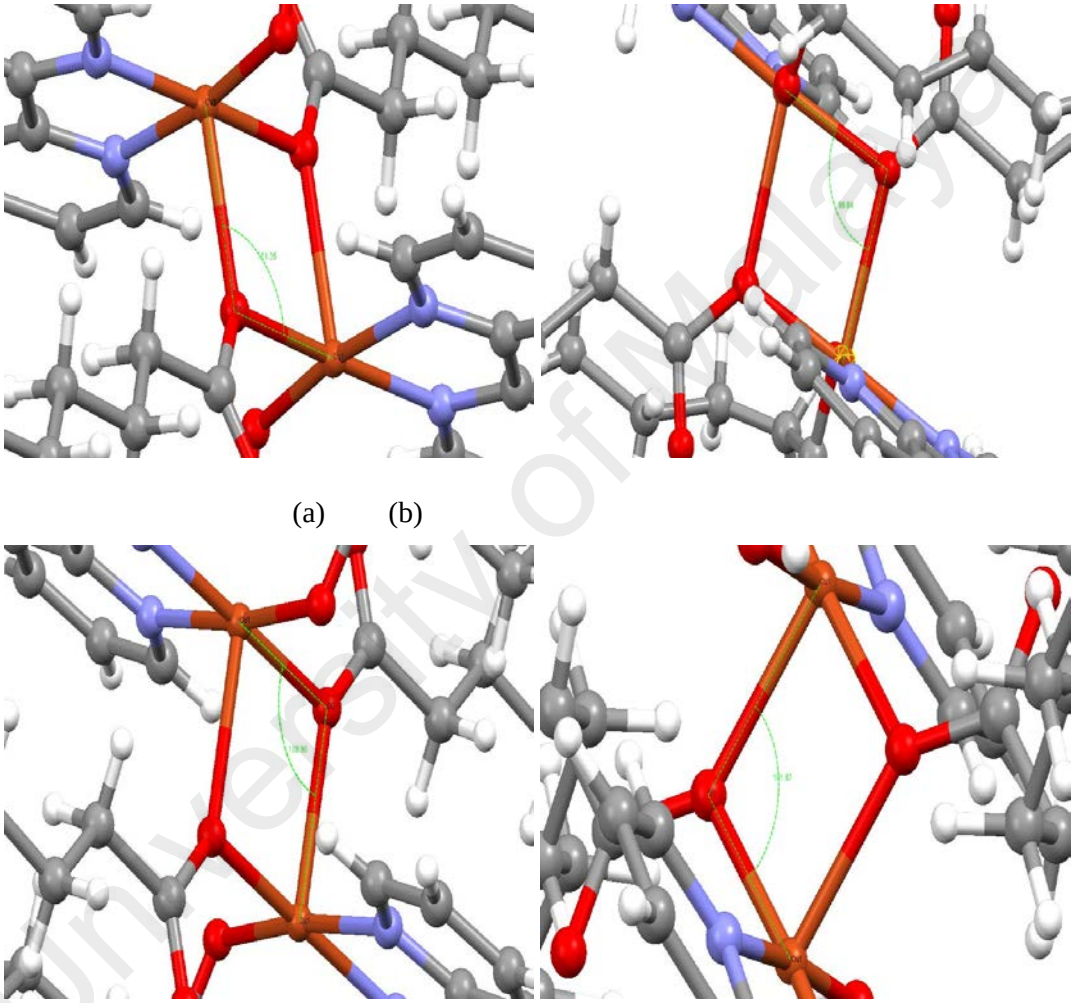

Figure 4.147 Cu-O-Cu bond angles for (a) **1**; (b) **2**; (c) **3**; and (d) **5**

Table 4.21 Magneto-structural correlation data for **1, 2, 3** and **5** based on the crystal data

Complex	Cu-O-Cu (^{o})	2*J* (cm^{-1})	T_N (^{o}C)
$[Cu_2(CH_3(CH_2)_6COO)_4(bpy)_2]$ (**1**)	101.3	-279.9	-147.4
$[Cu_2(CH_3(CH_2)_8COO)_4(bpy)_2]$ (**2**)	99.8	-168.1	-197.7
$[Cu_2(CH_3(CH_2)_{10}COO)_4(bpy)_2]$ (**3**)	100.9	-250.1	-160.8
$[Cu_2(CH_3(CH_2)_{14}COO)_4(bpy)_2]$ (**5**)	101.8	-317.2	-131.2

The above results are in agreement with the relationship proposed by Baggio *et al*. [29]. However, the experimental magnetic data (**Section 4.2.6**) showed that the interaction between the two copper(II) atoms were ferromagnetic based on the assumption that the geometry of copper(II) atoms was octahedral (g = 2).

Molecular modelling was then performed for all copper(II) complexes but was only successful for **1**. The minimized energy from the optimized structure of **1** (**Figure 4.148**), was -6127.99 a.u (-1.61 x 10^7 kJ mol^{-1}). Some selected geometrical parameters, such as the predicted bond lengths and angles, were compared with the X-ray diffraction data (**Table 4.22**). The theoretical and experimental data showed that the bond lengths and angles were similar. Based on the theoretical Cu-O-Cu bond angles, the 2J value was -220.3 cm^{-1} and T_N was -174.2 ^oC, which were in good agreement with the values calculated from the experimental data.

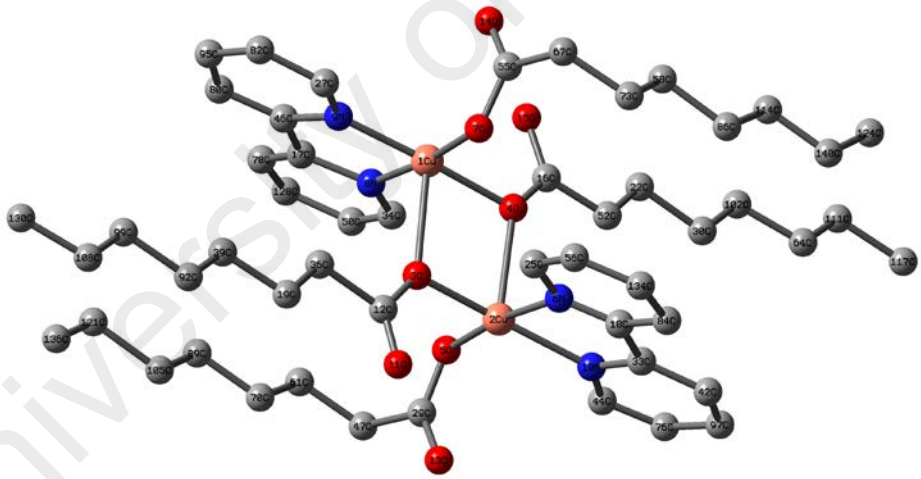

Figure 4.148 Optimised structure of **1**

Table 4.22 Comparison of bond lengths (Å) and angles (^{o}) for **1**

	Theoretical	**Experimental**
Bond length		
Cu(1)-O(4)	1.999	1.930
Cu(1)-O(7)	1.950	1.968
Cu(1)-O(3)	2.389	2.381
Cu(1)-N(9)	1.963	2.006
Cu(1)-N(8)	1.980	2.048
Angle		
O(4)-Cu-O(3)	78.36	78.70
O(4)-Cu-N(8)	102.43	103.60
O(3)-Cu-N(8)	174.13	173.60
O(4)-Cu-N(9)	93.44	93.60
O(3)-Cu-N(9)	94.77	95.50
N(8)-Cu-N(9)	80.71	80.20
O(4)-Cu-O(7)	90.65	91.40
O(3)-Cu-O(7)	90.59	90.35
N(8)-Cu-O(7)	173.83	172.50
N(9)-Cu-O(7)	95.15	95.64

4.6.2 Computational results and FTIR comparison for iron(II) complexes

All iron(II) complexes were not single crystals, and their structures were proposed based on combined instrumental data.

The minimized energy from the optimized structure of **6** (**Figure 4.149(a)**) and **16** (**Figure 4.149(b)**) obtained using 6-31G basis set, were -5346.83 a.u (-1.40 x 10^{7} kJ mol^{-1}) and -3535.68 a.u (-9.29 x 10^{6} kJ mol^{-1}), respectively.

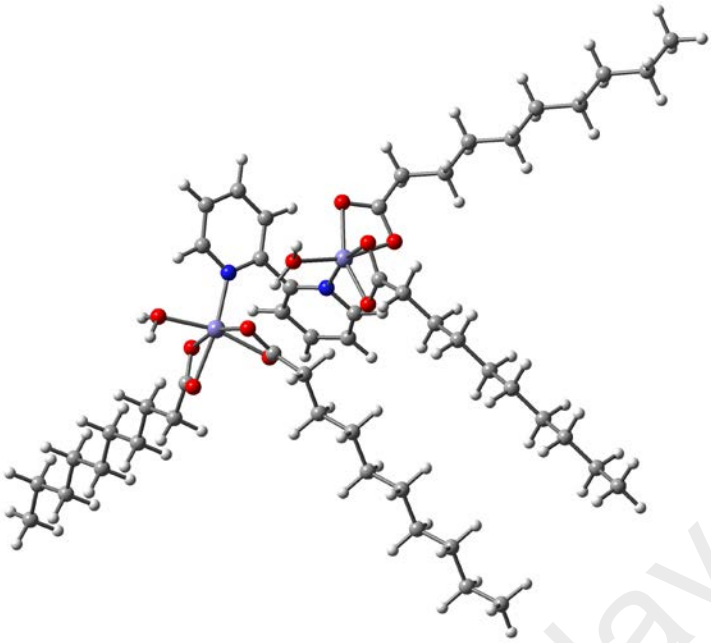

(a)

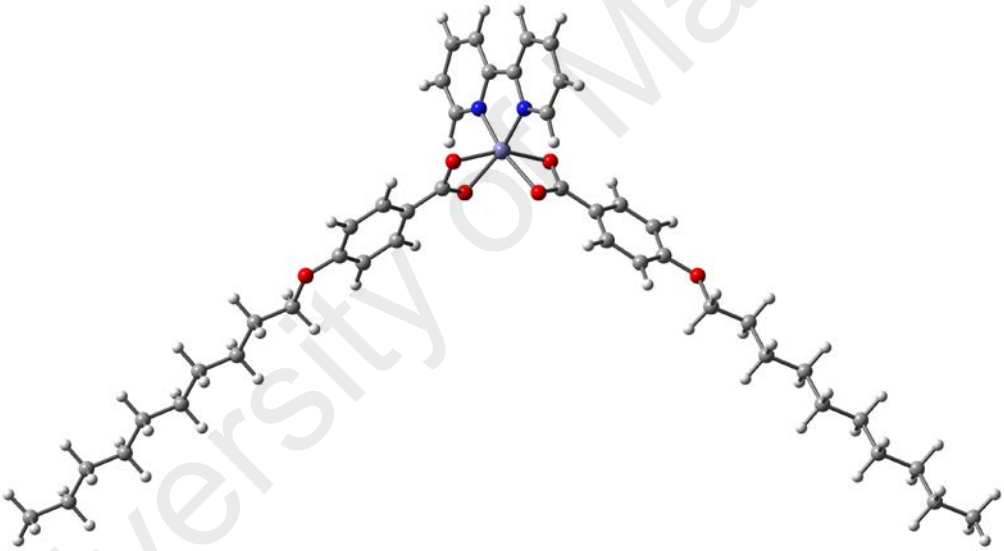

(b)

Figure 4.149 Optimized structure of: (a) **6,** and (b) **16**

The calculated FTIR intensities were then compared to the experimental intensities (**Figure 4.150**). The frequencies were scaled by a factor of 0.98 because of the overestimates calculation by B3LYP method [66]. The main functional groups of this complex were COO of the carboxylate ligand, C=C of the aromatic ring, C-N of bpy, and CH_2 of the alkyl chain. To achieve structural characterization, it is important to determine the vibrations of these groups. The assignments of the peaks were tabulated in **Table 4.23**, which shows good agreement between the theoretical and experimental

values. Hence, it may be concluded that the structures of these complexes are correctly proposed.

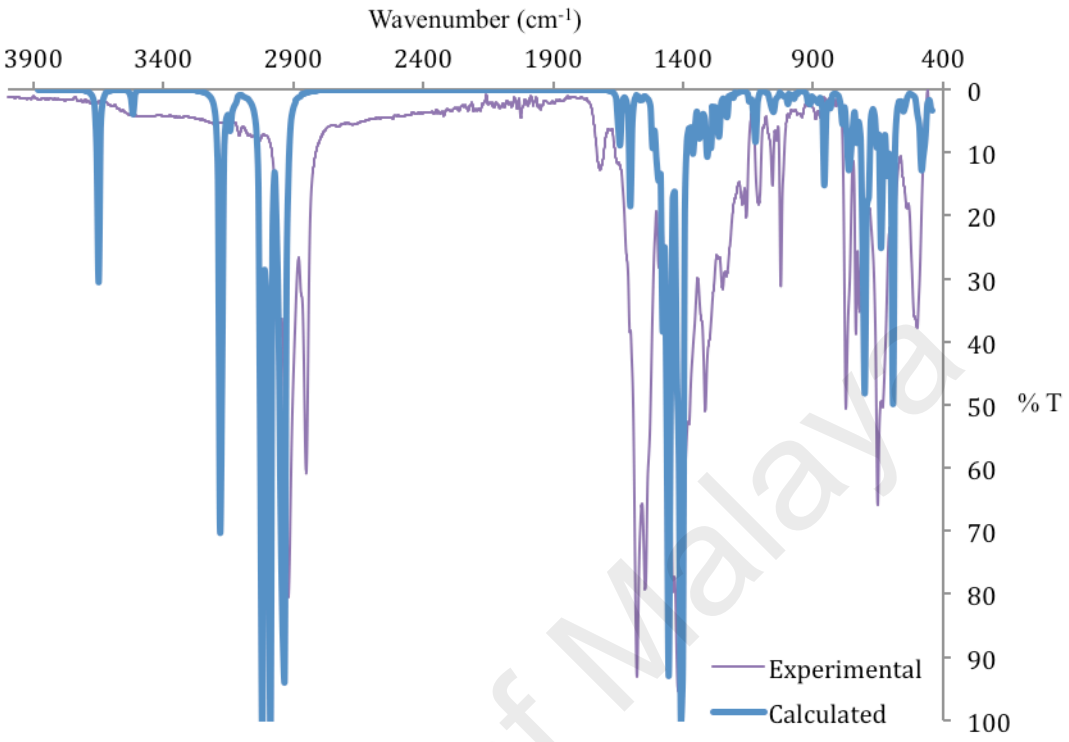

(a)

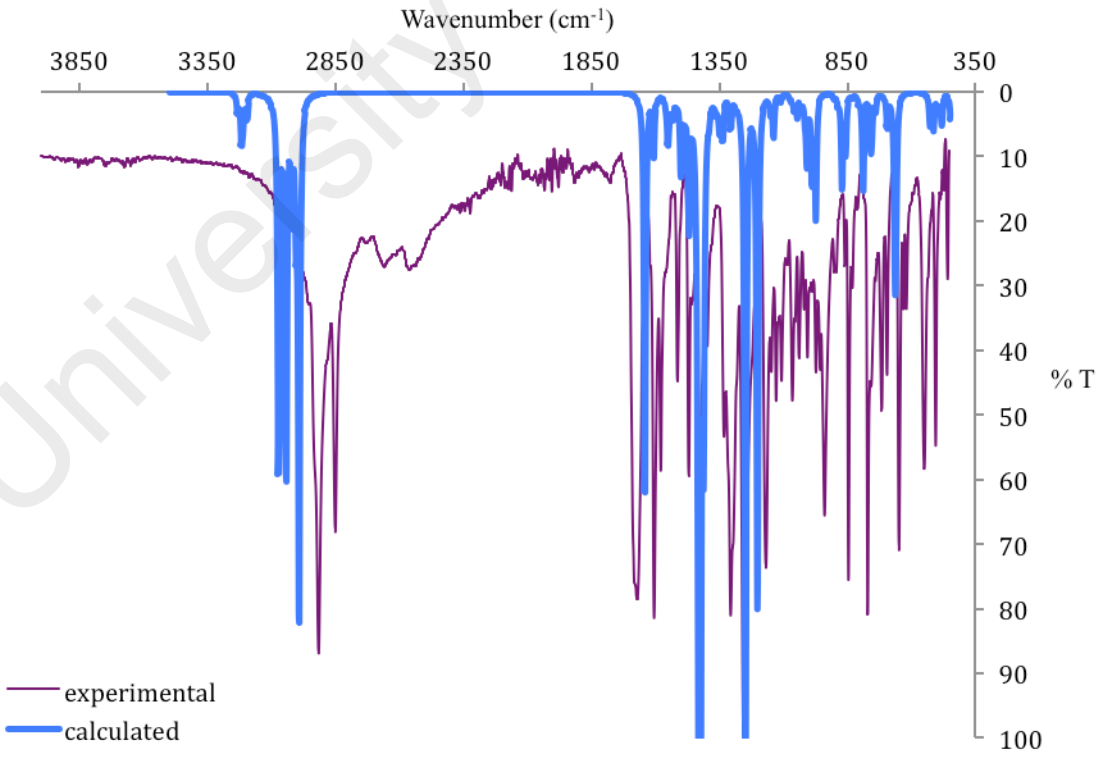

(b)

Figure 4.150 FTIR intensities for: (a) **6**; and (b) **16**

Table 4.23 Comparison of experimental and calculated data for FTIR peaks of **6** and **16**

	6		**16**	
Functional group	**Theoretical**	**Experimental**	**Theoretical**	**Experimental**
$CH_{2(asym)}$	2991, 2944	2923	2997	2916
$CH_{2(sym)}$	2936	2854	2993	2851
$COO_{(asym)}$	1507	1549	1608	1598
$COO_{(sym)}$	1445	1442/1411	1434	1470
C=C	1606	1580	1643	1606
C-N	1296	1318	1307	1307

CHAPTER 5: CONCLUSIONS AND SUGGESTIONS FOR FUTURE WORKS

5.1 Conclusions

Complexes of copper(II) and iron(II) alkylcarboxylates and *p*-alkyloxybenzoates with 2,2'-bipyridine as ligand were successfully synthesized and characterized. Their structural formulae are shown in **Table 5.1** and **Table 5.2**.

Table 5.1 Structural formulae of copper(II) and iron(II) alkylcarboxylates with bpy as ligand

Copper(II) complexes	Iron(II) complexes
$[Cu_2(CH_3(CH_2)_6COO)_4(bpy)_2]$ (**1**)	-
$[Cu_2(CH_3(CH_2)_8COO)_4(bpy)_2]$ (**2**)	$[Fe_2(CH_3(CH_2)_8COO)_4(bpy)(H_2O)_2]$ (**6**)
$[Cu_2(CH_3(CH_2)_{10}COO)_4(bpy)_2]$ (**3**)	$[Fe_2(CH_3(CH_2)_{10}COO)_4(bpy)_2(H_2O)_2].2H_2O$ (**7**)
$[Cu_2(CH_3(CH_2)_{12}COO)_4(bpy)_2]$ (**4**)	$[Fe_2(CH_3(CH_2)_{12}COO)_4(bpy)(H_2O)_2]$ (**8**)
$[Cu_2(CH_3(CH_2)_{14}COO)_4(bpy)_2]$ (**5**)	$[Fe_2(CH_3(CH_2)_{14}COO)_4(bpy)(H_2O)_2]$ (**9**)

Table 5.2 Structural formulae of copper(II) and iron(II) *p*-alkyloxybenzoates with bpy as ligand

Copper(II) complexes	Iron(II) complexes
$[Cu_2(R1COO)_4(bpy)_2].2H_2O$ (**10**)	$[Fe_2(\mu\text{-}R1COO)_2(R1COO)_2(bpy)]$ (**14**)
$[Cu_2(R2COO)_4(bpy)_2]$ (**11**)	$[Fe_2(\mu\text{-}R2COO)_2(R2COO)_2(bpy)]$ (**15**)
$[Cu_2(R3COO)_4(bpy)_2]$ (**12**)	$[Fe(R3COO)_2(bpy)]$ (**16**)
$[Cu_2(R4COO)_4(bpy)_2]$ (**13**)	$[Fe(R4COO)_2(bpy)]$ (**17**)

R1 = p-$CH_3(CH_2)_9OC_6H_4$; R2 = p-$CH_3(CH_2)_{11}OC_6H_4$; R3 = p-$CH_3(CH_2)_{13}OC_6H_4$; R4 = p-$CH_3(CH_2)_{15}OC_6H_4$

All copper(II) complexes were dinuclear with square pyramidal copper(II) atoms, monodentate nonbridging and *syn-anti* monodentate bridging carboxylato and chelating bpy ligands. Complexes **1**, **2**, **3** and **5** were crystals in the triclinic systems. Complex **1** showed negligible magnetic interactions between two copper(II) centres, while the other complexes showed ferromagnetic interactions when their effective magnetic moments were compared with the calculated value using the equation for two non-interacting copper(II) atoms with g = 2. However, the magneto-structural correlation studies using the Cu-O-Cu bonds from the X-ray data for the crystalline

complexes and the calculated 2*J* values showed strong antiferromagnetic interactions between the two copper(II) atoms. The latter results was supported by the results of molecular modeling for **1**, which showed good agreement between the experimental and calculated structures. Their decomposition temperatures were in the range of 161 – 240 ^{o}C, and in general, showed a gradually decreasing trend with increasing number of carbon atoms in the alkyl(oxy) chains. Complexes **1 – 5, 10** and **11** behaved as thermotropic liquid crystals, while **12** and **13** were not mesomorphic.

All iron(II) complexes with alkylcarboxylato were dinuclear with chelating carboxylato and bridging bpy ligands. On the other hand, complexes with *p*-alkyloxybenzoato ligands were dinuclear involving bridging and chelating carboxylato and bridging bpy ligands for **14** and **15**, and mononuclear involving chelating carboxylato and bpy ligands **16** and **17**. Molecular modelling performed for **6** and **16** showed good agreement between the experimental and simulated FTIR spectra, supporting the proposed structure formulae for these complexes. All dinuclear complexes were made up of both HS and LS iron(II) atoms at room temperature with higher percentage of LS iron(II) atoms, while all mononuclear complexes have 100% LS iron(II) atoms at room temperature. The complexes were thermally stable in the temperature range of 121 ^{o}C to 172 ^{o}C. Their decomposition temperatures decreased with increasing number of carbon atoms in the alkyl chain, as similarly observed for copper(II) complexes. All complexes with the alkylcarboxylato ligands have higher percentages of HS Fe(II) on heating, due to dissociation of $[Fe_2(R)_4(bpy)(H_2O)_2]$ to $[Fe(R)_2(bpy)]$ and $[Fe(R)_2(H_2O)_2]$. Complexes **6**, **8** and **9** were not mesomorphic while all other complexes behaved as thermotropic liquid crystals. On heating, it is proposed that the bridging bpy ligands in **14** and **15** dissociated and the molecules formed $[Fe_2(RCOO)_4]$ with the paddle-wheel structure.

5.2 Suggestions for Future Works

Variable-temperature small and wide angles X-ray scattering (SWAXS) experiments for the mesomorphic complexes are needed to confirm their mesophases.

In designing novel functional metallomesogens with more challenging requirements and for high-technology applications, combination of spin crossover and liquid crystalline behavior may lead to a number of advantages. For example, convenient processing SCO materials in the form of thin films, enhancement of spin transition signals, switching and sensing in different temperature regimes, or achievement of photo- and thermochromism in Fe(II) containing liquid crystals [89-94]. Hence, to gain further insight about the SCO, Superconducting Quantum Intefering Device (SQUID) is an important tool to use as it measures the molar magnetic susceptibility as a function of temperature. From the SQUID data, important data, such as the SCO temperature ($T_{½}$) and thermal hysteresis (ΔT) can be determined for the iron(II) complexes.

The SCO studies may also be extended to complexes of manganese(II) (valence electronic configuration d^5) and cobalt(II) (valence electronic configuration d^7).

Other potential uses of the copper(II) complexes, such as in medical applications, and of the iron(II) complexes, such as in dye-sensitised solar cells [95-97] and thermoelectricity, which converts heat energy directly to electricity [62,98], may be explored.

Finally, this research may be extended for complexes with carboxylato ligands with odd number of carbon atoms and branched chains, and with alkyl(oxy) substituted 2,2'-bipyridine in order to reduce their melting temperatures, and hence minimised decomposition and structural changes on heating.

REFERENCES

[1] Marcos. M., Romero, P.; Serrano, J. L. (1985) J*ournal of Chemical Society, Chemical Communications*, 1641

[2] Barberá, J.; Levelut, A. M.; Marcos, M.; Romero, P.; Serrano, J. L. (1991) *Liquid Crystals*, **10**, 119-126

[3] Valko, M., Mazur, M., Morris, H., Klement, R., Williams, C. J., Melnik, M. (2000) *Journal of Coordination Chemistry*, **52**, 129-138

[4] Hamza, F., Kickelbick, G. (2009) *Macromolecules*, **42**, 7762-7771

[5] Moncol, J., Vaskova, Z., Stachova, P., Svorec, J., Silanpaa, R., Mazur, M., Valigura, D. (2010) *Journal of Chemical Crystallography*, **40**(2), 179-184

[6] Yu, Y. –H, Ren, C.Y., Hou, G. –F., Ye, H., Gao, J. –S. (2012) *Journal of Coordination Chemistry*, **65**, 4137-4146

[7] Doyle, A., Felcman, J., Gambardella, M. T. P., Verani, C. N., Tristao, M. L. B. (2000) *Polyhedron*, **19**, 2621-2627

[8] Kozlevcar, B., Leban, I., Petric, M., Petricek, S., Roubeau, O., Reedjik, J., Segedin, P. (2004) *Inorganica Chimica Acta*, **357**, 4220-4230

[9] Agterberg, F. P. W., Provokluit, H. A. J., Driessen, W. L., Reedjik, J., Oevering, H., Buijis, W., Veldman, N., Lakin, M. T., Spek, A. L. (1998) *Inorganica Chimica Acta*, **267**(2), 183-192

[10] Iqbal, M., Ahmad, I., Ali, S., Muhammad, N., Ahmed, S., Sohail, M. (2013) *Polyhedron*, **50**(1), 524-531

[11] Wein, A. N., Cordeiro, R., Owens, N., Olivier, H., Hardcastle, K. I., Eichler, J. F. (2009) *Journal of Flourine Chemistry*, **130**(2), 197-203

[12] Cabaniss, S. E., McVey, I. F. (1995) *Spectrochimica Acta Part A: Molecular and Biomolecular Spectroscopy*, **51**(13), 2385-2395

[13] Rodil, S. E., Ferrari, A. C., Robertson, J., Muhl, S. (2002) *Thin Solid Films*, **420**, 122-131

[14] Joobeom Seo, S. –T. M., Kim, J., Lee, S. S., Park, K. –M. (2003) *Bulletin of Korean Chemical Society*, **24**, 1393-1395

[15] Chen, Y., Zhang, Y. –H., Zhao, L. –J. (2004) *Physical Chemistry Chemical Physics*, **6**, 537-542

[16] Mithun, R. A. K. P., Mukherjee, A., Munirathinam, N., Akhil, R. C. (2007) *Indian Journal of Chemistry*, **46**A, 227-237

[17] Gómez-Saiz, P., Garcia-Tojal, J., Maestro, M. A., Mahia, J., Arnaiz, F. J., Rojo, T. (2002) *Polyhedron*, **21**(22), 2257-2263

[18] Vafazadeh, R., Hayeri, V., Willis, A. C. (2010) *Polyhedron*, **29**(7), 1810-1814

[19] Wang, Y. Y., Shi, Q. Z., Gao, Y. C., Huo, X. (2000) *Polyhedron*, **19**(8), 891-898

[20] Bharati, K. S., Sreedaran, S., Rahiman, A. K., Rajesh, K., Narayanan, V. (2007) *Polyhedron*, **26**, 3993-4002

[21] Pajtasova, M., Ondrusova, D., Jona, E., Mojumdar, S. C., L'Alikova, S., Bazylakova, T., Gregor, M. (2010) *Journal of Thermal Analysis and Calorimetry*, **100**, 769-777

[22] Kahn, O. (1993) *Molecular Magnetism*, VCH Publisher, Inc., USA

[23] Shriver, D. F., Atkins, P. W., *Inorganic Chemistry*, Oxford University Press 4rd ed., p600

[24] Kato, M., Jonassen, H. B., Fanning J. C. (1964) *Chemical Reviews*, **64**, 99-128

[25] Youngme, S., Cheansirisomboon, A., Danviturai, C., Pakawatchai, C., Chaichit, N., Engkagul C., Van Albada, G. A., Costa, J. S., Reedjik, J., (2008) *Polyhedron*, **27**(7), 1875-1882

[26] Melnik, M. (1982) *Coordination Chemistry Reviews*, **42**, 259-293

[27] Rodríguez-Fortea, A., Alemany, P., Alvarez, S., Ruiz, E. (2001) *European Journal of Chemistry*, **7**(3), 627-637

[28] Crawford, V. H., Richardson, H. W., Wasson, J. R., Hodgson, J., Hatfield, W. E. (1976) *Inorganic Chemistry*, **15**(9), 2107-2110

[29] Baggio, R., Garland, M. T., Manzur, J., Peña, O., perec, M., Spodine, E., Vega, A. (1999) *Inorganica Chimica Acta*, **286**(1), 74-79

[30] Abdullah, N., Al-Hakem, Y., Abdullah, N., Samsudin, H., Ahmad Tajidi, N. S. (2014) *Asian Journal of Chemistry*, **26**(4), 987-990

[31] Castro, M. A., Rusjan, M., Vega, D., Peña, O., Weyhermüller, T., Cukiernik, F. D., Slep, L. D. (2011) *Inorganica Chimica Acta*, **374**, 499-505

[32] Mohamaddin., M. I., Abdullah, N. (2010) *Central European Journal of Chemistry*, **8**, 1090

[33] Santos-Martell, R. G., Ceniceros-Olguin, A., Larius-Lopez, L., Rodriguez-Gonzales, R. J., Navarro-Rodriguez, D., Donnio, B., Guillon, D. (2009) *Liquid Crystals*, **36**(8),787-797

[34] Serrano, J. L. (2008) *Metallomesogen: Synthesis, Properties, Applications*. Weinham, Federal Republic of Germany: VCH Verlagsgesellschaft mBH

[35] Park, L. Y., Rowe, J. M. (1998) *Chemistry of Materials*, **10**, 1069-1075

[36] Rodriguez, F., *Principles of Polymer System*, 4th edn. Washington: Taylor & Francis

[37] Elias, H. G. (1984) *Macromolecules: Structure and Properties* New York: Plenum Press

[38] Maldivi, P., Bonnet, L., Giroud-Godquin, A. M., Ibn-Elhaj, M., Guillon, D., Skoulious, A. (1993) *Advanced Materials*, **5**, 909

[39] Attard, G. S., Cullum, P. R. (1990) *Liquid Crystals*, **8**(3), 299-309

[40] Ramos, M. R., Martinez, F. J. C., Lopez-Andres, S., Garcia-Perez, M. V., Redondo, M. I. Y., Torres, M. R., Garrido, L., Rodriguez, J. A. C. (2008) *Crystal Growth and Design*, **8**(7), 2547-2554

[41] Donnio, B. (2002) *Current Opinion in Colloid and Interface Sci*ence, **7**, 371-394

[42] Demus, D., Richter, L. (1978) *Textures of Liquid Crystals*; Verlag Chemie Berlin p92

[43] Reger, D. I., Debreczeni, A., Smith, M. D. (2012) *Inorganic Chemistry*, **51**, 1068-1083

[44] Che Mat, A. N., Abdullah, N., Khaledi, H., Tee, J. T. (2011) *Acta Crystallography*, **67**, 599-600

[45] Baggio, R., Calvo, R., Garland, M. T., Peña, O., Perec, M., Slep, L. D. (2007) *Inorganic Chemistry Communications*, **10**, 1249

[46] Martin, R. L., Waterman, H. (1959) *Journal of the Chemical Society*, 1359-1370

[47] Harrison, W., Rettig, S., Trotter, J. (1972) *Journal of the Chemical Society-Dalton Transactions*, 1852-1856

[48] Konar, S., Manna, S. C., Zangrando, E., Chaudhuri, R. N. (2004) *Inorganica Chimica Acta*, **357**, 1593-1597

[49] Abdullah, N., Hashim, R., Ozair, L. N., Al-Hakeem, Y., Samsudin, H., Anita Marlina, Salim, M., Mohd Said, S., Subramanian, B., Nordin, A. R. (2015) *Journal of Material Chemistry C*, **3**, 11036-11045

[50] Tafili-Kryeziu, M., Weil, M., Muranka, T., Bousseksou, A., Hasegawa, M., Jun, A. (2013) *Dalton Transactions*, **42**, 15796-15804

[51] Konig, E., Madeja, K. (1966) *Chemical Communications*, 61-62

[52] Mohammed, R., Chanstanet, G., Tuna, F., Malkin, T. L., Barret, S. A., Kilner, C. A. (2013) *European Journal of Inorganic Chem*istry, 819-831

[53] Lu, X., Chau, K. –S., Wei, S., Deng, Z., Ding, N., Zhao, L., Wu, C. –M. L., Guo, W. (2013) *Jourrnal of Organometallic Chemistry*, **741-742**, 168-175

[54] Ha, N. N., Mai, A. T., Dang, X. T., Luong, T., Thu, T. (2014) *Journal of Solar Energy Engineering*, **137**(2),21006-21010

[55] Yoneda, K., Adachi, K., Hayami, S., Maeda, Y., Katada, M., Fuyuhiro, A., Kawata, S., Kaizaki, S. (2006) *Chemical Communications*, 45-47

[56] Reynolds, R. A. III, Dunham, W. R., Coucouvanis, D. (1998) *Inorganic Chem*istry, **37**(6), 1232-1241

[57] Coucouvanis, D., Reynolds, R. A. III, Dunham, W. R. (1995) *Journal of American Chemical Society*, **117**,7570-7571

[58] He. C., Lippard, S. (2001) *Journal of Inorganic Chemistry*, **40**, 1414-1420

[59] Edit, Y., T., Lippard, S. J. (2014) *Chemical Reviews*, **104**, 987-1012

[60] Abdullah, N., Mohd Said, S., Anita Marlina, Roslan, M. F., Azil, A., Nordin, A. R. (2015) *The Scientific World Journal*, 1-8

[61] Ferrere, S. (2000) *Chemistry of Materials*, **12**,1083-1089

[62] Abdullah, N., Elsheikh, M. H., Nik Ibrahim, N. M. J., Mohd Said, S., Mohd Sabri, M. F., Hassan, M. H., Anita Marlina (2015) *Royal Society of Chemistry Advances*, **5**, 50999- 51007

[63] Zheng, Y. –Z., Xue, W., Tong, M. –L., Chen, X. –M., Grandjean, F., Long, G. J. (2008) *Inorganic Chemistry*, **47**, 4077-4087

[64] Dykstra, C. E. (1986) *Ab Initio Calculations of the Structure and Properties of Molecules*, Elsevier Amsterdam

[65] Sagdinc, S., Pir, H. (2009) *Spectrochimica Acta Part A*, **73**, 181-194

[66] David, M. C., Meijer, A. J. H. M., Tsoi, W., C., Charlton, M. D. B., Kim, J. –S., Lidzey, D. G. (2010) *Journal of Physical Chemistry A*, **114**, 11920-11927

[67] Sheldrick, G. M. (1996) *SADABS*. University of Göttigen, Germany

[68] Bruker (2007) *APEX2 and SAINT*. Bruker AXS. Inc., Madison, Winconsin, USA

[69] Sheldrick, G. M. (2008) *Acta Crystallography Sect A*: **64**, 112-122

[70] Macrae, C. F., Edgington, P. R., McBabe, P., Pidcock, E., Shields, G. P., Taylor, R., Towler, M., Van de Streek, J. (2006) *Journal of Applied Crystallography*, **39**, 452-457

[71] Agterberg, F. P. W., Kluit, H. A. J. P., Drissen, W. L., Oevering, H., Buijis, W., Lankin, M. T., Spek, A. L., Reedjik, J. (1997) *Inorganic Chem*istry, **36**(20), 4321-4328

[72] Maldonado-Rogado, M. A., Vinuelas-Zahinos, E., Luna-Giles, F., Bernalte-Garcia, A. (2007) *Polyhedron*, **26**, 1173-1181

[73] Garcia-Tojal, J., Lezama, L., Pizarro, J. L., Insausti, M., Arriortua, M. I., Rojo, T. (1999) *Polyhedron*, **18**. 3703-3711

[74] Wang, A. (2012) *Acta Crystallography E*, **68**, 43

[75] Asem, S., Buchanan, R. M., Mashuta, M. S. (2011) *Acta Crystallography E*, **60**, 577

[76] Perlepes, S. P., Huffman, J. C., Christou, G. (1992) *Polyhedron*, **11**, 1471-1479

[77] Chisholm, M. H., Kober, E. M., Ironmonger, D. J., Thornton, P. (1985) *Polyhedron*, **4**(2), 1869-1874

[78] Petric, M., Leban, I., Segedin, P. (1995) *Polyhedron*, **14**, 983

[79] Moita, M. F. R., Duarte, M. L. T. S., Fausto, R. (1994) *Journal of Chemical Society Faraday Trans*actions, **90**(19), 2953-2960

[80] Korendovych, I. V., Kryatov, S. V., Reiff, W. M., Rybak-Akimova, E. V. (2005) *Inorganic Chem*istry, **44**(24), 8656-8658

[81] Deacon, G. B., Philips, R. J. (1980) *Coordination Chemistry Rev*iews, **33**, 227-250

[82] Hogg, R., Wilkins, R.G. (1962) *Journal of Chemical Soc*iety (Resumed) 341-350

[83] Judge, J. S., Baker Jr, W. A. (1967) *Inorganica Chimica Acta*, **1**, 68-72

[84] Sorai, M. (2004) *Heat Capacity Studies of Spin Crossover Systems, in Spin Crossover in Transition Metal Compounds III*. Springer Berlin Heidelberg, 153-170

[85] Becke, A. D. (1993) *Journal of Chemical Physics*, **98**, 5648-5652

[86] Lee, C. Yang, W., Parr, R. G. (1988) *Physical Review*, **37**B, 785-789

[87] Cao-Yuan, N. (2011) *Crystal Growth & Design*, **11**, 2874-2888

[88] Jotham, R. W., Kettle, S. F. A., Marks, J. A. (1972) *Journal of Chemical Society Dalton*, 428-438

[89] Gaspar, A. B. Ksenofontov, V., Seredyuk, M., Gütlich, P. (2005) *Coordination Chemistry Rev*iews, **249**, 2661-2676

[90] Seredyuk, M., Gaspar, A. B. Ksenofontov, V., Galyametdinov, Y., Kusz, J. Gütlich, P. (2008) *Journal of American Chemical Soc*iety, **130**(4), 1431-1439

[91] Seredyuk M., Gaspar A.B., Ksenofontov V., Galyametdinov Y., Kusz, J., Gütlich, P. (2008) *Advanced Functional Materials*, **18**, 2089-2101

[92] Seredyuk, M., Gaspar, A.B., Ksenofontov, V., Reiman, S., Galyametdinov, Y., Haase, W., Rentschler, E., Gütlich, P. (2006) *Chemistry of Materials*, **18**, 2513-2519

[93] Seredyuk, M., Gaspar, A.B., Ksenofontov, V., Reiman, S., Galyametdinov, Y., Haase, W., Rentschler, E., Gütlich, P. (2006) *Hyperfine Interact*ions, **166**(1-4), 385-390

[94] Seredyuk, M., Gaspar, A.B., Ksenofontov, V., Galyametdinov, Y., Verdaguer, M., Villain, F., Gütlich, P. (2008) *Inorganic Chem*istry, **47**(22), 10232-10245

[95] Ferere, S., Gregg, B. A. (1998) *Journal of American Soc*iety, **120**, 843-844

[96] Ferere, S. (2000) *Chemistry of Materials*, **12**, 1083-1089

[97] Ferere, S. (2002) *Inorganica Chimica Acta*, **329**, 79-92

[98] Abraham, T. J., MacFarlane, D. R., Pringle, J. M. (2013) *Energy & Environmental Science*, **6**, 2639-2645